The Role of Tumour Vasculature in Fluid Flow and Drug Transport in Solid Tumours

By

Moath Zaid A Alamer

A Thesis submitted in fulfilment of the requirements for the degree of

Doctor of Philosophy and Diploma of Imperial College London

Department of Chemical Engineering

Imperial College London

November 2019

Declaration of originality

I hereby certify that the work in thesis is my own unless otherwise stated and that all contributions have been appropriately acknowledged. Work derived from published and unpublished work of others has been appropriately referenced.

Copyright Declaration

Abstract

The aberrance of the vasculature in tumours has been linked to increased aggressiveness and poor drug delivery in tumours. Complexities in the microarchitecture of tumour vasculature occurring on microscopic scales can affect fluid flow and drug transport making it difficult to predict tumour response to treatment. Given this, mathematical models can play an important role in understanding the various aspects of the tumour vasculature that can promote invasiveness and limit drug delivery. In this work, computational models are developed to investigate the effect of tumour vasculature on fluid flow and drug distribution and novel imaging methods are assessed for their ability to characterise the tumour vasculature in whole human tumours. A mathematical angiogenesis model is used to generate microscopic details including individual vessel properties on a whole vascular network scale which are coupled with a fluid flow and drug transport model. The interstitial fluid pressure (IFP) in the tumour model was found to be elevated with increased heterogeneity caused by the presence of a necrotic core and heterogenous vessel permeability. Subtle changes to the network on a microscopic scale significantly influenced fluid flow in the tumour vessels and tissue.

Delivery of doxorubicin to tumours was found to be highly dependent on the properties of tumour vasculature and blood flow, where regions with excessive branching and vessel tortuosity had reduced drug concentrations due to poor blood flow. Hence, the vascular density was not found to be the main factor in the accumulation of the drug within the tissue space and it's uptake by cancer cells. An interplay between treatment strategy including dose and administration mode and properties of the vasculature was found by evaluating the spatial intracellular concentration. The fluid flow and drug transport models showed the significant effect of incorporating the microscopic properties of the tumour vasculature which can influence fluid flow and drug distribution on a macroscopic scale.

The imaging methods assessed in this work shows that Optical projection tomography combined with fluorescent Immunohistochemistry labelling methods can be used to extract angiogenesis related parameters in whole human tumours. Additionally, the method was able to extract clean network topologies that show promise in application to understanding fluid flow and drug transport in real tumours.

Acknowledgements

I would like to express my thanks to my supervisor Professor Xu for her guidance and support during my PhD. She has been gracious with her time and provided a productive and stimulating environment to pursue my research.

In my PhD I've had the opportunity to collaborate and work with a number of people which has been valuable. I would like to express my gratitude to Dr Paula Cunnea who has been extremely helpful in answering my questions, providing guidance in staining the tumour tissue samples and allowing access to the use of her lab. I would also like to thank Professor Christina Fotopoulou who performed the surgeries, provided these samples and provided feedback on some of the imaging work. I'd like to thank Professor Paul French and Dr James McGinty for allowing access to the OPT imaging system at the Crick Institute and Samuel Davies for imaging the samples and his input in answering any queries I had. I want to express my thanks to Dr Hari Arora for providing training to use the Histocutter and Joel Eustaquio and Marta Garcia-Bellmunt for their technical support in using the Histocutter.

My PhD was generously supported by UKSACB for which I'm thankful. I'm also grateful for all their members of staff who have been extremely supportive throughout the years.

I would like to thank the members of the Xu group who have been friends and great colleagues during my PhD including Boram, Selena, Andris, Claudia, Nasrul, Howard, Yu, Karl, Chloe, Emily and Sampad.

Finally, I'd like to thank my family and friends who provided me with moral support and with whom I have formed many great memories during my PhD.

Table of Contents

List of Figures

1 Introduction

1.1 Cancer Background

According to the World Health Organization, cancer is one of the leading causes of mortality and morbidity, with approximately 14.1 million new cases and 8.2 million deaths recorded in 2012. By as early as 2025, 20 million new cases are expected annually [1]. Significant time and resources have been invested in addressing cancer that have led to vital discoveries in the genetic and functional properties of cancer and the development of novel treatment strategies. Although overall mortality rates have reduced, the age-adjusted mortality rate for cancer has not seen significant change in the past 50 years [2]. The disease is difficult to tackle due to its complexity; it can affect different of types of tissue and arise from mutations based on the individual's genes. As a result, cancer treatment methods have in many cases shown limited efficacy with inconsistent outcomes for different patients and cancer types.

Solid tumours make up approximately 90% of all human cancers. They pose a great challenge for treatment with the most common types of treatments being surgery, chemotherapy and radiotherapy [3]. Surgery can be most efficient for benign tumours that are isolated and easily accessible, where the risk of complication is low. However for some invasive and metastatic tumours that might extend into the surrounding tissues or other parts of the body, surgery alone is not a viable form of treatment [4]. Radiation therapy involves the use of high energy particles to convert oxygen molecules into potent free radicals that damage the DNA of cancer cells [5]. The ability of radiation therapy to target the tumour and reduce side effects is desirable however hypoxia, commonly found in tumours, limits the use of radiation therapy alone, making it employed more as an adjuvant form of treatment [6]. Additionally, chemotherapy which involves the use of intravenously injected chemicals has been shown to be inconsistent in the treatment of tumours [7]. Whilst the inefficiency of cancer treatments can be partially attributed to the molecular mechanisms of drug resistance at cellular level, numerous studies have shown that the tumour microenvironment limits the ability of anticancer drugs to distribute evenly within the tumour and to reach cancer cells at lethal concentrations. The unique physiology of tumours presents several obstacles for current therapeutic methods. Heterogeneous vascular structure and distribution,

high interstitial fluid pressures, dense interstitial matrix and the presence of hypoxic regions are all features of tumours that contribute to the limited success of current cancer treatment methods. All these characteristics of the tumour microenvironment are incredibly dynamic that vary spatially and temporally, change from patient to patient and are tightly coupled where alterations in one property of the tumour microenvironment can influence the other. Hence, a detailed understanding of the properties of the tumour microenvironment and their effects on fluid flow and drug transport are needed. In what follows, a brief overview of the tumour microenvironment and the barriers to drug delivery is given.

1.2   The Tumour microenvironment – An overview

Cancer cells initially form from a single cell or a group of cells that have mutated to exhibit a loss of control on growth and division [8]. These cells can proliferate in an unregulated manner to form a neoplastic lesion embedded in a tissue [9]. Cancer cells in this lesion can interact with normal cells in the surrounding tissue to induce changes to the tissue that can promote growth and spread of the lesion leading to the formation of a malignant solid tumour. Hence, solid tumours can be described as organs made up of cancer and normal cells of different types embedded in an extracellular matrix (ECM) with its own vascular supply [10]. Unlike normal tissue, the changes induced by cancer cells cause solid tumours to exhibit abnormal properties including aberrant vasculature, poorly functional lymphatics, and high interstitial fluid pressure which can play a significant role in the transport and delivery of therapeutics [11, 12]. These properties are described more in depth in this subsection.

1.2.1   Vasculature

Blood vessels play a critical role in supplying oxygen, nutrients and any required therapeutic molecules to cells in tissues. The vasculature in tumour tissue differs strikingly from that found in normal tissue featuring several aberrant properties. A better understanding of the origin of the vasculature in tumours and how it develops can provide insight into the causes of these abnormalities in tumour vasculature.

1.2.1.1   Tumour angiogenesis

Small tumours with a diameter no larger than 2 mm utilize the host vasculature to supply nutrients to cells [13]. As the tumour begins to outgrow its own vasculature, avascular regions emerge that lead to hypoxia and cell death. Hence for a tumour to grow, new vasculature is formed through sprouting and outgrowth from pre-existing vessels in a process termed angiogenesis [14]. The process is regulated by a balance

between activator and inhibitor molecules. Activator molecules include diffusible angiogenic factors such as vascular endothelial growth factor (VEGF) and basic fibroblast growth factor (bFGF). Angiogenesis is a normal process that occurs throughout life, playing a role in growth and wound healing [15]. In normal angiogenesis, newly formed blood vessels mature rapidly and become stable as the pro and anti-angiogenic molecules are tightly regulated. In tumour tissue, angiogenic factors secreted by cancer cells and other tissue cells are upregulated whilst anti-angiogenic factors are downregulated causing a net balance favouring angiogenesis. As a result, new vessels are continuously remodelled and never allowed to mature and stabilize, hence, tumours are described as wounds that never heal [16]. The tip in balance toward angiogenesis in tumours has not been clearly elucidated, however several stimuli are thought to be triggers including hypoxia, low pH, mechanical stress caused by proliferating cancer cells and immune/inflammatory response [17-19]. The angiogenesis process involves a number of steps as illustrated in Figure 1.1. Initially, factors secreted by cancer cells diffuse and form a gradient to nearby blood vessels. Receptors on endothelial cells lining these blood vessels identify these factors and the cells begin to secret chemicals that breakdown the basement membrane. Tip endothelial cells of the sprout migrate in response to angiogenic factor gradients whilst stalk cells proliferate as a result of angiogenic factor concentration. The tube-like structures formed can then differentiate into arterioles, venules and capillaries [20, 21].
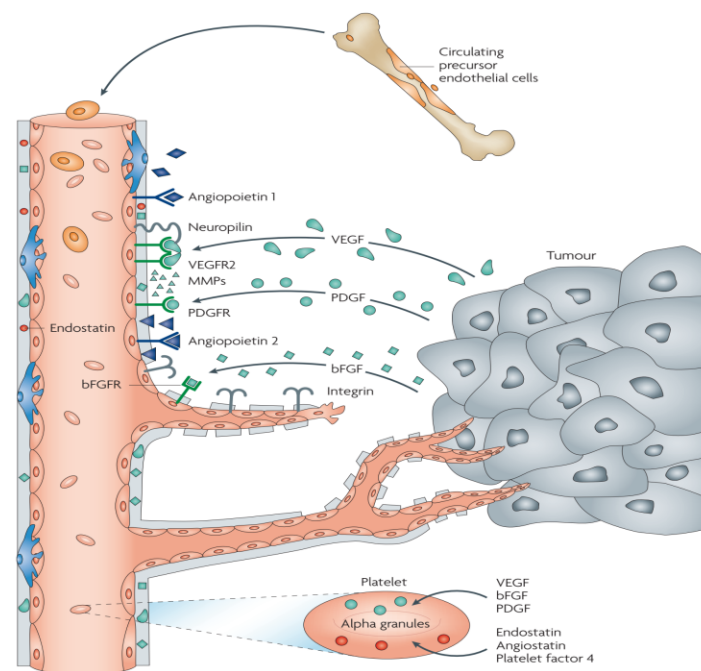
Figure 1.1: *Illustration of key regulators in angiogenesis (extracted from [20])*

1.2.1.2   Morphology and Architecture

The vessels formed through angiogenesis in tumours have been found to be heterogeneous and differ greatly from their respective normal counterparts [22]. This can be attributed to the abnormalities found in the cellular components making up the tumour vessels [23]. Blood vessels are normally made up of different cellular components depending on the type and role of the vessel. Capillaries and venules are made up of endothelial cells, pericytes and a basement membrane whilst arterioles are also lined with smooth muscle cells and are absent pericytes. Endothelial cells play a vital role in regulating blood flow and the exchange of nutrients and other permeable solutes with the tissue space. In normal tissue, endothelial cells are quiescent forming a single monolayer with tight inter-endothelial junctions that allows for efficient exchange of nutrients and other permeable solutes with the tissue space. Cells are aligned in the direction of blood flow in a streamlined fashion to optimize perfusion. Tumour endothelial cells are activated and are poorly organized as they can stack on top of each other leaving open wide junctions with fenestrations that can cause excessive leakiness [24]. The molecular signalling of tumour endothelial cells is heterogeneous resulting in a lack of features that define arterioles, capillaries or venules [25]. Pericytes that play a role in stabilizing vessels and regulating response to mechanical and metabolic stimuli in normal tissue. In tumours, they are highly active, immature and detached from endothelial cells resulting in poor pericyte coverage on the vessels which contributes to abnormal flow properties [26]. The basement membrane that lines the endothelial cells acts to provide stability to the vessels and control the extravasation of solutes and nutrients. Whilst normal vessels possess a thin homogenous layer of basement membrane, in tumours, it can be heterogeneous in coverage and thickness [27].
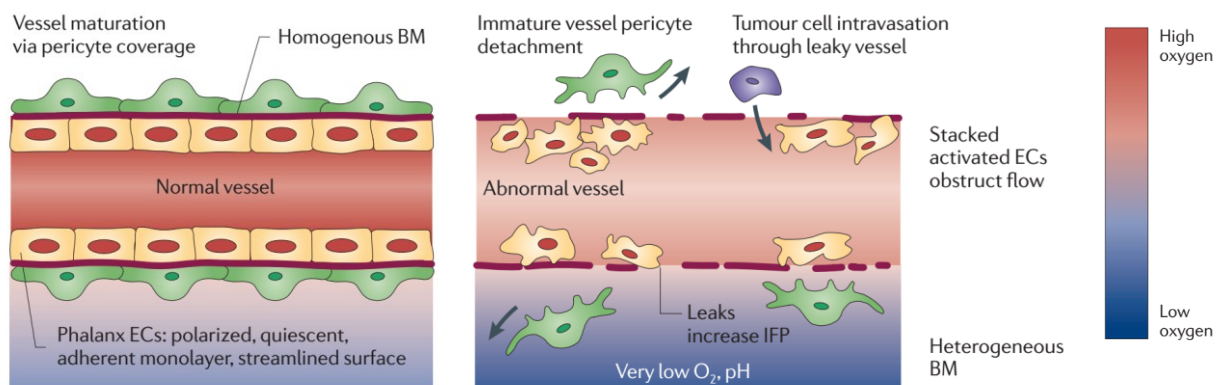
Figure 1.2: Cells features of microvessel walls in normal vessels (left) and tumour vessels (right) (extracted from [25])

14

As a consequence of the abnormalities in cells lining the tumour vessels, they exhibit higher vessel leakage [28, 29]. Therefore, the permeability of vessels is generally higher in tumours and can vary depending on the tumour type and size [30, 31]. An 8-10 fold increase in permeability has been observed in tumour tissue compared to normal tissue [32]. The permeability has also been found to be heterogeneous in tumour tissue with different regions exhibiting substantially varied permeability [33].

In normal tissue, vessels are well distributed and are organised within the tissue space in a hierarchical manner starting from arteries branching to arterioles and then capillaries which merge to form venules and veins. This structure allows for efficient transport of oxygen and nutrients to cells in the tissue. The tumour vasculature lacks this hierarchy with no clear distinction between different vessel types (Fig 1.3.) which can be attributed to the abnormal cellular properties [3, 34].
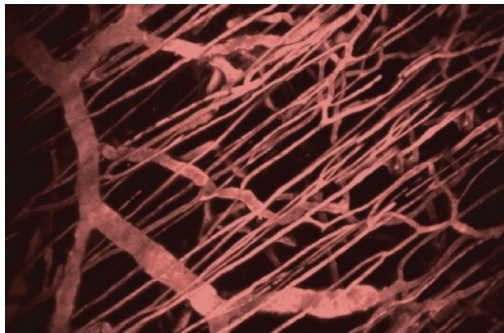
Normal tissue vasculature   **Tumour tissue vasculature**
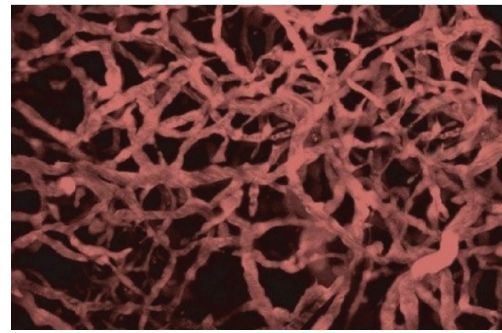
Figure 1.3: Images of the normal and tumour microvasculature (extracted from [35])

Due to the constant remodelling in angiogenesis, the architecture of the vasculature in tumours becomes tortuous and features complex patterns. Less et al. quantitatively analysed the branching patterns and geometric properties of vasculature in a mammary carcinoma [36]. They found the branching patterns consisting of several loops including self-loops and nonplanar loops with many branches. Trifurcations were a common feature and venous convolutions were found in regions near arterial vessels (Fig. 1.4). Vessels exhibited erratic changes in diameter during branching where small vessels were found to branch off vessels that were an order of magnitude larger in diameter.
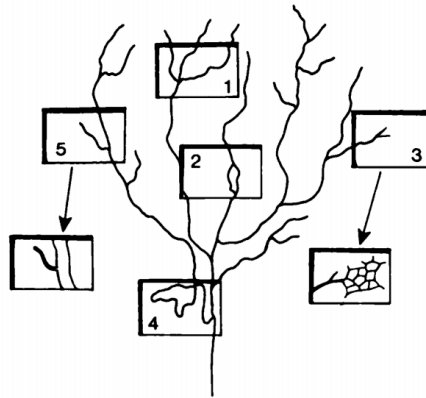
Figure 1.4: Several features of tumour vasculature topology including trifurcations (1), self-loops (2), characteristic polygonal structure of the capillary meshwork, (4) venous convolutions, and (5) small (20~40 μm) vessels branching off of large (200 μm) vessels (extracted from [36])

The intercapillary distance is an important parameter as it determines the distance required for nutrients and oxygen to reach cells. The diffusion limit of oxygen is 100-200 μm with evidence showing that hypoxia can develop when the intercapillary distance exceeds 140 μm [37]. Konerding et al. performed another study evaluating the vascular architecture of four different tumour cell lines transplanted in mice and compared them with the architecture found in two normal tissues, the gut and muscle [38]. The mean intercapillary distance varied significantly depending on the tumour and ranged from 76-213 μm. Overall the distance was greater than that found in normal tissue which ranged from 35-63 μm. The structure and distribution of the tumour vasculature were found to be heterogeneous with some regions being avascular. The mean vessel diameter was found to be 2-3 times larger than that in normal tissue, with variations in vessel diameter being significantly higher in tumour tissue that in normal tissue.

1.2.2   Blood flow

The flow behaviour of blood in vessels is governed by several factors, mainly being the microvascular pressure difference between the arterial and venous ends, the geometric resistance to flow and rheological properties of blood. The difference in the vasculature between tumour and normal tissue is reflected in the blood flow behaviour in tumours. Perfusion characteristics in rat mammary tumours and normal tissue were compared showing that the maximum perfusion capacity was lower in tumours and decreased as the tumour increased in size [39]. This is caused by the higher geometric vascular resistance which was found to be 1-2 orders of magnitude higher than normal tissue [40]. The complex vascular architecture with excessive branching and erratic changes in diameter are known to be a cause.

Additionally, vessels have a reduced cross-sectional area for fluid flow due to compression by proliferating cells which consequently increases resistance and affects shear rate and perfusion [41]. Increased geometric resistance to flow was found in P22 carcinosarcoma implanted in different sites. Resistance increased with tumour size and varied depending on the tumour site [42]. The viscosity of blood is governed by the haematocrit defined as fractional volume of red blood cells (RBC) in the blood. In tumours the apparent viscosity is found to be higher, due to plasma loss caused by leaky vessels and erratic changes in diameter during branching which increases haematocrit [43, 44]. The change in viscosity can affect the pathways taken by the blood and consequently limit flow in some vessels. These discrepancies in geometric and viscous resistance to flow in tumours result in some abnormal blood properties including unstable flow directions, plasma skimming, stagnant flow and irregular velocities [45]. The presence of arterio-venous shunts has been shown to cause blood flow to completely bypass a network of capillary vessels and thus divert flow away from some pathways [46].

1.2.3   Lymphatics

Lymphatic vessels play a vital role in blood circulation, tissue fluid homeostasis and immune function. Excessive fluid in the interstitium is drained by lymphatic vessels and transported to the lymph nodes, which act as filtering stations, after which the fluid is transported back into systemic circulation [47]. In tumours, the function of these lymphatic vessels is impaired. The distribution of lymphatic vessels in tumour tissues tends be heterogeneous where in most cases they occur mostly in the peritumoural region. Lymphatics vessels in the peritumoural region are characterised by their dilated, disorganised and excessively leaky nature in comparison to vessels in the intratumoural region which tend to be compressed and deformed due to the high proliferation of cancer cells [48-50]. As a result, fluid in the intratumoural region is not drained which can lead to pressure build up.

1.2.4   Interstitial fluid pressure

The interstitial space is an important mediator in the exchange of oxygen, nutrients and waste products between blood vessels and cells. In normal tissue, the transcapillary flow is governed by the hydraulic conductivity and protein reflection coefficient in addition to the hydrostatic and osmotic pressure differences between the capillaries and the interstitium. Additionally, interstitial fluid pressure (IFP) is influenced by the interactions between the stromal cells and ECM molecules as well as the functioning of lymphatics. The fluid leakage from capillaries to the interstitium in tumours is several orders of magnitude

larger than in normal tissue [51]. This combined with poor intratumoural lymphatic drainage results in the hydrostatic and osmotic interstitial pressures of most tumours to be higher than in normal tissue and reach values close to 60 mmHg in some tumours [52, 53]. Measurements of the IFP profiles showed uniform pressures throughout the core of the tumour with a rapid drop at the periphery [54]. An illustration of the differences in the forces that govern transcapillary fluid exchange between normal and tumour tissue is shown in Fig 1.5.
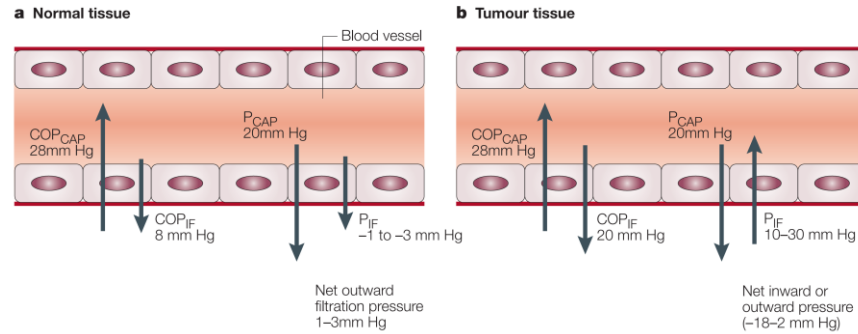
Figure 1.5: Forces governing transvascular fluid exchange (extracted from [55])

Although the lack of lymphatic drainage and high vessel leakiness are known to play a major role in raising IFP in tumours, other factors are thought to come into play including changes to the morphology of fibroblasts and modification of the ECM. Measurements of osmotic pressure in tumours showed that the transcapillary oncotic pressure gradient was close to zero [56]. This demonstrates that the transcapillary fluid exchange in tumours is governed mainly by the hydrostatic pressure difference [57].

1.2.5   Implications for drug delivery

Intravenous infusion is the most commonly adopted form for delivery of chemotherapy drugs. In order for the drug to be effective, the therapeutic agent must travel from the injection site and accumulate within the cancerous cells at large enough concentrations to induce cell killing. Several drug specific properties can affect its delivery from the injection site to the intracellular compartments including the pharmacokinetics and pharmacodynamics of the drug, size, surface charge and solubility. After injection, pharmacokinetic parameters such as clearance of the drug determine how long the drug remains within the individual's blood stream and the rate at which it is eliminated. Pharmacokinetic parameters depend on the drug and individual factors including age, gender and metabolism. The longer the drug remains in the system the more likely it is to induce cancer cell death. However, chemotherapeutic drugs are also

toxic to normal cells, causing damage to the heart and healthy tissue. Hence, exposure of bioavailable drug in the systemic circulation is likely to increase toxicity [58].

The drug transport process from injection to tumour cells involves several steps that occur on multiple time and length scales. The transport of therapeutic molecules within the body occurs mainly through two modes of transport, diffusion and convection. Diffusion is slow and only effective over short distances whilst convection is much faster but requires the presence of fluid flow; hence convection is necessary to transport particles across large distances. The relative contribution of each mode of mass transfer in drug transport is measured by the Peclet number, *Pe*

$$Pe = \frac{Lu}{D} \tag{1.1}$$

where *L* is the length scale, *u* is the fluid velocities and *D* is the drug molecules diffusivity. Peclet numbers larger than 1 suggest that the transport process is convection dominated and numbers lower than 1 show transport to be diffusion dominated. Upon injection the drug distributes rapidly within the body through convection via blood circulation. After entering the target tissue through the feeding arteries, the drug is transported mainly through convection within the tumour vasculature where the Peclet number is much greater than 1. The extravasation of drug from the vessel to the interstitial space occurs through a combination of diffusion and convection. The diffusive flux is dependent on the vessel permeability and the drug concentration difference between the vessel and interstitial space. Convective flux is dependent on the rate of fluid leakage from the vessel which is in turn governed by the transvascular pressure difference [59]. Drug transport within the interstitial space is achieved through a combination of diffusion and convection, but the latter is usually weakened. Cancer cells in the tissue space take up the drug through the cell membrane by passive or active transport where the drug binds to the DNA to induce cell death [60].

The steps involved in drug transport can be affected by the properties of tumour microenvironment in multiple ways. In the target tissue, the presence of vessels plays a critical role in allowing the drug to reach all parts of the tissue. The chaotic and tortuous nature of the vasculature in tumours can impede blood flow and consequently limit the distribution of the drug within the vessels [61]. Heterogeneous vascular distribution with some avascular regions can lead to non-uniform drug distribution within the tumour tissue. The presence of arterio-venous shunts described in section 1.2.1 can cause the drug to completely bypass a network of capillary vessels [46]. Hence, cells in these regions or in avascular regions can escape

treatment. Whilst the leakiness of tumour vessels might be thought to aid in the transport of the drug from the vessel into the interstitial space, in many cases the opposite is found to be true where poor extravasation of the drug occurs. In normal tissue transvascular transport occurs mainly by convection through fluid flux, however in tumours the high IFP caused by the leaky vessels reduces transvascular flux and extravasation. Therefore, drugs move across the vessel wall in tumours mainly through diffusion which occurs on a slower time scale [62]. Intratumoural and intertumoural variations in vessel leakiness contribute to heterogeneous extravasation of the drug and uptake by the interstitial space. This provides another barrier to drug delivery in tumours and causes varying responses to treatment within a tumour and from patient to patient.

If the drug is able to penetrate the vessel walls and enter the extravascular space, its transport in the interstitial space is dependent on fluid flow velocities and the diffusive properties and uptake kinetics of the drug. Convective transport through fluid flux can allow the drug to traverse long distances in short time scales. In tumour tissue the IFP is high in the center with pressure gradients nearing zero which limits the convective transport of drugs. Hence, transport can occur only through diffusion which is distance limited and is relatively slow. Hence, regions beyond a certain distance from the vessels are not able to receive adequate concentrations of the drug. The pressure at the tumour periphery has been found to drop rapidly, creating a large pressure gradient with the tumour center which presents another issue [63]. Large fluid fluxes towards the tumour periphery are likely to exist which could cause the drug to be cleared out of the tumour. The structure and mechanical features of the tumour extravascular space can also limit drug transport. The dense ECM in tumours not only presents a physical barrier for drug transport and increases diffusion distance, but the components of the ECM can bind to the drug thereby limiting uptake by cancer cells [64]. High proliferation of cancer cells in the tumour tissue reduces the amount of space available for drugs to diffuse through [65].

1.3   Objectives

The aforementioned properties of tumour microenvironment highlight the multiple physical barriers posed that can limit the distribution of anticancer drugs and promote tumour growth and metastasis. Additionally, the genetic nature of tumour development can cause these features to vary both intertumourally and intratumourally, resulting in a heterogeneous response to treatment. Therefore, an in-depth understanding of the tumour microenvironment and its influence on transport is required in order to develop new strategies for enhanced treatment efficacy. Computational modelling methods hold

some promise in understanding the complex interplay between the intrinsic properties of tumours and the influence of these properties on drug uptake and distribution within tumour tissue. These modelling tools can provide a cost-effective approach and potentially useful insights that are not fully accessible through experimental means, thereby reducing empiricism and uncertainty. Computational models allow for comprehensive sensitivity analyses to identify the most influential properties of the tumour microenvironment and vasculature on drug transport. The multiple steps involved in drug delivery can be examined exclusively and various parameters related to the drug such as dose, physical and chemical properties can be easily controlled to optimize treatment strategies. Hence, given this and in the context provided in the preceding subsections, the overall aim of this work is to develop an understanding of the heterogeneity of the microvasculature and its role on fluid flow and drug transport using computational methods integrated with laboratory data. The strategy is to incorporate details of the vasculature on a microscopic scale whilst still retaining macroscopic view, so that the work is multi-scale in nature. To achieve this, we set out the following objectives:

1. Perform a thorough literature review on the current research analysing the tumour vasculature, and models describing drug transport and fluid flow in tumours.
2. Mathematically create a geometry of the tumour vasculature that can capture the properties of vasculature in real tumours.
3. Investigate fluid flow behaviour in the geometries generated in objective 2 using fluid flow models that incorporate the microscopic features of tumour vasculature. Examine the influence of morphological features of tumour vasculature on fluid flow.
4. Couple the fluid flow and tumour vasculature model with a drug transport model to describe the transport, distribution and uptake of anti-cancer drugs in solid tumours. Examine the influence of various properties of the tumour vasculature and drug on its cellular uptake.
5. Develop and assess protocols to image and characterize the vasculature in a whole tumour (cm scale) at microscopic resolution. The 3D images of the vasculature in tumours are used to determine angiogenesis parameters and characterize the vascular structure in addition to validating the angiogenesis model used in the fluid flow and drug transport models.

1.4   Overview of thesis

This thesis is divided into 6 chapters which follow the order of the objectives set. In chapter 2, a comprehensive review of the methods used to characterize and describe the vasculature in solid tumours

is provided first. This is followed by a review of the studies investigating fluid flow and drug transport in solid tumours with a specific focus on those employing computational and mathematical methods. Chapter 3 presents a mathematical model developed to generate the vasculature in tumours using angiogenesis-based models and the coupling of this with fluid flow models to examine various aspects of fluid flow in solid tumours. Chapter 4 combines the model developed in chapter 3 with a drug transport model to investigate the interplay between the tumour vasculature and drug properties and their influence on drug distribution and uptake. In chapter 5, work is presented on developing a protocol to image the vasculature in whole tumours at μm scale. The feasibility of the imaging protocol to extract key parameters is demonstrated which can be used to assess angiogenesis and the structure of vasculature in real tumours. Finally, main findings and contributions of the study are summarized in chapter 6, along with recommendations for future work.

2 Literature review

In this chapter, a review of the topics related to the objectives of this work are presented. At first, the mathematical and imaging methods used to describe the tumour vasculature and obtain important parameters related to angiogenesis are reviewed. Secondly, a comprehensive review of the techniques used to analyse and understand fluid flow in tumours is presented with a focus on mathematical and computational models. Thirdly, previous mathematical modelling studies on drug transport in tumours are reviewed. Finally, a summary is provided of the gaps in literature and opportunities to expand on current knowledge.

2.1 Characterizing the tumour vasculature

As described in section 1.2.1, angiogenesis is one of the hallmarks of cancer and is a critical determinant of its aggressiveness, invasiveness and potential response to treatment [66]. Without vascular support through angiogenesis, tumours can become dormant, necrotic or apoptotic [67]. Angiogenesis has been found to occur in a number of different tumours and a considerable amount of attention has been given to angiogenesis and the tumour vasculature in recent years in order to develop more effective treatment strategies for tumours [68]. The tumour vasculature can serve as a therapeutic target and a prognostic marker; hence methods that are able to describe the tumour vasculature and extract important information such as architecture, heterogeneity and density are valuable. In this subsection, the methods available that can be used to capture the geometric features and structural abnormalities of the tumour vasculature are described.

2.1.1 Mathematical models for tumour induced angiogenesis

Experimental *in vitro* models where vasculature is grown in 3D tissue can provide an understanding of the different processes involved in tumour angiogenesis. However, there are numerous processes involved in the formation of capillary networks acting on different spatial and temporal scales that have not been understood. Incorporating these complex properties is challenging and can be expensive when using purely experimental-based methods. Computational and mathematical models can replicate features of experimental systems offering a time and cost-efficient tool to provide insight into the problem. Several mathematical models have been developed describing the process of tumour-induced angiogenesis which allow for the simulation of capillary network formation [69]. Some of these models use a continuum

approach to incorporate different aspects of the tumour angiogenesis process, capturing details such as capillary network growth rate and average vessel density [70, 71]. However, they are unable to capture details regarding the structure and morphology of the vascular network. Anderson and Chaplain provided a breakthrough in representing realistic tumour vasculature through mathematical models when they developed a discretized model to track the movement of endothelial cells at the capillary sprout [72]. Within the model, the movement of the capillary sprout is dependent on three factors: Random motility (analogous to molecular diffusion), Chemotaxis in response to tumour angiogenic factors (TAF) secreted by cells in the tumour and Haptotaxis in response to fibronectin gradients. Initially discretized distribution fields for TAF, fibronectin and endothelial cells are generated. Then a focus is placed on the endothelial cells at the sprout tips which are assumed to be non-proliferative. The movement of cells at the capillary sprout is tracked in response to the TAF gradient allowing the model to describe the formation of a discrete network of vessels and to capture features including branching, anastomosis and looping. This method is based on a five-point central difference scheme where the capillary network is represented in 2D while the movement of capillary sprouts can occur in 4 directions. In their work, Anderson and Chaplain considered the source of diffusing angiogenic factors to be fixed (i.e fixed tumour). Welter and Reiger (2010) developed a 3D model investigating the influence of the emerging tumour vasculature by angiogenesis on a pre-existing normal arterio-venous network [73]. They incorporated factors in their model including vessel regression, tumour cell proliferation and death. Additionally, the changing dynamics of blood flow which can influence oxygen delivery and subsequently the angiogenic factor distribution were investigated. Vavourakis et al. further developed this model to account for influence of mechanotaxis caused by solid stress resulting from tumour growth [74]. Whilst the models developed by Welter and Reiger [73] and Vavourakis et al. [74] do well to incorporate the processes involved in vascular growth, they are complex and can be difficult to couple with some fluid flow models.

2.1.2 Imaging angiogenesis

Mathematical angiogenesis models can provide an estimate of the complex vascular network in tumours, however, these model does not incorporate all mechanisms involved in the angiogenesis process. Imaging techniques provide an opportunity to obtain real information on the vasculature that can be used to analyse and quantify various properties of the vascular network. Visualization of the tumour vasculature can be divided into two parts, labelling of the vasculature and imaging which are described below.

2.1.2.1 Labelling the vasculature

The method of vascular labelling determines the type of imaging modality used. A common method used to label the tumour vasculature is vascular casting which can provide a 3D structure. This approach requires the draining of blood then the intravascular injection of a fixative to preserve the tissue, followed with the injection of a casting material such as gelatines, resins or inks [75-77]. Vascular casting can provide a highly detailed replica of the entire tumour vasculature making it possible to examine vessel geometry, branching patterns and intercapillary distance. In tumours there is a lack of vessel organization and visual distinction between the different vessel types. Hence, vascular casting techniques are not able to provide distinction between angiogenic vessels or different vessel types such as arterioles, venules and capillaries.

Immunohistochemistry (IHC) techniques allow for the labelling of proteins in cells using antibodies that bind specifically to these cells. Endothelial cell protein markers such as CD31, CD34 and von Willebrand factor (vWF) can be stained to label the vasculature [78, 79]. During angiogenesis some endothelial cells such as tip cells express unique molecular markers which can be stained to specially image properties related to angiogenesis [80]. Additionally, arterioles, venules and capillaries are made up of different cellular components as described in section 1.2.1. Molecules expressed by cells specific to arterioles or venules can be stained to define the types of vessels being imaged. In fluorescence IHC, after staining with antibodies specific to the molecule expressed in the cells of interest, a fluorescent second antibody is used that binds specifically to the primary antibody to provide contrast and help visualize the cells. This makes fluorescent IHC a valuable technique that can help visualize cells of interest and distinguish between different vessel types at the cellular level. A limitation of such a method is that although the cells lining the vessels are stained, it does not establish if blood is flowing through these vessels. Another method that can address this issue is the use of tracers such as fluorescent lectin or dyes that are injected intravenously and can only reach and label vessels through circulation [81]. This allows the capture of functioning vessels and makes it possible to determine blood flowing through channels lined by cancer cells which has been observed in some highly metastatic tumours [82].

2.1.2.2 Imaging techniques

The imaging method used to visualize the labelled vasculature will usually depend on the labelling method used. A wide range of imaging methods are available that can provide information in multiple dimensions and across different spatial scales. Here the focus is on those that are able to achieve resolutions high

enough to visualize tumour vessels where the diameter ranges from a couple of micrometers to several hundred micrometers [31]. *In vivo* imaging techniques are desirable as they provide a real time representation of the tumour vasculature and are able to provide information on the response to treatment. These include techniques such as magnetic resonance imaging (MRI) and computerized tomography (CT) which have been applied in assessing the tumour vasculature [83-85]. The resolutions achieved by these methods are on the order of several hundred micrometers making them unsuitable when attempting to obtain a detailed 3D visualization of the tumour vasculature at high resolutions. Alternatively, intravital microscopy is an *in vivo* imaging technique which can provide high resolution images of the tumour vasculature. This technique is combined with the intravenous injection of tracers and has been applied to obtain *in vivo* 3D images of the vasculature from mammary adenocarcinomas and osteosarcoma's implanted in mice where they were able to resolve spatial heterogeneities at the microscopic level [86-88]. However, a major limitation of intravital microscopy is the depth of tissue region that can be analysed (200-400 μm) which accounts for only a small fraction of the tumour size.

Up till now, ex-vivo imaging techniques have remained most useful in their ability to image the tumour vasculature at high resolutions whilst providing a global view of the vascular structure. Micro-computed tomography (μCT) is an ex-vivo imaging method where 2D X-ray projections are taken at defined angular steps around an axis of rotation which are then used to obtain a 3D reconstruction of the vasculature. The resolutions achieved can be on the order of several micrometers providing sufficient resolution to distinguish between individual capillaries [89]. Vascular casting is usually employed as a method for vascular labelling with μCT when imaging the tumour vasculature. Folarin et al. applied this technique to mice tumour models derived from human colorectal cancer to quantify parameters of the vascular architecture including branch angles, intercapillary distance and vessel diameter distribution [90]. Savai et al. combined vascular casting and μCT imaging to evaluate the effect of anti-angiogenic therapy on the vasculature in xenograft mouse models of lung cancer by comparing the vascular density in tumours treated with an anti-angiogenic drug, bevacizumab, and tumours in a control group [91]. High resolution 3D images of vasculature from breast cancer xenograft models have been generated to quantify structural properties of the tumour vasculature and simulate blood flow within the network to elucidate the hemodynamics of tumours [92, 93]. Downey et al. combined Microfil with μCT to image the vasculature in subcutaneously tumours grown from human breast cancer cell lines where they analysed structural features and identified regions of hypoperfusion which could be linked with necrosis [94]. Using this

technique, they were able to investigate the effects of vascular distributing agents on the tumour vasculature.

μCT imaging techniques combined with vascular casting, which is quite a complex technique, requires fresh material and can only be applied to animal tumour studies. IHC vascular labelling combined with microscopy-based imaging techniques provides a more accurate method of assessing angiogenesis by imaging vessel structures with angiogenic molecular markers and the technique can be applied to human tumours excised from patients. The main limitation of IHC techniques and confocal microscopy is that they are only able to produce 2D images from a thin section of the tissue which may not accurately represent the heterogeneity of the vasculature and angiogenic phenotype within the whole tumour. Several studies have attempted to address this by combining serial sections of the tumour tissue to reconstruct 3D volumes of the vasculature [95-97]. To prepare the tissue, traditional IHC techniques were used which included fixation, paraffin embedding and staining. A series of 2D images were obtained from serial sections which were then aligned using automated registration techniques. The method was able to provide a high-resolution 3D reconstruction of vasculature in the tumour specimens where the derived parameters concerning the architecture of the vasculature were consistent with other traditional imaging methods. These studies were however limited by the labour-intensive task of obtaining each section and imaging them which limited the depth of the total imaged volume to 300 μm. A recent novel imaging system named the "Histocutter" has been developed in house at the Imperial College London that overcomes this issue and is based on the same principle of aligning serial sections to reconstruct a 3D volume [98]. The system couples a traditional microtome to an imaging hardware to produce a fully automated robotic device that is able to construct high resolution 3D images by capturing and aligning thousands of high-quality images as thin as 1 μm. The imaging system has already demonstrated its ability to image soft tissues including the brain and lungs which provides promise in imaging blood vasculature in tumour tissue [99, 100].

Optical projection tomography (OPT) is a relatively new 3D imaging method that has been developed in the last decade [101]. OPT shows promise as it bridges the gap between conventional microscopy and MRI. It is able to image specimens as large as 15 mm at high resolutions, making it possible for quantitative analysis of data spanning 3 orders of magnitude from μm to cm. The imaging technique can be used in combination with fluorescent staining as a vascular labelling method. After labelling, optical clearing methods are used to make the sample transparent and thus reduce scattering and absorption of light. The specimen is then mounted on a motor which is rotated at incremental angles from which images are taken

over a 360 revolution. The set of images obtained from these angles are then processed and reconstruction algorithms are applied to obtain a 3D image of the specimen [102]. The method has been applied to image vasculature in zebrafish [103, 104]. Recently, it has been applied to vasculature in tumours grown subcutaneously from murine gliomas and human colorectal carcinoma xenograft. The vasculature was labelled using intravenously injected lectin that allowed binding to the active blood channels. From these images, it was possible to quantify and validate several structural parameters of the tumour vasculature [105].
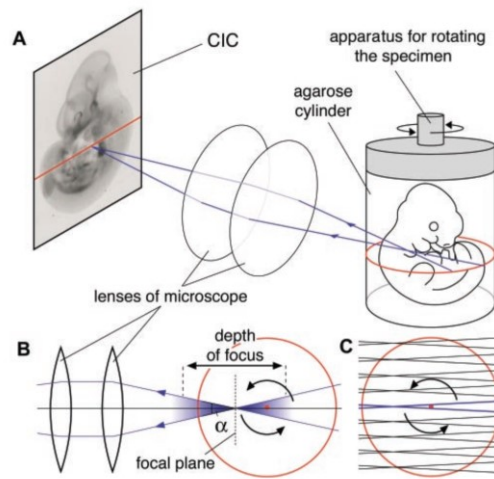
Figure 2.1: Illustration of OPT imaging (extracted from [101]).

2.1.2.3   Clinical relevance of imaging angiogenesis

Given the role of angiogenesis in tumour growth and invasiveness, there has been much interest in assessing its significance as a prognostic factor. Microvessel density (MVD) has been used as a marker for angiogenesis and has been shown to be an independent prognostic indicator in a number of different cancers including breast, lung, prostate, colon and cervical carcinomas [106]. A number of different methods have been used to measure MVD. The method developed by Weidner et al. [107] has been widely adopted, which involves the identification of vascular "hot spots" in 2D histological sections by finding the regions with the greatest density of vessels and counting the number of vessels in this region. Other methods sample different regions and calculate density at different magnifications of the microscope. IHC staining techniques are used to label blood vessels with endothelial cell specific markers such as Ulex, Von Willerband factor (vWF), CD31 and CD34 which are then used to determine the MVD. Alternative methods to quantify angiogenesis include the use of VEGF expression, but MVD has been shown to provide more consistent results. This was demonstrated in a study by Inda et al. of VEGF and

MVD in two lineages of non-small cell lung cancer (NSCL) that were expected to have the same clinical prognosis [108]. They found that although the mean VEGF was different for the two types of tumours, MVD was not significantly different between them suggesting that CD34 might be a better prognostic marker of angiogenesis.

Although angiogenesis has shown prognostic value in different types of tumours, it's significance in some types of cancers such Epithelial ovarian cancer (EOC) remains unclear. A large amount of work has been devoted to elucidating the role and significance of angiogenesis in EOC in the last 20 years. Hollingsworth et al. was first to evaluate the association between MVD and the outcome in advanced stage (III and IV) ovarian carcinomas to find that high vessel counts confer worse prognosis [109]. In their work they used the endothelial cell marker CD34 to count the vessels. This generated significant interest in understanding the significance of MVD in prognosis of ovarian tumours. Van Diest et al. assessed the significance of microvessel quantification as a tool for prognosis using Ulex as marker for vessels in EOC treated by debulking surgery and cisplatin [109]. However, they found no association between MVD and prognostic variables including tumour stage and grade. Gasparini et al. used CD31 markers and found MVD to vary significantly between the different histotypes. MVD was found to be a significant indicator of OS in univariate analysis, however this significance was not retained in multivariate analysis [110]. Volm et al. used vWF markers to find a significant correlation between high MVD and formation of metastasis in primary ovarian carcinomas [111]. Abulafia et al. used vWF as a vessel marker and found that MVD in omental metastasis but not in primary ovarian tumours was correlated with pre-operative CA125 levels and patient survival with no correlation found between MVD and the tumour stage or histotype [112]. Schoell et al. used vWF, CD31 and CD34 markers to show significant differences in vascularisation between survivors of ovarian cancer and those who died of the disease [113]. Brustmann et al. used vWF to find increased MVD and heterogeneity of capillary distribution in malignant epithelial tumours when compared with benign tumours. [114]. Similarly Darai et al. used CD31 markers to find higher MVD in malignant ovarian tumours than borderline and benign tumours [115]. Obermair et al. used CD34 markers to find that low MVD was correlated with better survival in univariate analysis, however, MVD failed to attain a significant value for multivariate analysis with other prognostic parameters such as age, stage and grading [116]. Subsequently, a large amount of literature has been devoted to assessing the role angiogenesis in ovarian cancers by quantifying MVD using a number of different antibodies [117-124]. More recently, Rubatt et al. examined the independent prognostic value of MVD in untreated advanced EOC using CD31 and CD105 as markers for vessels [125]. High MVD using CD105 but not CD31 was found

to be an independent prognostic factor for worse progression free survival. This could be attributed to CD105 being a marker for proliferating endothelial cells which marks angiogenic vessels. Pirtea et al. built on standard IHC studies by investigating the Ki67 proliferative index of tumour vessels highlighted using CD34 and CD105 markers [126]. Ki67 was not found to react positively with CD105 stained vessels but achieved co-localization with CD34 in some vessels. They were able to find differences in the proliferative index between endothelial cells at the tumour core and those at the periphery. Rustico et al. investigated changes in MVD in paired primary and recurrent HGSOC tissue samples and its impact on patient clinicopathological outcomes [127]. They found MVD and VEGF profiles to not be major drivers in cancer evolution *in vivo*, but rather remain supportive factors.

From the number of studies highlighted above, it is evident that there is significant interest in understanding the role of angiogenesis in tumour growth, metastasis and response to therapy. MVD is a commonly used parameter to quantify angiogenesis and to correlate with prognostic factors. However, in ovarian carcinomas, the prognostic significance of MVD varies considerably between different studies which can be attributed to several factors. The methodology used in these studies introduced many variables including the type of marker used to label the vessels, the tissue processing and staining methods, and the technique used to count the vessels. In the cases of the labelling marker used, several studies have analysed the expression of vWF compared to other markers in malignant and benign tumour tissue. The markers for CD31 and CD34 have consistently yielded positive and equally intense staining of malignant intratumoural endothelial cells in comparison to vWF regardless of the tissue processing method [128-130], although CD31 is expressed during differentiation which could lead to cross reaction with plasma cells and lymphatic B cells [107, 131]. CD34 is more stable than CD31 and is an easily reproducible highlighter for endothelial cells [132]. Another reason for the inconsistencies in the findings is the method used to quantify angiogenesis. The vascular hot spot method is most commonly used, but several problems arise with such a method. The regions of vascular hot spots are chosen by the observer which can introduce subjectivity and inter-observer variability and this in combination with the variability in staining intensity caused by the use of different antibodies, can further add to the degree of variability [133]. Additionally, there was no standardized process to set the cut-off values used to classify high and low MVD areas as a function of imaged area or microscope magnification. Some studies have used median values as a cut-off for high MVD whilst other studies used values ranging from 10-40 vessels/field. These methodological problems could bias results and may be responsible for the inconsistent findings. In addition to the methods used to assess MVD, the failure to replicate observations associating MVD with

prognosis in ovarian carcinomas can be attributed to the nature of ovarian tumours. The vasculature in ovarian tumours has been shown to be more chaotic and significantly more heterogenous compared to breast or cervical tumours [134]. Assessing MVD over a number of 2D tissue sections might not be able to capture this heterogeneity introducing bias into the data. Zhang et al. recently investigated the use of 3D MVD counting to assess angiogenesis in gastric tumours grown in animal models [135]. Using normal and tumour models the 3D MVD was evaluated and found to be correlated with tumour angiogenesis. This suggests that 3D imaging methods can be used as tools to assess angiogenesis in a way that captures the complexity and heterogeneity of the vasculature which is not available using 2D techniques.

2.2   Modelling fluid flow in tumours

Most drugs for solid tumours are delivered intravenously where they rely on convective and diffusive fluxes to reach cancer cells. Successful treatment of solid tumours has been shown to be hampered by abnormal fluid flow properties which limit the transport of therapeutic macromolecules in the vasculature, across the capillaries and in the tumour interstitium [136, 137]. The abnormal fluid flow properties are linked to the complex interplay between properties of the tumour microenvironment including intravascular flow, capillary filtration, interstitial flow and ECM [57, 138]. Several studies have shown that the manipulation of these properties towards normalization can reduce proliferation of cancer cells and enhance drug delivery for tumours [139-141]. Awareness that modulations of the fluid flow properties can enhance treatment of solid tumours has led to a substantial interest in understanding the processes that affect flow dynamics in tumours. A number of experimental methods have been employed to acquire information on flow and IFP in tumours. These include invasive methods such as the micropuncture technique or the wick-in-needle technique which have been used for *in vivo* measurements of IFP, showing elevated IFP in tumours and differences between the tumour center and periphery [52, 54, 142]. However, the invasive nature of these methods can affect the local microenvironment and only provide IFP measurements at isolated spots. Noninvasive *in vivo* methods have been developed such as dynamic contrast-enhanced MRI (DCE-MRI) to assess tumour IFP using interstitial fluid velocity measurements [143, 144]. Whilst this method provides spatial information on IFP in tumours, the limited maximum resolution of 230 µm does not capture the flow distribution at microscopic scale which can affect flow behaviour on the full tumour scale.

Due to the lack of noninvasive methods that are able to capture the interstitial flow distribution at microscopic scale, mathematical models have been developed to describe fluid flow in tumours and

capture the interplay between intravascular and interstitial flow heterogeneities. Jain et al. developed a model for the tranvascular exchange and interstitial transport in a spherical solid tumour [63, 145]. In their model, interstitial flow was described by Darcy's law whilst fluid filtration from the vessels is described by Starling' law. The vasculature was assumed to be uniformly distributed with no lymphatic vessels present in the tumour model. Interstitial pressure and fluid velocity profiles were estimated as a function of radial position in the tumour showing that pressure was highest at the tumour center and drops rapidly at the periphery resulting in radially outward velocity. The model was later developed to incorporate lymphatics and heterogeneous perfusion by defining a spherical region at the tumour center which was assumed to be necrotic and avascular. The presence of necrosis at the tumour center did not reduce the interstitial pressure and a similar pressure profile was found which dropped rapidly at the tumour periphery [145]. The series of pioneering works by Jain and co-workers have strongly influenced subsequent studies. El-Kareh and Secomb applied this model to investigate the effect of vessel hydraulic conductivity and tumour shape on fluid filtration and IFP [146]. Soltani and Chen applied this model to investigate the effect of tumour shape and size on IFP distribution [147, 148]. These models assumed a uniformly distributed vasculature within the tissue space that acted as a source term for the fluid. Their results showed that IFP increased with microvascular density (MVD). However, none of these studies explicitly considered the effect of vascular flow and vessel size on interstitial pressure and fluid filtration.

Several studies have attempted to incorporate realistic tumour properties such as size and geometry in their model. Goh et al. applied Jain's transport model to a 2D tumour geometry generated from a CT scan of a hepatoma [4]. The tumour model was divided into 3 domains that featured a necrotic core, a viable zone featuring partially functional vessels that are uniformly distributed and a normal tissue zone. Their results showed that interstitial pressure in the necrotic core and tumour tissue reached steady state within 800s with profiles showing a rapid drop at the tumour boundary. Zhan et al. reconstructed 3D geometries of different tumours from MR images to investigate the effect of tumour size on drug transport [149-151]. These macroscopic models were able to predict fluid flow properties in tumours at an organ scale, however, they neglected the influence of spatial heterogeneities in tumour tissue such as microvascular density and rate of vessel leakage. The effect of varying microvascular density and distribution was examined by Mohammadi and Chen who found a correlation between IFP and microvascular distribution although their model did not explicitly resolve blood flow in the vasculature, assuming a uniform vascular pressure [152]. Some studies have attempted to incorporate heterogeneities of flow and vasculature in tumour models by integrating spatial variations in fluid filtration and

permeability mapped from DCE-MRI [153-155]. However, the resolution achieved by DCE-MRI lacks the ability to resolve heterogeneities at the microscopic scale.

2.2.1 Fluid flow in simplified vascular geometries

The permeability of vessels in normal tissue is relatively low, limiting the amount of fluid that extravasates. Fluid leakage into the tissue is also tightly regulated by the osmotic pressure gradient that causes fluid to flow back into the vasculature. Additionally, any excess fluid in the interstitial space is drained by the functioning lymphatics, reducing IFP in normal tissue close to zero. Therefore, in normal tissue, it can be assumed that there is no coupling between blood and interstitial flow. In tumour tissue, high vessel leakiness, lack of functioning lymphatics and osmotic pressure gradient increases IFP which requires coupling between vascular, transvascular and interstitial flow. Netti et al. first studied this potential coupling by investigating the effect of vessel leakiness on blood flow in tumours [156]. They used a perfused animal tumour model to investigate the macroscopic pressure flow relationship in the tumour vascular network which was represented as a single, compliant and permeable vessel embedded in a fluid at uniform pressure. Investigation of the effects of various properties on arterio-venous pressure and pressure profile along a vessel suggested that blood flow and distribution were coupled to transvascular flow. Baish et al. expanded on this to incorporate the effect of interstitial flow by unifying vascular, transvascular and interstitial fluid flow in a single theoretical framework [157]. A network of permeable compliant vessels embedded in an isotropic porous medium organized in a regular mesh and a pair of countercurrent vessels was used to describe the tumour geometry. Coupling of vascular, transvascular and interstitial flow described by Poiseuille's, Starlings and Darcy's law respectively, showed a strong dependence of blood flow distribution on increased IFP. Milosevic et al. further investigated the effect of IFP on blood flow considering the time-dependent behaviour of vessel diameters and found a strong association between high IFP and restricted blood flow in tumours [158]. These models assumed a uniformly elevated IFP on the outer surface of the vasculature. Pozrikidis developed an integrated model coupling vascular, transvascular and interstitial flow, showing that this assumption can carry errors when attempting to estimate extravasation rates [159]. The model was built on the mathematical model by Fleischman et al. [160] where the pressure field in the tissue was described as a continuous set of point sources distributed along the vessel center line with the density of point sources being described through outward flux from the vessel wall without considering the effect of inward flux. Such a formulation might not lead to significant errors when applied to normal tissues exhibiting physiological vascular hydraulic conductivity values that would result in an overall high net outward flux from the vessels. However, the

33

excessive vessel leakiness encountered in tumours can increase the effect of inward flux and lead to significant errors. Pozrkidis addressed this by modifying the flux boundary condition to include the distribution of dipoles on the surface of the vessel in addition to the distribution of sources [159]. The problem is then represented as a coupled system of integral and differential equations describing the distribution of vascular and interstitial pressure over the inner and outer surface of the vessels. This formulation was applied to a simple model of a single capillary, tubular in shape, embedded in a porous medium which showed heterogeneous distribution of extravascular flux rate along the capillary, highlighting the importance of incorporating nonuniformities in IFP on the outer surface of the vessel.

2.2.2   Fluid flow using complex vascular networks

The fluid flow models described in the previous section were able to provide great insight into the coupled behaviour of vascular and interstitial flow by considering flow in a single capillary or a simple array of capillaries representing the tumour network. Simulating fluid flow using realistic tumour vascular networks can provide an understanding of fluid flow behaviour in tumours that is grounded in physical reality. As discussed in chapter 2.1.1 several mathematical models have been developed to describe tumour induced vascular network growth by incorporating key processes of angiogenesis in tumours. The method of Anderson and Chaplain [72] is an example of such an approach that has been used to generate theoretical capillary networks that capture many features of the tumour vasculature including anastomosis, branching and looping. The method reduces computational demand associated with other methods and coupling this with a fluid flow model provides an advantage in that the networks generated are underpinned by governing biological processes. McDougall et al. applied this approach to generate a 2D theoretical capillary network and incorporate blood flow in the vessels [161]. In this model the capillary network is divided into a series of short cylindrical tubes defined by a specific radius and length where Poiseuille's law is used to simulate blood flow in the network assuming mass conservation at each node. Stephenou et al. extended this work to generate 3D capillary networks based on tumour induced angiogenesis, and compared results with those obtained from the 2D simulations [162]. McDougall et al. took this further to incorporate the non-Newtonian behaviour of blood and coupled this with vessel growth to simulate adaptive vessel remodelling in response to hemodynamic forces [163]. They were able to investigate the effect of the vascular network structure and various properties such as vessel radius and blood viscosity on blood flow distribution. Welter and Rieger simulated blood flow in a network developed using a vascular remodelling model that describes the transformation of an original arterio-venous vascular network of the host tissue into a tumour vessel network during tumour growth [73].

The aforementioned studies have only described blood flow in the network and did not consider transvascular or interstitial flow. Several models have simulated vascular and interstitial flow in tumour models with complex network architecture [e.g. [164-166]]. Given the complex nature of tumour vasculature with its irregular geometry and excessive branching, several different approaches have been developed to address the coupling between vascular and interstitial flow in tumour models with complex vascular networks. One approach involves combining the heterogeneous capillaries and interstitial tissue in a small domain into a homogenous continuum from which its transport properties are calculated that are then homogenized to give a continuum description of the problem in terms of vascular density for larger domains [167]. A similar homogenization approach has been used in several models coupling tumour induced angiogenesis with fluid flow. Zhao et al. applied a fluid flow model coupling vascular, transvascular and interstitial flow to a tumour vascular network generated using Anderson and Chaplain's approach [165]. The original angiogenesis model was modified by using a 2D nine-point discrete scheme to allow the vessels to move in 8 directions. Vascular, transvascular and interstitial flow were described by Poiseuille's, Starlings and Darcy's laws respectively. In their model, capillary flow was first simulated assuming mass conservation at each junction and hence through the entire network. The vascular network was allowed to occupy the same lattice space used to discretize for interstitial flow where each vascular node corresponds to a discretized site of the interstitial space. Hence, the exchange between the vessel node and interstitial node is proportional to starling's equation which describes fluid flux as a function of the term *S/V* denoting the vessel surface area per unit tissue volume and a matrix *A* defining the local vascular density. Wu et al. developed a similar model incorporating the non-Newtonian behaviour of blood flow and capillary compliance [164]. Their results were able to demonstrate the interplay between vascular and interstitial flow quantitatively and predict interstitial pressure profiles that are consistent with experimental observations. In these works, the *S/V* term was a uniform value obtained from literature data which doesn't describe the fluid flux as a function of the local vascular geometry. Wu et al. further extended their method by developing the capillary network into a 3D geometry, including spatial variations in the *S/V* term to correspond to local vessel radius and connectivity [168]. Interstitial flow within the tumour was found to be slow due to uniformly high interstitial pressure across the tumour. Soltani and Chen modelled vascular, transvacular and interstitial flow in adaptive capillary networks that allow the radius to change in response to hemodynamic and metabolic stimuli [166]. Their capillary network was generated using Anderson and Chaplain's angiogenesis method with the fluid flow model following the approach of Wu et al. [164] and vascular adaption following the work of Pries et al. [169]. A

number of other studies quantified the heterogeneity of interstitial pressure distribution by coupling interstitial and vascular flow using similar methods [74, 170-172].

Another approach developed to exchange information between vessels and the tissue space describes vessels as a line of sources in similar manner to the Dirac distribution [173]. Welter and Rieger applied this approach to simulate Interstitial fluid flow in tumours where the vasculature was generated in 2D using their framework for vascular remodelling [174]. Their network model incorporated features such as vessel collapse, dilation and varying vessel permeability that depend on vessel maturation level. To describe fluid flow between the vasculature and interstitial space, they applied the immersed boundary method and replaced the Dirac distribution with a smoothed kernel that allows for the source distribution to be resolved on a grid of finite cell size. This immersed boundary method has also been applied by Cattaneo and Zunino where they described interstitial fluid flow using vascular geometries built from imaging experiments [175]. In their work, finite element methods were applied to formulate the solution for elliptic equations with Dirac terms. The majority of these models described blood flow in the network by assuming conservation at each node and hence did not incorporate the extravasated fluid into the mass balance for capillary flow. The flux of the fluid from vessels is determined by using uniform vessel surface areas per unit volume obtained from literature or by using averaged values corresponding to vascular density in tissue nodes and therefore Starlings law is not applied in its exact form. These assumptions provide approximations and generalizations that could introduce errors when attempting to predict the rate of transvascular fluid flux, blood and interstitial flow.

As described previously, Pozikridis developed an approach to model the exchange between the vessels and tissue where the boundary conditions are set on the vessel walls using the boundary integral method which was applied in their to single straight vessel embedded in an infinite tissue domain [159]. Using the Green's function method, pressures can be approximated at the surface of each vessel segment. Pozkridis incorporated a distribution of sources and a distribution of dipoles in their flux boundary condition for a strong coupling between blood and interstitial flow [159]. Arbitrary geometries can be used by dividing the vessel into cylindrical segments with circular cross sections which can be distributed in a nonuniform fashion to allow for enhanced resolution at places where pronounced spatial variations arise. They extended their application from a single capillary model into a network model where the vasculature was represented as bifurcating capillary segments that branch based on deterministic and random parameters [176]. The model was able to predict the effect of vascular permeability and interstitial hydraulic conductivity on the rate of fluid leakage from the capillaries. However, the network structure used in their

model featured a high level of geometric regularity which does not truly capture the structures observed in tumour tissues.

Sweeney et al. [177] simulated fluid flow in tumours where the vasculature was imaged and explicitly segmented. A Green's function method based on Hsu and Secomb's method for oxygen transport was applied to solve for interstitial flow which allows for the whole vascular structure to be incorporated whilst reducing computational intensiveness. Their model was able to predict the elevated interstitial pressures and perfusion data that were in agreement with physiological data. The model did not incorporate vascular adaption and heterogeneities in vascular hydraulic conductivity which can have implications on fluid flow overall, however the study provides an understanding of fluid flow in realistic tumour geometries.

2.3   Modelling drug delivery in tumours

To provide an improved basis for the design of better therapeutic strategies, it is important to understand the interplay between the tumour and drug properties and determine the ability of the drug to effectively accumulate within cancer cells and induce a positive response to treatment. Mathematical and computational models combined with experimentally measured parameters for drug transport provide a cost-effective approach to this problem for a number of reasons: A comprehensive set of parameters can be tested for sensitivity analyses to determine the key and influential factors; the drug transport process involves multiple steps which can be examined individually and in an integrated manner; and finally, clinically relevant parameters, such as the dosage and administration mode of the drug, can be incorporated into the model over a wide range values, reducing the number of experiments required. A wide spectrum of mathematical models have been developed towards achieving these goals. These models can be generally divided into pharmacokinetics (PK) models and transport models. Physiological based PK models (PBPK) are a subset of the former and are based on dividing the tissues and organs of interest into compartments that, as a whole, make up a biological system in which adsorption, distribution, metabolism and excretion can be determined [178]. Pharmacodynamics (PD) models can be incorporated into the model to study the effect of the drug on the body. PBPK models describe the temporal concentration profile of the drug as an average within the compartments, with each compartment being treated as a well-mixed system [179]. Unlike compartmental models which are described by a set of ODEs, transport-based models use PDEs for explicit descriptions of fluid flow and drug transport in a pre-defined domain of interest, so that they can predict not only temporal variations

but also spatial distributions of therapeutic agents [150]. Transport based models can be further divided into macroscopic and microscopic transport models depending on the scale of the processes and domain of interest. Macroscopic models treat the tumour as an isotropic, porous medium where blood vessels are assumed to be a uniformly distributed source term. This reduces the complexity of the model and allows for spatial and temporal profiles of the drug to be evaluated over large length scales. Several studies have employed these macroscopic models to describe the distribution of therapeutic molecules in tumour tissue [4, 148, 149]. These models can be coupled with tumour geometries obtained from medical images to predict the spatial concentration in realistic tumour geometries [4, 149]. The major limitation of macroscopic models being that they neglect key microscopic properties that are known to be heterogenous in solid tumours such as the vasculature morphology, permeability and ECM and cancer cell distribution which can have a significant effect on the transport and uptake of anticancer drugs. Microscopic based models can describe the spatial profile of the drug at the single capillary level and take into account various microscopic properties of the tumour [180]. A number of microscopic models having been developed focusing on different aspects of the drug transport process including the effect of vasculature, vessel permeability and interstitial space architecture [170, 171, 175, 181, 182]. These studies are reviewed in this section.

2.3.1   Vascular transport studies

A geometric model representing the *in vivo* tumour microenvironment is required to describe drug transport in tumours. One type of model representing the tumour geometry are tumour cords which have been applied in studying tumour growth and drug transport [183]. In these models a single straight cylindrical blood vessel is surrounded by a cylindrical unit composed of uniformly distributed cells and the whole tumour is considered to be an assembly of these tumour cords as show in Figure 2.2. Cord models allow for an understanding of the transport of drugs in the tumour interstitial space in relation to distance from a blood vessel and its ability to penetrate multiple layers of cells.
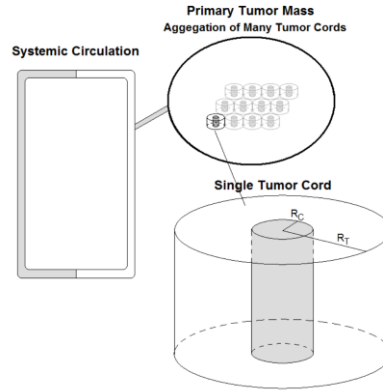
Figure 2.2: *Illustration of tumour cord model geometry where R_C is the capillary radius and R_T is the tumour cord radius. (extracted from [184]*

Eikenberry investigated the influence of dosage on therapeutic efficiency by applying a tumour cord geometry model. The concentration within the vessel was spatially averaged and determined using a PK model which was coupled with solute transport principles to describe drug extravasation, interstitial transport and cellular uptake in the tissue space [184]. The cellular uptake and efflux were incorporated using Michaelis Menten kinetics whilst cell killing was described as a function of peak intracellular concentration. The findings showed that rapid bolus administration was more suitable for low doses whilst at high doses, a 1-hour continuous infusion was more effective. The effect of various properties of the tumour microenvironment such as vessel morphology, cell packing density and tumour cord radius were investigated and their results showed that higher cell density resulted in a non-uniform drug distribution within the cord. Several other forms of the tumour cord model have been applied in other studies [185, 186]. A major limitation of the tumour cord model is their treatment of the tumour vasculature in a highly idealized manner as seen in Figure 2.2 without accounting for the complex branching properties, high tortuosity and heterogenous distribution. Incorporating these properties with an explicit representation of the vasculature remains a significant challenge not only because it would be computationally intensive but obtaining a realistic representation of the vasculature is also a difficult task.

Some studies have applied mathematical models of tumour-induced angiogenesis (section 2.1.1) to generate capillary networks formed in response to angiogenic factors secreted by cells in tumours [72]. In these models the vasculature formed is divided into cylindrical segments through which blood flow is described by Poiseuille's law. The interstitial space is assumed to be a homogenous porous medium composed of cancer cells and extracellular material through which flow is modelled by Darcy's law.

Vascular and interstitial flow equations are coupled by transvascular flow modelled by Starling's filtration law. Sefidgar et al. applied these principles in combination with Anderson and Chaplains tumour-induced angiogenesis model to investigate the effect of heterogenous vascular networks on blood flow and drug transport and compared the results with macroscopic models that assume the vasculature to be a uniformly distributed source term [181]. Their findings showed that a model with a uniformly distributed vasculature predicted higher and more uniform drug concentrations than when the heterogeneity of the vasculature is considered. Imaging techniques have been used to obtain the geometrical details required to represent the tumour vasculature as described in section 2.1.2 which can be incorporated into the mathematical fluid flow and drug transport models. Solving the drug transport equations in tumour geometries featuring an explicit representation of the vasculature with all its intricacies is a difficult task. To tackle this, Kojic et al. developed a multi-scale finite element method for convective and diffusive mass transport [187]. Their model is adapted for application to large tissues where the large vessels are modelled as 1D finite elements whilst regions with complex capillary networks are merged with the surrounding tissue to form 3D continuum finite elements with corresponding hydraulic and diffusive transport parameters. Application of their model to tumour geometries showed gradients in the concentration field within the large vessels and in the tissue space. Gradients were also observed between the vascular and interstitial space which was attributed to the transport from blood vessels to the tissue space. The homogenization of the capillary and tissue domain into a continuum increases the efficiency and allows for application to large tumours or whole organs, however steep spatial gradients that occur on a micron scale are not captured. Cattaneo and Zunino applied a finite element based numerical method to describe drug transport on microscopic scale by coupling vascular, transvascular and interstitial flow equations to simulate flow in the tumour whilst solute transport was modelled using the convection-diffusion equation [175]. To reduce the computational intensity of the problem, the tumour microvasculature was represented as a network of 1D channels immersed in the interstitial volume, where they acted as a set of sources for transvascular flow as shown in Figure 2.3. Mass transport principles were applied to simulate the drug delivery and compare the effectiveness of bolus administered tirapazamine (TPZ) with its nanoparticle formulation. The nanoparticles were assumed to transport within the vasculature and attach to the vessel walls where the encapsulated drug is released, hence, transvascular transport of nanoparticles and their migration in interstitial space were never considered. When comparing the different modalities of drug administration, the nanoparticle formulation produced the highest concentrations at all time-points.
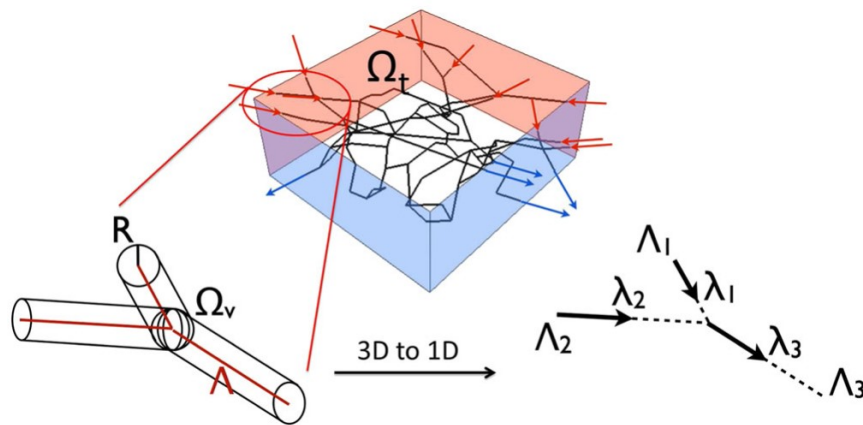
Such models implementing finite element or finite difference methods for drug delivery can readily incorporate features such as time dependence and reaction. However, the heterogenous and tortuous nature of the tumour vasculature can result in steep spatial gradients in drug concentration in regions near the vessel wall. To resolve these gradient, small spatial steps are required which increases the computational cost. More so, small time steps are required for fine meshes in order to satisfy the Courant–Friedrichs–Lewy (CFL) condition required for numerical stability and accuracy, which limits the timescale of the simulation. Considering this limitation, Secomb developed a Green's function based numerical method for solute transport where each vessel is divided into multiple segments which represent a distribution of solute sources whilst the tissue space is discretized to represent a distribution of sinks [188]. Solute distribution within the tissue space can then be expressed as the sum of these sources and sinks and hence is a function of the vascular structure and morphology. The application of this method reduces the number of unknowns whilst not placing significant restrictions on the time and spatial steps. Secomb demonstrated the application of this method by analysing the kinetics of solute washout from heterogeneous vascular networks obtained from rat cremaster muscle. The method demonstrated the ability to simulate the time-dependent convection and diffusion of an inert solute in complex vascular geometries without restricting the time and spatial steps to values that satisfy the CFL conditions necessary for convergence in finite element methods. Troendle et al. [189] developed a new method utilising molecular mechanics to predict the spatial drug delivery efficiency in tissues. Distribution of drug within the vascular network was modelled exclusively through diffusion without incorporation of blood flow and its effect on drug distribution. Tranvascular transport was modelled using a kinetic Monte Carlo

approach whereby first order rate constants for drug exchange between compartments obtained from PK models is first converted into a per-particle probability. The transport in the extravascular space was modelled through diffusion. They modelled the transport of doxorubicin and its nanoparticle formulation, doxil, using clinically relevant dosing where injection was simulated by placing all the drug molecules at a source point in the artery. In their model the vascular network was represented in 2D and some were generated manually to represent normal and complex vascular networks. Additionally, a vascular network was modelled by tracing of a PET image of tumour vasculature. To analyse the therapeutic efficiency of the drugs administered at various doses, a minimum effective dose was defined in the tissue space. In this study, Troendle et al. were able to show that the vasculature plays critical role in the optimal dosage required and demonstrated the enhanced delivery of liposomal doxorubicin over its free form. Although the work provides a framework for analysing the spatial distribution of drugs administered, the study did not incorporate the effect of blood flow and convection on the transport within the tumour vasculature which can consequently affect the spatial distribution in the tissue space. The reaction and uptake of the drug by cells in the tissue space was not incorporated which can have significant implications for its ability to penetrate the tissue and distribute as drugs have different uptake and efflux rates. The number of vessels was limited to 50 cylinders in the generated vascular networks and 200 cylinders in the network extracted from the PET image.

d'Esposito et al. [105] combined mathematical transport modelling with high resolution imaging of the vasculature in intact tumour tissue extracted from mice to predict the fluid flow and spatial distribution of therapeutic agents in real tumours. In their work, the vessels were labelled and imaged as described in section 2.1.2.2 which were then skeletonized and converted into graph format. To resolve fluid flow, blood flow in the network was modelled using Poiseuille's law where flow was assumed to be conserved in each node. Flow in the vasculature was coupled to interstitial flow, modelled by Darcy's law, using the Green's function approach developed by Secomb et al. [190] for oxygen transport where the vessels are divided into a set of sources. Pharmacokinetic models were used to define a vascular input function that determines the amount of drug entering the vascular network. Once at the arterial point, a propagating front approach was used to describe the movement and distribution of the drug within the vascular network based on network architecture and blood flow. The interstitial space was divided into a grid with an isotropic resolution of 100 μm and a forward finite difference approach was implemented in which the vessels were segmented and divided into radial sources of the drug. Transport across the vessel wall was assumed to occur mainly through diffusion and is a function of the difference in vascular and interstitial

concentration and hydraulic conductivity of the vessel wall. Drug transport across the vessel wall was assumed to occur as a function of a vascular density term S/V which was averaged over the whole tumour. The work demonstrated the elevated IFP and heterogenous perfusion observed in tumours which led to heterogeneous distribution of Gd-DTPA within the vascular network and interstitial space.

2.3.2 Transvascular transport studies

Transvascular transport can be a limiting step in the process of delivering therapeutics to cancer cells. A number of mathematical models have focused on developing a better understanding of factors that can enhance or limit penetration of the drug into the tissue during transvascular transport. Chauhan et al. investigated the effect of vessel pore size and distribution on the penetration and distribution of nanoparticles in tumours [171]. Vessels were generated using a 2D percolation model exhibiting a range of different pore sizes and varying degrees of heterogeneity. Coupled vascular, transvascular and interstitial flows were described by Poiseuille's, Starling's, and Darcy's laws respectively. The vasculature was discretized and assigned values of hydraulic conductivities and reflection coefficients to simulate heterogenous pore size distribution. Their results showed that the IFP in tumours could be lowered by reducing pore size which could potentially allow for small nanoparticles to extravasate from the vessels at a greater rate. However, the decreased pore size increases steric and hydrodynamic forces which made it challenging for large nanoparticles to penetrate through the vessel walls. For pore sizes large than 140 nm, the IFP was elevated which limited convection and reduced drug penetration. The work showed a correlation between pore size and nanoparticle size in its ability to penetrate the tissue as the optimum penetration was found to occur for nanoparticles smaller than 12 nm. Stylianopoulos et al. [170] built on this model to account for the effect of nanoparticle surface charge and its electrostatic interactions with the vessel wall. The vascular network was generated using Anderson and Chaplains 2D angiogenesis model [72]. Nanoparticle transport in the vasculature was modelled as a function of the blood velocity, interstitial transport was modelled using the convection-diffusion equation and transvascular transport was modelled by starling's approximation. The permeability and reflection coefficients of the vessel wall were modified to account for hydrodynamic and electrostatic interactions between the particles and wall pores which were described using the Poisson Boltzmann equation. The results produced from the model showed that when the pore size was reduced, transvascular transport of the nanoparticle was significantly hindered whilst for large pore diameters, the effect of electrostatic repulsion on transvascular transport was negligible.

2.3.3   Extravascular transport studies

In the mathematical drug transport models reviewed so far, the interstitial space was treated as a homogenous medium with the cancer cells, ECM and other extravascular components being uniformly distributed across the domain of interest. In reality, the extravascular space of tumours can exhibit a high degree of heterogeneity which can consequently affect interstitial transport and distribution of therapeutic agents. This has been demonstrated in *in vitro* and *in vivo* studies which showed that transport in the interstitial space can be affected by the distribution of the ECM and packing density of cancer cells [64, 65]. Rejniak et al. further investigated this by developing a computational model that explicitly took into account the cellular structure of tumour tissue [182]. In their model the tissue morphology was explicitly defined in a 2-D domain representing a small patch of the tumour tissue on a length scale of a few hundred microns. The boundary on left-hand of the domain was modelled as source term for particles from the blood vessels. Transport of the particles in the tissue domain was modelled explicitly through a combination of convection and diffusion. To estimate the magnitude of the convective transport component, the method of regularized stokeslets was applied to calculate fluid flow whilst the diffusive component was modelled by Brownian motion. The model was applied to different tissue geometries with varying cell packing densities and degrees of heterogeneity. Furthermore, the model was applied to tissue structures generated from digitized histological images of ovarian tumour tissues. From their simulations, they concluded that cellular porosity and density can influence the penetration of molecules in a non-linear manner. The molecules were found to travel at a slower rate in highly porous tissues compared to denser tissues. The degree of heterogeneity in tissue morphology led to a non-uniform distribution of the molecules which resulted in tissue zones with poor exposure to drugs. Large particles were able to penetrate deeper into the tissue, however they accumulated at lower concentrations in regions near the vessels whilst smaller particles were able to distribute more uniformly in regions near the vessels.

2.4   Summary

In this chapter, a detailed review is provided of the methods used to develop an understanding of the tumour vasculature, angiogenesis and fluid flow and drug transport. For fluid flow and drug transport a focus was placed on mathematical models and whilst a considerable amount of literature has been devoted to study and characterise fluid flow and drug transport in solid tumours, most of these models focus on the macroscopic scale and neglect the influence of microscopic properties of the vasculature and blood flow [63, 147]. Variations in fluid flow and transport on a microscopic scale need to be incorporated

to gain a wider understanding of the barriers to drug delivery and fluid flow. Although a number of fluid flow studies have attempted to incorporate the architecture and distribution of the tumour vasculature, in 2D [153, 164, 166, 170, 174, 181, 191] and 3D [168], as described in section 2.2, these models did not explicitly incorporate several key microscopic properties when analysing fluid flow. When coupling vascular and interstitial flow, these models applied homogenization methods where properties of the vasculature were averaged over discretized cells. By applying Starlings law using these homogenization techniques, only an approximation of the effect of vascular distribution on fluid flow was investigated. Macroscopic parameters for the whole tumour such as the surface vascular density term was predefined using literature values and used to solve Starling's equation rather than consider the morphology and architecture of the network generated. Blood flow in the networks was assumed to be conserved and the effect of fluid extravasation was neglected. However, at the single capillary level, the strong coupling and interplay between blood flow and interstitial flow has been demonstrated [157, 159]. In all the models reviewed, the permeability of the vasculature was assumed to be uniform across the vascular network which does not capture the heterogenous pore size distribution in the tumour vasculature as it can range from 7-1200 nm [192]. In terms of evaluating fluid flow in tumours, models need to be developed that can model fluid flow in whole tumours with explicit incorporation of the effect of individual vessel morphology, such radius, length, orientation and permeability for whole tumour networks whilst capturing the strong coupling between blood and interstitial flow. For drug delivery, although a large amount of literature is available where drug delivery is evaluated in tumours on a macroscopic scale or using average compartmental models [149, 179, 193], limited amount of work has been devoted to investigating the spatial distribution of drugs with incorporation of microscopic features of the tumour vasculature and blood flow. Secomb [188] has developed a model that describes the distribution of solutes in tissues with complex vascular networks. Although it shows significant promise, it has yet to be applied to model the distribution of anticancer drugs in tumour tissue. The model developed by Troendle et al. [189] shows similar promise however, it application was limited to a 2D domain with a relatively small tumour network where the important influence of blood flow and reaction/uptake in the extravascular space was neglected. Multiple steps are involved from the point of drug injection to the point where they can induce a therapeutic effect including transport within the vasculature, extravasation, interstitial transport and uptake/efflux. These steps and their interactions on a microscopic scale with the microvascular network need to be considered and at present time, no work has truly investigated this issue.

Given the important role of the tumour vasculature in fluid flow, drug transport and its clinical relevance as discussed in section 2.1.2.3, methods need to be developed that can extract key properties of the vasculature. These properties can be used to develop a better understanding of fluid flow and drug transport in real tumour geometries and evaluate the significance of the vasculature on the invasiveness of the tumour. Previous studies assessing the prognostic significance of MVD in tumours have relied on 2D methods which led variable and conflicting results. This can be attributed to the nature of the tumour vasculature where 2D slices are not able to truly capture its heterogeneity. This limitation can be overcome by the use of 3D imaging methods to describe the vasculature at high resolutions over a large scale. However, most 3D imaging methods applied to examine the tumour vasculature involve the use of µCT and vascular casting which is not specific to angiogenic vessels. In their review He et al. [194] showed that MVD detected by CD34 was more relevant as prognostic marker, hence IHC based 3D imaging methods where specific molecules can be targeted are required to quantify properties specific to angiogenesis. Several novel IHC based imaging techniques show promise in their ability to provide 3D images of the tumour vasculature however so far these methods have been mainly applied to animal models.

As discussed in section 1.3, the overall goal of this project is to develop an understanding of the heterogeneity of the tumour microvasculature and its role on fluid flow and drug transport using computational methods and assess the ability of novel imaging methods to extract the tumour vasculature with high fidelity. To achieve this, the aim is to integrate a fluid flow and drug transport model that addresses the issues highlighted in the reviewed studies and incorporate microscopic properties of the tumour vasculature to capture a more realistic view of fluid flow and drug delivery in tumours. Additionally, novel IHC based 3D imaging methods are assessed in their ability to extract the tumour vasculature at a microscopic scale in human tumours. These 3D images can be used to provide key properties that can be used to assess the prognostic significance of angiogenesis and be used as an input to understand various processes in solid tumours such as fluid flow and drug transport.

3 Tumour vasculature and its influence on fluid flow

3.1 Introduction

In solid tumours, the delivery of oxygen, nutrients and potential therapeutic drugs is highly dependent on fluid flow properties of the tissue. Abnormal fluid flow in tumours such as high IFP has been associated with increased metastatic potential and poor prognosis [195]. Developing an understanding of the fluid flow behaviour in tumours is key in order to improve the therapeutic efficiency of anticancer drugs. As discussed in section 2.2, experimental methods have been applied in measuring and calculating IFP in solid tumours, however these are limited to resolutions on the order several hundred microns. Mathematical modelling methods provide a cost-effective approach to gaining insight into fluid flow in solid tumours at multiple scales. Models that have been applied so far face several limitations as described in section 2.4 where the strong coupling between vascular and interstitial flow was not incorporated. Additionally, the physical architecture and morphology of the vasculature was not accounted for when modelling the transvascular flux using Starling's law.

In this work a mathematical model is developed by coupling Anderson and Chaplain's tumour induced angiogenesis model [72] with Pozrikidis's fluid flow model [159]. Anderson and Chaplain's angiogenesis model was extended to 3D to describe unique features of the tumour vascular network including excessive branching, looping and high tortuosity. Pozrikidis's fluid flow model for flow in a single capillary that captures the strong coupling between vascular and interstitial flow, was extended from a single capillary and applied to complex vascular networks. Applying Pozrikidis's model, the interstitial pressure is integrated over the surface of the vessel, hence the physical structure of the vessel, including length, radius and orientation are considered when calculating the pressure profile in the tumour. With this model, the effect of transvascular leakage and interstitial flow on blood flow are explicitly incorporated. Fluid behaviour in tumour tissue is investigated, along with the effects of various properties such as vascular architecture, distribution, tumour necrosis and microscopic details of the tumour network. The model was further coupled with a vessel adaption model that describes the variations in vascular permeability in order to capture the strong heterogeneity found in tumour vascular networks.

3.2   Methods

3.2.1   Tumour induced angiogenesis model

To generate the vascular network, a method based on Anderson and Chaplain's mathematical model for tumour induced angiogenesis was implemented. Their model was based on an experimental system designed by Gimbrone et al. and Muthukkaruppan et al. where a small solid tumour was implanted in the cornea, close to the limbal vessels of a rabbit and mouse test animal [196, 197]. As mentioned previously in this thesis, tumour induced angiogenesis first begins when cancer cells secrete angiogenic factors (TAF) which then diffuse through the tissue space and create a chemical gradient between the tumour and nearby vasculature. Endothelial cells lining these vessels degrade the basement membrane and then migrate toward the tumour in response to chemical gradients (chemotaxis). Endothelial cells at the tip of the sprout tend to be inactive and endothelial cell proliferation occurs mostly in regions behind the cluster of cells at the sprout tip. As the sprout moves toward the tumour it must travel through the ECM which is mainly composed of collagen and fibronectin. The interaction of the tip endothelial cells and the ECM can significantly impact directional migration of the cells in a process termed Haptotaxis. Specifically, fibronectin in the ECM has been shown to enhance cell adhesion to the matrix. Anderson and Chaplain used three variables, endothelial cell density n, TAF concentration c and fibronectin concentration f to develop a hybrid discrete-continuum model that describes the movement of endothelial cells in response to chemotaxis and haptotaxis. The path of endothelial cells at the tip of the sprout are tracked to generate the network structure where no proliferation or cell death is assumed to occur at these sprout tips. In addition to chemotaxis and haptotaxis, the motion of endothelial cells is governed by random motility in a similar manner to molecular diffusion and hence endothelial cell flux J_n can be given by

$$J_n = J_{random} + J_{chemotaxis} + J_{haptotaxis} \qquad (3.1)$$
$$J_{random} = -D_n \nabla n$$
$$J_{chemotaxis} = \chi(c) n \nabla c$$
$$J_{haptotaxis} = \rho_0 n \nabla f$$

Where D_n is the random motility coefficient, $\chi(c)$ is a chemotactic function and ρ_0 is a constant haptotactic coefficient. The conservation equation for endothelial cell density is given by

$$\frac{\partial n}{\partial t} + \nabla . J_n = 0 \qquad (3.2)$$

Anderson and Chaplain were able to develop a set of nonlinear partial differential equations that govern the endothelial cell density, TAF concentration and fibronectin concentration as follows

$$\frac{\partial n}{\partial t} = D_n \nabla n - \chi(c) n \nabla c - \rho_0 n \nabla f \tag{3.3}$$

$$\frac{\partial f}{\partial t} = \beta n - \gamma n f$$

$$\frac{\partial c}{\partial t} = -\eta n c$$

Where β and γ are the production and degradation rates of fibronectin by endothelial cells respectively and η is a coefficient describing the rate of TAF uptake by endothelial cells. The system of partial differential equations is discretized in 3D using the Euler finite difference approximation

$$n_{l,m,w}^{q+1} = n_{l,m,w}^{q} P_0 + n_{l+1,m,w}^{q} P_1 + n_{l-1,m,w}^{q} P_2 + n_{l,m+1,w}^{q} P_3 + n_{l,m-1,w}^{q} P_4 \tag{3.4}$$
$$+ n_{l,m,w+1}^{q} P_5 + n_{l,m,w-1}^{q} P_6$$

$$f_{l,m,w}^{q+1} = f_{l,m,w}^{q} \left[1 - k\gamma n_{l,m,w}^{q} \right] + k\beta n_{l,m,w}^{q}$$

$$c_{l,m,w}^{q+1} = c_{l,m,w}^{q} \left[1 - k\eta n_{l,m,w}^{q} \right]$$

Where *l,m,w* indicate the position on the discretized space and *q* indicates the time point. The set of coefficients P_0 to P_6 are used to determine the probability of sprout endothelial cells to remain stationary (P_0), move forward or backwards along the x-axis (P_1,P_2), y-axis (P_3,P_4) and z axis (P_5,P_6) [162]. The equations for these probabilities are given in appendix A.1. In the model no birth or death of cells is incorporated hence a zero-flux boundary condition is imposed where the endothelial cells are conserved within the domain as follows

$$\zeta \cdot \left(J_{random} + J_{chemotaxis} + J_{haptotaxis} \right) = 0 \tag{3.5}$$

Equation 3.3 was non-dimensionalised to replace parameters D_n and $\chi(c)$ and ρ_0 with non-dimensionless parameters D, χ and ρ. Parameters D and χ were estimated by Anderson and Chaplain using experiments that quantitatively analysed random and chemotactic movement of endothelial cells to obtain estimates for D_n, χ_0 and reference values for c [198, 199]. No data is available to estimate ρ_0, β, γ and η, hence a

non-dimensional value for ρ was used with the assumption that χ is larger. All parameter values used have been obtained from Anderson and Chaplain [72]. The time parameter is given in normalized form as

$$t = \frac{\bar{t}}{\tau} \tag{3.6}$$

With where t is the normalised time, $\bar{t}$ is the real time and $\tau = \frac{L^2}{D_c}$ being the timescale given as a function of L, the length scale of the domain and D_c, the TAF diffusion coefficient. In the experimental work that Anderson and Chaplain based their model on, the average distance of a tumour from the parent vessel was 1-2 mm, hence a length scale of L = 1.5 mm is assumed in this study. The simulation is carried out in a dimensionless domain [1 x 1 x 1] divided into 40 grid points in each axis. D_c is taken to be 1.6×10^{-7}cm^{2}s^{-1} which is based on estimates from experimental data [200] which gives a timescale, $\tau =$ 1.6 days. Parameter values for D, χ, ρ, β, η and γ were obtained from Anderson and Chaplain's work and are summarised in Appendix table A.1. To generate the vascular network, Equation 3.4 is solved to give a continuous distribution field of the TAF, fibronectin and subsequently the endothelial cell density at different time points. Using the distribution of endothelial cells with time, the movement of sprout tip cells can be tracked discretely which can be used to determine the vascular network formed.

3.2.1.1   Initialization and solution of continuous model

Angiogenesis is triggered by the formation of a TAF chemical gradient between the tumour and nearby vessels, hence the initial distribution of TAF, c, within the domain is first defined. The initial distribution of TAF can be used to defined different tumour model shapes of interest. Assuming a tumour implanted at the edge of the domain, the concentration profile of TAF secreted by the tumour cells can be defined as follows

$$c(x, y, z, 0) = e^{-\frac{(1-x)^2}{\epsilon_1}} \tag{3.7}$$

To simulate the distribution of fibronectin, Anderson and Chaplain highlighted that after activation of the endothelial cells in the parent vessels by the TAF gradient they begin to break down the basement membrane which allows for plasma fibronectin to leak from the vessel and diffuse into the surrounding tissue. The fibronectin binds to the ECM surrounding the parent vessels and creates a high concentration of fibronectin around the parent vessel initially. This assumption is supported by experimental observations [201]. Hence the initial distribution of fibronectin is described in relation to where the parent vessel is located in the simulation and the concentration profile is given by

$$f(x, y, z, 0) = ke^{-\frac{x^2}{\epsilon_2}} \tag{3.8}$$

Where $\epsilon_1 = \epsilon_2 = 0.45$ and $k = 0.75$. The initial distribution of endothelial cells n can describe the location of the parent vessels within the domain. In this work it is assumed that the cells form three clusters along the y-axis at $x = 0$ where the parent vessel is located, and the tumour is at $x = 1$. This can be described by

$$n(x, y, z, 0) = e^{-\frac{x^2}{\epsilon_3}} \sin^2(6\pi y) \tag{3.9}$$

Figure 3.1 shows the initial concentration profiles for TAF, fibronectin and endothelial cells using these conditions. The TAF concentration profile is the highest at $x = 1$ where the edge of the tumour containing the cancer cells is located. The TAF secreted by these cells diffuses and forms a gradient with nearby parent vessels located at $x = 0$. When the TAF activates, the endothelial cells begin to break down the basement membrane of the vessel and aggregate to form clusters of cells which then sprout to form new vessels. These clusters are represented in the endothelial cell distribution plot (bottom fig 3.1) as three peaks. Fibronectin distribution is initialised to be highest in regions near the parent vessel as seen in Figure 3.1.
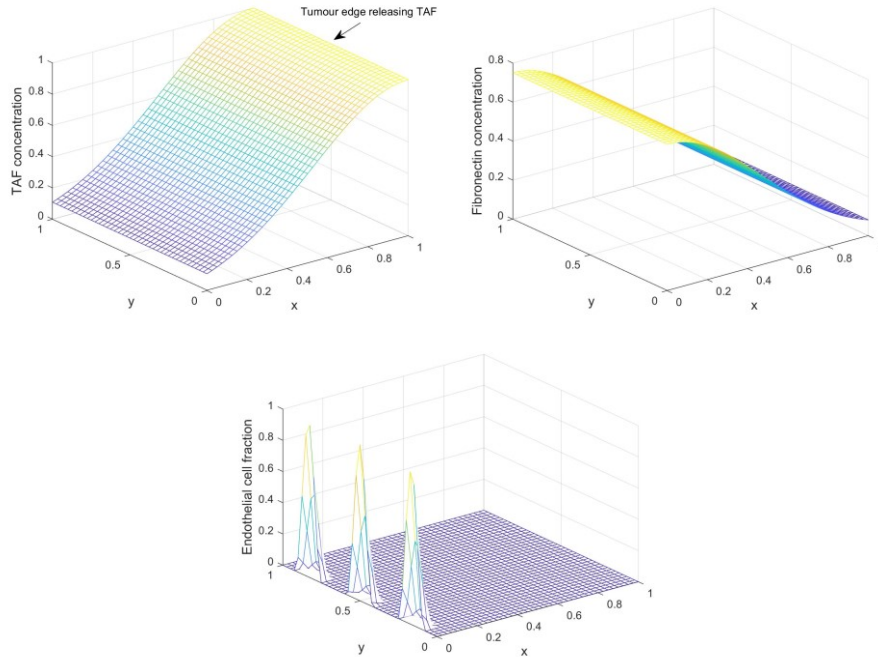
Figure 3.1: Initial TAF (Top left) and Fibronectin (Top right) concentration profiles determined using equation 3.7 and 3.8. Bottom plot shows initial endothelial density determined using equation 3.9 which can be described as three clusters sprouting from parent vessel at x = 0. All plots are show at z = 0.5.

TAF and Fibronectin concentrations don't exhibit significant changes during the simulation however, endothelial cell density distribution changes with time in response to the TAF gradient as shown in Figure 3.2. Initially, the endothelial cells are clustered in regions near the parent vessel. At t = 2.5 (4 days) the peak endothelial cell concentrations formed by clusters have moved across the domain in response to the TAF gradient and towards the tumour. At t = 5 (8 days) the endothelial cells have advanced approximately 40% of the way to the tumour and there appears to be merging between the clusters where they now form a band. At t =10 (16 days) a 4th cluster appears to have formed as endothelial cells migrate in a lateral motion and the initial 3 clusters overlap. At t = 15 (24 days) the endothelial cells form a continuous band that has virtually reached the tumour.
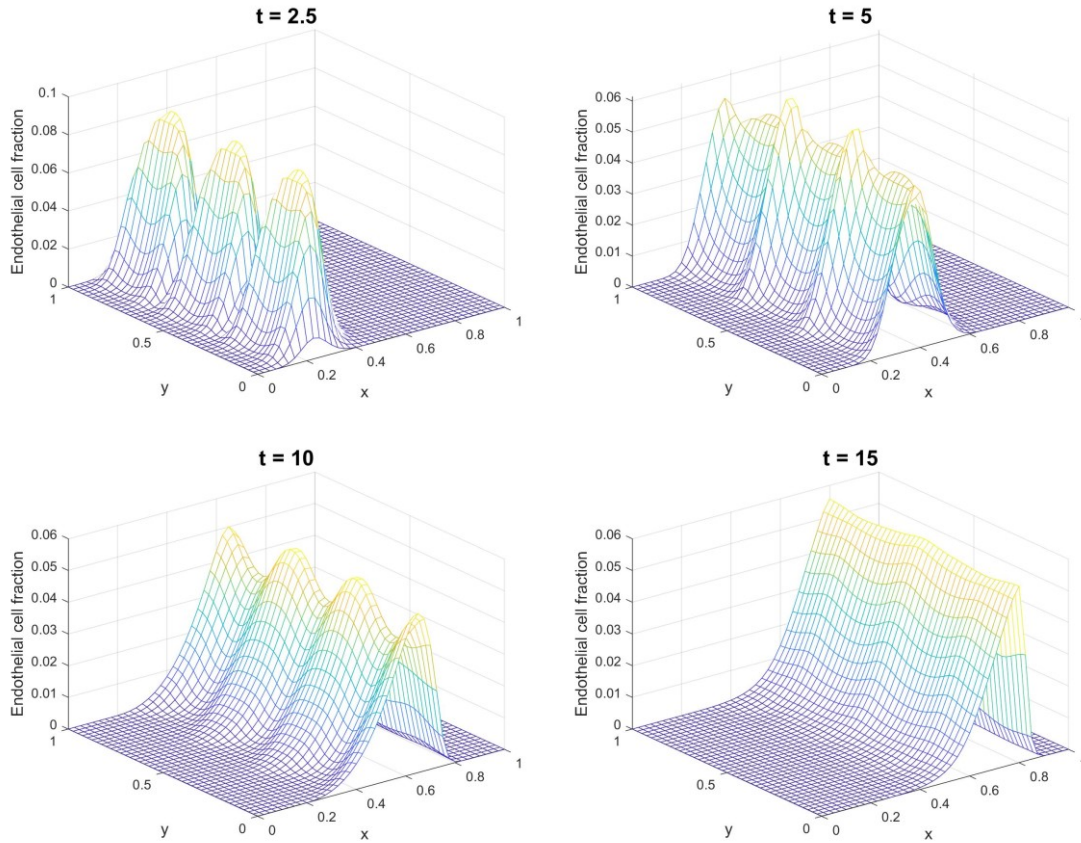
Figure 3.2: *Spatio—temporal profile of endothelial cell distribution in domain. The endothelial cell density is shown at dimensionless time t = 2.5, 5, 10 and 15 which corresponds to real time of 4, 8, 16 and 24 days respectively given a domain length scale of L = 1.5 mm.*

The results displayed in Figure 3.2 correspond with what was shown in Anderson and Chaplain's work using their 2D model [72] where they attributed the degree of lateral endothelial cell movement to the haptotactic effect when the value of ρ was increased. In their work they also demonstrated that the rate

of endothelial cell migration was dependent on the haptotactic coefficient and TAF concentration gradient. Increasing haptotactic coefficient resulted in reduced endothelial cell migration whilst increasing the steepness of the TAF gradient increased the rate of endothelial cell migration. This highlights the interplay between endothelial cells, TAF and fibronectin, which can potentially be used to generate different vascular geometries of interest.

Consider a case where a spherical tumour is assumed to be located at the center of the domain at $x = y = z = 0.5$. The tumour is assumed to have a dimensionless radius of 0.5, hence it extends from 0.25-0.75 in the x, y and z axis. With this in mind, the initial conditions for the TAF concentration, c, within the domain can be described as follows

$$c(x,y,z,0) = \begin{cases} 1, & r < 0.25 \\ \dfrac{(v-r)^2}{v-0.25}, & r \geq 0.25 \end{cases} \tag{3.10}$$

$$r = \sqrt{(x-0.5)^2 + (y-0.5)^2 + (z-0.5)^2}$$

Where v is a positive constant and r is the distance from the tumour center assuming the tumour is centred at (0.5, 0.5, 0.5) within the domain. It is assumed that parent vessels exist on each face of the domain facing the tumour, and hence fibronectin can be assumed to be uniform as it is being released by each face of the domain. Figure 3.3 shows the initial distribution of TAF and endothelial cells described by equation 3.10. The steep gradients in TAF concentration towards the center of the domain are defined to promote rapid movement of endothelial cells towards the tumour where vascularisation occurs.
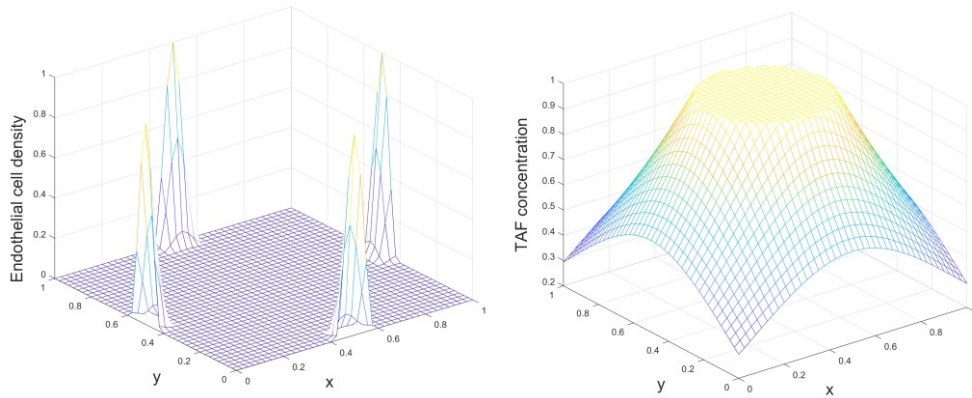
Figure 3.3: Initial endothelial cell concentration (left) and TAF concentration (right) for a case where tumour is centred in the domain with dimensional radius 0.5.

Figure 3.4 displays the spatial and temporal distribution of endothelial cells in the domain, showing the migration of the cells towards the central tumour.
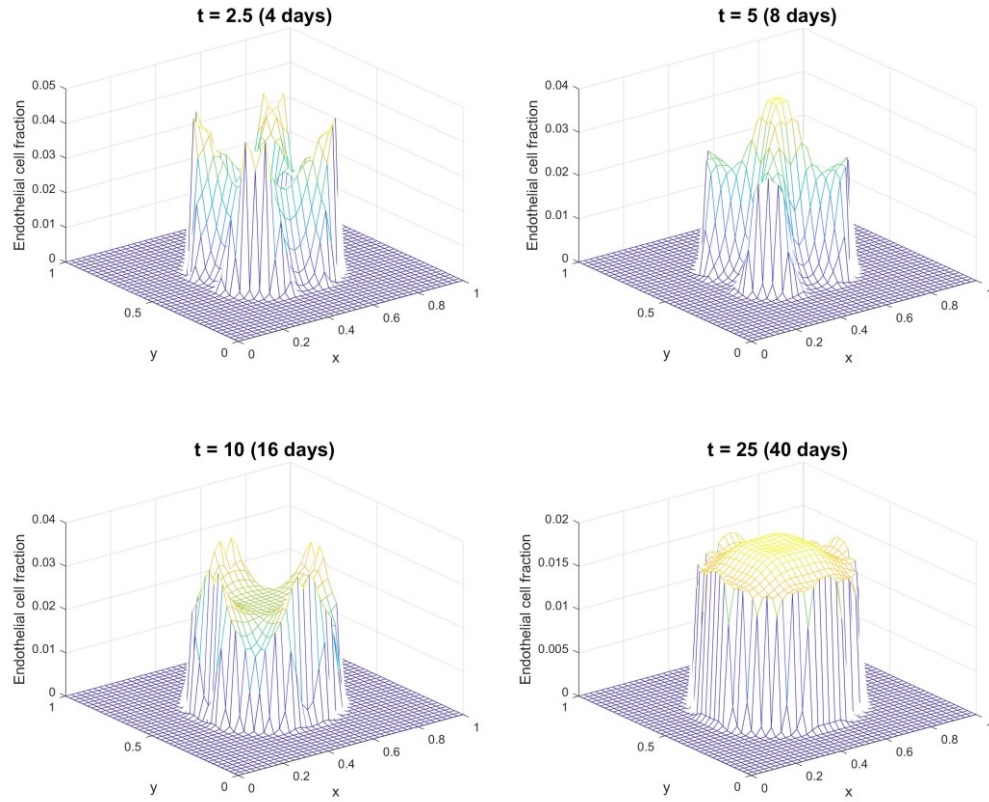
Figure 3.4: *Spatial and temporal variations of endothelial cell density with a tumour located at the center of the domain.*

The model formulation can be used to generate geometries of interest by defining different initial conditions. In tumours, cellular proliferation and poor blood supply cause hypoxia and depletion of nutrients for cells, resulting in necrosis in the core regions of the tumour. Necrotic regions have dead cancer cells that do not secrete TAF and hence the region may be avascular. This feature can be described using equation 3.11 which models the presence of a necrotic core at the center of a tumour as follows

$$c(x,y,z,0) = \begin{cases} 0.9, & r \leq 0.04 \\ 0.8 + 2.5r, & 0.04 \leq r \leq 0.08 \\ 1, & 0.08 \leq r \leq 0.25 \\ \dfrac{(v-r)^2}{v-0.25}, & r \geq 0.25 \end{cases} \qquad (3.11)$$

In equation 3.11 a tumour of dimensionless radius 0.25 is centred in the domain and assumed to have a necrotic radius of 0.08. Utilizing the dependency of endothelial cell movement on positive TAF gradients, a negative gradient is defined within a radius of 0.08 from the tumour center. Hence, endothelial cells would not move into this region. The initial endothelial cell density and fibronectin conditions are the same as in the case of a non-necrotic tumour. Figure 3.5 shows the initial TAF concentration for a necrotic tumour with the negative gradient apparent at the tumour center.
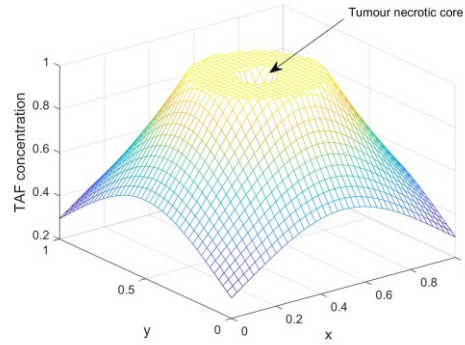
Figure 3.5: *Spatial profile of TAF concentration in a domain where a tumour with a necrotic core is located at the center.*

The spatial and temporal distributions of endothelial cell density is simulated as shown in Figure 3.6. The endothelial cells move towards the tumour, however the density in the necrotic region with a radius of 0.08 remains close to zero which is apparent when comparing the plots in Figure 3.4 and 3.6.
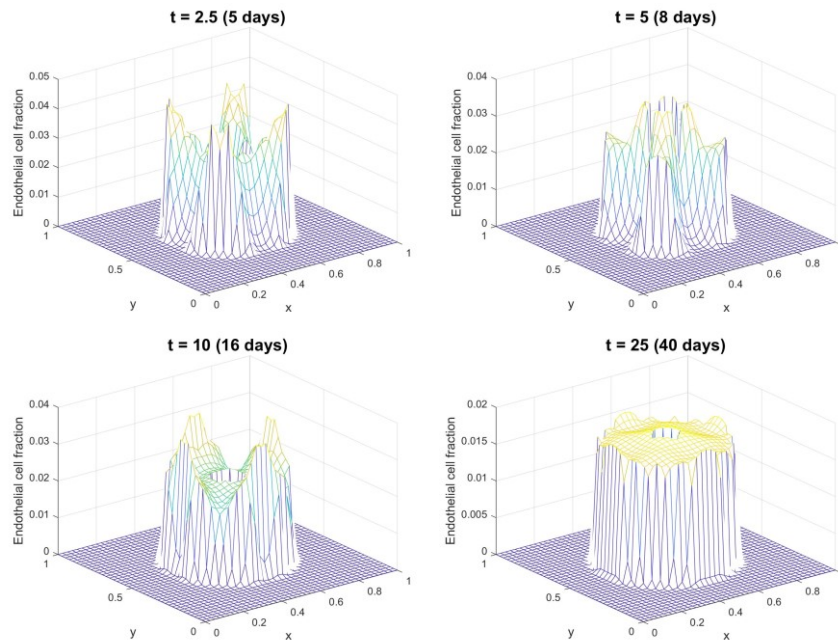
Figure 3.6: Spatial and temporal evolutions of endothelial cell density in a domain where a tumour with a necrotic core is located at the center.

3.2.1.2   Discrete generation of tumour vasculature

Anderson and Chaplain's method applies a discrete model to describe the formation of vascular networks using the continuum fields generated for endothelial cell density. Their model tracks the movement of endothelial cells at the tip of the sprouting vessel and assumes the movement of these tip cells governs the motion of the entire sprout. By tracking the path of the cells, the geometry of the entire network formed can be captured. Motion of endothelial cells is determined by calculating the coefficients P_0 to P_6 define the probability of the sprout tip moving in a certain direction. The probability coefficients are based on three components: random, chemotactic and haptotactic movement. As mentioned previously, chemotactic movement is dependent on the presence of TAF gradients and haptotactic movement is dependent on the fibronectin concentrations, hence the movement of the endothelial cells is governed by the interplay between the TAF profile and fibronectin concentrations in the ECM. Branching and anastomosis are common features in tumour vasculature, and these are represented following the approach of Anderson and Chaplain [72] which is summarized here. Branching from a sprout is dependent on three factors: (1) branching age - a sprout must reach a mature state, measured by a threshold branching age, for it to branch, (2) space - there must be space for the sprout to branch into, checked by ensuring there are no other sprouts around the tip, (3) the number of endothelial cells at the tip - an endothelial cell density threshold must be satisfied for the sprout to branch. If the above three conditions are met, the branching of a sprout is given as a probability that is dependent on the local TAF concentration. The higher the TAF concentration, the greater the chances are for a sprout to branch. Overall, this model describes the movement of a sprout tip from the parent vessels where there is little branching due to the age and as the sprouts reach the tumour, the increased age combined with the high TAF concentration increases the chance of vessel sprouting. Anastomosis or merging of vessels is described simply when a sprout moves into a space occupied by another sprout. The sprout that continues to exist is chosen at random.

The movement of endothelial cells in the domain can be used to generate a vascular network by solving equation 3.4 subject to the boundary conditions given by equation 3.5 and the rules for branching and anastomosis. We first take the case of a tumour placed at the edge of the domain where the parent vessel is at x = 0 and the tumour edge is at x = 1 and the initial conditions for endothelial cell density, TAF and fibronectin are described by equations 3.7, 3.8 and 3.9. Figure 3.7 shows the movement of the sprouting tips with time and the resulting vascular network. The branching is minimal initially, however, as time

passes, and the tips reach the tumour where the TAF concentration is high, branching occurs more frequently.
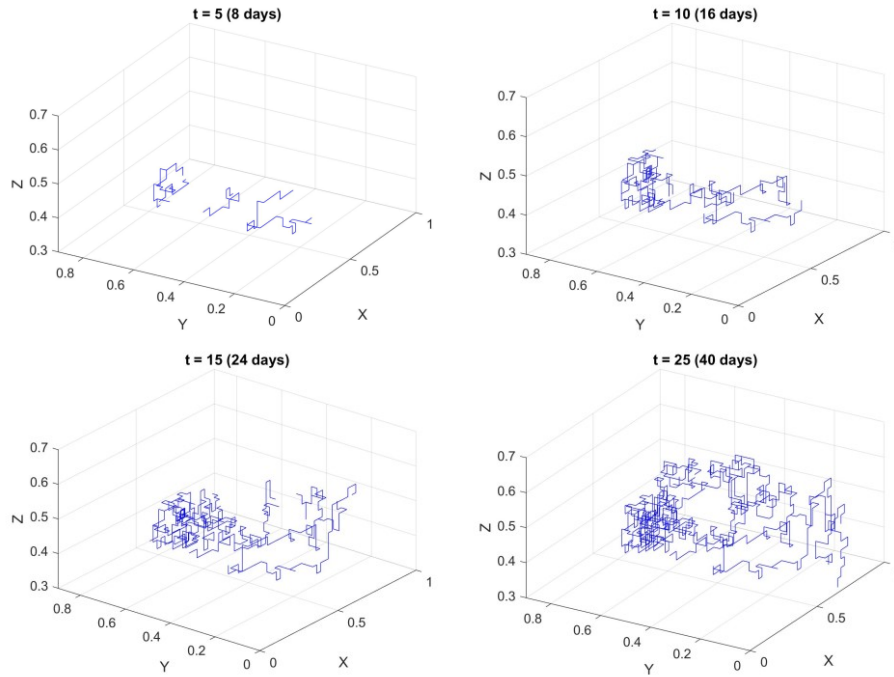
Figure 3.7: Formation of capillary network for a tumour at the edge of domain (x =1).

Figure 3.8 shows the formation of a vascular network for a tumour centred at the domain with a dimensionless radius of 0.25 using initial TAF conditions given in equation 3.10. The sprouts move towards the center of the domain and reach the tumour by t = 5 (8 days). At t = 10 (16 days) the sprouts have branched off and multiplied excessively within the tumour to form a vascular structure. Branching and anastomosis continue to take place up to the final simulation time of t = 25 (40 days).

The formation of a vascular network for a tumour with a necrotic core is simulated using the initial TAF concentration described by equation 3.11. The sprout tips move towards the tumour in a similar manner to what is observed in Figure 3.8, however, as the tips penetrate the tumour, they are unlikely to branch or move into the region where a negative TAF concentration gradient is defined. This is highlighted in Figure 3.9 where the vascular networks generated at t = 25 (40 days) for both non-necrotic and necrotic tumours are shown in the defined necrotic region within a non-dimensional radius of 0.08 from the center. In the left plot of figure 3.9 showing the core region of the non-necrotic tumour, a dense network of vessels is observed which is in contrast to the plot on the right showing the core region of the necrotic tumour where only a small number of vessels can be observed.
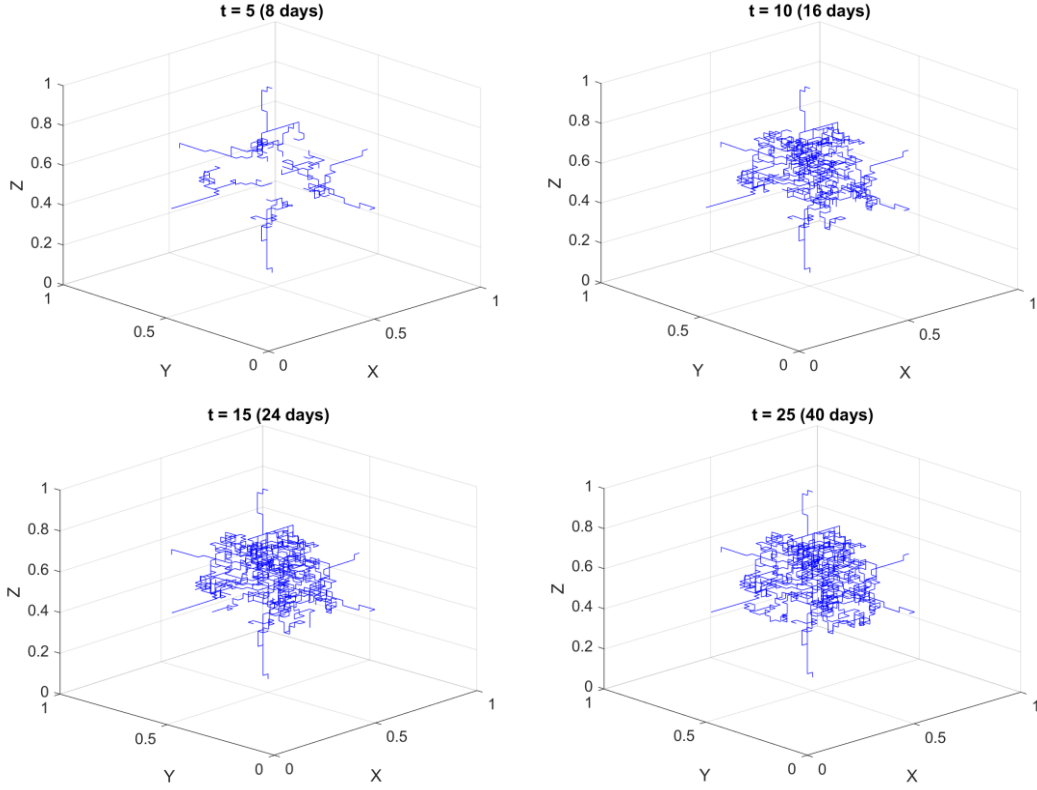
Figure 3.8: *Formation of a vascular network for a non-necrotic tumour cantered in the domain with a dimensionless radius of 0.25.*
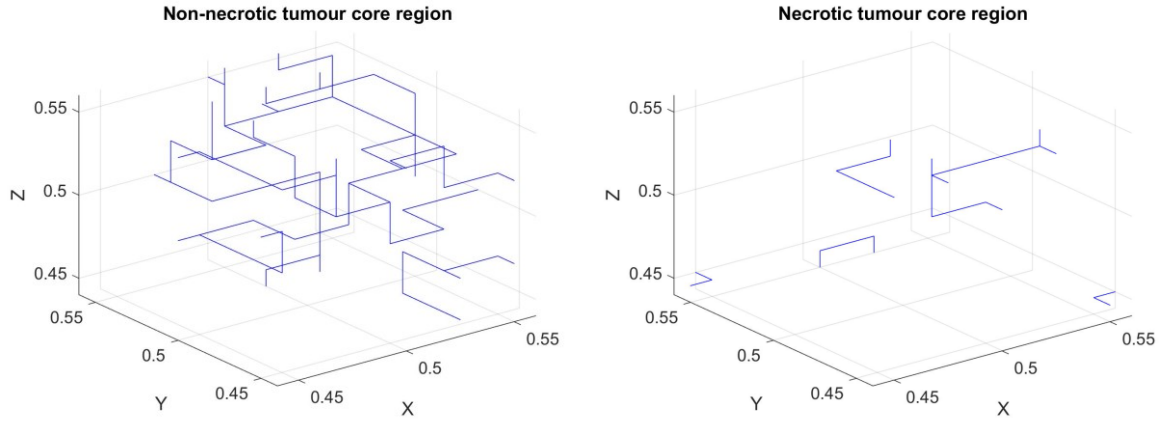
Figure 3.9: *Vascular network in spherical tumour with no necrosis (left) and tumour with a necrotic core (right) at final time t = 25 (40 days).*

3.2.2   Fluid flow model

In this section, a fluid flow model is presented and applied to the geometries generated using the angiogenesis model described in the preceding section. The model is based on the fluid flow model for a

solid tumour developed by Pozrikidis [159] which has been described briefly in Chapter 2.2. To apply the fluid flow model, the vascular network is divided into cylindrical segments connected through nodes at both ends of the segments. Each segment can be taken to represent an individual vessel. In tumour vessels, blood flow can be described as incompressible, low Reynolds number (<1) flow [43, 202]. As the radius of the vessel is much smaller in comparison to its length, it would be reasonable to assume that blood flow within tumour vessels is described by Poiseuille's law that relates the flowrate Q, to the pressure gradient along the vessel length and resistance to flow as follows:

$$Q(l) = -\frac{\pi R^4(l)}{8\mu}\frac{dp_v}{dl} \qquad (3.12)$$

Where l is the distance along the vessel length, $R(l)$ is the local vessel radius at l distance along the segment, μ is the blood viscosity, and p_v is the vascular pressure. The interstitial space can be described as a porous medium composed of cellular and ECM components with fluid flow in between these structures. Fluid velocities in the interstitial space are typically on the order of 1 μm s^{-1}, and interstitial fluid can be assumed to be incompressible and Newtonian [203]. In this case interstitial flow can be described using Darcy's law for flow through porous media

$$u_i = -K\nabla p_i \qquad (3.13)$$

Where u_i is the interstital velocity, p_i is the interstitial pressure and K is the interstitial hydraulic conductivity defined as $K = \lambda/\mu_i$. λ is porosity of the interstitial space and μ_i is the viscosity of the interstitial fluid. Applying mass conservation using equation 3.13 and assuming that K is constant, the interstitial pressure satisfies Laplace's equation

$$\nabla \cdot u_i = 0 \qquad (3.14)$$
$$\nabla \cdot (-K\nabla p_i) = 0$$
$$\nabla^2 p_i = 0$$

For which the solution satisfies the Dirichlet boundary condition where pressure p_i far from the capillary surface at the tumour surface is equal to the ambient pressure p_0. Starling (1896) determined that fluid filtration across a capillary wall is dependent on the hydrostatic pressure difference and oncotic pressure difference across the capillary. Starling's law for the transport between the vessels and interstitial space is given as follows

$$q_e(l) = L_p(l)\big[p_v(l) - p_i(l) - \sigma_d\big(\pi_v(l) - \pi_i(l)\big)\big] \tag{3.15}$$

Where q_e is the fluid flux across the vessel, L_p is the hydraulic conductivity of the vessel wall, σ_d is the oncotic reflection coefficient and π_v and π_i are the vascular and interstitial oncotic pressures respectively. In tumours, the high vascular permeability reduces the oncotic pressure difference between the interstitial and vascular space and this was proven experimentally [56]. Hence, equation 3.15 can be reduced to

$$q_e(l) = L_p(l)[p_v(l) - p_i(l)] \tag{3.16}$$

Where p_i is evaluated on the exterior surface of the vessel and is assumed to be independent of the angular position due to the small size of the capillaries. Assuming mass is conserved in the capillary, blood flow in the vessel can be coupled to transvascular flux as follows

$$\frac{dQ}{dl} + 2\pi R(l) q_e(l) = 0 \tag{3.17}$$

Equations 3.12 and 3.16 can be substituted into equation 3.17 to give a second order differential equation coupling interstitial and vascular flow.

$$\frac{d^2 p_v}{dl^2} + \frac{4}{R(l)}\frac{dR}{dl}\frac{dp_v}{dl} = -\frac{16\mu}{R^3(l)} L_p(l)[p_v(l) - p_i(l)] \tag{3.18}$$

For a vessel of constant radius, the second term on the left-hand side of equation 3.18 is eliminated. In the equation, if the interstitial pressure is constant, the capillary flow becomes decoupled from the interstitial flow as is the case in normal tissue. In Pozkridis's work, the mathematical formulation was completed by setting the flux on the vessel surface described by Darcy's law equal to Starling's law

$$\frac{\partial p_i}{\partial l_n} \equiv n(\mathbf{x})\nabla p_i(\mathbf{x}) \approx -\frac{L_p}{\kappa}(p_v - p_i) \tag{3.19}$$

Where l_n is the normal arc length and $n(\mathbf{x})$ is the unit vector normal to the vasculature pointing into the interstitium. The boundary integral formulation can be applied to solve equation 3.14 using Green's function method, giving an expression for the interstitial pressure at field point $\mathbf{x}_0$ in terms of a combination of a single- and a double-layer potential defined over the surface of the vasculature.

$$p_i(\mathbf{x}_0) - p_0 = -\int\int_{S_V} G(\mathbf{x}, \mathbf{x}_0)\big(\mathrm{n}(\mathbf{x})\nabla p_i(\mathbf{x})\big)dS(\mathbf{x}) \tag{3.20}$$

$$+\int\int_{S_V}(p_i(\mathbf{x}) - p_0)\big(\mathrm{n}(\mathbf{x})\nabla G(\mathbf{x}, \mathbf{x}_0)\big)dS(\mathbf{x})$$

Where $S(\mathbf{x})$ denotes the tumour surface boundary, $\mathrm{n}(\mathbf{x})$ is the unit vector normal to the tumour surface S_V is the surface of the vasculature and $G(\mathbf{x}, \mathbf{x}_0)$ is the Green's function solution to Laplace's equation that is dependent on the tumour geometry. Equation 3.20 gives the interstitial pressure as a function of the boundary conditions at the tumour surface and over the surface of the vasculature and hence interstitial pressure is described as a function of vascular distribution and vascular pressure. For a tumour of infinite size Green's function is given by

$$G(\mathbf{x}, \mathbf{x}_0) = \frac{1}{4\pi|\mathbf{x} - \mathbf{x}_0|} \tag{3.21}$$

When the point $\mathbf{x}_0$ approaches the surface of the vessel, the limit of the double layer potential differs and can be expressed using its principal value (*PV*). The volume being integrated over in equation 3.20 becomes half leading to the following

$$\frac{1}{2}[p_i(\mathbf{x}_0) - p_0] = \int\int_{SV}^{PV}(p_i(\mathbf{x}) - p_0)\big(\mathrm{n}(\mathbf{x})\nabla G(\mathbf{x}, \mathbf{x}_0)\big)dS(\mathbf{x}) \tag{3.22}$$

$$+\int\int_{SV} G(\mathbf{x}, \mathbf{x}_0)(\mathrm{n}(\mathbf{x})\nabla p_i)dS(\mathbf{x})$$

As mentioned earlier, the interstitial pressure can be assumed to be independent of angular position. With this assumption, substituting the right-hand side of equation 3.19 into equation 3.22 gives

$$\frac{1}{2}[p_i(\mathbf{x}_0) - p_0] = \int\int_{SV}^{PV}(p_i(l) - p_0)\big(\mathrm{n}(\mathbf{x})\nabla G(\mathbf{x}, \mathbf{x}_0)\big)dS(\mathbf{x}) \tag{3.23}$$

$$+\int\int_{SV}\frac{L_p(l)}{\kappa}(p_v(l) - p_i(l))G(\mathbf{x}, \mathbf{x}_0)dS(\mathbf{x})$$

Hence, the problem is reduced to solving equations 3.18 and 3.23 subject to arterial and venous pressure values, p_a and p_v and the tumour surface pressure p_0.

The vasculature is divided into *N* cylindrical segments as shown in Figure 3.10. Each vessel segment is assigned a vessel radius R_j and length L_j.
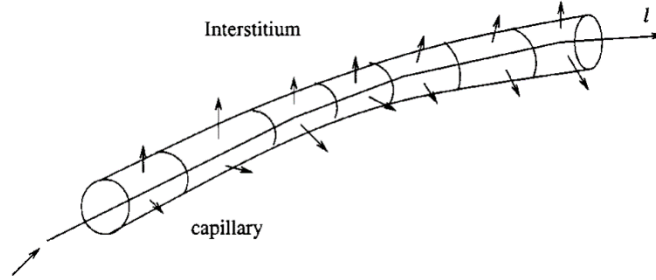
Placing the point $\mathbf{x}_0$ on the surface of the vasculature can allow for equation 3.23 to be written as

$$\frac{1}{2}[p_i(\mathbf{x}_0) - p_0] = \sum_{j=1}^{N_v} \int_{S_v^j} (p_i(l) - p_0)\big(\mathrm{n}(\mathbf{x})\nabla G(\mathbf{x}, \mathbf{x}_0)\big)dS(\mathbf{x})$$

$$+ \sum_{j=1}^{N_v} \int_{S_v^j} \frac{L_p(l)}{\kappa}(p_v(l) - p_i(l))G(\mathbf{x}, \mathbf{x}_0)dS(\mathbf{x})$$

(3.24)

Where N_v is the number of vessel segments and S_v^j is the surface of the *jth* segment where *j = 1,2,3,.....,N_v*.

As the vasculature is discretized with each segment assigned specific values for radius, length and hydraulic conductivity, equation 3.24 reformulated

$$\frac{1}{2}[p_i(l_0) - p_0] = \sum_{j=1}^{N_v} \frac{L_p^j}{\kappa}(p_v^j - p_i^j)A^j\,(l_0) + \sum_{j=1}^{N_v}(p_i^j - p_0)B^j\,(l_0)$$

(3.25)

Where l_0 is the arc length, A^j and B^j are the influence coefficients for the single and double-layer potentials given as

$$A^j(l_0) = \int\int_{E_j} G(x, x_0)dS$$

(3.26)

$$B^j(l_0) = \int\int_{E_j}^{PV} \mathrm{n}(\boldsymbol{x})\nabla G(\boldsymbol{x},\boldsymbol{x_0})dS$$

Where E_j is the cylindrical surface of the jth vessel segment. The evaluation point at arc length l_0 can be moved to the mid-point of the nth element at arc length l_n^m where $n = 1,2,3,……,N_v$. This provides a system of linear equations for the interstitial and vascular pressures. Moving the interstitial pressure in equation 3.25 to the left-hand side and evaluating at the mid-point give the following

$$\sum_{j=1}^{N}\left[\frac{1}{2}\delta_{nj} + \frac{L_p^j}{\kappa}A^j\;(l_n^m) - B^j\;(l_n^m)\right]p_i^j = \sum_{j=1}^{N}\frac{L_p^j}{\kappa}A^j\;(l_n^m)p_v^j + p_0\left[\frac{1}{2} - \sum_{j=1}^{N}B^j\;(l_n^m)\right]$$

(3.27)

Where δ_{nj} is Kronecker's delta function. Subsequently, equation 3.18 is discretized using a second order finite difference method assuming a constant radius for each vessel segment.

$$\frac{p_v^j - 2p_v^{(j+1)/2} + p_v^{j+1}}{\Delta l^2} = \frac{16\mu}{R^3}L_p\;[p_v^{(j+1)/2} - p_i^{(j+1)/2}]$$

(3.28)

Where $\Delta l = L/2$ and L is the vessel segment length. p_v^j and p_v^{j+1} are the vascular pressures at the either ends of the vessel segment and $p_v^{(j+1)/2}$ and $p_i^{(j+1)/2}$ are the vascular and interstitial pressures at the midpoint of the vessel segment. Equation 3.28 can be rearranged to give the midpoint vessel pressure in terms of the end point values

$$p_v^{(j+1)/2} = \frac{p_v^j + p_v^{j+1} + \beta p_i^{j+1/2}}{2 + \beta}$$

(3.29)

$$\beta = 4\frac{\mu L_p L^2}{R^3}$$

The transvascular pressure gradient is expressed as follows

$$p_v^{(j+1)/2} - p_i^{j+1/2} = \frac{p_v^j + p_v^{j+1} - 2p_i^{j+1/2}}{2 + \beta}$$

(3.30)

This can be used to determine extravasation from the vessels in the discretized equation 3.25. The pressure gradient can be calculated at the end nodes of vessel segment j using the second order finite difference methods for the first derivative as in Pozkridis's work and then combined with equation 3.29

$$\left(\frac{dp_v}{dx}\right)^j_{E_j} \cong \frac{-(3\beta + 2)p_v^j + 4\beta p_i^{j+\frac{1}{2}} + (2 - \beta)p_v^{j+1}}{(2 + \beta)L} \tag{3.31}$$

$$\left(\frac{dp_v}{dx}\right)^{j+1}_{E_j} \cong \frac{-(2 - \beta)p_v^j - 4\beta p_i^{j+1/2} + (3\beta + 2)p_v^{j+1}}{(2 + \beta)\Delta L}$$

Where E_j denotes the end node of segment j. The flowrates at both ends of the segment can be determined by applying Poiseuille's law given in equation 3.12

$$Q^j_{E_j} = \left(-\frac{dp_v}{dx}\right)^j_{E_j} \frac{\pi R^4}{8\mu} = \left(c_A p_v^j - c_C p_i^{j+1/2} - c_B p_v^{j+1}\right)\frac{\pi R^4}{8\mu\Delta L} \tag{3.32}$$

$$Q^{j+1}_{E_j} = \left(-\frac{dp_v}{dx}\right)^{j+1}_{E_j} \frac{\pi R^4}{8\mu} = \left(c_B p_v^j + c_C p_i^{j+1/2} - c_A p_v^{j+1}\right)\frac{\pi R^4}{8\mu\Delta L}$$

Where

$$c_A = \frac{(2+3\beta)}{2+\beta} \qquad c_B = \frac{(2-\beta)}{2+\beta} \qquad c_C = \frac{4\beta}{2+\beta} \tag{3.33}$$

Hence, the rate of fluid leakage is given by

$$Q_e = Q^{j+1}_{E_j} - Q^j_{E_j} = \left((c_B - c_A)p_v^j + 2c_C p_v^{j+1/2} - (c_A - c_B)p_v^{j+1}\right)\frac{\pi R^4}{8\mu\Delta L} \tag{3.34}$$

In a case where capillary flow is a simulated in a network with defined nodes and segments, mass conservation at the nodes shared between elements requires

$$Q^{j+1}_{E_j} = Q^{j+1}_{E_{j+1}} \tag{3.35}$$

Combining equation 3.35 with equation 3.32 and rearranging provides a tridiagonal system of equations for the capillary pressure

$$p_v^{j+1}\left(c_A^{(1)} + c_A^{(2)}\right) - c_B^{(1)}p_v^j - c_B^{(2)}p_v^{j+2} - c_C^{(1)}p_i^{j+\frac{1}{2}} - c_C^{(2)}p_i^{j+\frac{3}{2}} = 0 \tag{3.36}$$

For *j = 2,3,4,......, (N_v − 1)* where $r = {L_j}/{L_{j+1}}$. The right hand side is the interstitial pressure on the surface of the vessel. For *j = 1* and *j = N_v* , boundary conditions are applied where $p_v^1 = p_{arterial}$ and $p_v^{N_v} = p_{venous}$.

In the case where branching or merging of vessels occurs as shown in Figure 3.11, mass conservation at the bifurcating node is applied as follows and is solved for p_0

$$p_v^{j+1}\left(c_A^{(1)} + c_A^{(2)} + c_A^{(3)}\right) - c_B^{(1)}p_v^j - c_B^{(2)}p_v^{j+2}$$

(3.37)

$$- c_B^{(3)}p_v^{j+3} - c_C^{(1)}p_i^{j+\frac{1}{2}} - c_C^{(2)}p_i^{j+\frac{3}{2}} - c_C^{(3)}p_i^{j+\frac{5}{2}} = 0$$
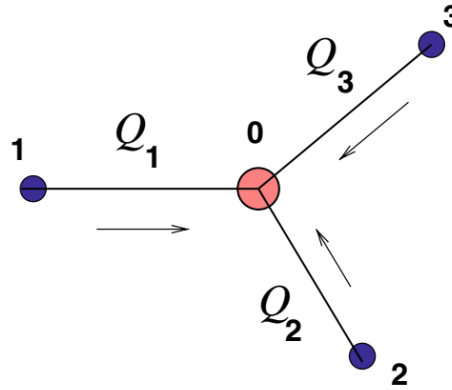
Figure 3.11: Bifurcating capillary mass balance relating the pressures at the four nodes 0, 1, 2 and 3 for segments 1, 2 and 3. (Extracted from [176])

Equation 3.27 can be reformulated as

$$-\frac{L_pA_j}{k(2+\beta)}p_v^{j+1} - \frac{L_pA_j}{k(2+\beta)}p_v^j + \left(-B_j + 2\frac{L_pA_j}{k(2+\beta)}\right)p_i^{j+\frac{1}{2}} = \frac{1}{2}p_0 - B_jp_0$$

(3.38)

Equations 3.36, 3.37 and 3.38 provides a linear system of equations which is solved subject to arterial and venous boundary pressures and interstitial tumour surface pressure.

The solution procedure is as follows:

1. Inlet and outlet capillary nodes are assigned arterial and venous pressure $p_{arterial}$ and p_{venous} respectively.
2. Interstitial pressures at the surface of the capillary midpoints are assigned a value p_0.
3. Using equations 3.36 and 3.37 and 3.38 a tridiagonal system of equations is generated and solved for the nodal capillary pressures and interstitial pressure.

Once the nodal capillary pressures and the interstitial pressure at the surface of the segment are determined, the interstitial pressure in the tissue is solved using the discretized boundary integral formulation in equation 3.25 where the transmural pressure term $(p_v^j - p_i^j)$ is substituted using equation 3.30. The interstitial space is discretized and the single- and double-layer potentials A^j and B^j are used to evaluate the influence of the vessel segments on each discretized tissue point. Using the influence coefficients, the vessel topology, the nodal capillary pressures and interstitial pressure at the vessel surface, the contribution of the vessel towards the pressure in interstitial space at point $\mathbf{x}$ is calculated, where $\mathbf{x}$ = (x, y, z). The interstitial pressure at point $\mathbf{x}$ is then calculated as a sum of these contributions and the influence of the tumour surface pressure as follows

$$p_i(\mathbf{x}) = \sum_{j=1}^{N_v} B^j\,(l_n^m)\left(p_i^{j+1/2} - p_0\right) + A^j\,(l_n^m)\frac{L_p}{\kappa}\frac{p_v^j - 2p_i^{j+1/2} + p_v^{j+1}}{2 + \beta} \qquad (3.39)$$

3.2.3   Vascular network regulation

In order to apply the fluid flow model described above to the vascular network generated from the angiogenesis model, the geometry of the network must be regulated and further defined. First nodes are assigned to coordinates where tip merging or branching occurs and where the tips initially sprout and end. Then further nodes are created along this path that the tip moves. A connection matrix logging the connectivity between the nodes is formed based on the data from the raw vascular network generated. A depth-first search algorithm is then used to move down from the initial node creating segments based on the connection matrix. To define the diameter of the vessels, a maximum diameter is set at the initial parent vessels which are assumed to be maintained for subsequent vessels down the network except in the case where branching or merging occurs. When this occurs the diameter of the daughter vessel is

assumed to decrease in size. The change in radius from a vessel of the *n*th generation to the (*n*+1)th generation can be modelled as monotonously decreasing as follows

$$D_{n+1} = \left(\frac{D_{min}}{D_{max}}\right)^m D_n \qquad (3.40)$$

Where D_{min} and D_{max} are defined minimum and maximum diameters and *m* is a coefficient less than 1. Applying the vascular regulation algorithm to the networks generated from the angiogenesis model yields the vascular geometries shown in Figure 3.12.
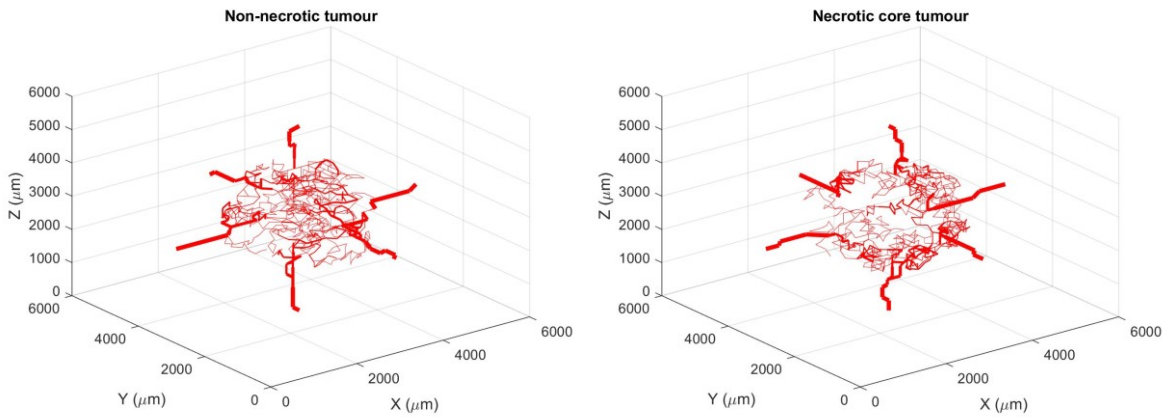
Figure 3.12: *Microvascular tumour networks for a non-necrotic tumour (left) and necrotic core tumour (right) generated after regulation*

3.2.4 Tumour network and fluid flow validation

In order to validate the tumour network generation model and the fluid flow model, a list of morphological and hemodynamic parameters were calculated and then compared with literature values obtained from empirical studies. For morphological parameters the following properties were determined [89, 93]

$$\text{Tumour volume } V_t = \frac{4}{3}\pi r_t^3 \qquad (3.41)$$

$$\text{Vascular density } V_d = \frac{1}{4\,V_{tissue}} \sum_{i,j}^{N} \pi D_{ij}^2 L_{ij}$$

$$\text{Length density } L_D = \frac{1}{V_{tissue}} \sum_{i,j}^{N} L_{ij}$$

$$\text{Vessel surface to volume ratio } S/V = 4\frac{\sum_{i,j}^{N} \pi D_{ij} L_{ij}}{\sum_{i,j}^{N} \pi D_{ij}^2 L_{ij}}$$

$$\text{Maximum extravascular diffusion distance R} = \frac{1}{\sqrt{\pi L_D}}$$

Where r_t is the radius of the tumour tissue, D_{ij} and L_{ij} are the diameter and length of the vessel segment between nodes *i* and *j*. The following hemodynamic parameters were calculated to validate the fluid flow model

$$\text{mean velocity } u_{ij} = \frac{4Q_{ij}}{\pi D_{ij}^2} \tag{3.42}$$

$$\text{mean shear stress } \tau_{ij} = \frac{32\mu_{ij} Q_{ij}}{\pi D_{ij}^3}$$

$$\text{Vascular segment transit time } \text{VSTT} = \frac{\pi D_{ij}^2 L_{ij}}{4Q_{ij}}$$

$$\text{Flow weighted mean path lenght MPL} = \frac{\sum_{i,j}^{N} Q_{ij} L_{ij}}{\sum_{i,j}^{N} Q_{ij}}$$

3.2.5 Vessel remodelling framework

Blood vessels in tumour tissue are characterized by their heterogeneous nature where they can exhibit varying diameters and permeabilities. Blood vessels naturally adapt in response to mechanical and metabolic stimuli in order to ensure the tissue is well perfused and supplied with nutrients and oxygen. The mechanisms of vessel adaption have been described by Pries et al. [169] which provides a framework to model changes in vascular structure in response to stimuli. The parameters in their model were fitted specifically to the normal tissue which was studied in their work. Cellular abnormalities in the tumour vessels such as large inter-endothelial gaps limit signal conduction whilst the lack of pericyte coverage reduces the ability to undergo diameter changes. The impaired structural adaption in addition to the lack of experimental data the structural adaption of tumour vessels makes Pries model less applicable in this case. Hence, a simple framework is employed in this study, which was developed by Vavourakis et al. to model changes in vessel radius, wall thickness and pore radius [74]. In their work, vessel adaptivity is described by a single variable, the remodelling time t_m which is governed by the shear stress on the vessel and is given by

$$t_m(\tau) = \begin{cases} t_{m-T} & , & \tau \geq \tau_{ref} \\ t_{m-T} + \Delta t_m \exp\left[1 - (1 - \tau^2/\tau_{ref}^2)\right], & \tau < \tau_{ref} \end{cases} \quad (3.43)$$

where $\Delta t_m = t_{m-0} - t_{m-T}$. t_{m-T} is the time value for a vessel to reach the upper limit of remodeling if $\tau \geq \tau_{ref}$ and t_{m-0} is the time required if shear stress was zero. Wall remodelling occurs on a large time scale and t_{m-0} is set to zero whilst t_{m-T} is defined as 10 days based on the empirical value adopted by Vavourakis et al [74]. Hence, the rate of wall remodelling is inversely proportional to wall shear stress. The model assumes that a vessel becomes fully remodelled as it moves from a poorly perfused state to a well perfused state. This transition is modelled using equation 3.43 and the reference shear stress value τ_{ref}, which defines the transition of a vessel from a hypo-perfused state to a well perfused state. Vascular segment transit time is used as an indicator for hypo perfusion as it takes into account blood flow and vessel length in each segment. Kamoun et al. defined hypo-perfused vessels as those where velocities are below 0.05 mm/s, hence for an average vessel of 0.2 mm in length, the VSTT is approximately 4 seconds [204]. Therefore, shear stress can be evaluated in terms of VSTT of 4 second as follows

$$\tau_{ref} = \frac{8\mu L}{4\,R} \quad (3.44)$$

The change in capillary radius is modelled as a function of the time from when the vessel point was created and the remodelling time t_m which is a function of shear stress. Initially when a node is created through the movement of the vessel tip, the vessel is assigned a minimum radius R_{min} which then expands with time and as the shear stress increases. The radius R is described as a function of time as follows

$$R(\tilde{t}) = \begin{cases} R_{min} & , & \text{at tip node} \\ R_{min} + (R_{max} - R_{min})\exp[-B_R \exp(-C_R\,\tilde{t})], & \text{Elsewhere} \end{cases} \quad (3.45)$$

Where R_{max} is the maximum radius, $B_R = 11$ and $C_R = 4.4$. The dimensionless time is defined as $\tilde{t} = \frac{t - t_i}{t_m}$ where t_i is the time at which the node was created and t is the normalized time defined in equation 3.6.

Wall thickness, w, can be assumed to increase linearly as a function of time and is given as

$$w(\tilde{t}) = w_{max} + (1 - \tilde{t})w_{min} \quad (3.46)$$

Where w_{max} and w_{min} are the maximum and minimum wall thickness. The vessel pore size is also modelled as a function of time and shear stress.

$$r_p(\tilde{t}) = \begin{cases} r_{pmin} & , \quad \tilde{t} \geq 1 \\ 2(r_{pmax} - r_{pmin})\tilde{t}^3 + 3(r_{pmin} - r_{pmax})\tilde{t}^2 + r_{pmax}, & \text{elsewhere} \end{cases} \quad (3.47)$$

Where r_{pmin} and r_{pmax} are the minimum and maximum pore size respectively. Initially when a vessel is generated, it is assigned a radius R_{min}, pore size r_{pmax} and wall thickness w_{min}. This follows physiological behaviour as when a vessel initially sprouts and is in an immature state, it is highly porous with thin walls. The hydraulic conductivity of each vessel is determined as a function of wall thickness w, pore radius r_p and the fraction of vessel wall occupied by pores γ_p

$$L_p = \frac{\gamma_p \, r_p^2(\tilde{t})}{8\mu \, w(\tilde{t})} \quad (3.48)$$

Simulations were performed with and without network remodelling in order to examine the effects of vascular remodelling on fluid flow.

3.2.6   Model parameters

To obtain results that can be compared with literature values, baseline parameters for the network geometry and fluid flow model were obtained from a range of literature sources where the parameters were determined based on relevant experimental data. Table 3.1 shows the values of parameters used to generate the tumour vascular network and in the fluid flow model. The computational domain can be thought to be made up of normal tissue with a tumour located at the center with a diameter of half the length of the domain. At each face of the domain boundary, parent vessels are assumed to exist from which vessel sprouts protrude as shown in figure 3.12. The distance from the tumour to the parent vessels can range from 1-2 mm, hence a value of 1.5 mm is chosen, which gives a tumour radius of 1.5 mm. The hydraulic conductivity of tumour vessels has been shown to be significantly higher than that in normal tissue vessels [63]. In the computational model, vessels that are outside the defined tumour region are prescribed with normal tissue hydraulic conductivities whilst vessels within the tumour region are given tumour tissue hydraulic conductivity values as defined in Table 3.1. Arterial pressure is specified as a boundary condition at the starting point of a vessel from the parent vessels. The tips of the vascular network are assumed to be connected to the draining vessels and are assigned venous pressure values.

Table 3.1 Vascular network and Fluid flow model parameters

Parameter	Units	Tumour	Normal	Reference
Length from tumour to parent vessel	mm	1.5 mm	-	[205]
Length of domain L_D	mm	6 mm	-	[205]
Minimum vessel diameter R_{min}	µm	10	-	[161]
Parent vessel diameter R_{max}	µm	40	-	[161]
Vessel hydraulic conductivity L_p	m/Pa.s	2.1×10^{-11}	2.7×10^{-12}	[51]
Tissue hydraulic conductivity K	m^2/Pa.s	3×10^{-14}	3×10^{-15}	[51]
Osmotic vascular pressure π_v	mmHg	28	28	[56]
Osmotic interstitial pressure π_i	mmHg	20	8	[56]
Blood viscosity μ	Pa.s	0.004	0.004	[206]
Arterial pressure $p_{arterial}$	mmHg	25	-	[44]
Venous pressure p_{venous}	mmHg	10	-	[44]
Tumour surface pressure p_0	mmHg	0	-	[203]
Tissue density	kg/m^3	1050	-	[207, 208]

With regards to parameters required for network remodelling, vessels in the normal tissue region are assigned constant values for vessel pore size, wall thickness and the fraction of vessel wall occupied by pores as shown in Table 3.2

Table 3.2 Vascular remodelling parameters

Parameter	Units	Tumour	Normal	Reference
Maximum pore radius r_{pmax}	nm	200	5	[209]
Minimum pore radius r_{pmin}	nm	20	5	[209]
Fraction of vessel wall occupied by pores γ_p	-	1.008×10^{-2}	1.3×10^{-5}	[74]
Maximum wall thickness w_{max}	µm	4.01	5.5	[26, 74]
Minimum wall thickness w_{min}	µm	1.49	5.5	[26, 74]

3.3 Results and discussion

3.3.1 Validation of tumour geometry and fluid flow model

First of all, the generated vascular networks were analysed in terms of the morphological parameters defined in equations 3.41 to determine the degree to which the model can replicate properties found in real tumour vasculature. Values for the morphological parameters are summarised in Table 3.3. The tumour networks included those for a non-necrotic tumour generated using equation 3.10 and two other networks with varying degrees of necrosis using equation 3.11. One of the networks had a necrotic core with a normalized radius of 0.08 which accounts for 3% of the total tumour volume. Another vascular network was generated with a necrotic core radius of 0.16 making the core volume 14% of the tumour volume. The morphological parameter values for these tumour models were within the range reported in the literature, suggesting that the vascular network model can provide a good representation of real vascular networks. The fact that the average vascular density values hardly differ among the three networks suggests that as the degree of central necrosis increases, the tips would move away from the core and create more vessels in the peripheral tumour region. The variability in the values for the maximum extravascular diffusion distance was found to be minimal. However, the method used to calculate this parameter is based on the Krogh model for diffusion from capillaries and is determined based on the length density rather than the 3D geometry. Hence, they would not be representative when considering the whole tumour.

Table 3.3 Morphological parameters for different tumour networks with varying degrees of necrosis

Parameter	Units	Non-necrotic	Necrotic (3%)	Necrotic (14%)	Literature data	Reference
Tumour tissue volume	mm^3	14.137	14.137	14.137	-	-
Vascular density - V_d	%	0.304	0.295	0.312	0.15-1.25	[210-212]
Length density - L_D	mm/mm^3	6.962	6.238	6.671	10-72	[89]
Surface area to volume ratio (vascular) S/V	mm^2/mm^3	153.559	149.678	149.571	122-376	[213]
Maximum extravascular diffusion distance - R	µm	213.833	225.894	218.440	30-250	[38]
Mean vessel diameter	µm	21.198	22.436	22.373	5-225	[28, 36]
Mean vessel length	mm	0.192	0.189	0.189	0.06-0.3	[36, 214]

To check if the necrotic regions are avascular, morphological parameters were calculated in the core and peripheral regions of the tumour separately. Table 3.4 shows the corresponding comparisons for the different tumour vascular networks generated. The volume of the core region over which the parameters were calculated was 0.08 for the non-necrotic tumour, and 0.08 and 0.16 for the 3% and 14% necrotic tumours respectively. The normalized radius of the tumour for all cases was 0.25 of the tissue lengths. The periphery was defined as the difference between the total tumour volume and the core volume. It can be seen from table 3.4 that the vascular density for the non-necrotic tumour is higher at the core than in the peripheral region. For the necrotic tumours, the vascular density in the necrotic core is extremely low, which is expected. Vascular density in the peripheral region increases slightly from the non-necrotic tumour to the necrotic tumour with 14% necrosis. The maximum extravascular diffusion distance for the necrotic tumours at the core region is high and about 3-fold larger than the extravascular diffusion distance at the periphery. This shows that equation 3.11 is suitable for describing a tumour geometry with an avascular core defined by a specific radius.

Table 3.4 Morphological parameters at different the core and peripheral regions of the different tumour models

Parameter	Units	Core region			Peripheral region		
		Non-necrotic	Necrotic (3%)	Necrotic (14%)	Non-necrotic	Necrotic (3%)	Necrotic (14%)
Vascular density	%	0.512	0.043	0.084	0.300	0.297	0.338
Length density	mm/mm^3	19.658	0.768	1.434	6.722	6.280	7.256
Surface area to volume ratio	mm^2/mm^3	214.816	149.071	133.583	151.557	149.728	149.986
Maximum extravascular diffusion distance	µm	127.251	643.988	471.100	217.617	225.133	209.452
Mean vessel diameter	µm	17.875	26.833	25.236	21.405	22.43	11.158
Mean vessel length	mm	0.175	0.150	0.210	0.193	0.189	0.188

The geometries of the tumour vasculature were further analysed by calculating the vascular density in different regions within the tumour. The regions were defined using different ranges of radii from the tumour center. Figure 3.13 shows the distribution of vascular density in different regions in the three tumour models. The vascular density in the non-necrotic tumour is relatively uniform up to a normalized radius of 0.15 beyond which the vascular density drops at the periphery and on the outer tumour regions. In the tumour with 3% volume necrosis the vascular density is negligible at the center and a significant rise is seen at the boundary between the necrotic core and vascular region (0.05-0.1). Moving further away from the tumour center, the vascular density decreases and is correlated with distance away from the center. For the case of a tumour with 14 % necrotic core volume, the vascular density in the central region (0-0.1) is zero, which increases slightly within the defined core region (0.1-0.15), however the density is significantly lower than the peripheral regions. This is most likely caused by vessels protruding the tumour core. In this case, the vascular density at the outer region of the tumour 0.25-0.3 was found to be higher than in the case of the non-necrotic and 3% volume necrotic tumours. The 3% volume necrotic tumour core has an overall higher vascular density than the non-necrotic tumour in range between 0.05-0.2, whilst the 14% volume necrotic tumour has a higher vascular density in the range 0.2-0.3. The plots in Figure 3.13 highlight heterogeneity in vascular density for the different tumour models.
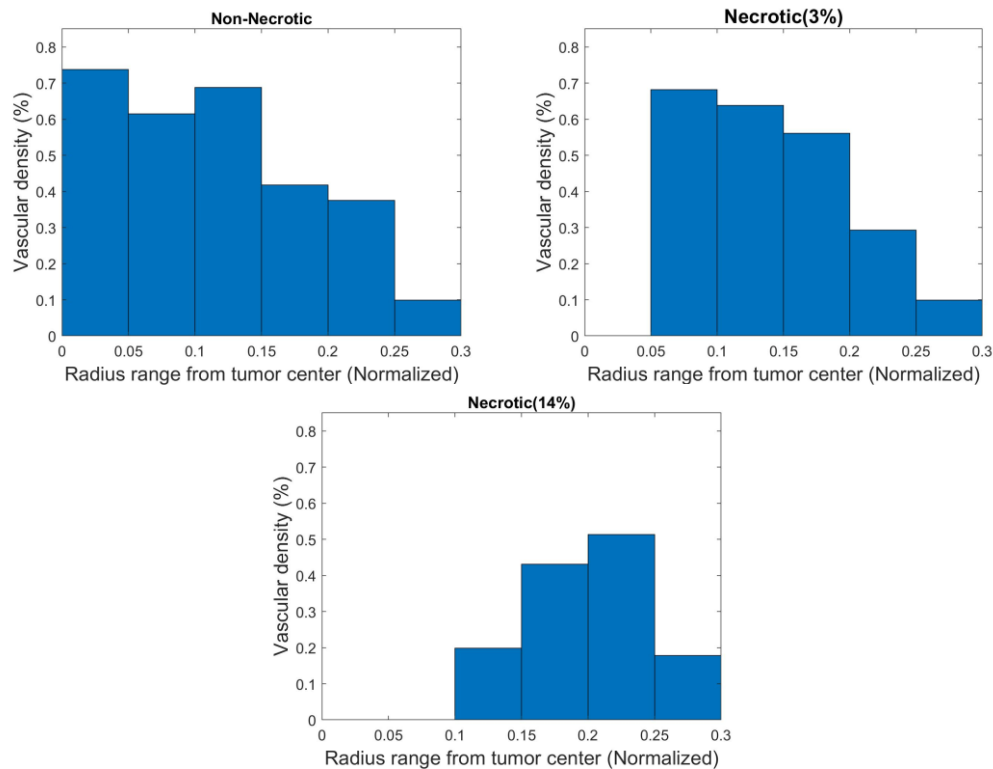
Figure 3.13: Vascular density for different tumour geometries in different regions defined by radius from center.

After evaluating the vascular networks generated for the different tumour models, the fluid flow model can be applied and validated by calculating the hemodynamic parameters listed in equations 3.42. Table 3.5 shows a summary of the tumour hemodynamic parameters averaged over the entire vascular network. The values calculated for the model networks correspond with experimentally measured hemodynamic parameters in tumours, suggesting the ability of the fluid flow model to capture the fluid dynamics in tumours.

Table 3.5 Hemodynamic parameters for different tumour networks

Parameter	Units	Non-necrotic	Necrotic (3%)	Necrotic (14%)	Literature data	Reference
Mean flow	nl/min	2.163	1.704	1.379	-	-
Mean velocity	mm/s	0.233	0.209	0.171	0.1-25	[204, 215]
Shear stress	Pa	0.699	0.661	0.543	1-10	[169]

3.3.2   Characterization of vascular network

The vasculature in solid tumours exhibits several abnormal structural and architectural features as highlighted previously including self-loops, vessel compression and blind ends. The presence of blind ends can cause very low or no flow in some vessels. Another feature which has been suggested is the presence of arteriovenous (AV) shunts where short low-resistance, high-flow pathways form in close proximity to the feeding vessels. A consequence of these AV shunts is that blood preferentially passes through them due the large pressure drop hence blood can completely bypass the entire capillary network. In the vascular network generated, some of the abnormalities of the tumour vasculature can be captured as shown in Figure 3.14. In the default vasculature generated the presence of AV shunts is not explicitly represented, hence to simulate this feature, vessels in close proximity to the arterial end are set to branch off where one end is connected to the tumour capillary network and the other end of this branch is assigned a venous pressure boundary condition. This allows for tumour vascular networks with and without AV shunts to be generated and the influence of this vascular abnormality can be examined.
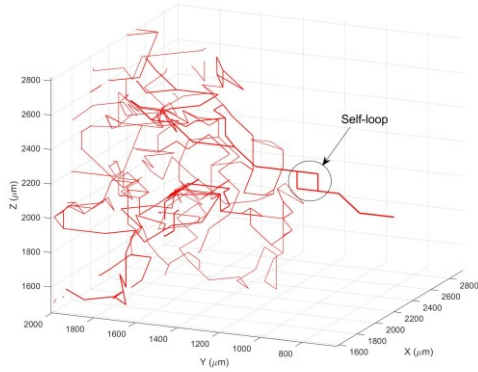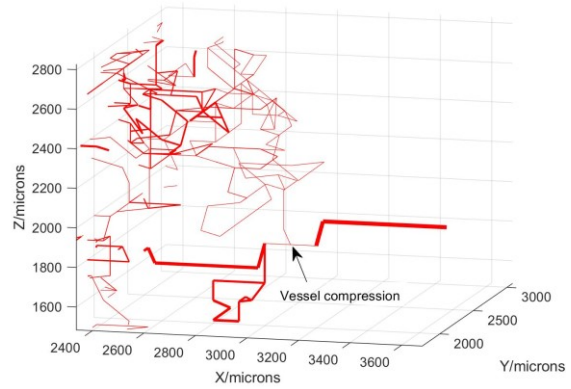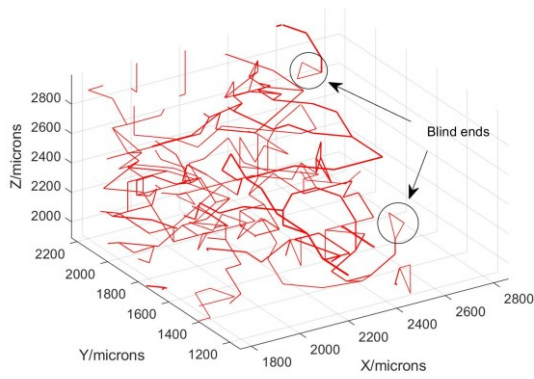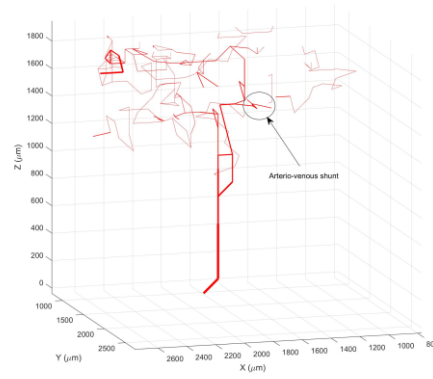
Figure 3.14: *Characteristic features of tumour vascular networks generated include (a) Vessel compression, (b) blind ends, (c) self-loops and (d) arteriovenous shunts*

3.3.3   Fluid flow in tumour tissue

Having obtained a tumour geometry that captures the heterogeneity and complexity of the tumour vasculature and a fluid flow model capable of predicting physiological values of blood flow in tumours, simulations were performed to examine the fluid flow behaviour in tumours and its sensitivity to tumour vasculature related properties. Initially, the case of a non-necrotic tumour without the presence of AV shunts is examined using the baseline parameters given in table 3.1. Figure 3.15a shows the simulated pressure distribution within the tumour vasculature. The intravascular pressure is maintained at a high level through most of the vascular network before it starts to drop rapidly as the tip vessel connected to the venule is approached. An average pressure drop per unit length of 0.35 Pa/μm was calculated in the vessels towards the venous end, which is in line with physiologically measured values [44]. The intravascular pressure in the tumour tissue averages to about 23.2 mmHg which is within the range of

values for intravascular pressures obtained through measurements and simulations in real capillary beds (10-40 mmHg) [44, 89, 145]. Figure 3.15b shows the pressure at the outer surface of each segmented vessel. The pressure distribution is seen to be heterogeneous with higher interstitial pressures at the surface of vessels close to the tumour center than in those in the peripheral region. The hydrostatic pressure reaches a maximum of approximately 12 mmHg at the surface of some tumour vessel with an average surface pressure of 8.6 mmHg. Pressures at the surface of vessels in the normal tissue were determined to be 3-4 mmHg which can be attributed to the low hydraulic conductivities prescribed to these vessels. These values were in range of interstitial pressures for normal tissue found in literature data (-8 to 6 mmHg) [216]. A standard deviation of 1.41 mmHg is found across the interstitial pressures on the vessel surface. The predicted interstitial pressures in the tumour region are within the range of measured values (4-50 mmHg) reported in the literature [52]. The rate of transvascular leakage calculated using equation 3.15 and parameter values in Table 3.1 are shown for each vessel in Figure 3.15c. A net outward fluid flux is observed in intratumoural vessels, which is significantly higher than for vessels in the normal tissue region where the net fluid flux is close to zero. The tip vessels which represent the venous ends also have a low flux which is found to be negative, causing an inward velocity flux. This is due to low pressures at the venous ends and net inward flux for venous vessels is consistent with physiological behaviour in capillary beds. A difference is observed in the transvascular flux between vessels at the tumour center and those at the peripheral region, where vessels in the central tumour region exhibit lower transvascular flux.

Whole tissue domain   **Tumour region**

a

b

c
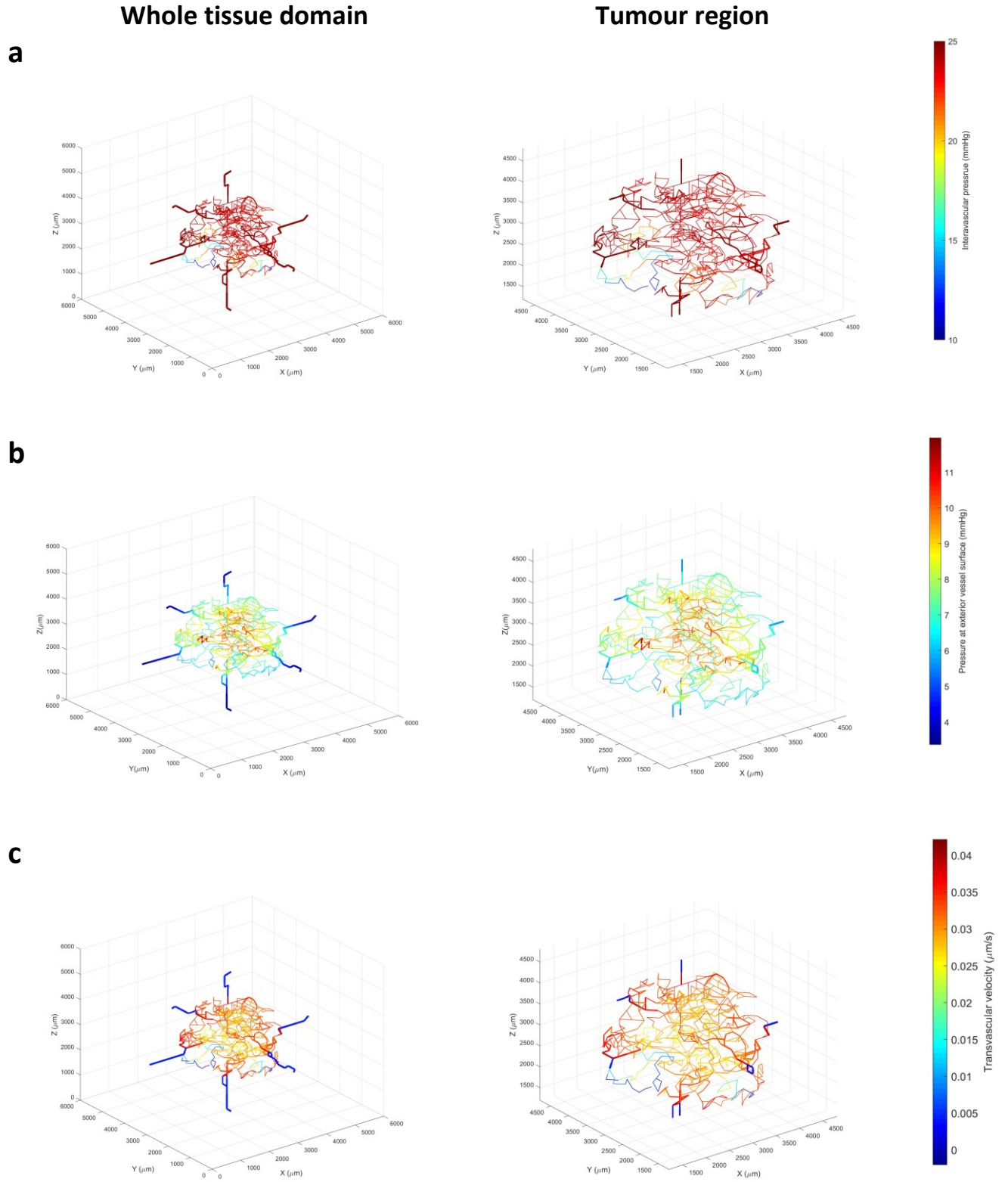
Figure 3.15: Maps of (a) the pressure distribution in the tumour vasculature, (b) on the exterior wall of the vessel and (c) the transvascular flux from vessels in the tumour.

To provide a 3D representation of the IFP in tumours, the tissue space was discretized in the orthogonal axis where pressure was determined at each point. Figure 3.16a shows the IFP distribution at a mid-height (z = 3000 μm) in the tumour tissue. IFP at this location is highest in the central tumour region with values up to 5.5 mmHg which then drops rapidly moving away from the tumour center where a pressure of around 1.5 mmHg is calculated at the tumour surface. This IFP profile corresponds with experimental and modelling based studies in the literature and further justifies the validity of the model in capturing the flow dynamics in tumour tissue. The IFP drops in the bottom left corner of the tumour which can be attributed to poor vascularisation in this region and that vessels in this region are connected to the venous ends as seen in Figure 3.15a. Hence, the lower intravascular pressure limits the pressure in the interstitial space. Figure 3.16b shows the pressure distribution where points with pressure values below 4 mmHg are rendered transparent to highlight the regions where IFP is highest. This shows the IFP to be highest and mostly concentrated at the tumour center.

a

b
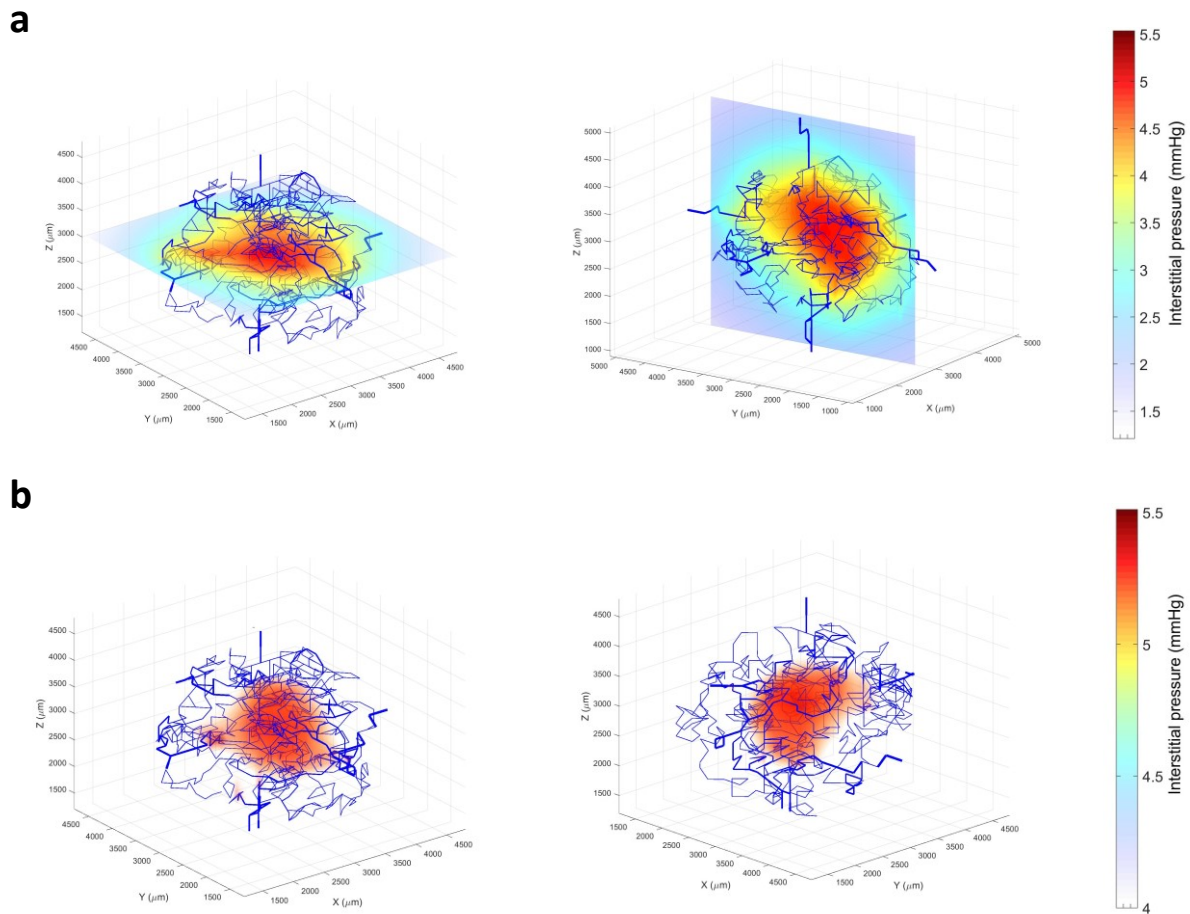
Figure 3.16: (a) Calculated interstitial pressure distribution in tumour tissue at half z-axis and x-axis (3000 μm). (b) 3D representation of IFP values above 4 mmHg from different angles. (Vessels are rendered blue for clarity).

3.3.3.1   Effect of vascular distribution and necrosis

To understand the effect of heterogeneous vascular distribution on fluid flow, simulations were performed using the tumour vascular networks generated with varying degrees of central necrosis. Distributions of vascular density within the tumour volume have been presented in Figure 3.13 and discussed in section 3.3.1. Figure 3.17 shows the distribution of IFP on the surface of the vessels and the transvascular velocity from each vessel for the tumour models with 3% and 14% necrotic core volume. The average interstitial pressure on the surface of the vessels is lower in the 3% necrotic tumour and is 8 mmHg. In the tumour with a higher degree of necrosis (14%) the average interstitial pressure on the vessel surface drops further to 7.68 mmHg. The transvascular velocity exhibits a similar trend to the non-necrotic case where flux is reduced in vessels close to the center of the tumour and in the venous ends.

Necrotic (3%)   **Necrotic (14%)**
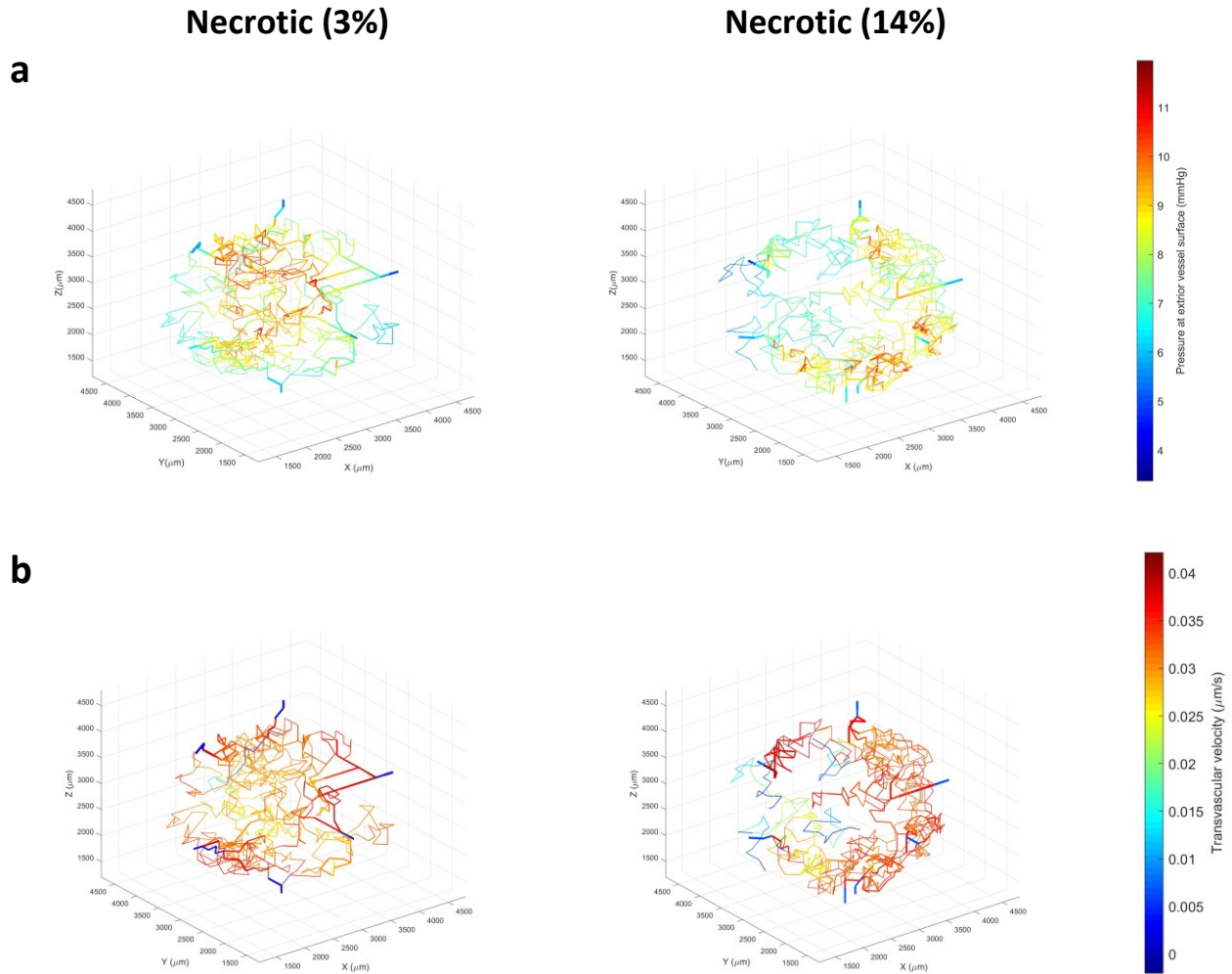
Figure 3.17: (a) Vessel surface pressure and (b) transvascular velocity in tumour geometries with different necrosis

Profiles of IFP at the mid-height (z = 3000 μm) in the tumour models are shown in Figure 3.18a. It is clear that the IFP profile is sensitive to the degree of necrosis, with a pronounced reduction in IFP in the avascular core in the 14% necrotic tumour. This is not so apparent in the tumour with 3% necrosis. Similar to Figure 3.16b, Figure 3.18b shows the 3D distribution of points above 4 mmHg to visualise the regions with the highest IFP. In the 3% necrotic tumour, high pressures are still seen in the tumour core, but with a slightly lower magnitude compared to the highest pressure found towards the upper periphery of the tumour. In the 14% necrotic tumour, IFP at the tumour center is significantly lower than the highest pressure distributed at the tumour periphery.

Necrotic (3%)   **Necrotic (14%)**
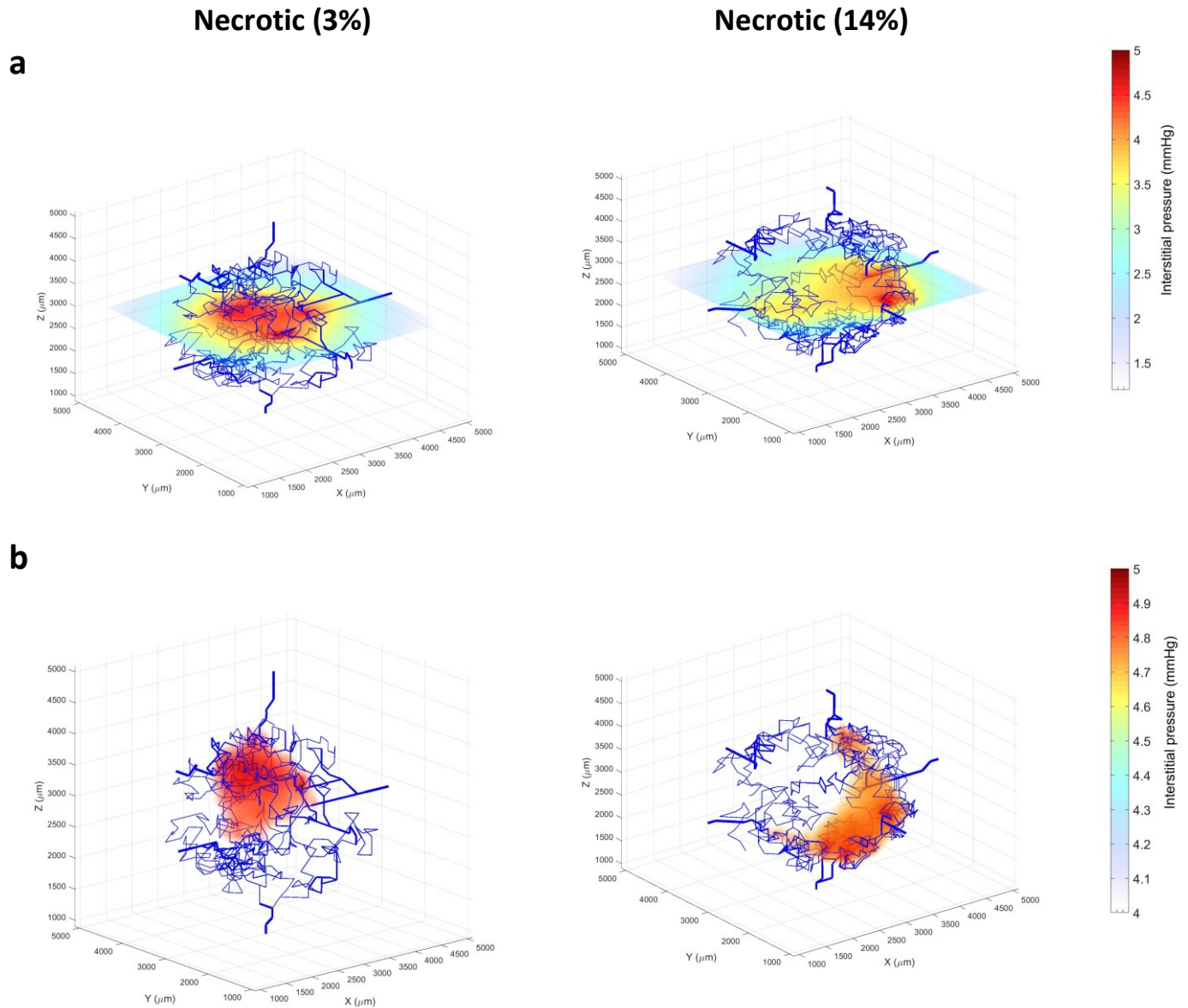
Figure 3.18: Interstitial fluid pressure distribution in tumour model with 3% necrosis (left) and 14% necrosis (right). (a) Shows pressure distribution at z = 3000 μm (b) shows the interstitial pressure distribution for values above 4 mmHg.

To further examine the heterogeneity in IFP, pressure profiles at the mid-plane along the y-axis are shown in Figure 3.19 for the three geometries. The necrotic tumour models with avascular cores exhibit peak IFP at the periphery rather than the center as observed in the non-necrotic tumour model. The pressure profile in non-necrotic tumour model is flatter in the central region (-0.1 to 0.1). The pressure gradient at the periphery is dependent on the degree of necrosis with a steeper gradient in the tumour with a larger avascular core showing that the distribution of the vasculature can play a significant role in tumour IFP.

Non-necrotic　　　　**Necrotic (3%)**　　　　**Necrotic (14%)**
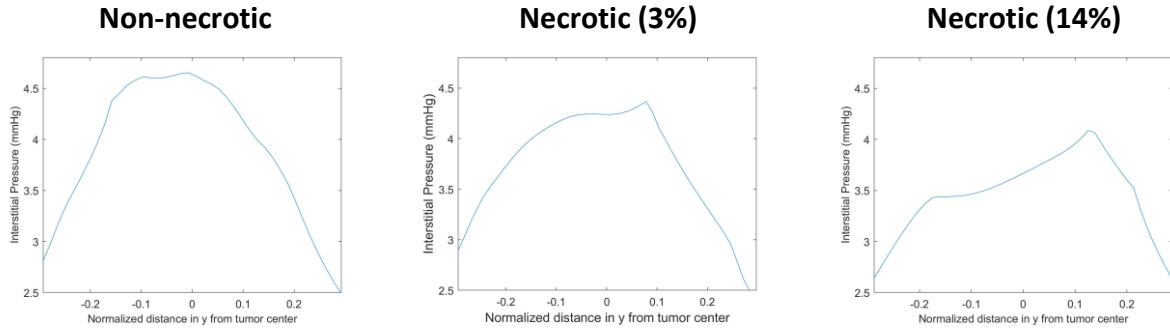
Figure 3.19: Pressure profile along the y-axis at the mid-plane for different tumour geometries.

3.3.3.2　Effect of vessel pruning and blind end removal

The vascular networks examined so far feature a number of blind ends that may affect the pressure drop and flow in the vascular network. To quantify this effect, the tumour vascular geometries were modified by removing several blind ends to open up the pathways for flow. To achieve this, the blind ends were identified within the network, which were then either removed or assigned as venous end vessels depending on their order within the network. Likewise, an AV shunt was also placed in a region near the arterial vessels as shown in figure 3.14. The macroscopic properties of the tumour microvasculature are similar as seen in table 3.6. The average of the mean vascular segment transit times (VSTT) and percentage of hypo perfused vessels were calculated using equation 3.42 and compared for the original and pruned networks. As shown in Table 3.7, removing blind ends leads to a significant reduction in VSTT and the number of hypo perfused vessels; the latter is reduced by approximately 40-65%.

Table 3.6 Morphological parameters for tumour vasculature

Parameter	Units	Original network	Pruned blind ends network
Vascular density - V_d	%	0.304	0.289
Length density - L_D	mm/mm^3	6.962	6.693
Surface area to volume ratio (vascular) S/V	mm^2/mm^3	153.559	154.468
Maximum extravascular diffusion distance - R	μm	213.833	218.160
Mean vessel diameter	μm	21.198	21.104
Mean vessel length	mm	0.192	0.193

Table 3.7 Comparison of hypo perfusion parameters between the original and pruned vascular networks.

Parameter	Original network			Pruned blind ends		
	Non-necrotic	Necrotic (3%)	Necrotic (14%)	Non-necrotic	Necrotic (3%)	Necrotic (14%)
Mean Vascular segment transit time (VSTT)	39.591	48.975	29.714	22.136	16.372	13.311
Hypo perfused vessels (%) VSTT > 4 seconds	70.190	78.193	65.819	36.182	29.278	34.463

Figure 3.20a shows the predicted intravascular pressure in the non-necrotic tumour after pruning. Compared to Figure 3.15a for the same tumour model before pruning, it is clear that pressure drop along vessels in the pruned vessel network is increased which can promote flow. Figure 3.20b shows that pressure at the vessel surface is reduced after pruning, especially in the tumour core where the maximum pressure drops from approximately 12 mmHg in the original network to 8.87 mmHg in the pruned network. Compared to Figure 3.15b, the pressure distribution tends to become more uniform after pruning, although differences between the tumour center and the periphery still exist. Pruning also leads to a noticeable reduction in transvascular flux from the vessels as shown in Figure 3.20c. The heterogenous intravascular pressure in the pruned network gives rise to a heterogeneous transvascular velocity from the vessels in the network.
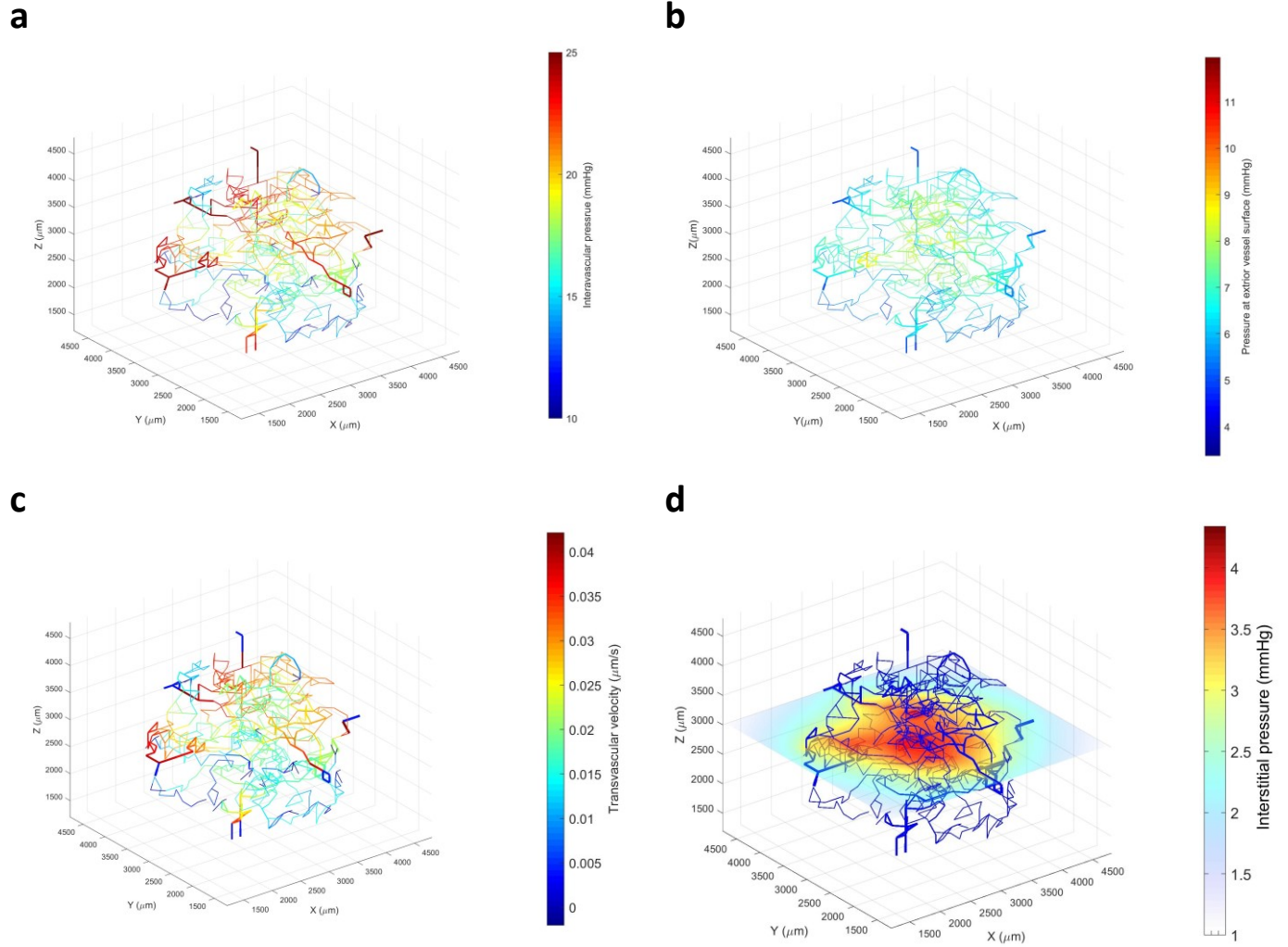
Figure 3.20: *(a) Intravascular pressure (b) surface vessel pressure (c) transvascular leakage and interstitial pressure in the pruned non-necrotic tumour.*

Figure 3.20d shows the interstitial pressure distribution at the mid-plane (z = 3000 μm), which displays a similar profile to that in the original network (Figure 3.16a), but the maximum pressure within the tumour drops by approximately 1.5 mmHg. These findings suggest that although the vascular distribution and macroscopic parameters of the vasculature in the tumour tissue is almost similar to the original network, microscopic changes such as the removal of blinds and addition of AV shunts can significantly alter the flow dynamics in the vasculature and consequently in tissue space. The ability of normalizing vessel networks has been suggested as a target to enhance treatment [217, 218]. Chauhan et al. simulated vessel normalization by reducing the permeability in vessels and the heterogeneity in vessel permeability

showing that IFP was reduced significantly [171]. Sweeney et al. investigated vessel normalization by reducing the vessel diameters and uniform vascular hydraulic conductivity to find IFP was reduced [177]. In this work, vascular normalization is simulated by reducing the abnormalities in the architecture of the tumour vasculature which showed similar findings in that the IFP was reduced.

3.3.3.3 Effect of vascular remodelling

To examine the effect of vessel adaption on fluid flow in tumours, the vessel remodelling framework discussed in section 3.2.5 is applied. To do this, the time over which the vascular network grows is discretized and the corresponding fluid flow is calculated. Shear stress and time are used as inputs to simulate changes in radius, pore size and wall thickness. The evolution of the vascular network with time is shown in Figure 3.21.

t = 5 (8 days)   **t = 10 (16 days)**

t = 20 (32 days)   **t = 25 (40 days)**
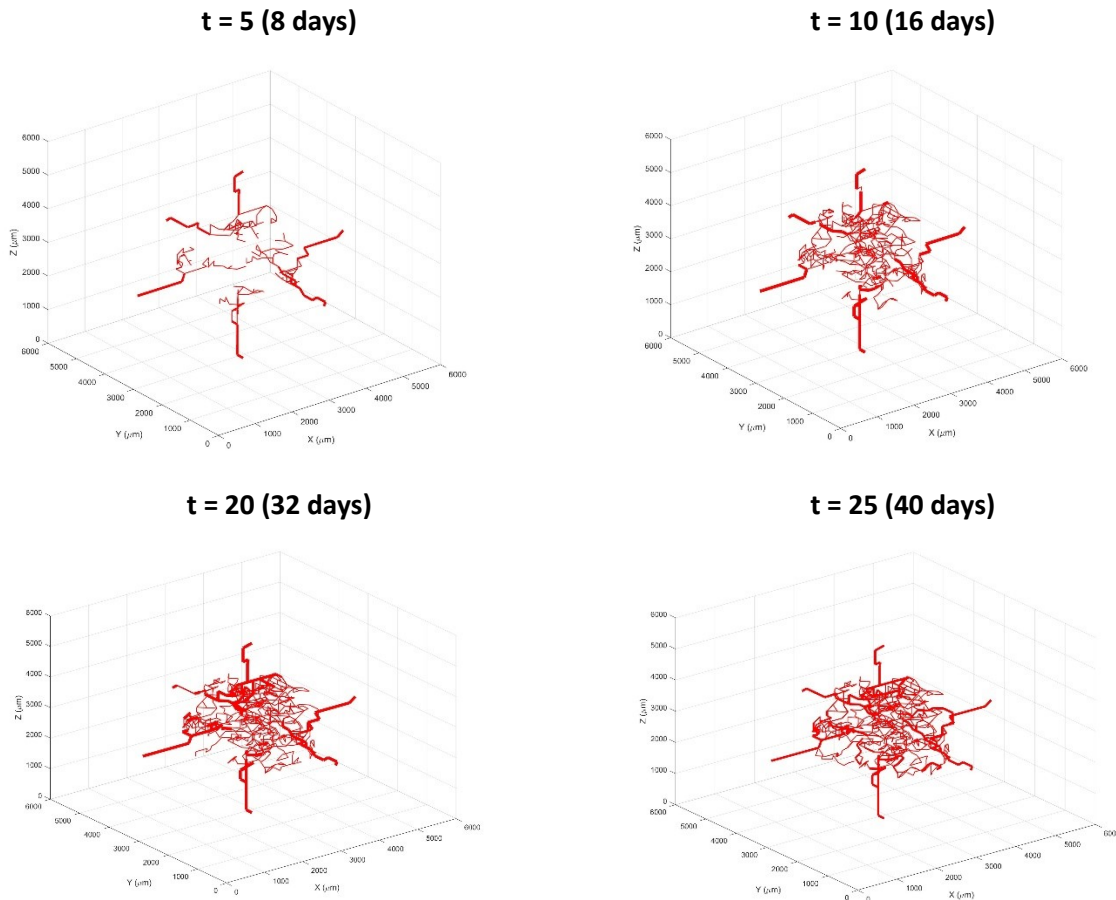
Figure 3.21: Growth of vascular network with time.

Figure 3.22 shows the transvascular flux, vessel surface pressure and interstitial pressure distribution in the adaptive tumour network. The interstitial pressure at the surface of the vessel is seen to be significantly higher compared to the non-adaptive network, reaching a maximum of around 28 mmHg, which is still within the interstitial pressure values measured in tumours. The transvascular flux is non-uniform and an inward flux is observed on most vessels in the tumour. Zero net flux can be seen on vessels that have fully remodelled and expanded to the maximum radius. The less mature vessels at tumour center have an inward flux of around 0.5-0.7 μm/s, whilst the new vessels towards the tip of the sprout have the highest inward flux. This is because more recently formed vessels have larger pores and hence the hydraulic conductivity of these vessels is higher.
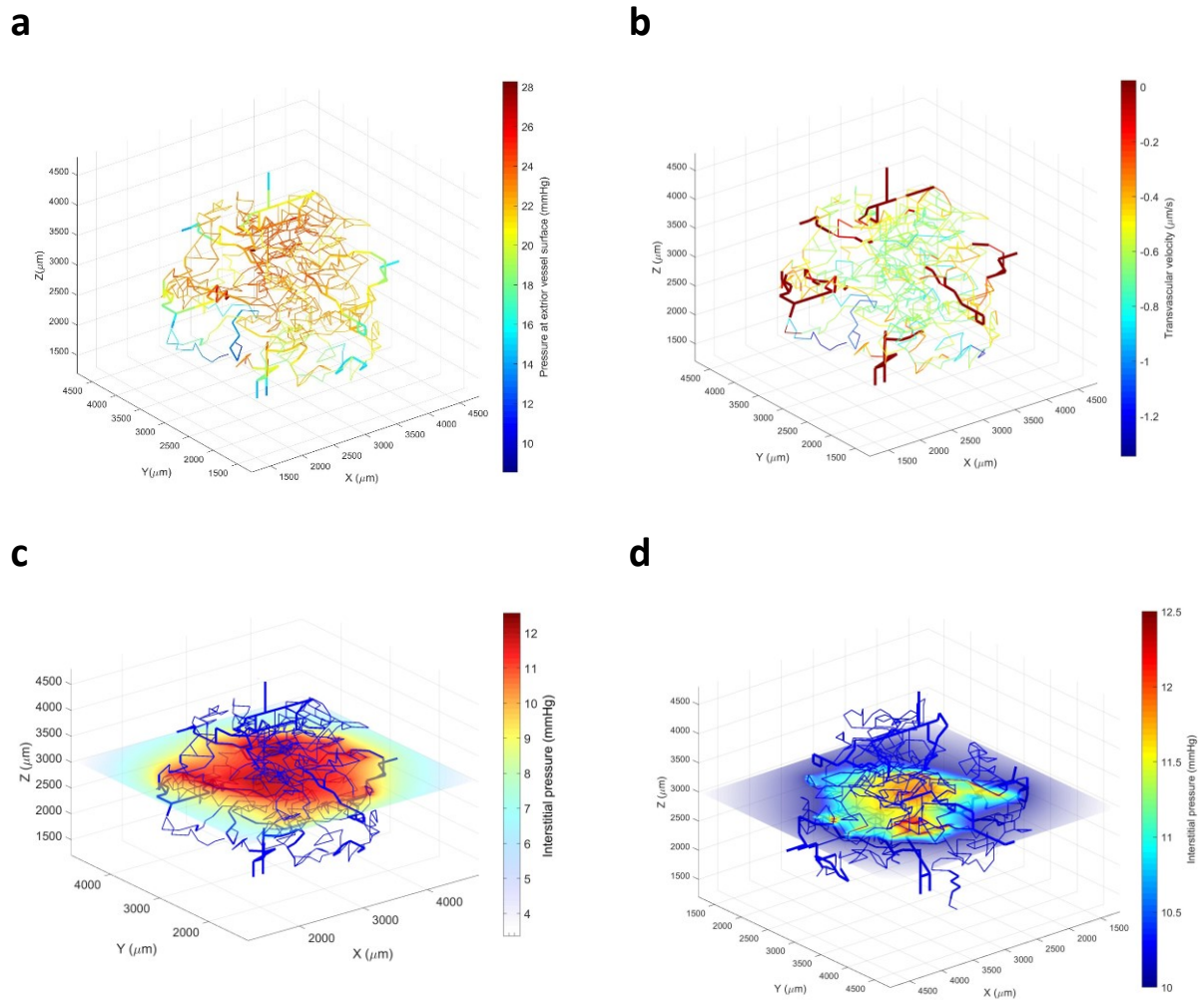
Figure 3.22: (a) Vessel surface interstitial pressure and (b) transvascular flux in adaptive tumour network. (c) Interstitial pressure distribution at z height = 3000 μm showing full pressure range and (d) pressure range from 10-12.5 mmHg to show heterogeneity.

Figure 3.22c shows that overall the IFP is significantly increased in the adaptive network with a maximum pressure of 12.4 mmHg, as newly formed vessels have a higher hydraulic conductivity when remodelling is considered. In Figure 3.22d, pressure distribution in the range of 10-12.5 mmHg is displayed to provide a clearer image of the heterogeneity in IFP distribution. When a uniform hydraulic conductivity was assumed as shown in Figure 3.16, high pressures are mostly concentrated in the central region. The inclusion of adaptive vessel hydraulic conductivity based on vessel maturity and flow dynamics in the tumour leads to a more heterogeneous IFP distribution even in the case of a well vascularized tumour as seen in figure 3.22. Chuan et al. [171] incorporated heterogeneous pore size distribution in their model. The vessels were assigned pore sizes assuming the unimodal distribution throughout the vasculature and hence did not explicitly incorporate the effect of fluid flow or vessel maturity on the permeability of the vessel. Their work showed similar findings where IFP was found to be heterogenous, however it could not be determined from their presented data whether this was due to the heterogeneity of the vessel pore size or the vascular distribution. In the model developed by Vavourakis et al. interstitial pressure was calculated incorporating heterogenous vessel permeability, however their model applied the homogenization technique reviewed in section 2.2 [74]. The tissue domain was divided into 3D finite elements with a minimum length of 70 µm where vascular properties where averaged within each tissue element. Vascular and interstitial flow were coupled using a vascular density term obtained from literature which did not represent the explicit morphology of the vascular network generated in their work. The interstitial pressure values in their work were described in 1D as a function of radial distance from the tumour center. The tumour IFP values in their work were approximately 8.5 mmHg which is comparable to the pressures found here, however the radial pressure profile in their tumour model was relatively uniform.

3.4   Summary

In this chapter a mathematical angiogenesis model is integrated with Pozrikidis's fluid flow model to investigate the flow dynamics in tumour tissue. With the angiogenesis model it is possible to capture the explicit distribution and geometry of the tumour vasculature and its abnormal features including loops, blind ends and AV shunts. Pozrikidis's fluid flow model has a distinct advantage of enabling vascular and interstitial flow to be strongly coupled through integration of flow in the vessels and interstitial space over the vessel surface, to provide approximations for fluid flow that are grounded in physical reality. The integrated angiogenesis and fluid flow model have been validated against data in literature and the effect

of various properties, including microvascular density distribution, necrosis, vascular architecture, and the effect of vascular remodelling have been examined.

The integrated model was initially applied to a case of non-necrotic well-vascularized tumour using baseline values and a uniform hydraulic conductivity. The predicted flow parameters correlate well with data reported in the literature, showing similar IFP values and profiles. With regards to the effect of vascular distribution, it has been shown to have a significant effect on IFP, with avascular regions exhibiting lower pressures than the highly vascularized regions. In the presence of a necrotic core, the maximum interstitial pressure in the tumour decreases where increases in the degree of necrosis resulted in lower IFP values. In contrast to the profile observed in a non-necrotic tumour, which features a more uniform interstitial pressure with a rapid drop at the periphery, the presence of a necrotic core at the tumour center results in a lower interstitial pressure in the core region with the highest IFP in the peripheral regions. These changes in the pressure gradient can affect the interstitial fluid velocities which could have implications for drug transport in the interstitial space.

As blind ends and AV shunts are common features of tumour vasculature, their effect on fluid flow has been investigated. The flow was analysed in two vascular networks with an almost identical vascular distribution and macroscopic parameters that differed only in the removal of blind ends and addition of AV shunts. The results showed that with the removal of several vessels that represent blind ends, a significant difference in flow within the vasculature and interstitial space was observed which resulted in a lower interstitial pressure. However, the intravascular pressure distribution and transvascular flux became more heterogenous which could have significant effects on the flow and transport within the network. This highlights the importance of not just incorporating the vascular distribution and macroscopic features of the vascular network but also the effect of intravascular flow dynamics on the predicted IFP.

Finally, the influence of vascular remodelling is examined, which is incorporated by allowing the radius, porosity and wall thickness of each vessel to vary depending on the age and flow properties. Whilst most of the previous studies investigated fluid flow in tumours using a uniform vessel hydraulic conductivity, the new vascular remodelling model defines hydraulic conductivity values for each vessel. The results show that accounting for vascular remodelling causes a dramatic increase in interstitial pressure, which in turn results in a strong inward transvascular flux across most of the tumour network. The distribution of transvascular flux is non-uniform, with vessels in the periphery having a lower inward flux whilst well-

perfused vessels having a net flux close to zero. The overall net inward flux could potentially limit the ability of therapeutic agents to permeate through the vessels and enter the interstitial space. The predicted IFP profile in the tissue could also pose an obstacle to the transport of therapeutics as its gradient at the edge of the tumour is steeper and the peaks in IFP are distributed heterogeneously within the tumour.

Previous models that assume a uniform vascular distribution or treat the vasculature as a source term do not capture the effect of neighbouring vessels on each other, which could potentially influence flow on the macroscopic scale. The use of the boundary integral method to distribute sources and dipoles along the vessel surface provides greater accuracy as the topology and geometry of the vasculature are taken into account and the effect of each vessel segment on IFP at any point in space is considered. Using this method, work presented in this chapter has demonstrated the importance of considering not only the explicit nature of the tumour vasculature but also the intravascular flow properties when predicting and evaluating fluid flow in tumour tissue.

4 Influence of the tumour vasculature and fluid flow dynamics on drug transport and uptake

4.1 Introduction

Most forms of anti-cancer treatments involve the intravenous administration of therapeutic molecules or nanoparticles. The properties of the vasculature are likely to play an important role in the transport of therapeutics to tumours where the vasculature is known to be highly abnormal and heterogenous. These abnormalities in tumour vasculature can impair blood flow, resulting in an overall low flow with some vessels exhibiting stagnant flow [44]. This can lead to low influx of drug into the tissue and a heterogenous distribution due to larger extravascular diffusion distances. Importantly, this allows cancer cells in regions that are poorly supplied by vessels to evade treatment and survive [219]. More so, these properties can vary from patient to patient resulting in heterogenous response to treatment across patients. Whilst drug delivery is highly dependent on the tumour properties, it is also dependent on drug properties such as size, surface charge, pharmokinetics and pharmacodynamics. Treatment strategies including dosage and dosing schedule can also play a pivotal role in the transport and uptake of anti-cancer drugs. Understanding the interplay between these factors is crucial to develop optimized treatment strategies that increase the chances of patient survival. Drug transport occurs mainly through a combination of convection and diffusion and the relative importance of each mechanism can be quantified through the Peclet number which gives the ratio of fluid velocities to particle diffusivity and size. The mode of transport can impact penetration as diffusion is slow and limited to short distances whilst convection is more effective over larger length scales. Larger drugs have low diffusivities and favour convection whilst smaller drug have higher diffusivities but are hence to limited to short distances. In the vasculature, high blood flow velocities make convection the dominant mode of transport while in the tumour tissue space, high IFP causes flow to stagnant making diffusion a more dominant form of transport.

 A large number of works have developed models attempting to predict the influence of various drug and tumour properties on the therapeutic effectiveness. Some of these studies have applied spatially averaged compartmental PK models to study the temporal drug concentration profile within different compartments such the vascular, tissue and cellular space and predict its effectiveness [179, 220]. Other models have been developed that simulate spatio-temporal distribution of the drug within the tumour, investigating the various tumour properties such as size, IFP profile and vessel permeability. However,

they treat the vasculature as a uniformly distributed source term where the microscopic effects of vessel morphology and flow dynamics are neglected. Given the aberrance of vasculature in tumours and the presence of avascular regions, steep spatial gradients in drug concentrations can occur and this can affect the overall effectiveness of drugs. Hence, providing an explicit representation of the tumour vasculature can give further insight into how drugs distribute in the tumour tissue. A limited number of studies have recognized this issue and developed models to predict the influence of the vasculature on drug distribution although the complexity of the vasculature was limited and key factors such as blood flow and intracellular uptake were neglected.

In this chapter a mathematical model for solute transport is modified and coupled with the angiogenesis and fluid flow models described in Chapter 3 to investigate the transport, distribution and uptake of the anti-cancer drug doxorubicin in tumour tissues with explicit representation of the vasculature. The transport of the doxorubicin within the vascular space, its flux from the vessels, diffusion in the tissue space and uptake by cancer cells are incorporated. The model has been applied to idealized tumour geometry with different tumour properties such as size, and vascular network architecture. Additionally, the influence of drug dosage and infusion time are investigated to understand the interplay between administration regimes for chemotherapy drugs and distribution within the tumour tissue.

4.2   Methods

In this work, the angiogenesis and fluid flow models described in the previous chapter are coupled with a solute transport model developed by Secomb (2016) [188]. The solute transport model is extended to describe the transport and uptake of doxorubicin in tumours. In this section the methodology of the overall model is described.

4.2.1   Tumour geometry

The geometry of the tumour vasculature is generated using Anderson and Chaplains method [72] as described in section 3.2.1. The space surrounding the vasculature is assumed to be surrounded by uniformly distributed cells that make up a fraction of the tissue whilst the other fraction of the tissue space is assumed to be occupied by the interstitial fluid. Using this model, complex spatially dependent vascular networks can be generated as demonstrated in Chapter 3, including tumours with and without a necrotic core. A vascular geometry is produced using equations 3.7, 3.8 and 3.9 which describes a tumour at the edge of the domain that secrets TAF. Fig. 4.1a-c shows the initial distribution of TAF, fibronectin

and endothelial cells. Fig 4.1d shows the formed vascular network in an 800 x 800 x 400 µm tissue volume. The vessels are divided into short cylindrical segments with defined radius and length that are assumed to be straight, rigid and permeable. The vascular network generated captures many features found in tumour vasculature including excessive branching, high tortuosity and heterogenous distribution.

a

b

c

d
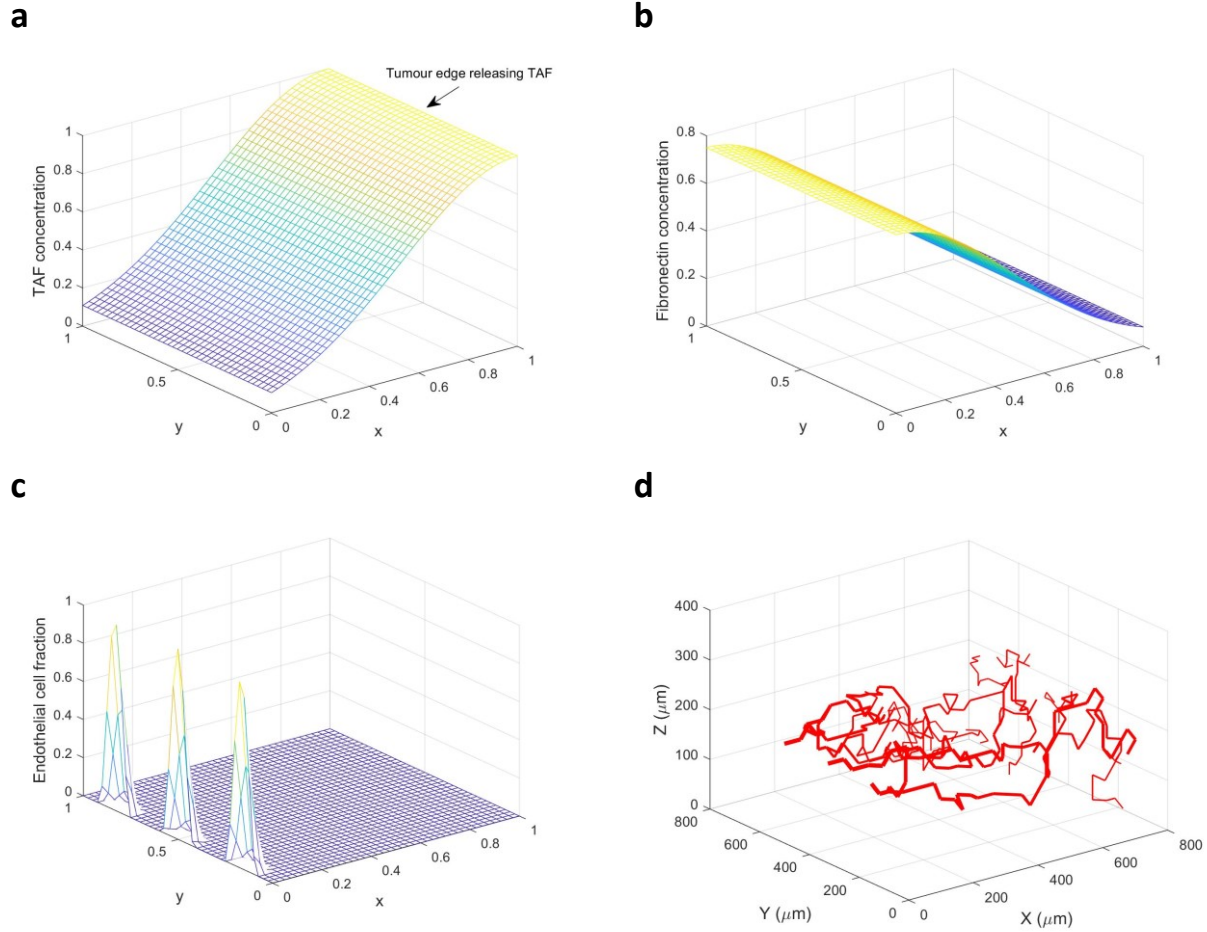
Figure 4.1: (a) Initial TAF and (b) Fibronectin concentration profiles determined using equation 3.7 and 3.8. (c) initial endothelial density which can be described as three clusters sprouting from parent vessel at x = 0. (d) Vascular network generated.

4.2.2   Drug transport model

4.2.2.1   Drug distribution in vasculature:

In tumour vessels, typical blood flow velocities U and vessel length scales L are about 1 mm s^{-1} and 0.3 mm respectively [204]. For a typical drug with diffusivity D of the order of 10^{-6} cm^2 s^{-1}, the Peclet number which defines the relative magnitude of convection to diffusion is found to be ~3000 [221]. Hence, drug transport within tumour vessels is assumed to occur mainly through convection and is given by

$$A_v \frac{\partial c_v}{\partial t} + Q \frac{\partial c_v}{\partial s} = -q_v \qquad (4.1)$$

Where A_v is the vessel cross sectional area, c_v is drug concentration in the vasculature, Q is the blood flow rate, s is the distance along the vessel segment and q_v is the rate of drug diffusing through the vessel walls per unit length. The transport of drug across the vessel wall to the tissue space is dependent on the permeability of the wall to the drug, P and the concentration gradient across the wall. The transvascular flux per unit length in a vessel of length L is given by

$$q_v = L\,P(c_v - c_s) \qquad (4.2)$$

Where c_s is the extravascular drug concentration on the surface of the vessel.

4.2.2.2   Interstitial drug transport:

In the interstitial space, interstitial fluid velocities are low and are on the order of <1 μm s^{-1} due to high interstitial pressure caused by leaky vessels. With typical extravascular diffusion distances of 100 μm, Peclet numbers are usually <1 for small drugs [221]. Therefore, drug transport in the tissue space can be assumed to be dominated by diffusion and described as follows

$$\frac{\partial c_e}{\partial t} - D_e \nabla^2 c_e = R(c_e) \qquad (4.3)$$

Where c_e is the extracellular concentration in the interstitial space, D_e is the isotropic diffusion coefficient, and R is a function describing the rate of uptake and efflux by cells.

4.2.2.3   Intracellular uptake and efflux

Drug uptake by cancer cells depends on the chemotherapy drug and the type of cancer cells. In this study doxorubicin is adopted as the chemotherapy drug and it has been shown that its uptake by cancer cells is strongly non-linear [222]. At a spatial point, the transport of drug across the cell membrane varies with the concentration in the extracellular space. Efflux for doxorubicin is found to occur mostly through passive diffusion and is a function of the intracellular concentration, c_i. Transmembrane transport including uptake, δ and efflux ω can be described by Michaelis-Menten kinetics as follows [223]

$$\delta = \frac{V_{max} c_e}{c_e + K_1 \varphi} \tag{4.4}$$

$$\omega = \frac{V_{max} c_i}{c_i + K_2} \tag{4.5}$$

Where V_{max} is the maximum rate of transport across the membrane, φ is the fraction of extracellular space in the tissue and K_1 and K_2 are the Michaelis constants for half-maximal transport as determined by Kerr et al. [222]. The intracellular drug concentration for cells is described exclusively as the difference between uptake and efflux.

$$\frac{dc_i}{dt} = \delta - \omega \tag{4.6}$$

Equation 4.3 describing the extracellular space concentration can then be given reformulated to incorporate the effect of uptake and efflux

$$\frac{\partial c_e}{\partial t} = D_e \nabla^2 c_e - \delta + \omega \tag{4.7}$$

Doxorubicin in the plasma and interstitial fluid binds extensively to proteins such as albumin. The bound formulation of doxorubicin with albumin exhibits different transport properties to its free form including lower permeability to the vessels and slower diffusion rates. Additionally, only free doxorubicin is able to cross the membrane of the cells therefore binding is expected to reduce the amount of drug available to enter the cells and consequently induce therapeutic effect on the cell. Greene et al. found that approximately 74-82% of doxorubicin is bound regardless of Doxorubicin and albumin concentrations [224]. Binding and dissociation of doxorubicin can be simply described by first order kinetics, however the rate at which these occur are fast relative to other processes such as diffusion and uptake, which would require a reduced time step and increase the computational burden. We neglect binding in this work as it would only be expected to result in a lower free drug concentration in the vascular and interstitial space, whilst not affecting the qualitative results obtained.

4.2.3   Model parameters

4.2.3.1   Dosage

For doxorubicin, the maximum lifetime dose a patient can receive is limited by the cardiotoxicity and ranges from 450 mg/m² to 550 mg/m² [225]. The total dose D in mg is dependent on the body surface

area (BSA) of the patient which will vary depending on age and gender. To understand the effect of the vasculature and drug properties on its transport and uptake we take a BSA of 1.79 m^2 averaged from 3619 cancer patients treated in UK in 2005 [226]. Doxorubicin is administered in cycles separated by 2-3 weeks, hence the drug remaining from the previous cycle is not expected to have an effect the next cycle. During each cycle 60-75 mg/m^2 is usually administered, however several studies have looked at the development of high dose chemotherapy allowing for 110 mg/m^2 to be administered over several cycles [227-229]. Using the BSA value chosen in this work, the total dose can range from 100-200 mg which are used within this work.

4.2.3.2   Drug injection kinetics

After injection the Doxorubicin is assumed to rapidly and uniformly distribute within the body's blood vessels through convection. The plasma concentration for a bolus injection are modelled as an exponential decaying function given by

$$c_v(t) = DAe^{-\alpha t} \tag{4.8}$$

Where D is the dose, A is the inverse volume of distribution, and α is time constant for Doxorubicin in plasma. Robert et al. determined the parameters A and α for a population of breast cancer patients [230]. For continuous infusion of time duration T they adopted a three-compartment model to describe plasma concentration through a tri-exponential decay function as follows

$$c(t) = \begin{cases} \dfrac{D}{T}\left[\dfrac{A}{\alpha}\left(1 - e^{-\alpha t}\right) + \dfrac{B}{\beta}\left(1 - e^{-\beta t}\right) + \dfrac{C}{\gamma}\left(1 - e^{-\gamma t}\right)\right] & , \quad t < T \\ \dfrac{D}{T}\left[\dfrac{A}{\alpha}\left(e^{\alpha T} - 1\right)e^{-\alpha t} + \dfrac{B}{\beta}\left(e^{\beta T} - 1\right)e^{-\beta t} + \dfrac{C}{\gamma}\left(e^{\gamma T} - 1\right)e^{-\gamma t}\right], & t \geq T \end{cases} \tag{4.9}$$

Where A, B, and C are compartment parameters and α, β and γ are time constant parameters in each compartment. For a bolus injection the terms B, C, β and γ are neglected as their compartments represent clearance with much slower rates of elimination. The parameters used in the drug transport model to describe drug injection kinetics, distribution and uptake within the tumour are summarised in table 4.1

Table 4.1 Drug transport parameters

Parameter	Units	Doxorubicin	Reference
Dosage D	mg	100-200	[227-229]
Diffusivity D_e	cm^2/s	2×10^{-6}	[231]
Permeability to vessels	cm/s	2.744×10^{-4}	[232]
Molecular weight	g/mol	543.52	[222, 233]
Rate of transmembrane transport V_{max}	µM/s	0.086	[222]
Michaelis constant for transmembrane constant K_e	µM	0.403	[222]
Michaelis constant for transmembrane constant K_i	µM	25.21	[222]
Inverse volume of distribution in plasma for compartment 1 A	/l	0.13	[230]
Inverse volume of distribution in plasma for compartment 2 B	/l	2.49×10^{-3}	[230]
Inverse volume of distribution in plasma or compartment 3 C	/l	5.52×10^{-4}	[230]
Time constant for doxorubicin in plasma for compartment 1 α	/s	2.432×10^{-3}	[230]
Time constant for doxorubicin in plasma for compartment 2 β	/s	2.83×10^{-4}	[230]
Time constant for doxorubicin in plasma for compartment 3 γ	/s	1.18×10^{-5}	[230]

4.2.4 Numerical Method for drug transport in tumour tissue

To solve the spatial profile of doxorubicin in the tumour geometry, the vasculature is represented as cylindrical segments where each segment j was subdivided into N_v number of cylindrical subsegments $i = 1,2,3, \ldots .. N_v$. The tissue space was divided into N_t number of cubes composed of a fraction φ representing the extracellular space and the cells occupying $(1 - \varphi)$ of the tissue space. The extracellular and intracellular concentrations (c_e and c_i) are averaged over the volume of the cubes in the tissue space, whilst c_v is averaged over the vessel segment. The time scales on which drug transport occurs are significantly faster than the processes that can affect fluid flow (such as vessel adaption and vascular remodelling), hence the fluid flow equations are solved first using the method described in Chapter 3. In the drug transport model time is discretized into n subintervals for $k = 1,2,3, \ldots .., n$ where t_0 and t_n are initial and final time points respectively. Initially at t_0 the drug concentrations at the arterial points are solved using the plasma kinetic equations 4.8 or 4.9 depending on the administration mode. The fluid flow solution is used to define flow rate within the vessels in the drug transport model. The distribution of the drug within the tumour vasculature is resolved by integrating equation 4.1 along each flow pathway where

intravascular concentration is determined as a function of the vascular concentration at the preceding time point and source strength from the vessels.

Secomb (2016) [188] formulated a solution for the vascular concentration of a solute in vessel segment *i* at time point *k* which can be applied to model the vascular concentration of doxorubicin as follows

$$c_v^{ik} = \underbrace{\sum_{j=1}^{N_b} \gamma_{ij} c_b^{jk}}_{\text{inflow}} + \sum_{j=1}^{N_v} \beta_{ij} c_v^{jk-1} - \sum_{j=1}^{N_v} \frac{\alpha_{ij} q_v^{jk} \Delta t}{V_j} \quad \text{for } i = 1,2,3 \dots N_v \qquad (4.10)$$

Where c_v^{ik} is the average vascular concentration of doxorubicin in node *i* at time point *k*, V_j is volume of segment *j* and γ_{ij}, β_{ij} and α_{ij} are convective coefficients. Equation 4.10 describes the vascular concentration in segment *i* at the end of each time step. To compute the amount of drug being drained by the venous ends, the following equation is used

$$c_b^{ik} = \underbrace{\sum_{j=1}^{N_b} \xi_{ij} c_b^{jk}}_{\text{inflow}} + \sum_{j=1}^{N_v} \omega_{ij} c_v^{jk-1} - \sum_{j=1}^{N_v} \frac{\varsigma_{ij} q_v^{jk} \Delta t}{V_j} \quad \text{for } i = 1,2,3 \dots N_b \qquad (4.11)$$

Where c_b^{ik} is the concentration of doxorubicin reaching venous node *i* during each time step *k* and ξ_{ij}, ω_{ij} and ς_{ij} are convective coefficients. The convective coefficients represent a set of matrices that are dependent on the network topology and the blood velocity distributions and are used as described in Secomb (2016).

Convective transport of the drug within the vasculature and diffusive transport in the interstitial space are coupled by implementing Secomb's Green's function approach for time-dependent solute transport [188]. Diffusion in the interstitial space is described by convoluting the concentration field at the beginning of the time step with the Green's function for time dependent diffusion equation which allows the solute to move across multiple spatial grid points in a single time step. Given the complexity of the vasculature and steep spatial gradients in drug concentration known to occur in tumours, the method provides an efficient way to incorporate the microscopic details of drug transport in tumours whilst the implicit nature of the method places no restriction on the time or spatial step. This allows for longer simulations that provide an efficient means to visualize drug transport over longer time scales.

The solution developed by Secomb for time-dependent solute distribution in the tissue space is modified to incorporate cellular uptake and efflux. The concentration of doxorubicin in the extracellular space is then given as

$$c_e^{ik} = \sum_{j=1}^{N_t} V_t G_{tt}^{ij}(c_e^{ik-1} - G_0^{k-1}) + \sum_{j=1}^{N_t} \bar{G}_{tt}^{ij}\left[V_t\left(-\frac{V_{max}\bar{c}_e^{ik}}{\bar{c}_e^{ik} + K_1} + \frac{V_{max}\bar{c}_i^{ik}}{\bar{c}_i^{ik} + K_2}\right) - V_t(G_0^k - G_0^{k-1})/\Delta t\right]$$

$$+ \sum_{j=1}^{N} \bar{G}_{tv}^{ij}q_v^{jk} + G_0^k \quad \text{for } i = 1,2,3 \dots N_t$$

(4.12)

Where

$$\bar{c}_e^{ik} = \frac{c_e^{ik} + c_e^{ik-1}}{2} \qquad\qquad \bar{c}_i^{ik} = \frac{c_i^{ik} + c_i^{ik-1}}{2}$$

(4.13)

The concentration on the surface of the vessel is averaged over the surface of vessel segment *i* and defined as

$$c_s^{ik} = \sum_{j=1}^{N_t} V_t G_{vt}^{ij}(c_e^{ik-1} - G_0^{k-1}) + \sum_{j=1}^{N_t} \bar{G}_{vt}^{ij}\left[V_t\left(-\frac{V_{max}\bar{c}_e^{ik}}{\bar{c}_e^{ik} + K_1} + \frac{V_{max}\bar{c}_i^{ik}}{\bar{c}_i^{ik} + K_2}\right) - V_t(G_0^k - G_0^{k-1})/\Delta t\right]$$

$$+ \sum_{j=1}^{N} \bar{G}_{vv}^{ij}q_v^{jk} + G_0^k \quad \text{for } i = 1,2,3 \dots N_v$$

(4.14)

Where c_e^{ik} is average concentration of doxorubicin in the extracellular space at tissue node *i* at time step *k* and c_s^{ik} is average concentration of doxorubicin on the surface of vessel *i* at time point *k*. V_t is the volume to tissue cube and G_{tt}^{ij}, G_{vt}^{ij}, $\bar{G}_{tt}^{ij}$, $\bar{G}_{tv}^{ij}$, $\bar{G}_{vt}^{ij}$ and $\bar{G}_{vv}^{ij}$ represent the diffusive interaction matrices obtained from Secomb's work where they are described in more detail [188]. In summary these matrices represent the tissue-tissue and vascular-tissue interactions that could influence drug concentration over the interval Δt and as a result of the preceding time point t_{k-1}. The average intracellular concentration in tissue region *i* is simply given as

$$c_i^{ik} = c_i^{ik-1} + V_t\left(\frac{V_{max}\bar{c}_e^{ik}}{\bar{c}_e^{ik} + K_1} - \frac{V_{max}\bar{c}_i^{ik}}{\bar{c}_i^{ik} + K_2}\right) \quad \text{for } i = 1,2,3 \dots N_t$$

(4.15)

The terms in equations 4.12, 4.14 and 4.15 representing the uptake and efflux of doxorubicin can denoted as source/sink terms in the extravascular space as follows

$$q_e = V_t \left(-\frac{V_{max}\bar{c}_e^{ik}}{\bar{c}_e^{ik} + K_1} + \frac{V_{max}\bar{c}_i^{ik}}{\bar{c}_i^{ik} + K_2} \right)$$

$$q_i = V_t \left(\frac{V_{max}\bar{c}_e^{ik}}{\bar{c}_e^{ik} + K_1} - \frac{V_{max}\bar{c}_i^{ik}}{\bar{c}_i^{ik} + K_2} \right)$$
(4.16)

The non-linearity of doxorubicin uptake can cause instabilities within the numerical method and increase the time required to achieve convergence. Hence to control the stability of the system, under relaxation methods are applied where the uptake and efflux functions are multiplied by an under-relaxation factor as follows

$$q_e^n = f \cdot q_e^n (1 - f) \cdot q_e^{n-1}$$

$$q_i^n = f \cdot q_i^n (1 - f) \cdot q_i^{n-1}$$
(4.17)

Where n is the iteration step and f is the under-relaxation factor which is set to 0.7 in this work. The tranvascular flux of the drug is described by the vessel source term at vessel segment i and time step k as

$$q_v^{ik} = l_i P_i \left[f^{-1}(c_v^{ik}) - c_s^{ik} \right]$$
(4.18)

Where l_i is the length of segment i.

Secombs method coupled intravascular concentration and the concentration on the surface segment by combining equations 4.18 into 4.10 and 4.14. From this point this work follows Secomb's iterative solution to the drug transport problem within the tumour tissue.

4.2.5   Solution process

The tumour geometry used is generated as described in section 4.2.1. Following the generation of the tumour model, blood flow within the vessels is resolved using the fluid flow model described in chapter 3 which couples the vascular and interstitial flow. The flow in the vasculature is used as an input for the drug transport model along with the network topology (vessel radius, length and connectivity). Time parameters are defined that include the time step and number of steps. Drug properties are defined including the number of including its diffusivity and uptake kinetics. The vascular network and tissue space are discretized, and the convective and diffusive matrices are calculated. Using the Pharmacokinetic equations 4.8 and 4.9, the drug concentration at the inlet arterial points of the network are defined at the

initial time point. The transport of the drug within the vascular network and its distribution in the interstitial space and uptake by the cells are calculated at each time point using Secomb's solution to the Green's function time-dependent solute transport problem and implementing the equations 4.10-4.18. The workflow of this process is given in Figure 4.2.
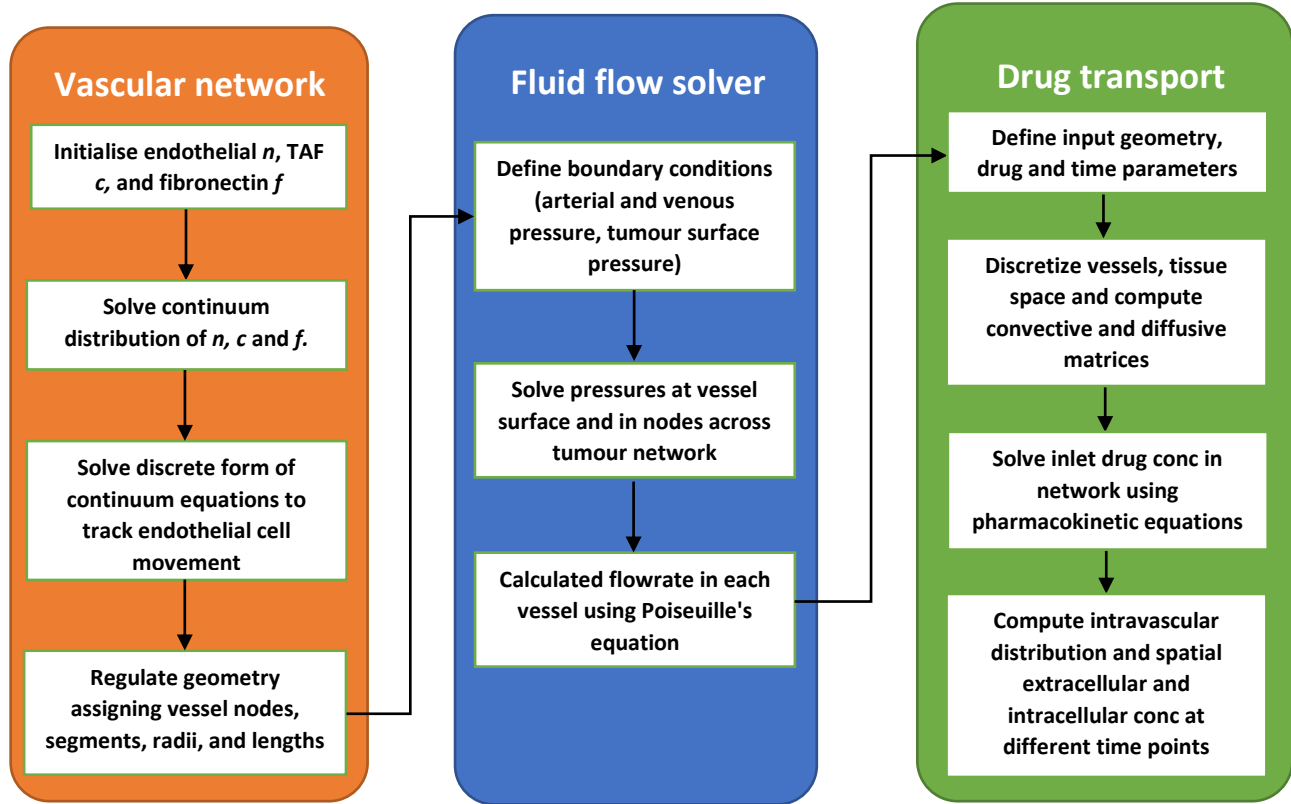

Figure 4.2: *Schematic of work flow to solve drug transport and uptake in tumour model*

The algorithm is solved using a modified code based on Secomb's CUDA C++ code [188] which allows for parallel computing on Graphical processing units (GPUs). When compared to solving the system using traditional C++ codes on CPUs, the CUDA code processed on GPUs greatly reduces the time required for each simulation and allows for more detailed analysis.

4.2.6 Time step and mesh resolution optimization

Choosing the appropriate time and spatial step is necessary to ensure that the simulation is stable and able to provide consistent reliable data. For explicit methods, time and spatial steps are limited by the courant number as follows

$$CL \equiv \frac{D\Delta t}{(\Delta x)^2} \leq \frac{1}{2} \qquad (4.19)$$

The implicit nature of Secomb's Green's function method is not subject to this limitation; hence results obtained with varying time steps and mesh resolution were analysed independently. The mean spatial extracellular and intracellular concentrations at each time point were calculated in the simulations. When examining the effect of time step, concentration values were found to converge and become consistent at time steps in the range of 3-15 seconds (Fig 4.3). Above this range, the simulation became unstable whilst lower values in the range of 0.5-2 seconds resulted in divergence of concentration values. Secomb found a similar trend in their work where smaller time steps resulted in a divergence of washout rate values in their simulation. A plausible explanation is that smaller time steps may lead to numerical diffusion where diffusive spread of the drug is artificially increased in the tissue due to averaging of drug concentrations over finite tissue regions. This was observed in the simulations where at all time points, the total amount of drug in the tissue space was similar for all time steps, however at smaller time steps the drug was found to be more homogenously distributed within the tissue leading to a low mean spatial concentration as a result of an artificial increase in diffusivity. Consequently, a time step of 10 seconds was chosen as this was within the convergent range for drug concentration values within the tissue and it was a good compromise between computational demand and accuracy.
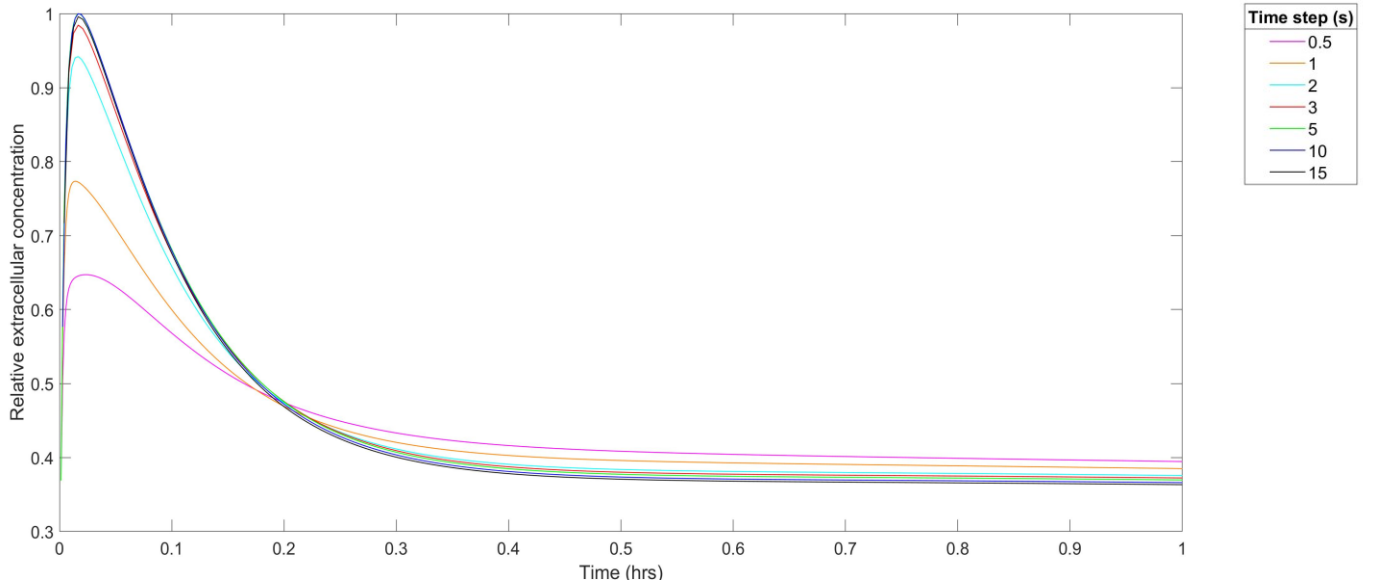

Figure 4.3: *Mean spatial extracellular concentrations for timesteps ranging from 0.5-15 seconds*

An analysis of the effect of mesh showed the model was less sensitive to the mesh resolution relative to the time step (Fig. 4.4). Increasing the number of nodes in the tissue space led to an increase in mean

concentration up to a certain extent where negligible changes in concentration occurred between tissues divided into 4000 points and those with 32000 points. This highlights that convergence can be achieved with 4000 points where the spatial step is 35 µm. Hence, the tumour tissue was discretized using this spatial step. It is worth noting that increasing the node points from 4000 to 8125 resulted an increase in computational time from approximately 3.5 hrs to 12.8 hrs on the HPC.
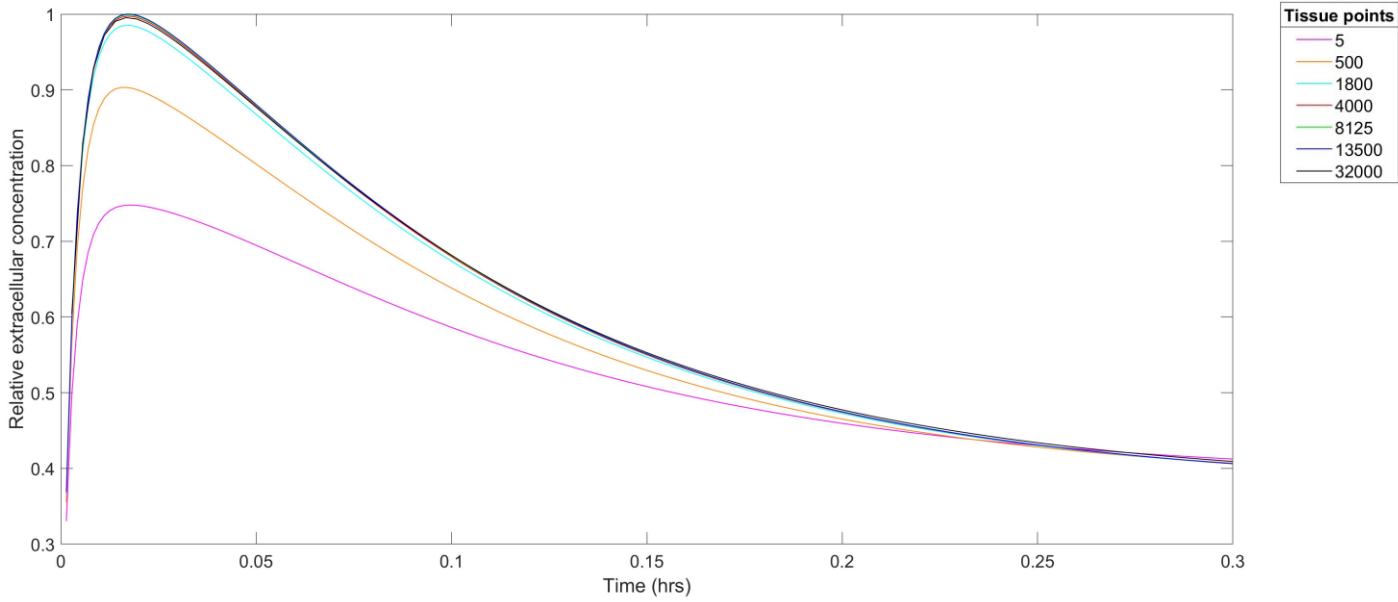

Figure 4.4: *Mean spatial extracellular concentrations for different mesh sizes.*

4.3 Results and discussion

4.3.1 Tumour geometry and blood flow

Two model geometries are used in this chapter: the newly created model describing a tumour at the edge of the domain as shown in Figure 4.1 and one of the models with a necrotic core (3%) presented in Chapter 3, which will be referred to as Model 1 and Model 2 respectively, hereafter. Before performing drug transport analysis on these geometries, their morphological parameters and basic hemodynamic parameters, as defined in Chapter 3, are evaluated and compared. Tables 4.2 and 4.3 show a summary of the calculated parameters and the corresponding data in the literature. Comparisons suggest that all the evaluated parameters are within the range previously reported based on imaged tumours.

Table 4.2 Morphological parameters for different geometries

Parameter	Units	Model 1	Model 2	Literature data	Reference
Tumour tissue volume	mm³	0.256	1.331		
Vascular density - V_d	%	0.601	0.205	0.15-1.25	[210-212]
Length density - L_D	mm/mm³	56.291	29.410	10-72	[89]
Surface area to volume ratio (vascular) S/V	mm²/mm³	322.52	409.391	30-250	[38]
Maximum extravascular diffusion distance - R	μm	75.198	104.035	5-225	[28, 36]
Mean vessel diameter	μm	10.805	9.102	0.06-0.3	[36, 214]
Mean vessel length	mm	0.036	0.065		

Table 4.3 Hemodynamic properties of the tumour vasculature and comparison with literature

Parameter	Units	Model 1	Model 2	Literature data	Reference
Perfusion	ml/g min	0.422	0.391	<2	[234]
Mean velocity	mm/s	0.654	1.378	0.1-25	[204, 215]
Shear stress	Pa	1.733	4.423	1-10	[169, 222, 233]

4.3.2 Drug distribution

Using the optimised time step and mesh resolution that ensures a convergent solution, the transport of doxorubicin in Model 1 following a bolus injection of 100 mg was simulated first. For qualitative analysis of the distribution of doxorubicin, drug concentrations in the vascular, extracellular and intracellular space were normalised relative to the maximum concentration reached within each compartment. Figure 4.5 shows the variation of intravascular drug concentration with time. At 10 seconds after injection, drug concentration is the highest near the feeding parent vessels with a large gradient along the network. As time is advanced (at 3 mins), drug concentration remains low in the distal segments of the vessel network whilst concentration levels in the proximal segments start to fall and after 15 mins, almost all the drug in the vasculature has either been cleared or entered the tumour tissue. The steep gradients in the concentration seem to occur in regions where there is excessive tortuosity and branching as seen in the upper left region of the tumour geometry (X>400 μm and Y>400 μm).
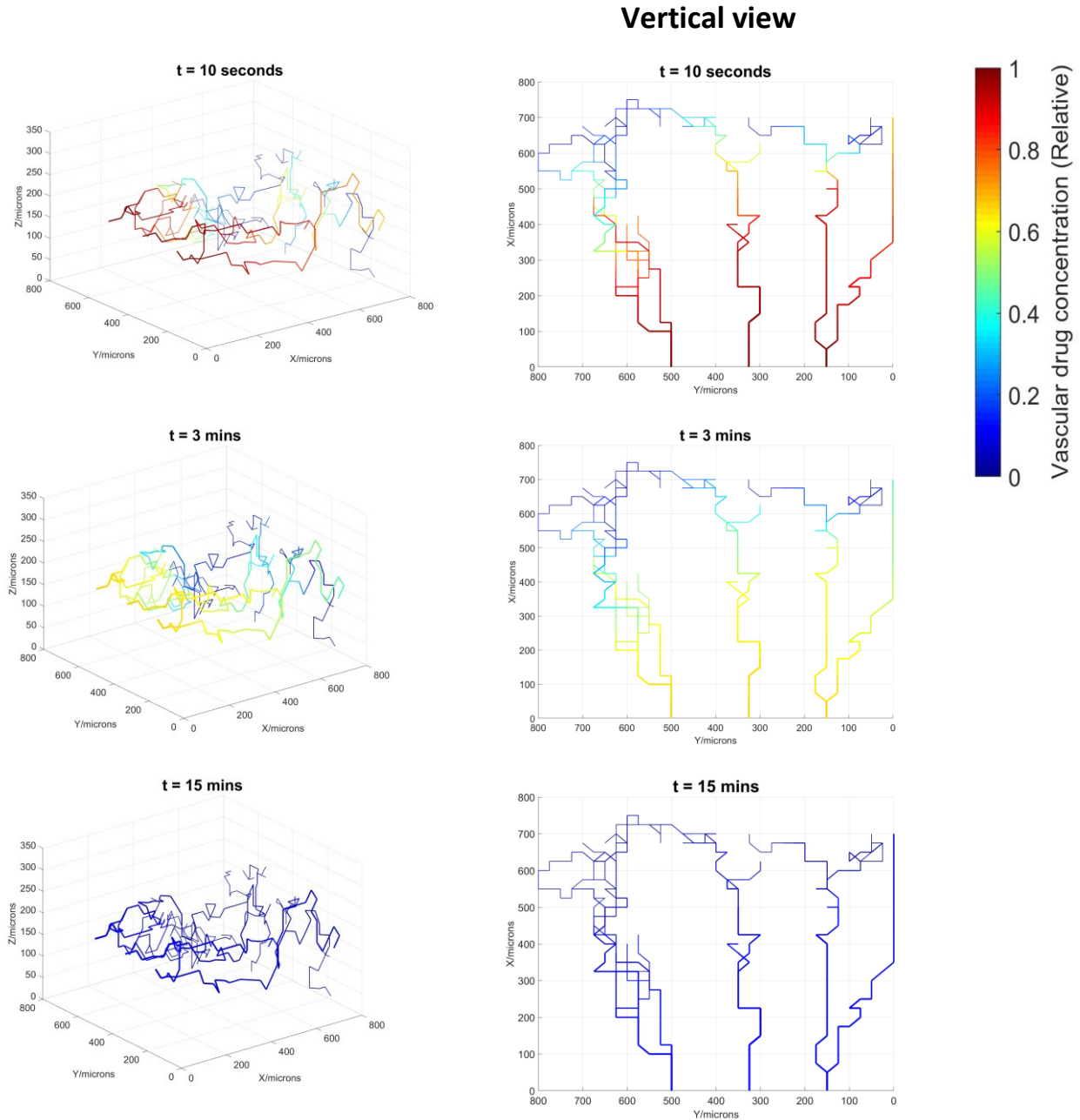
Vertical view

Figure 4.5: *Normalised intravascular concentration of doxorubicin at different time points for a bolus injection of 100mg (Model 1). Right side shows vertical view looking down z-axis.*

Figures 4.6 and 4.7 show spatial distributions of doxorubicin in the extracellular and intercellular space respecitively, where concentration maps at different transverse planes in the x, y and z axis are displayed to provide a better visualisation of drug distribution in a 3D space. For the coloring scheme, a ramp up approach to was used to set the transparency, where transparency is increased as the concentration value becomes smaller. Hence, regions where there is no colour filling correspond to concentration values near

zero. Figure 4.6 shows that doxorubicin diffuses through the vessel wall and is taken up rapidly by the tumour tissue where peak extracellular concentrations are almost achieved within 100 seconds of infusion. The drug in the extracellular space is seen to be concentrated in regions near well perfused vessels whilst regions near poorly perfused vessels with low intravascular concentration showed low extracellular concentrations. In regions with well perfused vessels, a steep drop in concentration is observed corresonding to distance from the vessels. After 5 mins, the extracellular concentration maps exhibit similar features where drug is present mostly in regions near the well perfused vessel, but the concentration levels are much lower compared to the maximum concentration achieved in the extracellular space. This is attributed to the high uptake rate of doxorubicin by the cancer cells in regions near the vessels and the lack of supply from the vascular space as the drug is cleared from the plasma. The concentration of doxorubicin in the extracellular space becomes almost uniform and very low only 15 mins after injection. An interesting observation from the snapshots of the extracellular concentration map is that drug distribution is not only dependent on the distance away from blood vessels, but also the microvascular morphology and vascular density. For example, the relative low drug concentration in the region (X>400 μm and Y>400 μm) is attributed to excessive branching and higher vessel tortuosity which impairs flow rate and consequently the amount of drug in the vasculature.

The intracellular concentration maps (Figure 4.7) show a similar spatial profile where regions nearest to the well perfused vessels have higher concentrations. Within 10 mins of bolus injection, a large amount of the drug in the extracellular space has been taken up by the cancer cells. At the 30-minute mark, the intracellular concentration approximately reaches its peak value with heterogeneities and steep spatial gradients present. These gradients become less apparent at the 1-hour mark with concentration becoming more uniform, however, the maximum concentration is almost half of the level at the 30-minute mark. After 3 hours the intracellular concentration has dropped significantly reaching 30-40% of its maximum value. This suggests that cancer cells nearest to blood vessels will be exposed to doxorubicin at high concentrations for a brief 30 mins. As described in equations 4.4 and 4.5, intracellular uptake rate is dependent on the extracellular and intracellular concentrations. The high ratio of intracellular to extracellular concentration in regions near blood vessels at 30 mins increases the efflux of the drug from the cells which then diffuses across the tissue before it is taken up in regions with low intracellular concentration. Although the spatial intracellular concentration distribution reaches a uniform state 3 hours after bolus injection, cells further away from blood vessels and in regions with high vessel tortuosity are only exposed to a fraction of the maximum concentration found in cells near the vessels. This would be expected to contribute to a heterogeneity in the cell kill rate within the tissue space, allowing for cells

further away from the vessels or those that are in regions with tortuous vessels in poorly perfused regions to escape treatment.
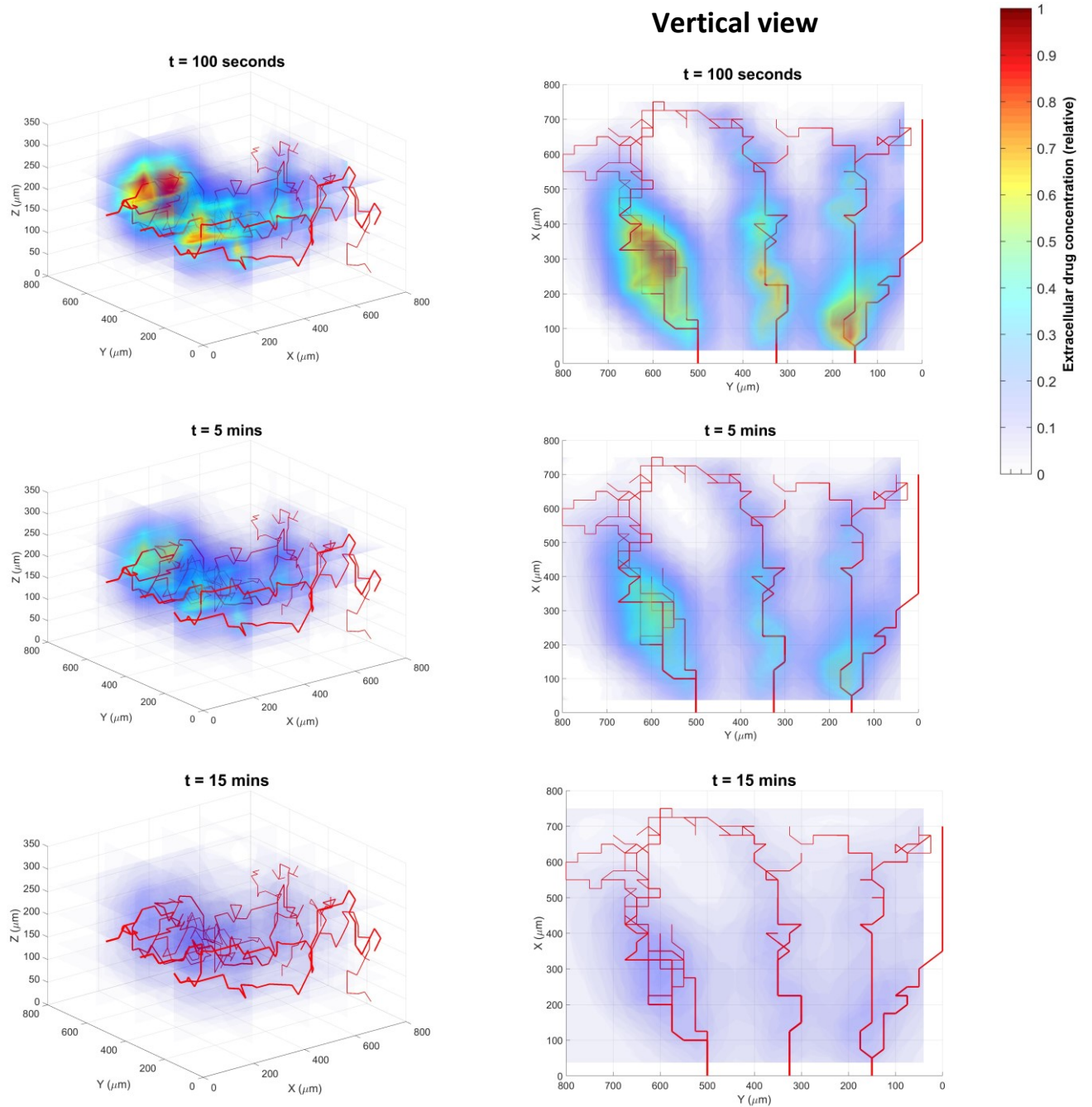

Figure 4.6: Normalised extracellular *concentration of doxorubicin at various time points for a bolus injection of 100mg (Model 1).*
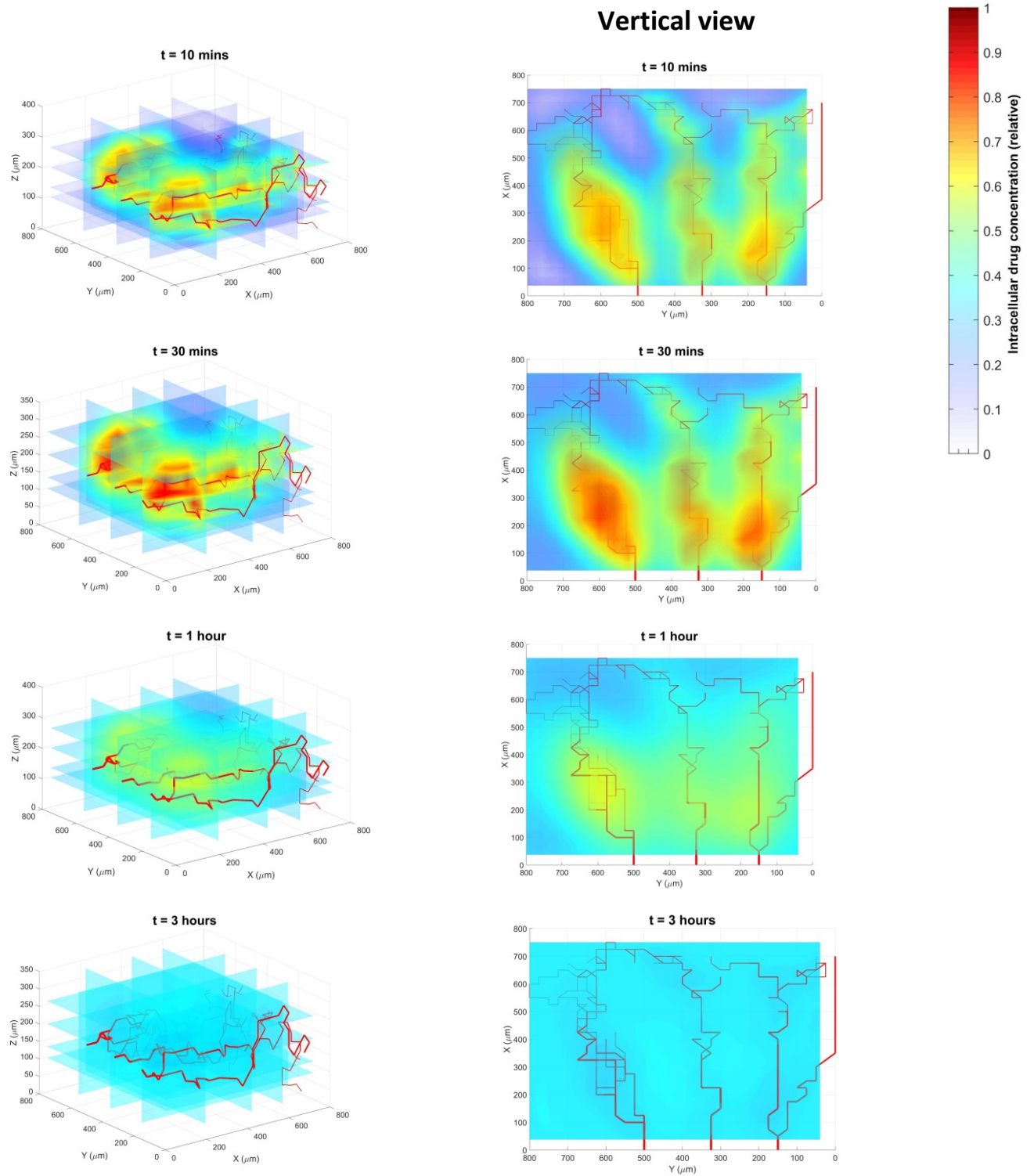
Figure 4.7: Intracellular *concentration of doxorubicin at various time points for a bolus injection of 100mg*

4.3.3　Effect of vascular properties

To provide a picture of the effect of vascular network properties on the delivery of doxorubicin to intracellular targets, simulations were performed for networks with different properties and architecture. First, a model is generated with the same vascular network architecture as in Model 1 but with a larger tumour volume.　The effect is that the extravascular diffusion distance and avascularity of the tumour would be higher. In the original Model 1, the maximum extravascular diffusion distance, R, is 75.2 μm and the vascular density is 0.60 %. Konerding et al. studied the vascular architecture of four different cancer cell lines transplanted in mice and found that the intercapillary distance can be as large as approximately 215 μm [38]. Hence, Model 1 was enlarged in an attempt to replicate these features, and the enlarged model has an R value of 150.4 μm and a vascular density of 0.15 %.

Figures 4.8 and 4.9 show the spatial concentration maps of doxorubicin in the extracellular and intracellular space in the enlarged model respectively. In order to qualitatively analyse the effects of inter capillary distance and vascular density, the concentration values are normalized by the respective peak concentration. Comparisons of Figure 4.6 and 4.8 show that larger extravascular diffusion distances lead to an overall low peak concentration in the extracellular space with certain regions having no drug exposure.　Similarly, the intracellular concentration maps in Figure 4.9 exhibit higher heterogeneities as a result of increased extravascular diffusion distance. There are more regions in the tissue space having extremely low intracellular concentration and it takes longer time to achieve a uniform distribution, however at this point the concentration values have dropped significantly to <10% of the peak intracellular concentration reached in regions near the vessels at earlier time points. This is expected to limit the overall therapeutic effect of doxorubicin for cells near the vessels and with cells further away being able to escape treatment.
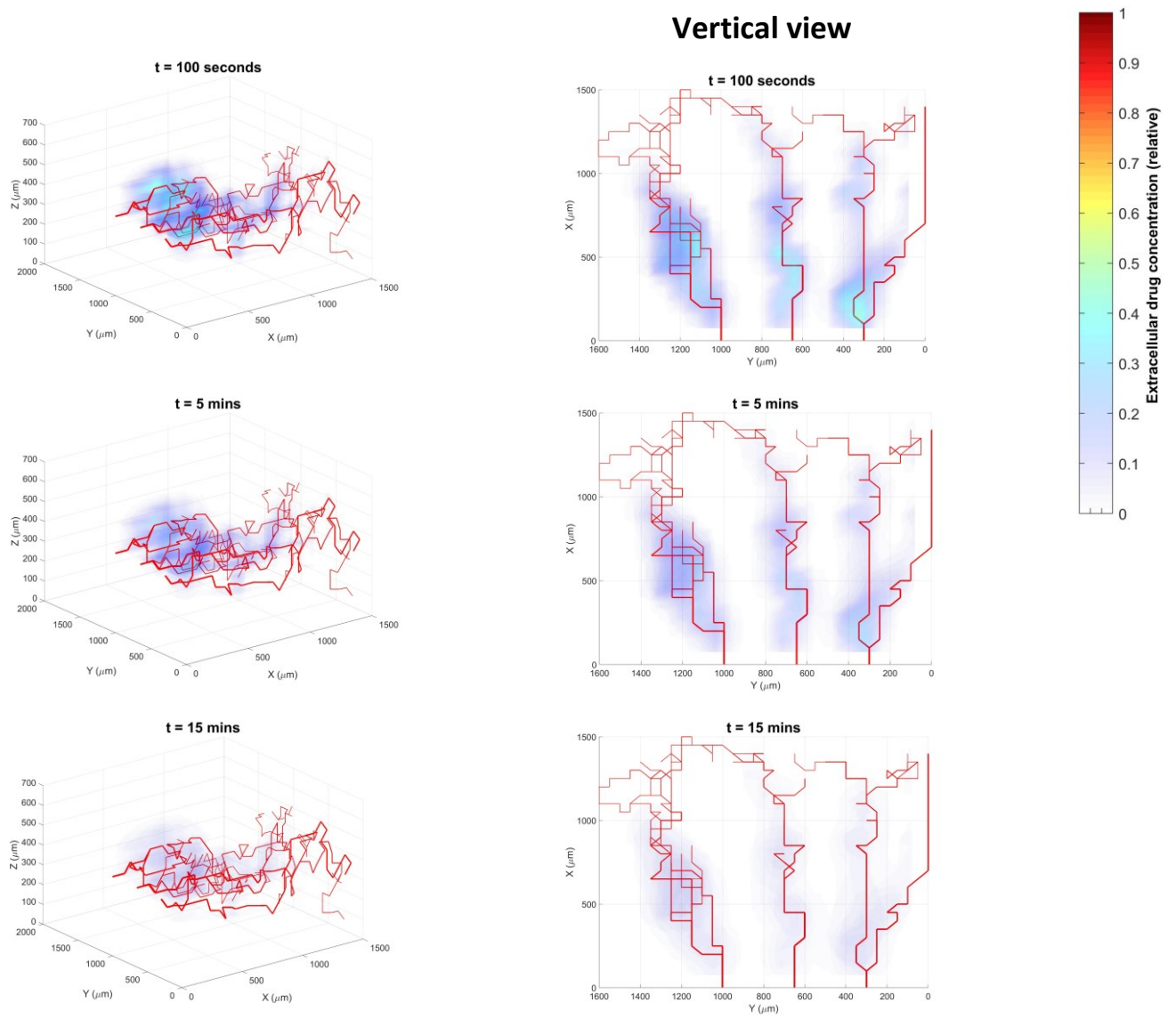
Figure 4.8: Normalised extracellular concentration of doxorubicin at various time points for a bolus injection of 100mg (enlarged Model 1).
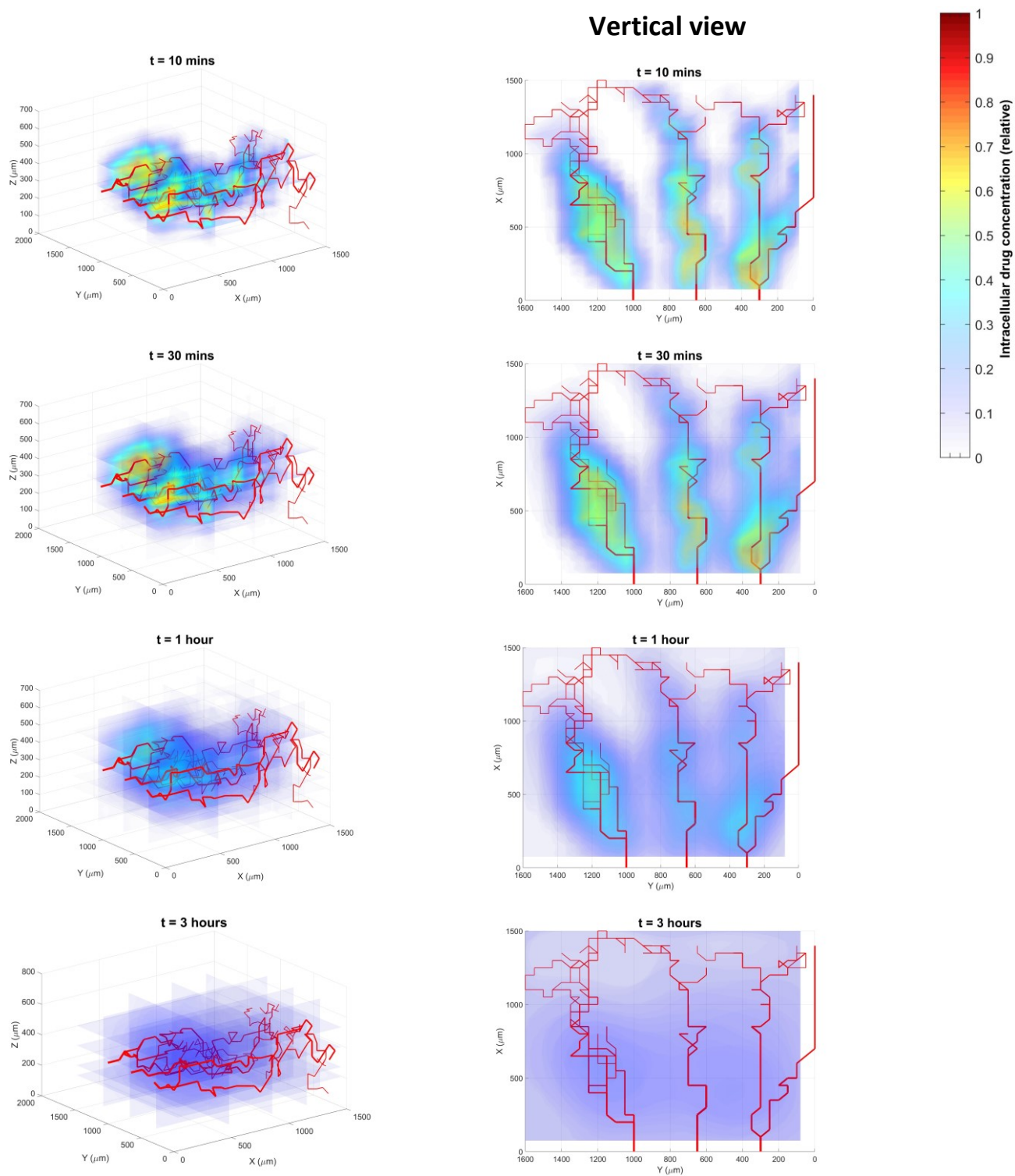
Figure 4.9: *Normalised intracellular concentration of doxorubicin at various time points for a bolus injection of 100mg (enlarged Model 1).*

To gain some insight into the effect of vascular architecture and heterogeneity on drug transport and uptake, simulations were performed on a tumour model with a different vascular network (referred to as Model 2 hereafter). A key feature of this network is the high vascularity at the tumour periphery and the presence of an avascular necrotic core at the tumour center. This characteristic of the vasculature has been observed in several tumours types where vessels are formed mostly in the peripheral tumour regions with vessels in the core being sparse [235, 236]. Morphological and hemodynamic properties of Model 2 are summarized in tables 4.2 and 4.3. Model 2 exhibits lower vascular density and larger maximum extravascular diffusion distance compared to Model 1. Figures 4.10 and 4.11 show the results for vascular extracellular and intracellular spatial distributions of doxorubicin in Model 2 with concentrations normalized with respect to the corresponding peak concentration.
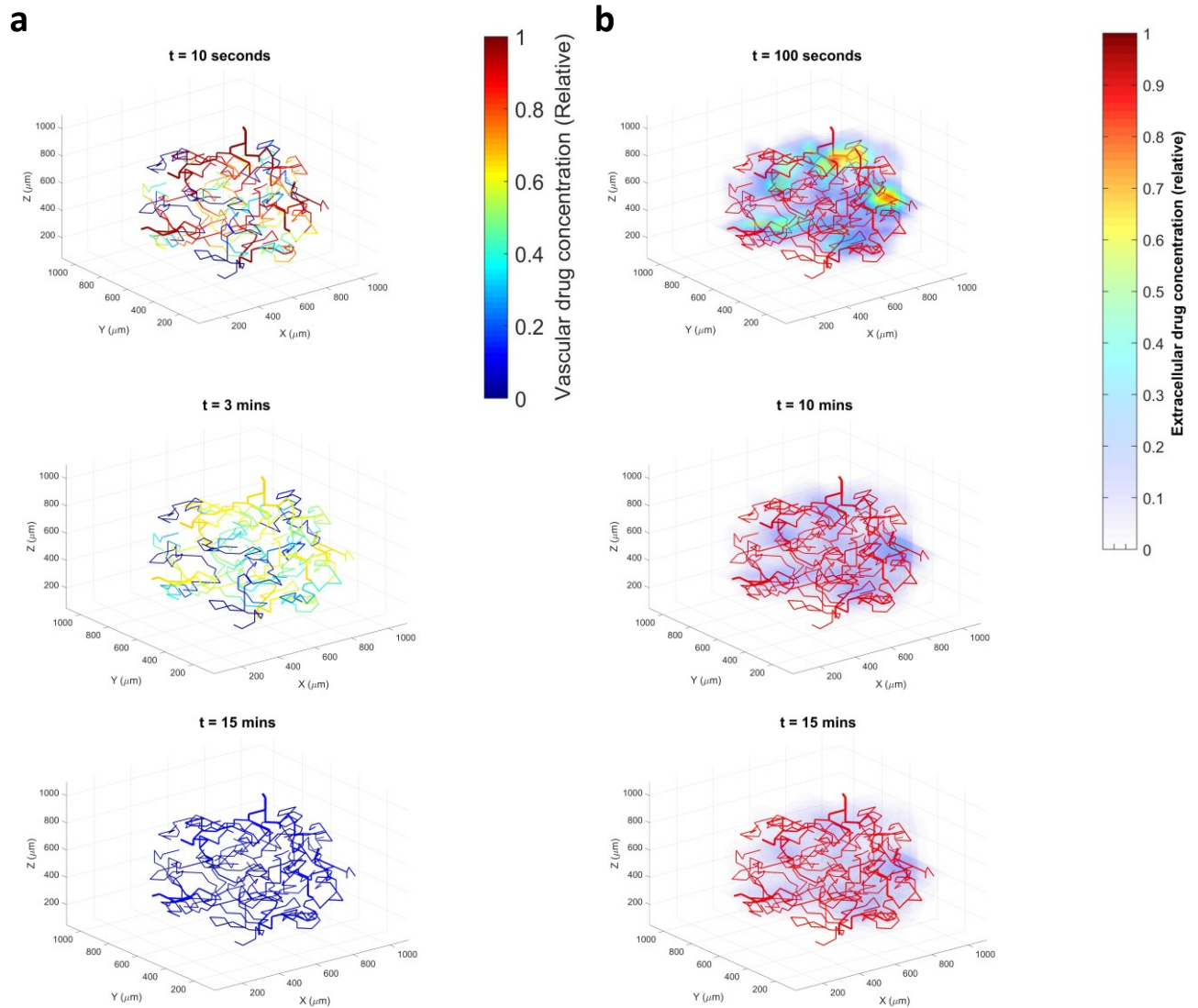

Figure 4.10: *Normalised vascular (a) and extracellular (b) concentration of doxorubicin at various time points for a bolus injection of 100mg (Model 2).*
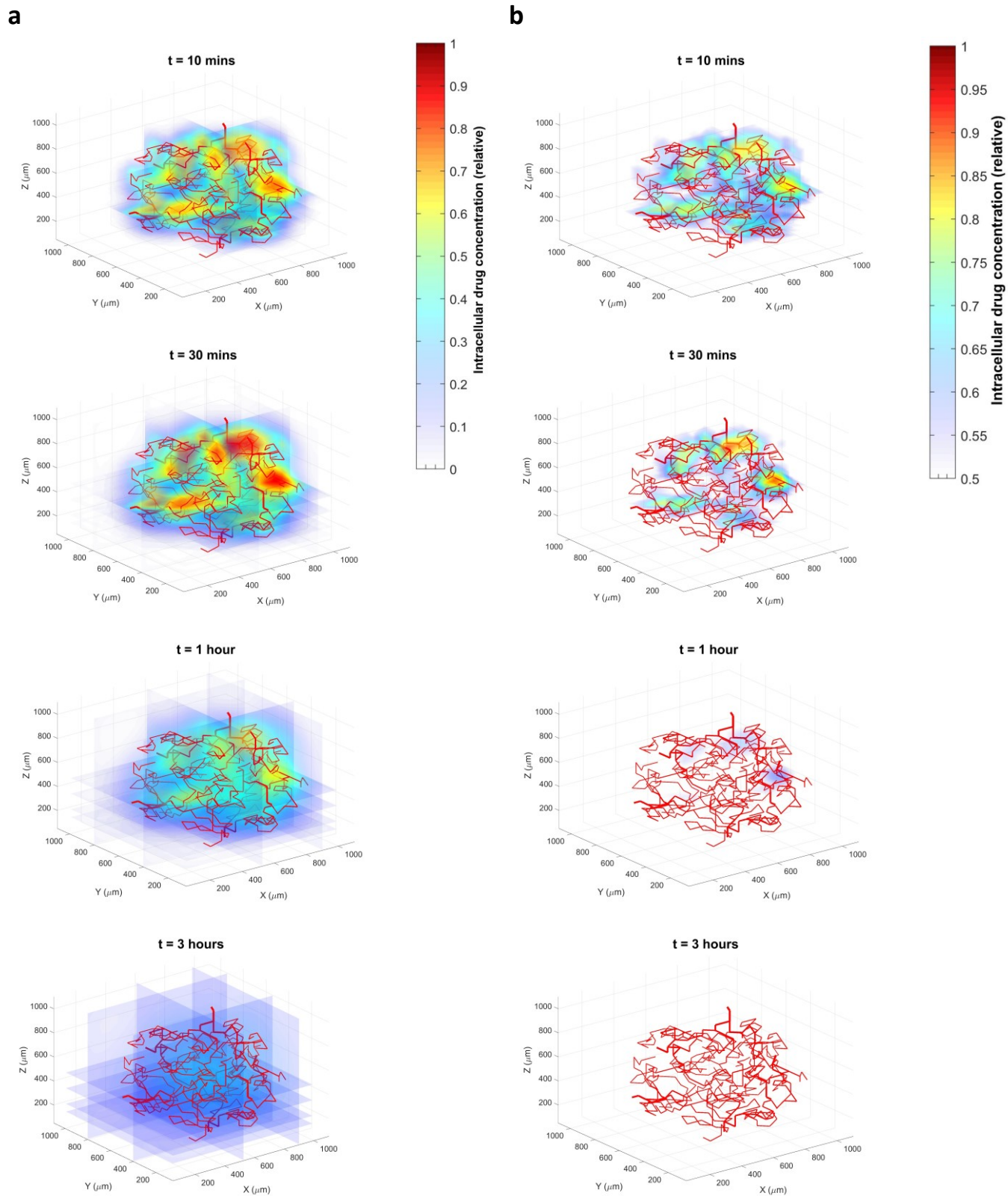
Figure 4.11: *Normalised intracellular concentration of doxorubicin at various time points for a bolus injection of 100mg (Model 2). (b) shows distribution points for concentration larger than 0.5 of normalised concentration.*

To quantitatively compare and analyse the spatial heterogeneity of extracellular and intracellular drug concentration between the different geometries, the non-uniformity factor (NUN) is evaluated which is defined as

$$\text{NUN} = \frac{\sum |c^i - c_{avg}| V^i}{c_{avg} V_{tumor}}$$

(4.20)

Where c_{avg} is the average concentration in the whole tissue, V_{tumour} is the volume of the tumour, c^i is the concentration of the drug at tissue node i and V^i is the volume of tissue node i. Figure 4.12 shows the calculated NUN values in extracellular and intracellular concentrations for the three models examined in this chapter. Compared to the original Model 1, heterogeneities in extracellular and intracellular concentrations are significantly higher in Model 2 and the enlarged Model 1. This greater heterogeneity was apparent for longer time periods, as it required 6 hours for the NUN factor in both geometries to reach values comparable with the original Model 1. The exposure of cells in the tissue space to non-uniform levels of doxorubicin for such a considerable time would be likely to result in different levels of cell killing within the tissue space. Additionally, once the concentration becomes more uniform after 6 hours, the level of intracellular doxorubicin is too low to exert its effect on cell killing.
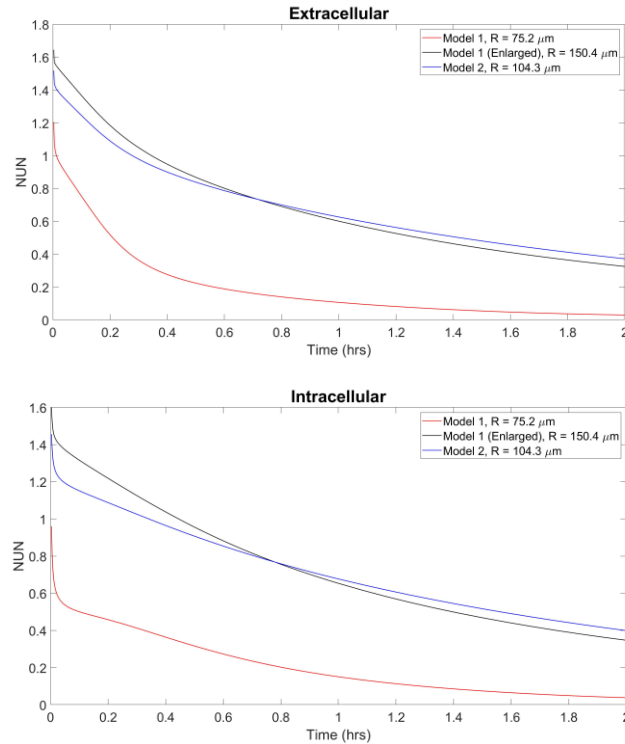

Figure 4.12: Variations of non-uniformity factor in extracellular (top) and intracellular (bottom) concentrations in different tumour models for a bolus dose of 100 mg.

115

4.3.4 Effect of dosage

In anti-cancer therapy, doxorubicin can be administered at different doses within a set limit. The effect of higher doses on intracellular drug distribution is examined. Bolus doses of 200 mg and 100 mg doxorubicin are chosen and applied to Model 1 first. Figure 4.13 shows the comparison of intracellular concentration maps for Model 1 with values normalized to the same peak value which is the highest concentration achieved in both cases. It is clear that increasing the dose resulted in a higher overall concentration in the intracellular space as expected. Regions near the vessels achieved higher concentrations than those further away from the vessels and spatial gradients are apparent. However, heterogeneities in concentration decreased in the case where a higher dose was injected. The higher peak concentrations are expected to lead to increased cell killing in regions near the vessels, whilst the reduction in heterogeneity can improve the overall therapeutic effect of doxorubicin due to more uniform cell killing.

The above findings were obtained in Model 1 where the maximum extravascular diffusion distance was 75.2 µm. To obtain a better understanding of the effect of dosage, simulations were performed on the enlarged Model 1 with a maximum extravascular diffusion distance of 150.4 µm. Figure 4.14 shows the calculated NUN factors for both the original and enlarged Model 1 and different doses administered. Whilst in the model with smaller inter-capillary distance (Model 1), a higher dose led to an apparent reduction in intracellular concentration heterogeneity; when the maximum extravascular diffusion distance within the tumour is increased (enlarged Model 1), the reduction in concentration heterogeneity was less obvious. This could potentially reduce any expected improvement in therapeutic effect from increased doses. Hence, the results here suggest that an enhancement in therapeutic effect of doxorubicin with increasing dose is dependent on tumour microvascular architecture, with larger intercapillary distance potentially resulting in almost no gain increase in therapeutic effect.
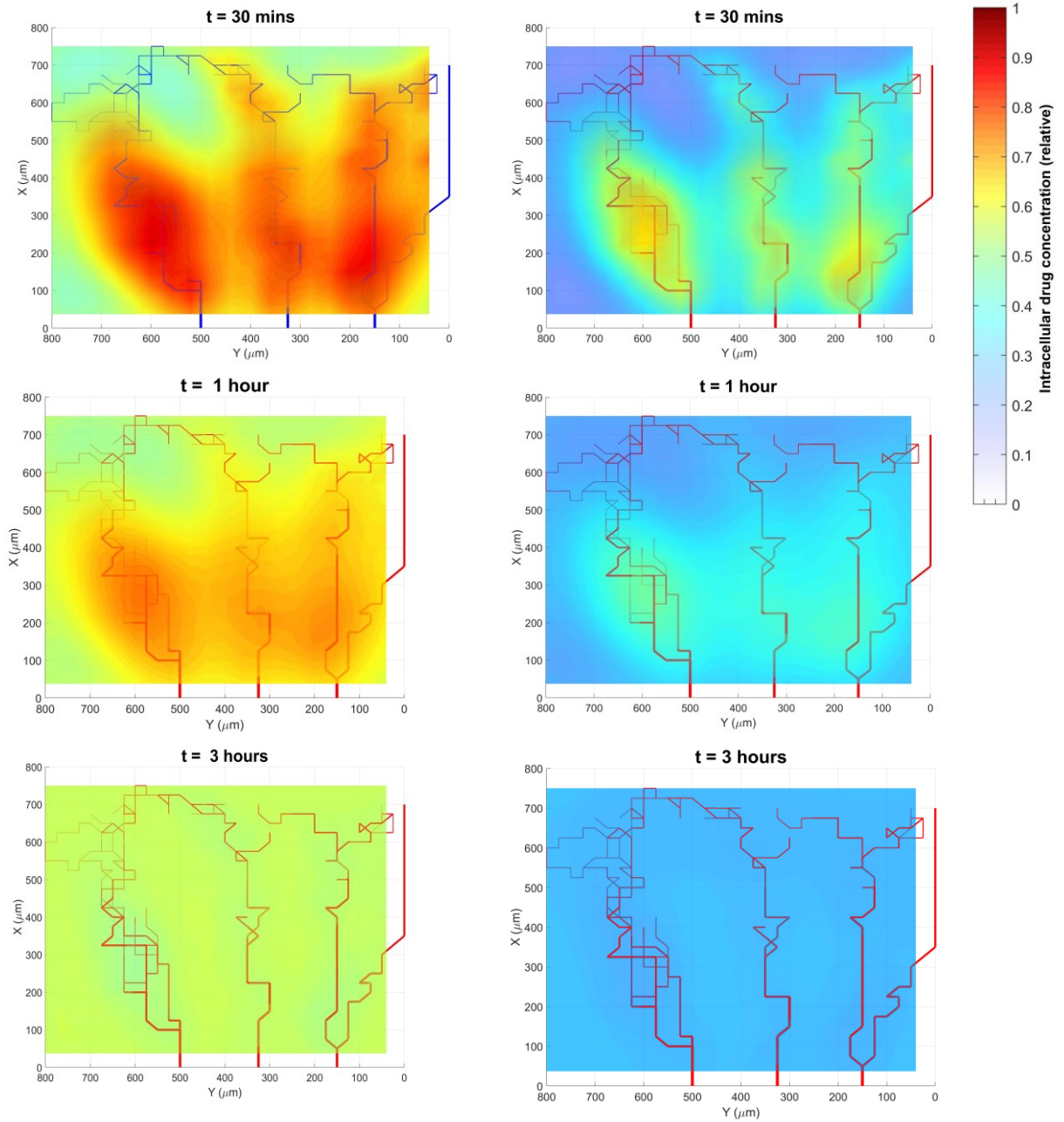
Figure 4.13: *Intracellular concentration for a bolus injection of 200 mg (left) and 100 mg (right).*
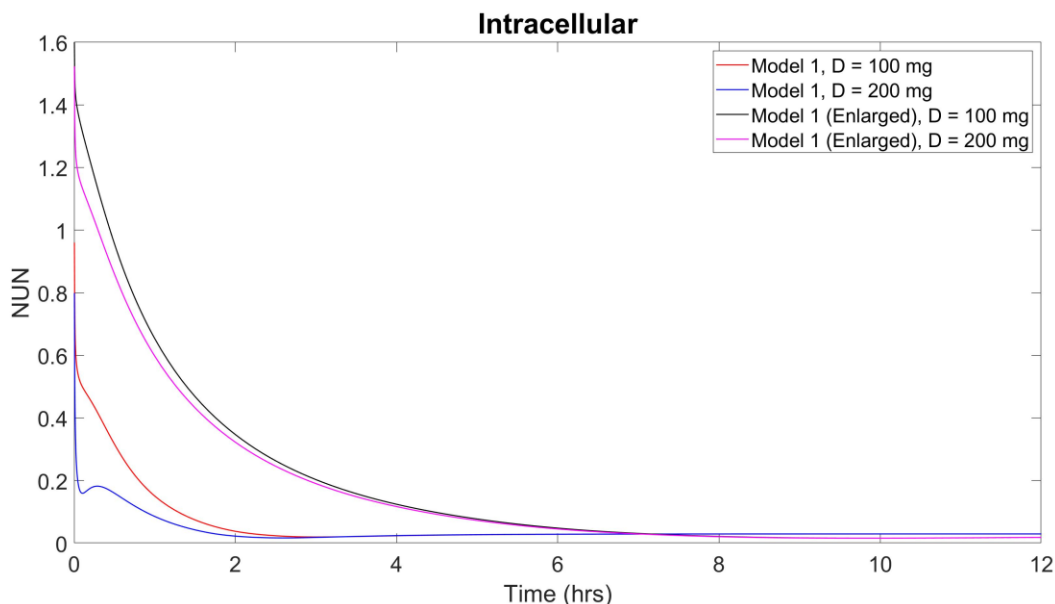
Figure 4.14: Variations of non-uniformity factor in Intracellular concentrations for doses of 100 mg and 200 mg in the original and enlarged Model 1

4.3.5 Effect of administration mode

Fractionation of doxorubicin during administration where the drug is infused continuously over a period of time has been shown to reduce cardiotoxicity in certain cases [237, 238]. When doxorubicin was infused over a short period of time in the range of 60-200 minutes, differences in predicted outcome were observed [179]. The effect of administration with infusion times of 60 and 200 minutes on intracellular concentration were examined to understand whether this would enhance or limit the distribution of doxorubicin. Figure 4.15 shows the intracellular concentration maps at various time points for different infusion modes. When doxorubicin is infused over 60 mins, higher peak intracellular concentrations in regions near the vessels are achieved when compared to bolus injection, which would enhance the therapeutic effect for cells in these regions. When the infusion is increased to 200 minutes the intracellular concentration in regions near the vessels is lower than that achieved for both bolus and 60-minute infusion. This suggests that although increasing the infusion time to 60 minutes can provide better therapeutic effect in cells nearby the vessels, further increase in infusion time could be detrimental to effective therapy. Although there was a difference in peak concentration achieved in regions near the vessels for different infusion times, the intracellular concentration of doxorubicin in regions further away from the vessels or in those regions where the vessels were tortuous is relatively low in all cases regardless

of the administration regime. Cells in these regions are exposed to reduced concentration of doxorubicin, potentially highlighting the heterogeneity in treatment.
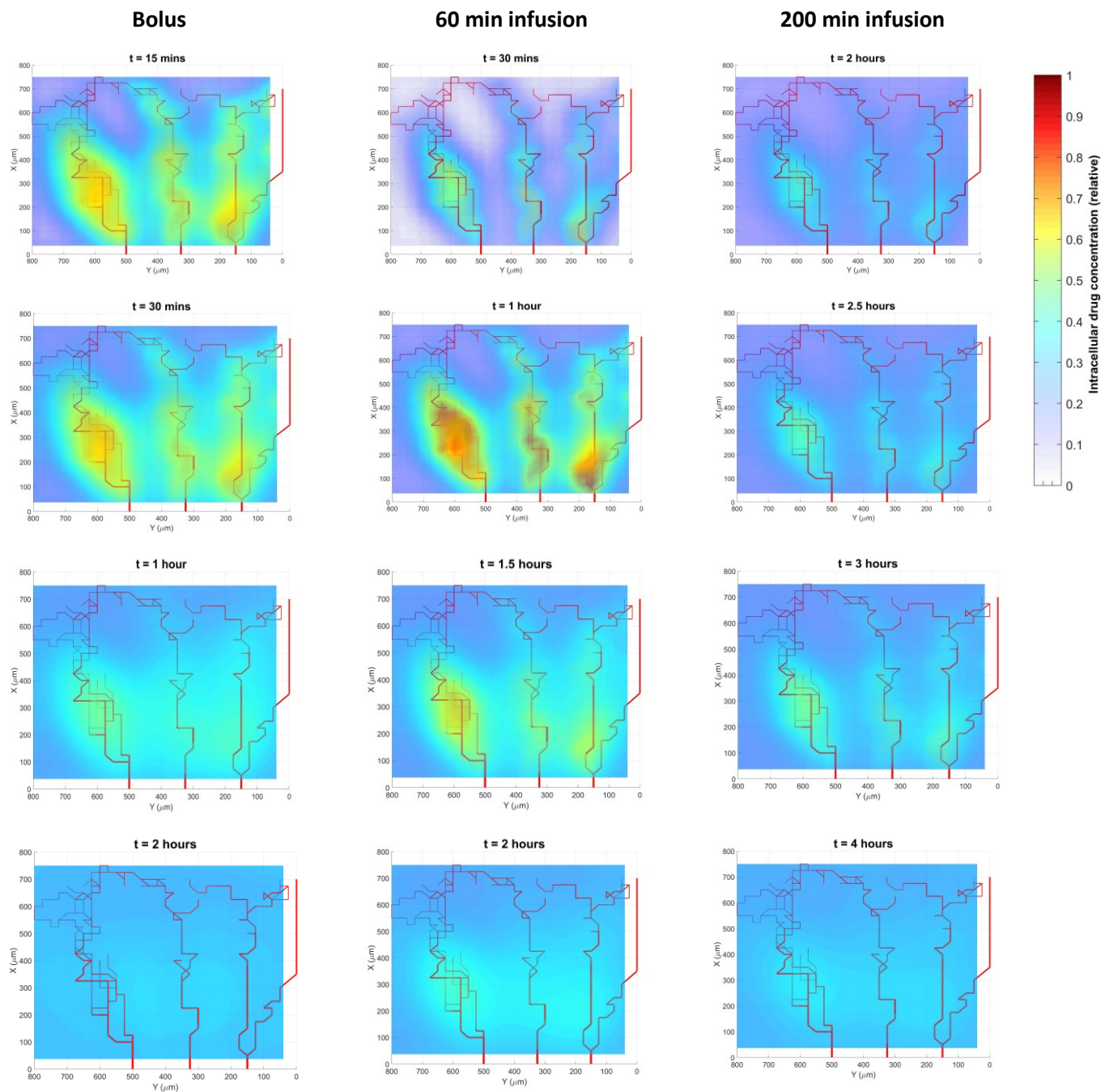

Figure 4.15: Intracellular concentration for 100 mg of doxorubicin administered through bolus injection, 60 minute and 200 minute continuous infusion in Model 1

To determine the effectiveness of the different infusion times, the peak intracellular concentrations in each tissue node *i* were determined over the simulated time course. To quantify the exposure of different tissue regions, the concentration in each tissue point was plotted against time and the AUC was determined for these tissue points. The AUC highlights the level of exposure of each tissue region to the drug where higher AUC are favourable. The peak intracelluclar concentrations and AUC are normalized to their respective peak values amongst the different adminstration modes. Figure 4.16a shows the peak intracellular concentration achieved using a bolus adminstration and continous infusion over 60 mins and 200 mins. The 60 min infusion achieved the highest peak concentration in regions near the vessels that are well perfused. Peak concentrations for the 200 min infusion were significantly lower in regions near well perfused vessels. In poorly perfused regions, the peak concentration was relatively low and did not differ significantly between all the admisntration regimes. From figure 4.16b variable results are seen in the spatial AUC where the bolus injection resulted in a more uniform AUC. Heterogeniety in the AUC increased with increased infusion times as the AUC in well perfused regions increased whilst the poorly perfused regions show low relative AUC values suggesting poor exposure to doxorubicin.
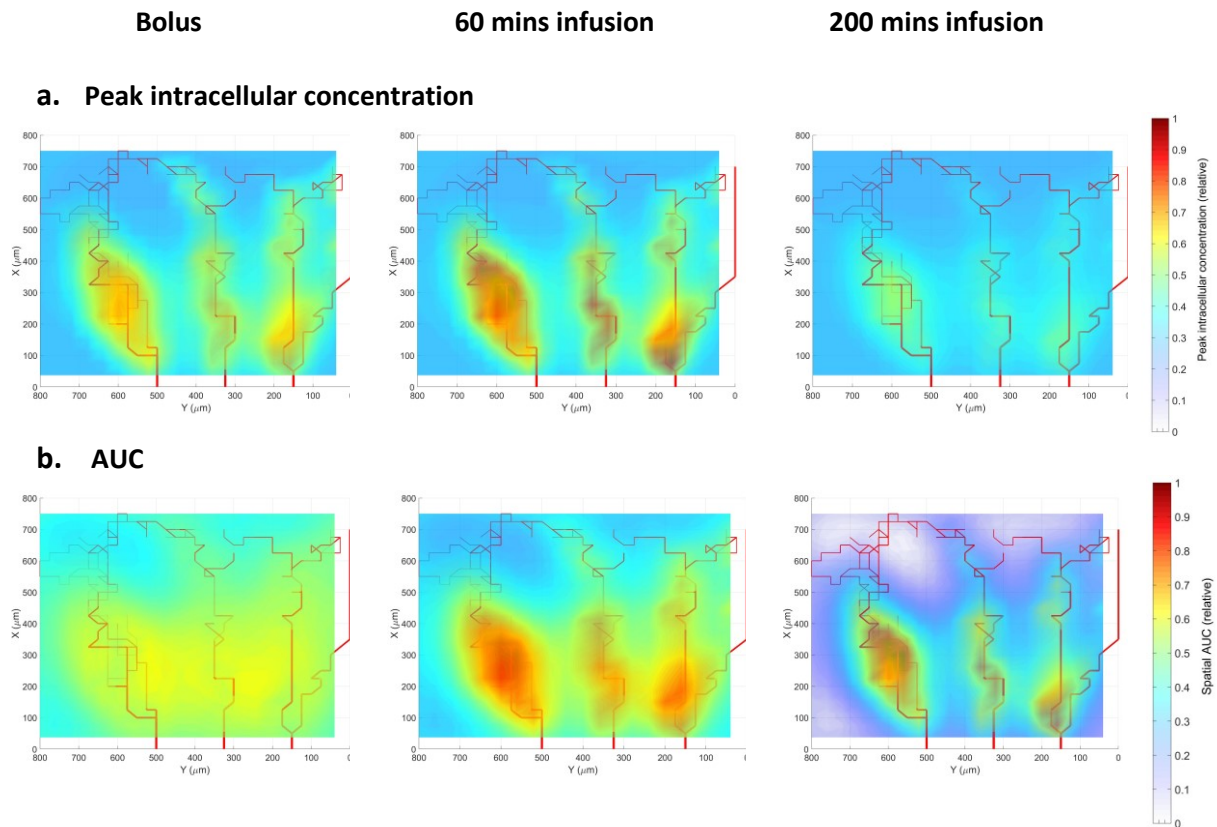
Bolus   **60 mins infusion**   **200 mins infusion**

a. **Peak intracellular concentration**

b. **AUC**

Figure 4.16: (a) Peak intracellular concentration in each tissue point achieved during time course of simulation and (b) AUC for intracellular concentration during time course of treatment.

4.4   Summary

In this chapter a time-dependent solute transport model describing the transport of doxorubicin in tumours is developed and coupled with the angiogenesis model and fluid flow model described in Chapter 3. The tumour model allows an explicit representation of the vasculature incorporating properties such as individual vessel diameter, length, and vascular tortuosity, branching and spatially dependent distribution. The transport model incorporates intracellular uptake and allows the spatial distribution of doxorubicin in the vascular, extracellular and intracellular space to be determined as a function of the vasculature and its spatially dependent properties. The effects of different administration modes and dosage levels on doxorubicin distribution have been evaluated.

The results show that extracellular and intracellular doxorubicin distributions are in part dependent on the distance away from nearby blood vessels. However, even in regions with a dense vasculature, drug concentrations could still be low if there were a greater number of branching vessels and tortuosity in the region that may contribute to reduced flow. Tumour vasculature can be extremely heterogeneous with large variations in architecture from case to case as evidenced by the inter-capillary distance ranging from 30 μm to 250 μm in different tumours. This effect has been analysed by simulating the transport in tumour models with similar architectures but different inter capillary distances, showing that increasing inter-capillary distance not only results in greater non-uniformity in drug concentration, but also reduces the peak intracellular concentration achieved in regions near vessels with low tortuosity, thereby reducing the therapeutic efficacy.

Higher doses were found to increase the concentration of doxorubicin in all regions of the tumour tissue and had a marked effect on reducing heterogeneity which is likely to enhance the therapeutic effect of doxorubicin. However, in the case where the intercapillary distance was increased, the effect of higher doses was almost negligible. These simulations suggest that increasing dosage can improve the therapeutic effect of doxorubicin in tumours with high vascular density and small intercapillary distance. For tumours with greater vascular heterogeneity and large capillary spacing, increasing dosage could potential offer little enhanced therapeutic effect at the expense of increased toxicity. The effect of administering the drug in fractions continuously as opposed to a bolus injection was dependent on the infusion time. A higher concentration was achieved in specific regions as the infusion duration was extended up to a certain point, after which reduced intracellular concentrations in regions were seen in comparison to bolus injection. Regardless of the infusion duration, drug concentration in regions with high

vessel tortuosity or in regions distant from the vessels, did not differ noticeably. These results highlight the interplay between drug distribution and explicit properties of the vasculature such as distribution, tortuosity, vessel diameter and length. The distribution of drug in the tissue space is not only dependent on the distance from the nearest vessels, but also on the overall architecture of vasculature, the tortuosity, and individual vessel morphology which determines the amount of drug in it.

5   Three-dimensional imaging of vasculature in whole tumour specimens

5.1   Introduction

Ovarian cancer is one of the most common types of cancers afflicting women. There are many different subtypes that are classified based on the cell from which the cancer originates. Ovarian tumours mainly develop in epithelial cells, that make up the outer surface of the ovary, germ-cells, or in stromal cells [239]. Epithelial ovarian cancer (EOC) is the most common form accounting for 90% of all cases. EOC can be further divided into distinct histological subtypes including serous, mucinous tumours, endometrioid and clear cell tumours which differ in risk factors, molecular composition and properties and clinical treatment [240]. High Grade Serous Carcinoma (HGSC) is most commonly diagnosed of these subtypes [241].

As described previously angiogenesis is an important process in the formation of blood vessels required for tumour growth and metastasis. Without vascular support through angiogenesis, tumours can become dormant, necrotic or apoptotic [67]. In malignant ovarian cancers angiogenesis has been detected in tumours as small as 20 mm^3 in size [242, 243]. Ovarian tumours have the capacity to grow 40 times the size of a normal ovary which has an average diameter of 2 cm. For ovarian tumours to grow, they must be supplied with sufficient oxygen and nutrients, hence angiogenesis plays a key role in this process. Currently accepted prognostic indicators for EOC included tumour stage, grade, residual tumour volume and response to chemotherapy. Given the role of angiogenesis in tumour growth, assessment and quantification of angiogenesis has been suggested as a tool for prognosis of ovarian tumours. As described in section 2.1.2.3, a significant amount literature has been devoted to this, however the prognostic significance of angiogenesis remains unclear due to the contradictory findings. This can be attributed to the variability in the methods used to quantify angiogenesis. These studies have largely applied microscopy methods where thin sections are obtained from the tumour and are used to assess MVD. In ovarian tumours the vasculature has been shown to be more heterogeneous than other tumours [134], hence the use of 2D methods where a small area is sampled does capture the complete structure of the tumour. There is a need to quantify the tumour vasculature and angiogenesis in ways that capture the heterogeneity over large scales of the tumour volume. Some of the 3D imaging methods described in section 2.1.2 may hold some promise in addressing the limitations associated with traditional 2D methods when assessing cancers.

5.1.1   Human, animal and invitro tumour models

As described in section 2.1.2, a number of 3D imaging methods are available to image the vasculature. Some of these have been applied to characterize the vasculature in different solid tumours. *In vivo* methods are limited to spatial resolutions on the order of several hundred micrometers. Intravital microscopy is an exception as it can provide high resolution 3D images, however it is limited to a depth of several hundred microns and is only applicable to animal models. Ex-vivo imaging techniques have been used to measure angiogenesis and characterize the vasculature of whole tumours in a number of studies. Most of these studies have used µCT and corrosion casting techniques which can be applied only to animal models or large organs where the feeding arteries can be easily identified and infused [244]. Other imaging methods including optical based techniques have also been applied to tumours obtained using animal models [105].

Studies assessing the vasculature in human tumour tissues have used 3D microscopy techniques which are limited to a tissue depth of several hundred microns. Hence most of our current understanding of the vasculature and angiogenesis in whole tumours stems from animal models and invitro. Although mouse models provide valuable insight into the biology of tumours, the lack of translational relevance and potentially less predictive ability of mouse models has been highlighted given the large percentage of drugs tested in Phase I trials which are not able to make it to market [245]. For example, anti-angiogenic treatments that have shown considerable promise in pre-clinical tests in mice have been less effective than predicted in humans [246, 247]. Invitro models provide a method to assess the tumour vasculature where they can vary in level of complexity and incorporate different aspects. These include simple cancer lines to complex 3D models that incorporate various aspects of the tumour microenvironment. Using endothelial cells, they can be seeded onto ECM scaffolds and the growth microvasculature can stimulated through angiogenic factors secreted by nearby cancer cells. This can be used to understand the processes of angiogenesis in addition to fluid flow, extravasation and drug uptake within the model. However, these models can lack physiological relevance and no universal protocol exist, hence it can be difficult to compare and contrast data with other models [248]. Mouse tumour models provide another method to assess the vasculature where patient derived xenografts (PDX) are engrafted into the mouse hence the tissue retains the heterogeneity and architecture of the original tumour. However, whilst some tumours are easy to cultivate, others cannot be grown and hence some cancer subtypes cannot be reproduced. Additionally, whist human tumours can originate from different anatomical sites which would influence properties of the tumour tissue specially vascularization, in mouse models, the tissue is almost always

implanted subcutaneously for easy access. When the tumour is implanted, the stroma is remodelled and replaced with mouse derived stroma which could potentially differentiate vascularization in tumours and response to therapy, therefore, the genetic background of the host mice has a great influence on their sensitivity to angiogenesis.

Considerable variations between the different tumour transplantation models also occur in the growth pattern of the vessels [246]. Pautu et al. analysed the vasculature in mouse models of melanoma and in human melanomas from different patients [249]. The found significant differences in the vascularization where the mice melanomas exhibited high vascular density and lumen size as opposed to the human samples. These differences could have potential implications when assessing the distribution of drugs. Dong et al. evaluated the effect of endothelial cell species on tumour growth and response to therapy [247]. They found that human tumours vascularized with human endothelial cells grow faster and were more resistant to treatment than xenograft tumours vascularized with endothelial cells. This shows that tumour xenograft vascularized with mouse blood vessels can overestimate the effect of treatment. Folarin et al. investigated 3D properties of vasculature in colonic tumours in both human clinical tissues and mouse colorectal xenografts [90]. The vasculature in mouse models was found to be more disorganized than human tumour tissues. Hence, more understanding of the vasculature in human tumour tissues is needed. However, animal models have remained popular for several reasons including the lack of infrastructure in place to collect, transport, store and maintain human tissue for lab use. There is a cultural reliance on animal models given the large amount of historical data that can be used to validate and contrast the model. Additionally, alternative methods will be required to process human tissues which would require significant amounts of time and resources [250].

This chapter is focused on assessing the feasibility of acquiring information on 3D vasculature from whole human tumour tissues by exploring the use of currently available imaging modalities. A protocol has been developed to visualize the vasculature in human ovarian tumour samples using a novel 3D microscopy imaging system named the "Histocutter" which was originally developed for bone imaging in the Department of Bioengineering at Imperial College London [98]. Optical projection tomography (OPT), another recently developed 3D imaging technique, is used to image the vasculature in human tumour tissues for the first time. Results obtained from the two imaging techniques are compared. The methods are assessed for their ability to extract parameters to quantify angiogenesis and vascular architecture in tumour tissues.

5.2 Methodology

5.2.1 Tumour tissue specimens

Following cytoreductive surgery for patients with advanced primary EOC, Omentum tumour samples were collected and transported to the Ovarian Cancer Action Research Centre lab at the Institute of Reproductive and Developmental Biology in Hammersmith for processing. These clinical samples were obtained in collaboration with Dr Paula Cunnea and Professor Christina Fotopoulou at the Ovarian Cancer Action Research Centre and supplied by the Imperial College Healthcare NHS Trust Tissue Bank, following full informed patient consent.

5.2.2 Whole tissue processing and IHC straining

As no standard protocol is available for the processing and staining of whole tissues, different protocols were attempted to prepare the specimen. The preparation process involves the diffusion of various liquid substances through porous tissue. The ability of a substance to diffuse a certain distance is a function of the concentration of reagents, operating temperature and time. The first and one of the most important steps in tissue preparation is fixation which allows for the morphology and antigenicity of the target molecule to be preserved. Fixation involves a number of variables that can affect the degree to which the tissue is fixed; these include the type of chemical, concentration, and the temperature and time over which the process is carried out [251]. If the tissue is not completely fixed (under-fixation), rapid degradation of the target proteins within the tissue may occur which would reduce its immunoreactivity. Over-fixation of the tissue can cause the target epitope to be masked or result in excessive non-specific background staining [252].

Fixation of the tissue samples in this work involves the following steps. The samples are immersed in 4% formaldehyde in PBS of volume that is 50 times larger than the volume of the tissue. Although there are many different types of fixatives such as alcohol and acetone, formaldehyde is the most commonly used fixative for IHC techniques and has shown good results in fixing tissues for vascular staining. Since the time of fixation and operating temperature play an important role in the fixation process, efforts were made to determine the fixation process that provides optimum staining quality. This was achieved by fixing the sample at room temperature (RT) (23 ^{o}C) while varying the time over which the tissue is fixed for different samples. Following fixation, each tissue sample was processed and stained using the same protocol to analyse the effect of varying fixation time. The fixation times used were 40 mins, 70 mins and 120 mins.

Following fixation, the tissues were washed 3 times with TBS1x for 30 mins to remove the fixative solution. The samples were blocked in a buffer solution (TBS1x+0.5% Triton+6% Goat serum) for 2 hrs at RT + overnight (o/n) at 4°C+ 2 hrs at RT. Primary incubation was the done with Anti-CD34 Rabbit monoclonal antibody at 1:100 dilution in TBS++(TBS1x+0.1% Triton+6% Goat serum) for 2hrs at RT + 72hrs at 4°C+ 2 hrs at RT. Following primary incubation, tissue samples were washed in TBS++ four times for 30 mins each. Secondary antibody incubation was performed using Alexa fluor 488 Anti rabbit at dilutions 1:200 in TBS++ for 2 hrs at RT + o/n at 4°C+ 2 hrs at RT. Tissue samples were then washed in TBS1x 4 times for 30 mins each. Having completed these steps, different protocols were used to prepare the tissues for imaging with the Histocutter and OPT.

The Histocutter is a novel imaging system based on a previous design [253] coupling a rotary microtome to an imaging hardware as shown in Figure 5.1. The imaging hardware is composed of a fluorescent light microscope, a white light source lamp and a high-resolution camera. The process is fully automated using a software developed in-house, Cutter Master CW (Java), which allows imaging parameters to be defined, such as section thickness (1-5 µm), fluorescence channel (UV, FITC, TEXAS RED or Cy5), magnification and exposure time. The system then automatically proceeds using a cut and view approach by which the tissue block is sectioned at the defined thickness, and serial images are taken of the block surface ensuring that focus is maintained and the block is aligned [254]. The series of 2D images can then be used to generate a 3D visualization of the sample.
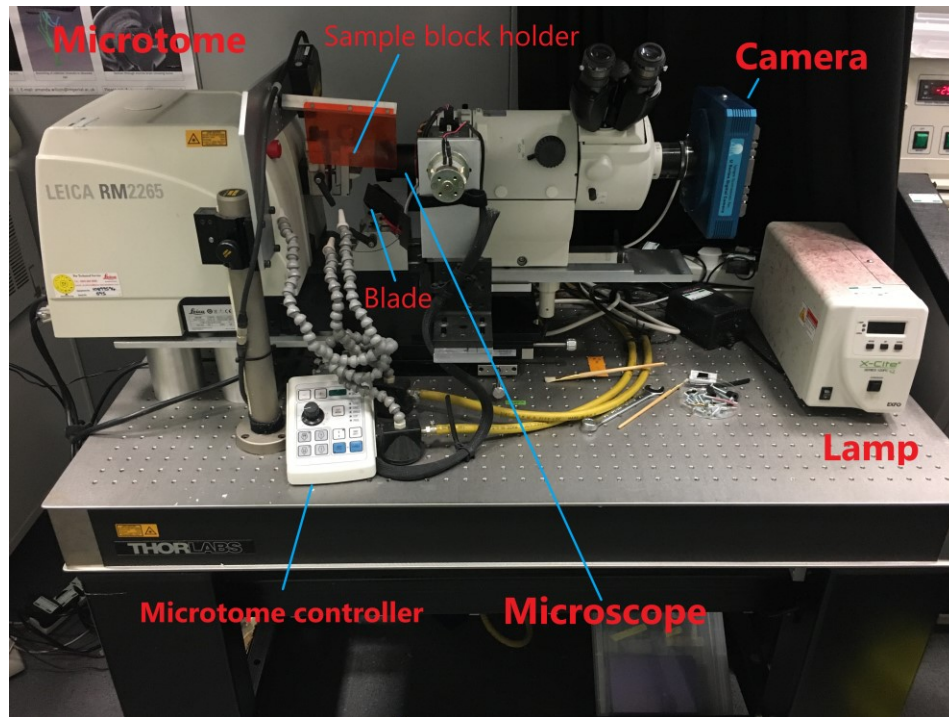
Figure 5.1: *Histocutter setup*

5.2.2.1   Histocutter - Tissue clearing and embedding

As the whole face of the tissue block is imaged using the Histocutter, it is important to ensure that the block is opaque to block background autofluorescence and fluorescence from vessels that are not at the plane surface in order to limit distortion in the 3D image. To achieve this, the tissue sample is infiltrated with dyes that absorb light emitted at deeper parts of the tissue and the paraffin block is stained with dyes that minimize penetration of the excitation light into the block. The dyes are chosen so that they can absorb both the light exciting the surface of the block and that emitted by the block. The fluorescence antibody used in the staining protocol (Alexa fluor 488) has an excitation and emission maximum wavelength of 490 and 525 nm, respectively, and a commonly used filter for this antibody is FITC. Sudan IV has a maximum absorption wavelength of 519-523 nm which is within our emission range whilst Sudan II has a maximum absorption wavelength at 494 nm which is within our excitation range [255, 256]. These two dyes are used to infiltrate the tissue samples and stain the paraffin wax used to embed the tissue. The steps followed to prepare the tissue samples for Histocutter imaging after staining are described below.

Dehydration:

Paraffin used in embedding is immiscible with water; hence the tissues must be dehydrated first by immersion in alcohol. Alcohol can penetrate the tissue quickly and replace the water contents in it, which can potentially cause shrinkage and hardening of the tissue. To avoid excessive distortion, the tissue samples are submerged in a series of solutions with increasing concentrations of lab grade ethanol as follows

- 30% ethanol at RT for 15 mins
- 50% ethanol at RT for 15 mins
- 75% ethanol at RT for 15 mins
- 96% ethanol at RT for 15 mins
- 100% ethanol at RT for 15 mins
- 100% ethanol at RT for 15 mins

Clearing:

Following dehydration, the samples are assumed to be cleared of water and replaced with ethanol. As ethanol is immiscible with paraffin, a solvent that is miscible with ethanol and paraffin is used to clear the tissue samples from ethanol. Xylene is a popular clearing agent used to perform this task, however, due to the concerns over its toxicity, Histoclear II (National Diagnostics™) - a safer clearing agent [257]- has been used as a substitute. Following dehydration, samples were sealed in a glass vial with Histoclear II for 1 hr at RT. The vial was then replenished with fresh Histoclear and left overnight at 4°C.

Infiltration:

As described earlier the tissue sample must be infiltrated with dyes that limit fluorescence from deeper regions of the block in order to minimize visual distortion. First the sample is immersed in a solution of Histoclear mixed with Sudan IV (0.5%) for 4 hrs at RT. An aqueous solution of stearic acid and Sudan II (4%) is prepared at 75 ^{o}C, which is used for secondary infiltration by immersing the tumour sample in solution and leaving in a vacuum oven at 600 mbar and 75 ^{o}C for 4 hrs.

Embedding:

An embedding medium is prepared using 10% stearic acid, 72% paraffin, 14% vybar, 2% sudan IV and 2% sudan II. Vybar is added to help eliminate air bubbles and dissolve the Sudan dyes. Stearic acid is needed to impart opacity and hold the block structure and shape. Tumour samples are immersed in the

embedding medium and left overnight in a vacuum oven at 600 mbar and 75 °C. Finally, pre-heated steel molds are used to embed the tissue samples in embedding solution. Blocks can settle at RT for a day before cutting.

5.2.2.2   Image acquisition

The blocks are mounted onto the Histocutter and trimmed until the tissue sample can be seen on the surface of the block. The fluorescent microscope was set to 2x optical zoom on a 4x magnifying lens with a Numerical Aperture (NA) of 0.4 and a working distance of 20 mm. The resolving power of this set up is given by the diffraction limit which defines the spatial resolution as follows

$$d_{min} = 0.61 \frac{\lambda}{\text{NA}}$$

(5.1)

where λ is the wavelength of the light and d_{min} is the smallest resolvable distance. Using an excitation wavelength of 520 nm gives a lateral (i.e XY) spatial resolution of 0.793 μm for the optical set up. The images were captured using a high-resolution camera (4096 x 4096 pixels) with a field of view (FOV) of 4 mm. This provides a pixel limited lateral resolution of 0.975 μm. The section thickness was set to 1 μm which is our theoretical axial resolution. The system was allowed to run overnight using the parameters specified in Table 5.1. The number of sections obtained is limited by the size of the block, and the number of usable sections varied depending on the thickness of each sample.

Table 5.1 Parameters for Histocutter

Cutting speed	2 (Speed range (1-5))
Thickness	1 μm
Lamp intensity	100%
Channel	Channel 1 (Excitation at 495 nm, Emission at 520 nm)
Exposure time	10 seconds
Camera	Apogee U-Series ALTA U16 s/n 091629 4096 x 4096 array 9 x 9 μm micron pixel
Objective lens	AZ-Plan Apo 4x Zoom 2x (NA 0.4)
Working distance	20 mm
Field of view (FOV)	4 mm (circle diameter)
Pixel size	0.975 μm

The Histocutter imaging system provided a stack of images that were processed using Fiji (open source: http://fiji.sc/Fiji) and Matlab [258]. The images were saved in 8-bit (0-255 dynamic range) lossless compression format (PNG) to ensure that original intensity data is preserved for analysis. During image acquisition noise could be introduced into the image through various sources, which can limit the visibility of the vasculature. Therefore, denoising is an important part of image processing that is required to enhance the image quality whilst preserving key features. This is especially important here as the stained endothelium is usually very thin and fluorescence microscopy images can be difficult to process due to uneven illumination, background autofluorescence, and inhomogeneous staining. Highly vascular dense regions are particularly difficult to resolve.

Different types of noise exist, including salt-and-pepper (Impulse), Gaussian and Poisson (Photon) noise. For images acquired with the Histocutter imaging system, the effect of Poisson noise is neglected which can be justified by the use of a relatively high exposure time to increase the photon count and the fact that Poisson noise reduces as the number of detected photons increases. When Gaussian noise is present, it is evenly distributed within the image where each pixel takes the sum of the true pixel value and a random Gaussian distributed value, so that the image histogram would resemble a Gaussian probability distribution. Gaussian noise is signal independent, and its standard deviation is constant with a noisier image having a larger standard deviation. Hence it is not dependent on the number of photons counted. To estimate the influence of Gaussian noise, images were acquired of a block without a fluorescent sample embedded in the medium to produce a homogenous image that would ideally be of constant intensity. Histograms of these images did not visually resemble a Gaussian distribution. A series of images were taken on the block, and the mean and standard deviation of pixel intensities in the field of view were evaluated as $\sigma = 0.880 \pm 0.004$ (n = 10). The images (see Figure 5.2) reveal the presecence of salt-and-pepper noise where sparse randomly distributed white pixels can be identified. To treat this type of noise, a 2D median filter (radius = 1px) is applied which moves through each pixel and applies the median value of nearby pixels. Applying this filter with a small radius allows for the removal of pixels which can be considered outliers whilst preserving small structures such as small vessels and vessel edges as shown in Figure 5.2. After application of the median filter, analysis of the pixel intensity within the same area of the blank block was performed and the corresponding mean and standard deviation were $\sigma = 0.124 \pm 0.006$ (n = 10).
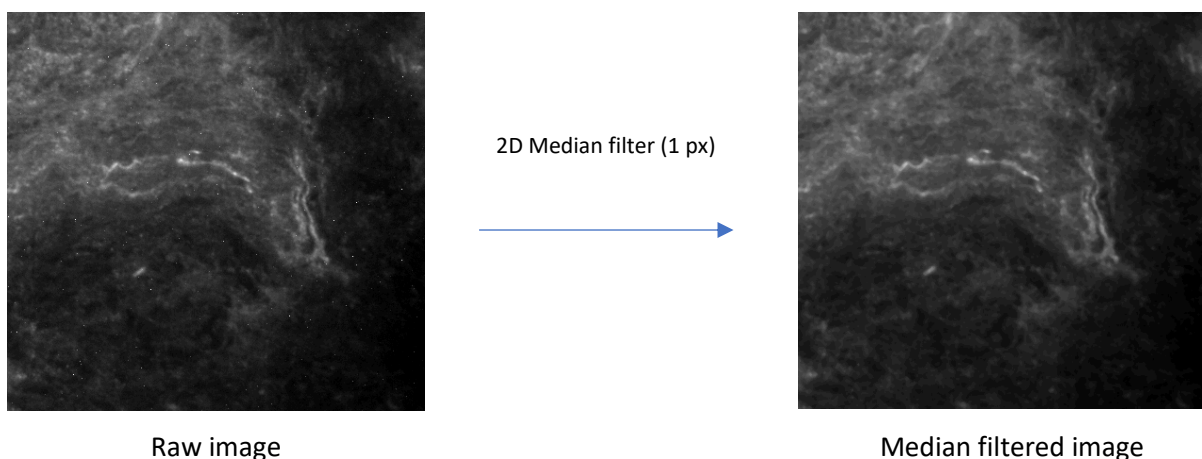
2D Median filter (1 px)

Raw image   Median filtered image

Figure 5.2: *Application of 2D median filter to salt and pepper image removes outlier pixels and preserves vessel structure*

5.2.2.4   Analysing fluorescence intensity

To reliably analyse fluorescence, care must be taken to ensure that no information is lost, and no image processing is performed that can distort the raw data. During image acquisition, an offset is added to the image intensity by the camera to ensure that the signal obtained from the CCD is above zero. To correct for the offset, a dark image was taken where no light was passed to the camera and the mean pixel value was calculated which was then subtracted from all the images in the stack. Saturation of images can present another problem for fluorescence quantification. The number of photons that can be collected in each pixel is limited by the capacity of the detector in the system. Once this limit is reached, photons reaching the pixel would not be counted and the image is considered saturated. When this occurs, the linearity of the detector is lost, and it would not be possible to determine the true intensity of the pixel, hence these images cannot be used to quantify fluorescence.

The sample fixed for 40 mins was processed first. A 10 second exposure time was chosen based on trial runs performed before automating the process to ensure that enough signal is collected to improve resolution whilst avoiding image saturation. However, analysis of some of the images revealed the presence of saturation. The number of saturated images accounted for approximately 7.9% of the total images acquired from the sample. Similarly, for the 120 min fixed sample, although the trial images showed no saturation, saturation was found in some images and accounted for 7.5% of the total images acquired for the sample. When acquiring images for the 70 min sample, a 10 second exposure time produced saturated images during initialization. Hence, the exposure time was reduced to 5 seconds in order to reduce or avoid saturation. After imaging the sample, no images in the stack were found to be saturated. The saturated images obtained from the 40 min and 120 min fixed samples were used for

visualization of the vasculature but were excluded from the set of images used to compare and quantify the fluorescence between the samples. To adjust for the different exposure times between the samples, the linearity of the detector is utilized where the number of photons detected should ideally be proportional to the exposure time. Pang et al. proposed a method to normalize images with different exposure times using dark pixel intensity [259]. Knowing this dark pixel intensity (DPI), the image obtained from one exposure time can be linearly scaled to represent an image obtained under a different exposure time. Mathematically this is expressed as follows

$$\frac{\text{Intensity}(t_1) - \text{DPI}}{t_1} = \frac{\text{Intensity}(t_2) - \text{DPI}}{t_2} \tag{5.2}$$

Where t_1 and t_2 are the respective exposure times. To obtain DPI a series of images at different exposure times were taken with the camera shutter closed to block light from reaching the CCD. The mean DPI determined from images after filtering salt-and-pepper noise was 16.015 ± 0.125. This value was used as the DPI value to recalculate and normalize the pixel intensity relative to exposure time.

Several measures have been used to quantify and compare fluorescence images. With a stack of images, the sum or the mean intensity of the slices is often used. However, these measures can be difficult to apply here as vessels are the object of interest in this study and they are known to be heterogeneously distributed. Hence, differences in sum intensity can be governed more by the heterogeneity or vascularity of the tumour. To compare fluorescence between the samples we use the maximum intensity value in each slice as an indicator. Another indicator used is the signal to background ratio (SBR) in slices. The ratio is expressed in decibel units as follows

$$SBR(dB) = 20 \times \log \left(\frac{mean\ signal\ intensity}{mean\ background\ intensity} \right) \tag{5.3}$$

The mean signal intensity was obtained from a region of interest (ROI) defined on the vessel. Mean background intensity was measured using the mean value of a ROI outside the vessel area as shown in figure 5.3.
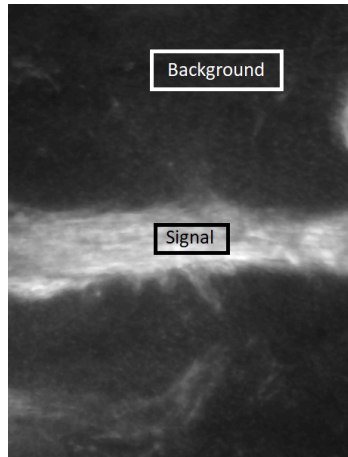
Figure 5.3: *ROI highlighting vessel and background areas used to calculate signal to background ratio.*

5.2.3 Optional projection tomography (OPT)

Optical projection tomography is a relatively new method that can be used to produce 3D images of a sample on a mesoscopic scale (1-15 mm), whilst maintaining resolutions on the order of several microns. Similar to X-ray computed tomography, in OPT the sample is rotated at incremental angles where a 2D wide-field projection is obtained over a 360º angle. The set of 2D images is then used to reconstruct a 3D image.

The OPT images were obtained in collaboration with Samuel Davies, Sunil Kumar, Dr James McGinty and Professor Paul French in the Department of Physics, Imperial College London. In order to obtain 2D projection images, the absorption and scattering of light within the tissue must be reduced which can be achieved using chemical clearing techniques that render the opaque tissue transparent. The cleared sample is then mounted on a magnetic rotor that automatically rotates the sample at incremental angles to provide a set of projections.

5.2.3.1 *Optical clearing*

Following fixation and staining, samples were optically cleared using a clearing agent. BABB (1:2 benzyl alcohol: benzyl benzoate) is a commonly used clearing agent and is compatible with the labelling method used in here. The samples were first suspended in 2% by weight agarose gel to stabilise the sample when it is being rotated during imaging. The sample was then dehydrated by immersing in increasing concentrations of methanol up to 100%. Following dehydration, the samples were immersed a 1:2

mixture of BABB until the methanol is completely displaced by the highly refractive BABB solution (refractive index ~1.56) to minimise refraction during imaging.

5.2.3.2 *Image acquisition and reconstruction*

The sample vial is mounted on a magnetic rotor that allows for the sample to be rotated at incremental angles. A laser diode based OPT system was used to image the sample. The fluorescent molecules in the sample were excited using a 470 nm LED, and the emitted fluorescence was spectrally selected with the 535 nm emission filter.

The imaging system comprised of a 1x telecentric lens (58-430; Edmund Optics) with a 5 mm DOF. The images were detected on an sCMOS camera (Zyla 5.5; Andor Instruments) with 2560 x 2160 pixels of 6.5 μm size providing a field of view (FOV) of 16.6 x 14.0 mm. The sample was fully rotated over 1280 equally spaced angles to provide a total of 1280 projections. Using equation 5.1 the system provides a diffraction limited lateral resolution of ~4.08 μm. The 2D projections were then used to reconstruct a 3D image using a filtered back projection algorithm where resolution is assumed to be isotropic and downgraded to approximately ~20 μm.

5.2.4 Blood vessel segmentation

To quantitatively analyse the structure of the vasculature and its features, segmentation tools are applied. Methods for segmentation vary depending on the target structure and imaging modality. In the case of vascular segmentation, significant research has been carried out which has been reviewed by Kirbas and Quek [260]. Most vascular segmentation algorithms have been designed for Magnetic resonance angiography (MRA) and CTA images where the vasculature is clearly visible with low noise. In our case, only the endothelium is stained providing visibility of only the outer wall so that the vessel appears as a hollow structure. In addition, the signals are usually weak, sparse and non-uniform with some discontinuous vessels. To address these challenges, the images need to be pre-processed using a pipeline to remove noise, correct illumination and to enhance the tubular structure of the vasculature for segmentation.

Generally, the process involves the use of filters to remove noise, background and autofluorescence, and the application of normalization and equalization techniques to even out illumination across all vessels. After correcting the image, algorithms are employed that are able to detect and enhance tubular or vessel

like structures to allow for easy thresholding. Given the large amount of data and images acquired in this project, manual or semi-automated segmentation is not feasible, hence an automated segmentation method has been sought. In this work an automated segmentation method was developed using Fiji (http://fiji.sc/Fiji). The images were first denoised using median filters. For OPT the image intensities in each slice were normalized to the mean intensity of the entire stack to compensate for loss of intensity in deeper tissue regions. Background in the images was corrected using a Rolling ball algorithm [261]. The sharpness of the vessels was enhanced by subtracting Gaussian filtered images with a sigma radius corresponding to the largest vessel. To extract the vessels an automated thresholding algorithm was implemented based on the triangle method [262]. Following automated thresholding, the analyse particle plugin developed in Fiji was applied to select objects with a certain degree of circularity to extract tubular objects. A binarized image is then produced which represents the vasculature of the tumour. To extract features of the tumour network the binary image was skeletonized using an algorithm based on the work by Lee at al. [263].

To validate the segmentation and binarization of the image, the original, skeletonized and binarized images are overlaid for visualization. To quantitatively validate the segmentation results, a small sample of images are segmented manually to obtain the ground truth and are then compared with the corresponding automatically segmented images using overlap-based metrics including the Dice coefficient (DICE) and volume similarity which determine the difference between the two images [264, 265].

5.2.5   Image analysis

It has been suggested that the expression of CD34 is associated with angiogenesis and tumour invasiveness [108, 266]. The density of CD34 is calculated in each slice as the ratio of the segmented area to the area of the image slice.

To analyse vascular morphology and network features, several parameters are calculated using the segmented and skeletonized vasculature. The analyse skeleton feature in Fiji was applied to obtain information on the lengths of each branch and the Euclidean distance between each point [267]. These include vascular volume density and length density as defined by Stamatelos et al. in their morphological analysis of vasculature in breast tumours [93]. MVD is usually estimated using 2D slices in highly vascular regions, however this could introduce bias and provide conflicting results. In this study MVD is calculated using the approach by Zhang et al. [135] which is based on vessel center lines. To calculate the mean cross-sectional area the volume of the segmented image is divided by the sum of the branch lengths in the

skeletonised image. To calculate the surface area of the vasculature, the 3D objects counter plugin in Fiji was applied which uses voxels connected with the background to determine the surface area of an object [268]. The tortuosity was calculated as an average for the entire network using the extracted lengths for each branch and the Euclidean distance. A summary of the parameters used for analysis of angiogenesis and vasculature and their definitions are given in Table 5.2.

Table 5.2 Description of parameters used for analysis of angiogenesis and vascular morphology.

Parameter	Units	Description	Formula
CD34 density	%	Ratio of segmented mask pixels to background pixels	$\dfrac{\sum \text{pixels on segmented object}}{\sum \text{pixels}}$
MVD	dimensionless	Ratio of skeleton voxels to tissue voxels	$\dfrac{\sum \text{voxels on vessel centerline}}{\sum \text{voxels on region of interest}}$
Vascular volume density	%	Ratio of vessel voxels to tissue voxels	$\dfrac{\sum \text{voxels on segmented object}}{\sum \text{voxels on region of interest}}$
Mean cross sectional area (A_D)	μm^2	Volume of segmented image over sum of branch lengths	$\dfrac{\sum \text{voxels on segmented object}}{\sum_{i=1}^{N_{branch}} \text{Branch length}}$
Vessel diameter	µm	Obtained from mean cross-sectional area.	$2\sqrt{A_D/\pi}$
Vessel surface area per unit tissue volume	mm^{-1}	Ratio of total surface area of 3D objects segmented to the total tissue volume	$\dfrac{\text{Total surface area of 3D objects}}{\text{Total tissue volume}}$
Mean vessel tortuosity	dimensionless	Mean ratio of branch length to shortest distance between points	$\sum_{i=1}^{N_{branch}} \dfrac{\text{Branch length}}{\text{Euclidean distance}} \Big/ N_{branch}$

5.3   Results and Discussion

5.3.1   Histocutter

5.3.1.1   Fluorescence analysis

When imaging the samples, they were centered within the microscope's maximum field view of 4 x 4 mm. Since the samples were as large as 5 mm in size with varying thicknesses, some parts of the samples were out of view. For samples fixed with 40 mins and 70 mins durations, the samples were trimmed, and the process was then automated to acquire 1535 and 1000 slices, respectively, before reaching the edge of the samples. For the sample fixed for 120 mins, 400 slices were obtained as a large portion of the sample was trimmed before a signal was established visually. The mean intensity for each slice was calculated and plotted as a function of the z-axis as shown in figure 5.4.
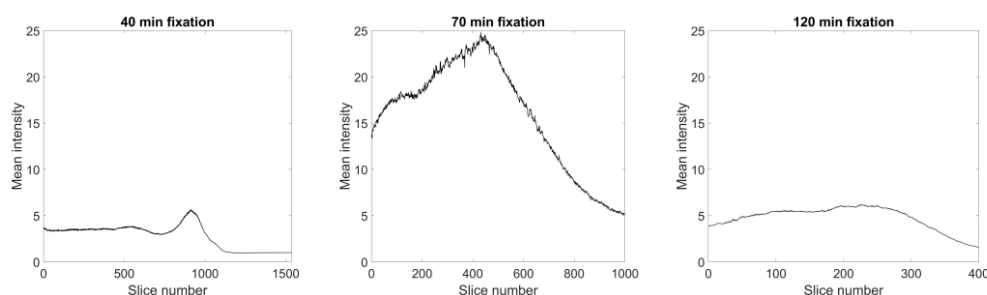
Figure 5.4: *Z-axis mean intensity profile of tissue samples with fixation duration of 40 mins (left), 70 mins (middle), 120 mins (right)*

It can be seen that the 70 min fixed tissue had higher mean intensity values than the other samples. However, this does not necessarily mean that a 70 min fixation would be optimal as this sample might have a higher vascular density. To analyse the fluorescence intensity of different samples, the maximum intensity at each slice is plotted as shown in Figure 5.5. The maximum intensity in the trimmed sample fixed for 40 mins had a relatively low max intensity value initially in the deeper parts of the tissue before rising as the cut plane moved towards the tissue surface. A gap in the data is present between slices 900-1000 as they correspond to saturated slices which cannot be used to quantitatively analyse fluorescence. The 70 min fixed sample showed higher maximum intensity values by approximately 4-fold which was consistent throughout slices before dropping as the tumour surface was reached (>700 slices). The 120 min fixed sample had a higher intensity relative to the central region of the 40 min sample, however, in the peripheral region, the intensity levels were similar. Overall the 70 min fixed sample showed consistently higher maximum intensity values than the samples fixed for 40 min and 120 mins.
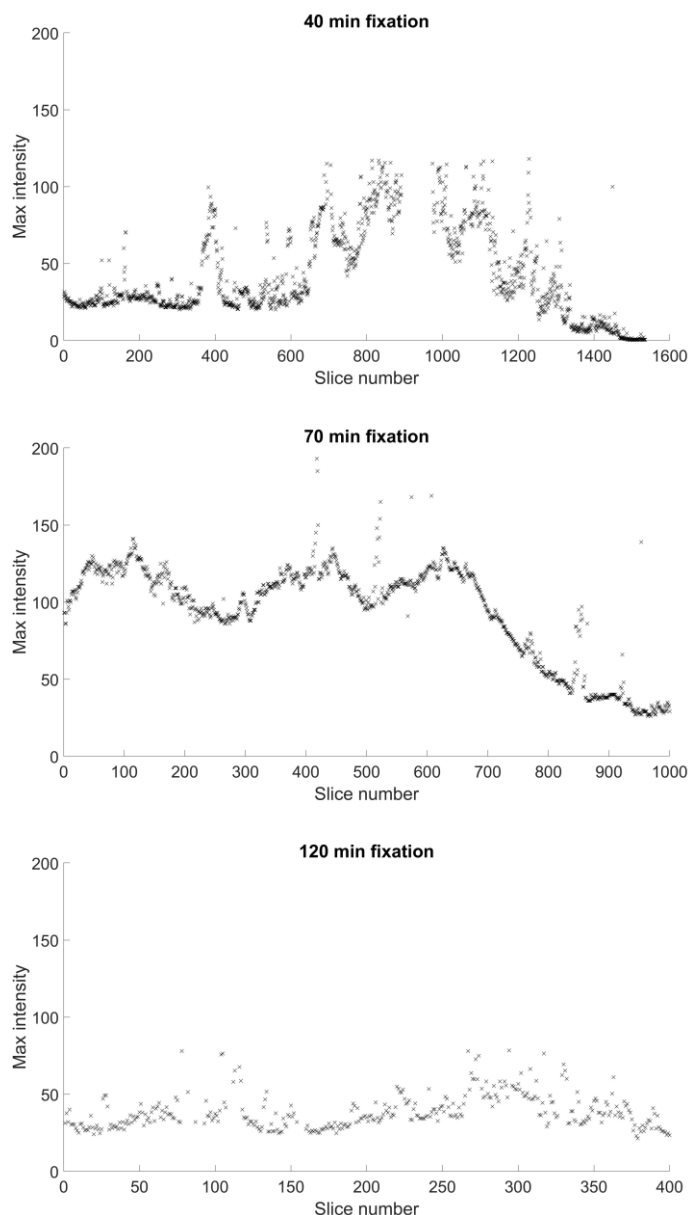
Figure 5.5: Maximum pixel intensity in stacks from sample fixed for 40 mins (top), 70 mins (middle) and 120 mins (bottom).

Figure 5.6 shows plots of the maximum intensity values in slices sampled from different regions of the tissues for 40 mins and 70 mins. The slices were obtained from central and peripheral regions within the tissue sample. The sample fixed for 40 mins showed significant variability in intensity between central and peripheral regions. In the central region the intensity was low and exhibited uniformity where no significant variations occurred. In the peripheral region the intensity was 1.5-4 times higher and showed significant variability from slice to slice. The sample fixed for 70 mins showed insignificant change in

intensity values between the periphery and deeper tissue regions and no erratic changes in intensity between slices. These data suggested that the 40 min fixation time was not enough to fix the whole tumour which resulted in uneven staining and heterogenous maximum intensity. The 70 min fixation provided consistent intensity between randomly sampled slices.
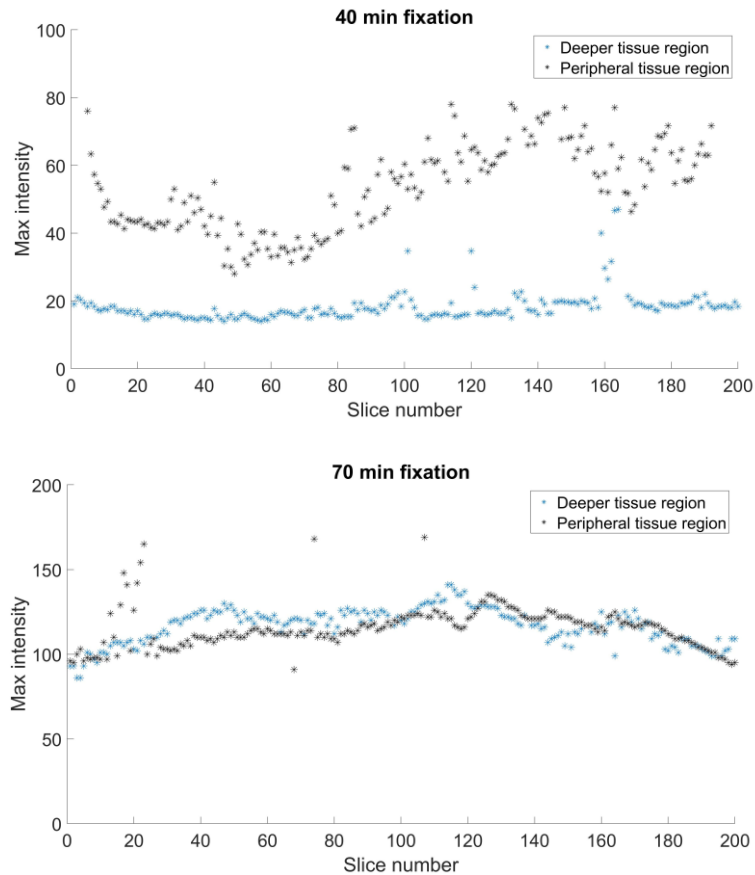
Figure 5.6: Maximum pixel intensity in stacks from sample fixed for 40 mins (top) and 70 mins (bottom) showing the difference in intensity between slices acquired from the tissue periphery and deeper tissue regions

To calculate the signal to background ratio the mean intensity values from the vessel area is divided by the background area as described in equation 5.3. Figure 5.7 shows the mean signal to background (S/B) ratios in slices obtained in the peripheral and central tumour regions. The S/B ratio in the 40 min fixed tissue was significantly lower in deeper tissue regions as opposed to the surface. The 70 min fixed tissue exhibited higher S/B and the mean value did not vary much between randomly sampled slices from the central and peripheral tissue regions.
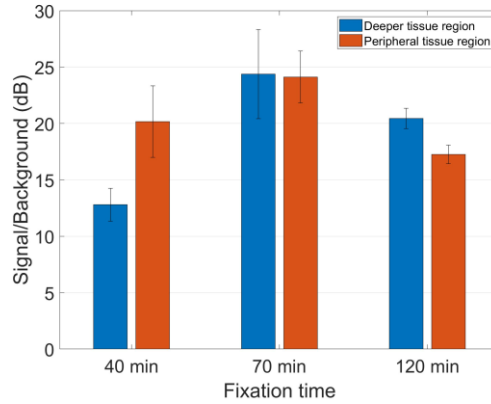
Figure 5.7: Signal to background ratio calculated from slices obtained from slices in the central and peripheral tumour region.

The contrast in intensity and S/B ratio between the central and peripheral regions of the 40 min fixed tissue suggested that it was inadequately fixed leading to uneven staining. The shorter fixation time could have caused poor antigen preservation in the deeper tumour regions where fixatives do not have enough time to penetrate. In the case of the 120 min fixed sample, data from obtained slices showed slightly higher intensities and S/B compared to the 40 min tissue, however it was not able to match the 70 min fixed sample and erratic changes in signal levels were observed from slice to slice. More so, when the sample was being trimmed, low or no signal was observed and most of the sample was trimmed before any signal was detected which led to only 400 slices being obtained. These observations are consistent with over fixation where excessive antigen masking is known to occur, causing a lack of signal and potential high background intensity. Based on these findings a fixation time of 70 mins was selected for the samples used in this study, which were approximately 5 mm thick.

5.3.1.2   3D vascular reconstruction and analysis

The image processing steps described in the previous section were performed with the aim of preserving raw gray values in order to quantify fluorescence within the tumour samples. In this section the focus is on image processing steps that can enhance vessel features and allow for easy segmentation and analysis of structural properties. Figure 5.8 shows the adopted workflow and illustrates its effect on image enhancement. To remove salt-and-pepper noise, images were processed using a 2D median filter. Background from the camera was corrected using dark field images obtained from the camera whilst background from Sudan dyes was subtracted using an image of a flat block. Background autofluoresence originating from the tissue was treated using a rolling ball algorithm and Gaussian filters [261]. To address loss of intensity caused by uneven illumination and staining, a local normalization algorithm was applied

which allows for signals from faint vessels to be enhanced whilst not oversaturating high signal regions. Figure 5.8 shows the ability of the adopted workflow to enhance vascular structures as small as 15 μm in diameter.
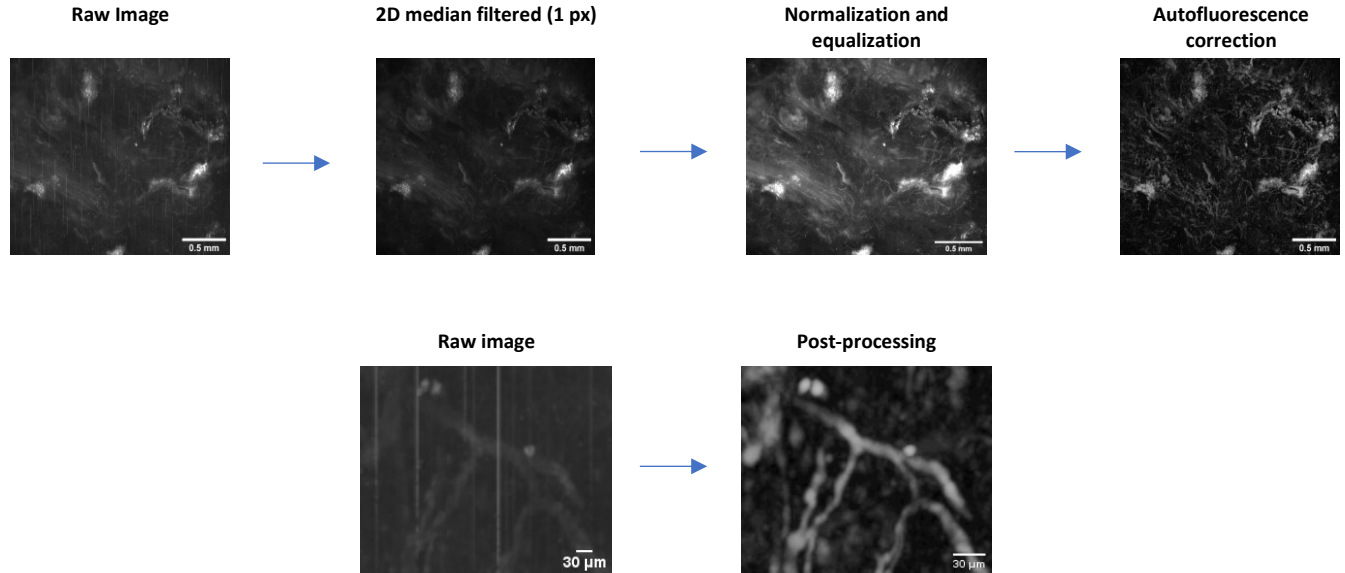
Figure 5.8: Image processing workflow to enhance image and vessel features. (Bottom) Zoomed-in image of small vascular structure in raw image and enhanced image.

Using the workflow described above, images from the samples were processed and visualized using maximum intensity projections (MIP) and 3D projections from different angle as shown in Figure 5.9 for the 40 min and 70 min fixed samples. In Figure 5.9a, for the 40 min fixed sample, the images show increasing vascular density and resolution of small vessels regions near the tumour surface which was more likely caused by the uneven staining rather than heterogeneity in vascular distribution. Although the intensity has been equalized, some vessels deeper in the tissue appear fainter with a lower contrast. The vessels visible show a range of diameters, with smaller capillaries near the tumour surface showing chaotic distribution and topology. The 70 min fixed sample showed more uniform staining as seen in Figure 5.9b where the vessels had a uniform brightness along the depth of the tissue.

a
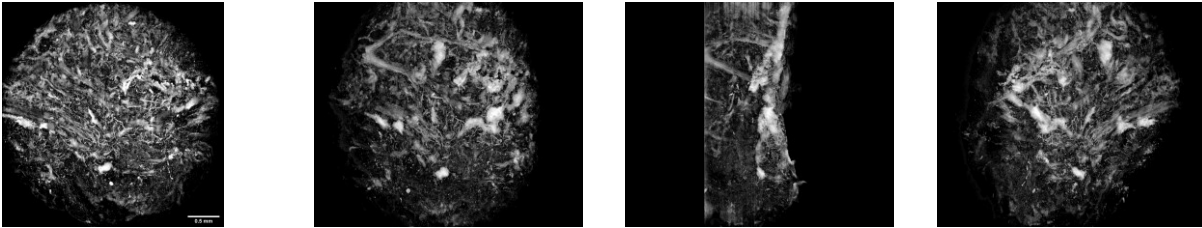
b
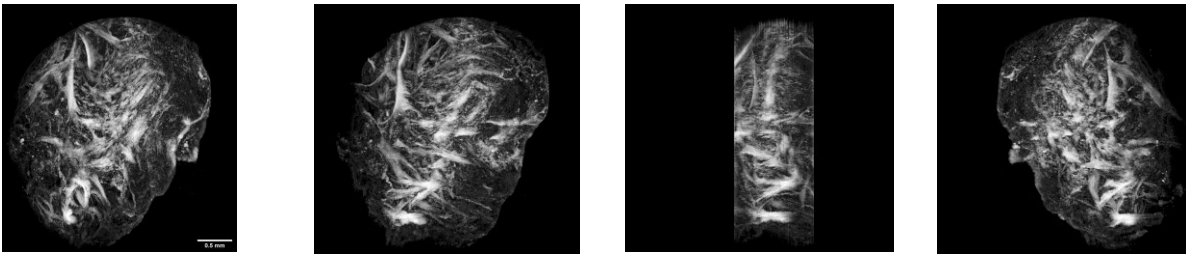
Figure 5.9: *Maximum intensity projections from different angles for a tumour tissue sample fixed for (a) 40 mins and (b) 70 mins.*

The vascular segmentation method described in the methodology in section 5.2.4 was applied. The segmentation process was visualized using a small sample of images within the stack as shown in figure 5.10.

| Processed image | Binary image from adaptive thresholding | Centerline extraction | Node assignment |
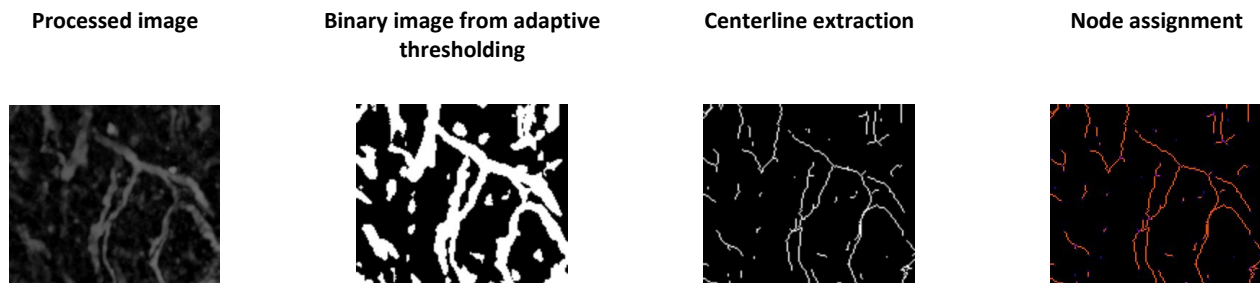
Figure 5.10: *Segmentation and skeletonizaiton of the vasculature. Far right picture shows the assigment of of node to the skeletized vasculature with blue points denoting end points and purple points denoting junctions*

To validate the segmentation method, the processed image in figure 5.10 was segmented manually by hand and compared with the image produced using the automated segmentation procedure. The Dice coefficient was close to unity whilst the volume similarity was 0.001, suggesting an excellent agreement between the two images. On a larger scale, manual segmentation for validation is not possible given the

large amount of data processed, hence an overlay of the segmented mask on the source image is used to evaluate the segmentation method as shown in figure 5.11. The overlay shows that the segmentation method is able to capture many of the major vessels that are visible.
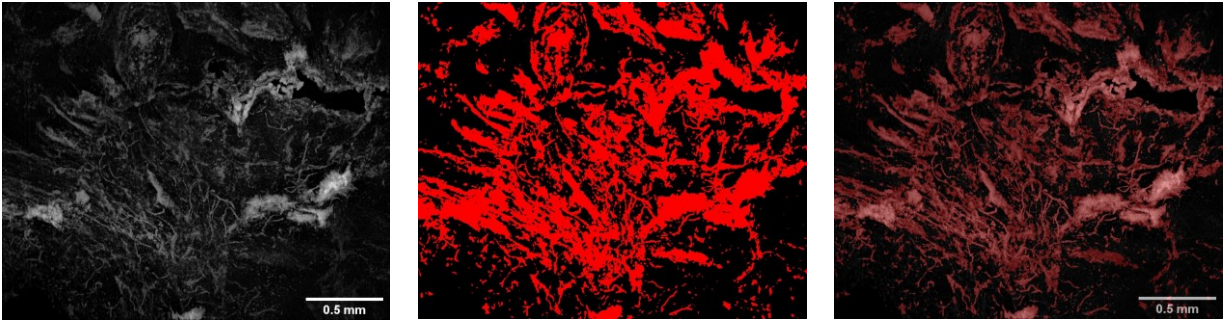
Figure 5.11 MIP of image stack (left), binary mask generated using adaptive threshold algorithm (center), Source image with mask overlay.

As shown in figure 5.10 the skeleton image of the tumour vasculature can be labeled with points denoting branching and ends. Using the reorganized dataset, the length of each branch can be calculated and the Euclidean distance (shortest length) between the start and end nodes of the branch can be calculated to derive vessel tortuosity. To quantitively analyse the vasculature, the set of equations listed in table 5.2 were used to calculate the morphological parameters of the vasculature based on the binary and skeletonized images of the 40 min tissue sample. The average diameter was found to be 14.09 µm with a mean length of 17 µm, and the tortuosity of the vessels was found to be 1.28±0.49. The mean length of vessels can be explained by the poor vessel staining in the sample which is highlighted by the low vascular volume density of 1.4%. In addition, small disturbances are seen in the alignment of slices (Figure 5.12) which can introduce error when the segmentation and skeletonization method attempts to register a vessel. Calculation of the CD34 density from different tumour samples yielded values up to 5% for the 40 min sample and 3% for the 70 min tumour and this was significantly lower than expected from the literature data [269]. The use of the Histocutter was discontinued at this point and an alternative imaging method was pursued.
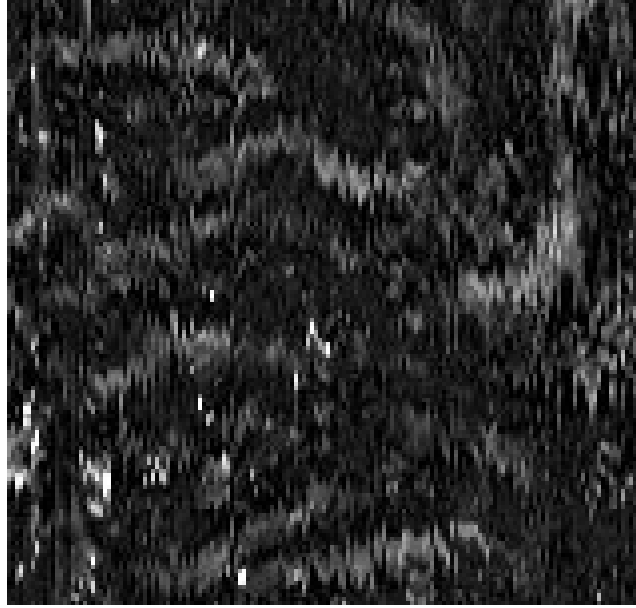
Figure 5.12: *MIP of Z-stack from y-axis showing some unalignment in the image stacks.*

5.3.2   OPT

The Histocutter is limited to a field of view of approximately 4 x 4 mm. OPT, a novel imaging method can image samples on the order of centimeters. Using this imaging modality, a tumour, 12 mm wide was examined. Reconstruction of the OPT images provided a stack of size 2160 x 2160 x 2212 which were visualized using the MIP as shown in figure 5.13. As the camera and imaging system differ from those with the Histocutter, different image processing methods were applied. Given that the tumour sample is imaged as a whole, depth related intensity losses are expected. To compensate for this, each optical slice was normalized by the mean value of the entire tumour sample to enhance illumination as described in section 5.2.4. The background autofluorescence was removed using a rolling ball algorithm [261]. A 3D Gaussian filter was applied with a width of 60 pixels based on the largest vessel structure visible which corresponds to 390 µm. The filtered images were subtracted from the originals to remove background and enhance vessel sharpness as shown in Figure 5.13 and Figure 5.14.
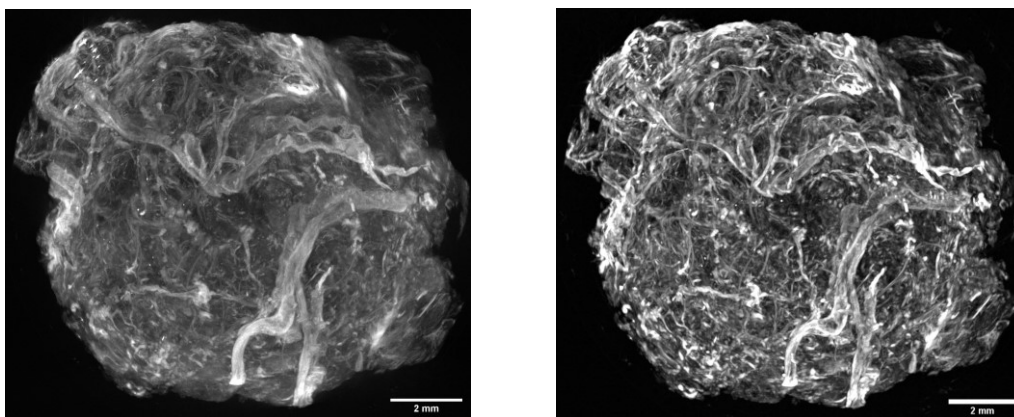
Figure 5.13: *Maximum intensity projections (MIP) for tumour sample imaged with OPT system. Left shows raw image and right shows image after processing*
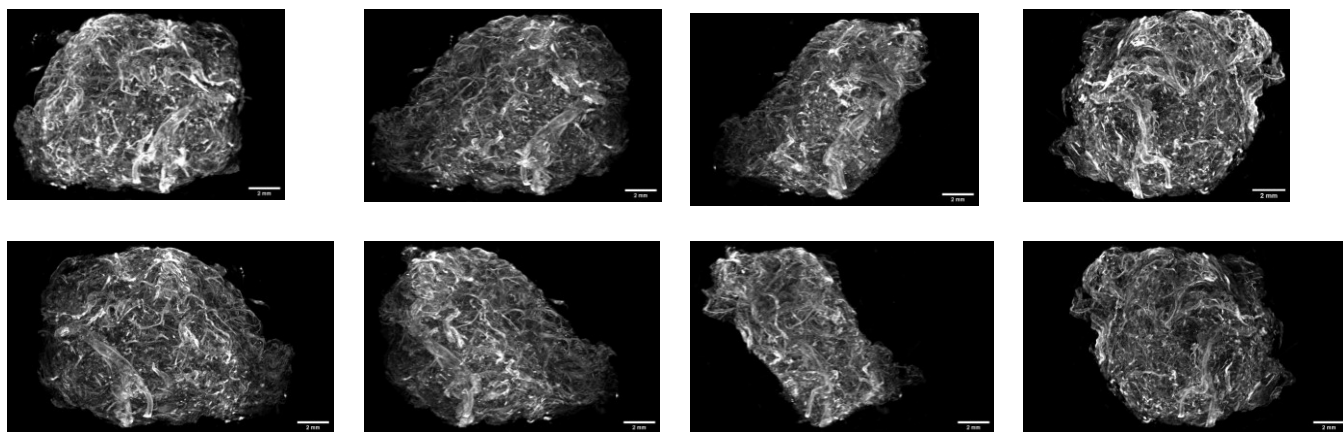
Figure 5.14: *MIP of tumour vasculature from different angles after image processing.*

The tumour vasculature was segmented and skeletonized using the same algorithm described in section 5.2.4. Figure 5.15 shows the response of the adaptive threshold algorithm and its ability to segment the vasculature from the OPT generated images. Visually, the overlay appears to cover major parts of the tumour vasculature with no apparent leakage or over segmentation.
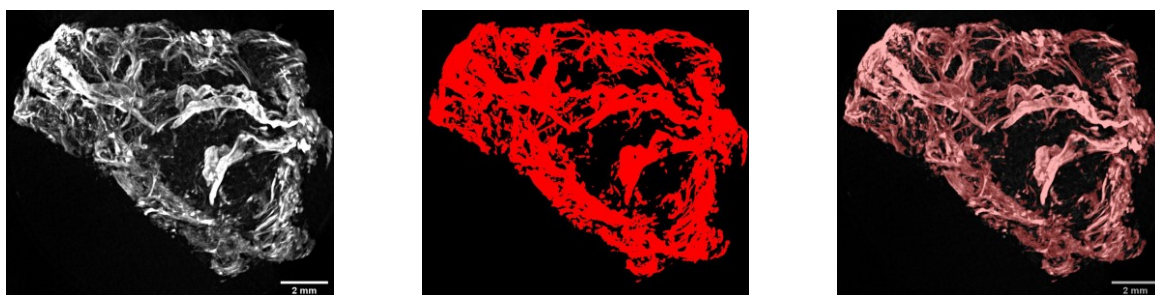
Figure 5.15: *MIP for slices 1800-2000 showing contrast enhanced vasculature (left), segmented mask (center) and overlay of mask on source image (right).*

The binary image produced from the segmentation of the vasculature was used to generate a skeleton of the vascular network as described previously. Different volumes of interest within the same tumour sample were defined to evaluate the intratumoural heterogeneity. A volume of interest (VOI) was also defined in each of the images from other samples collected and were used to evaluate intertumoural heterogeneity of CD34 expression. Figure 5.16a shows tumour sample 1 and the volumes interest defined in this tumour whilst Figure 5.16b shows the volumes of interest obtained from different tumour samples. Each slice within the VOI of the binary image was measured for CD34 density distribution over a data set of 500 each.
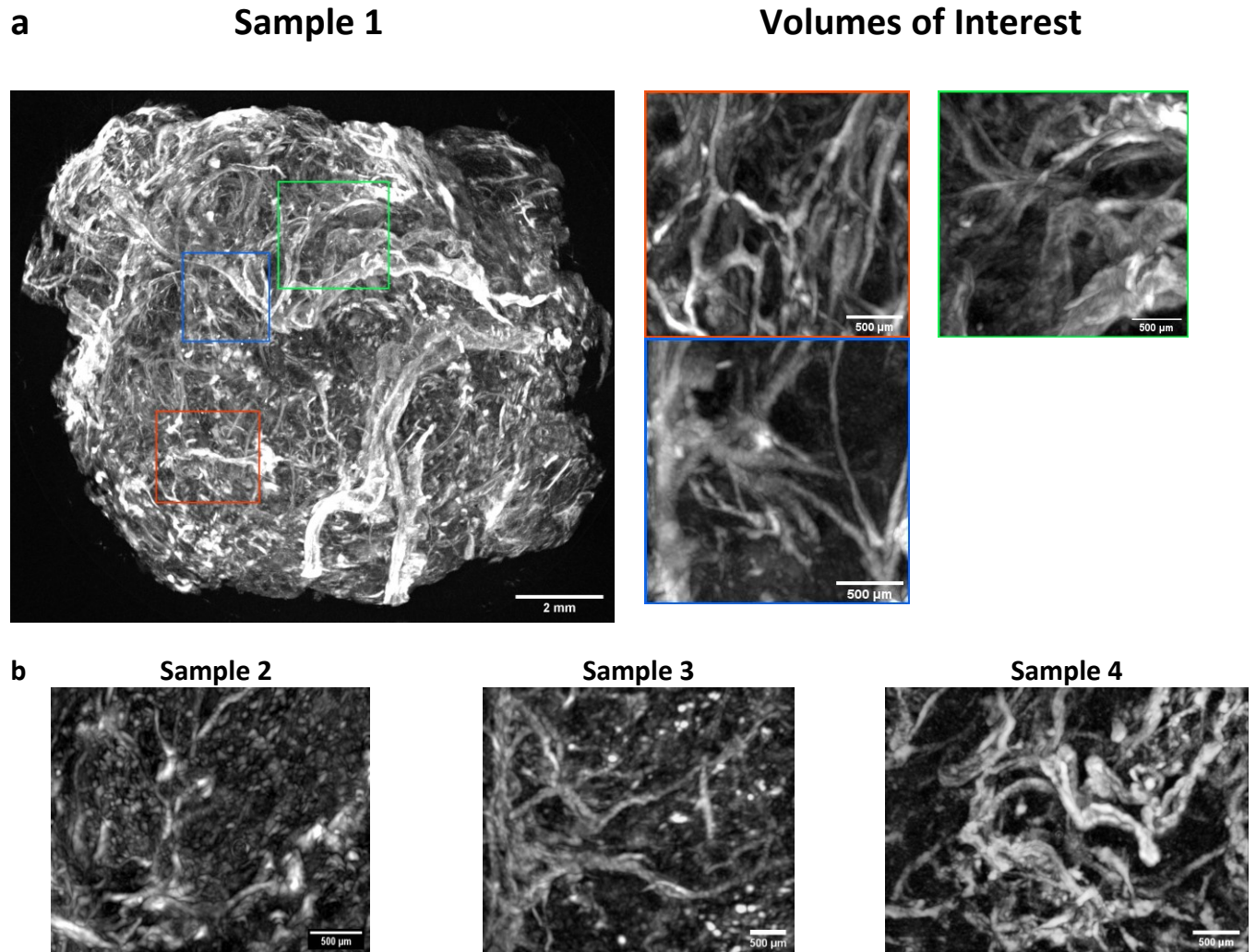
Figure 5.16: (a) MIP of tumour sample 1 (left) showing highlighted boxes that represent volumes of interest chosen. MIP of volumes of interest 1 (red), 2 (blue) and 3 (green) (right). (b) Volumes of interest in different tumour samples collected.

Boxplots of the CD34 density distribution are shown in figure 5.17 for different regions within the same tumour (Intratumoural) and in different tumour samples (Intertumoural). The CD34 density was found to be between 4 and 26% within the same tumour with the range varying between different regions. In Figure 5.17a, VOI 1 showed a larger range in CD34 density than the other VOIs. The variance was found to be highest in VOI 1 compared to other VOI suggesting a higher heterogeneity in CD34 distribution within VOI 1. Figure 5.17b shows a comparison between volumes of interest in different tumour samples. Negligible differences in the mean CD34 value were found between samples 2 and 3 which were obtained from the same patient. CD34 density was found be higher in sample 1 and the variance was found highest in this sample. Sample 4 exhibited a significantly lower mean CD34 density compared to other samples. The range of values obtained for CD34 density were consistent with other studies assessing CD34 density in different types of tumours [269, 270].

a
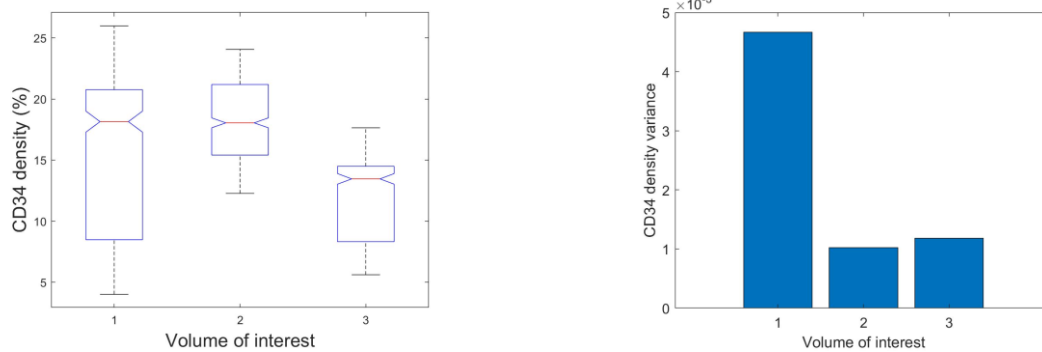
b
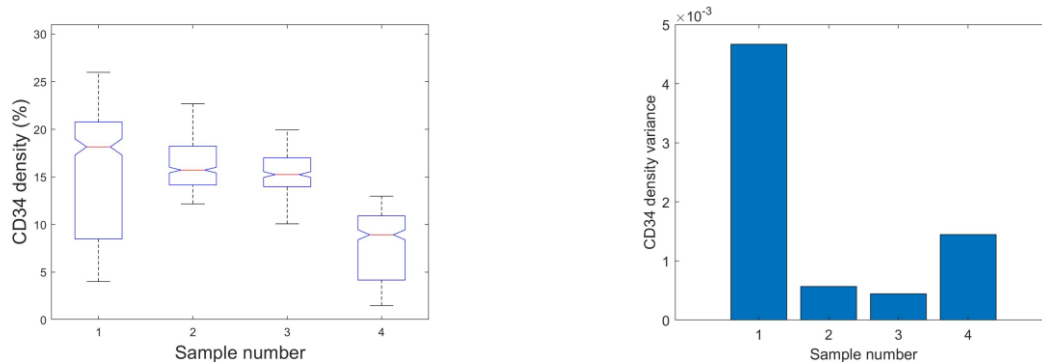
Figure 5.17: (a) CD34 density in different regions with the same tumour sample and (b) in different tumour samples (n=500).

The set of equations in table 5.2 were used to analyse the vasculature of tumours. Figure 5.18a shows boxplots of microvascular density (MVD) determined for different volumes of interest within the same tumour whilst Figure 5.18b shows the MVD for different tumour samples. The volumes were segmented into 100 sub volumes each containing 5 slices. The MVD was then calculated in each sub volume as described in table 5.2. The range of MVD values varies between the different regions, however VOI 1 and 2 exhibit large variance values, suggesting a more heterogeneous MVD distribution within these VOIs. The MVD values are in line with values obtained by Zhang et al. when assessing gastric tumours [135]. When comparing the MVD across the different tumour samples, variations were found where samples 2 and 3 obtained from the same patient had the highest mean MVD value, whilst sample 4 had significantly lower MVD values. Larger variances were found in the MVD of samples 1 and 2 suggesting greater heterogeneity in MVD across these samples.

a
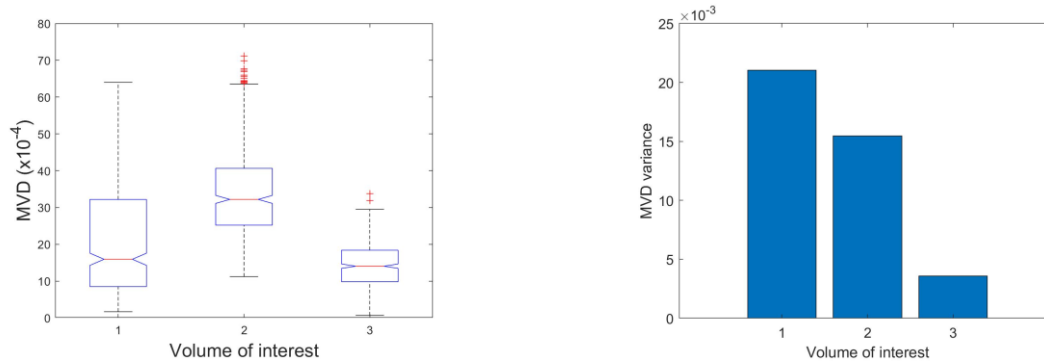
b
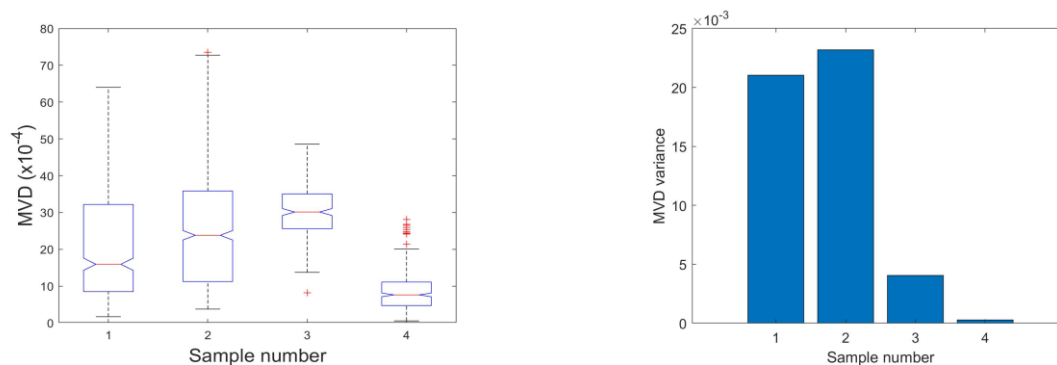
Figure 5.18: (a) MVD in different volume of interests within the same tumour and (b) across different tumour (n=100).

In the equation in table 5.2 the mean diameter for the entire tumour was calculated as an average using the total volume of the segmented mask and the total length of the skeleton. To obtain the diameter distribution in the tumour, an automated counting algorithm was employed to count objects in 3D. The diameter distribution of the vessels was determined using the mean distance from the objects center to its surface. The tumour tissue was found to exhibit a high degree of variability as seen in the diameter distribution shown in figure 5.19.
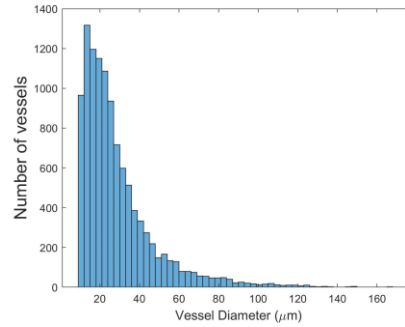
Figure 5.19: Vessel diameter distribution in tumour sample 1.

To assess the distribution of vessel diameters between different tumour regions and across different samples, the log values of the diameters are shown in the box plots in figure 5.20. The diameter range did not vary significantly between different regions within the same tumour; however, the plots show variability in diameters between different samples with sample 3 exhibiting larger average diameters.
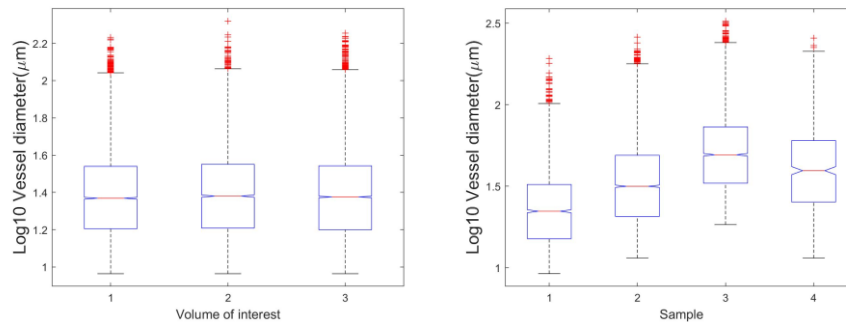
Figure 5.20: Vessel diameter boxplots for different tumour regions (center) and for different tumour samples (right).

The volumes of interest can used to extract skeleton networks which can be used as inputs for models to evaluate fluid flow and drug transport in solid tumours. The network presented in Figure 5.21 is extracted from volume 1 in sample1 which shows a well-connected network with minimal gaps highlighting the applicability of the imaging method in extracting vascular networks cleanly at high resolutions.
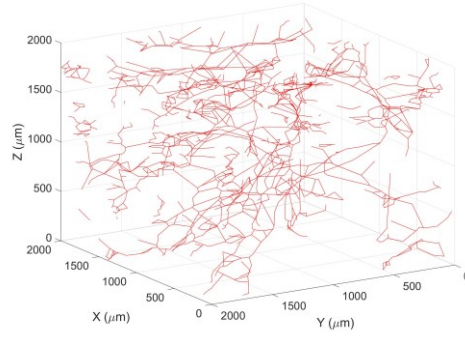
Figure 5.21: *Skeletonized network obtained from volume 1 in sample 1.*

Table 5.3 provides the mean values calculated for the geometrical properties of the tumour vasculature and a comparison with relevant data in the literature. Parameter values are widely available from animal studies, however given that the tumour vasculature can vary greatly between human and mouse, an attempt was made to prioritize data obtained from studies examining human tumours. When the corresponding human data is not available, values for mouse models are used for comparison. The parameters obtained from the OPT images correlated well with those found in literature using human samples. Vessel surface to volume and tissue volume areas were smaller than literature data obtained from mouse studies. Intuitively this is expected as the mouse vasculature is much denser whilst human vessels are larger, longer and sparse [271, 272].

Table 5.3 Averaged characteristic parameters calculated for the tumour vascular obtained from the different samples.

Sample number	1	2	3	4	Available literature data
MVD (x10^{-4})	20.60	25.04	30.26	12.90	4.1-20.72 [135](Mouse)
Vascular volume density (%)	12.87	14	13.08	5.8	5-15% [273] (Human)
Vessel diameter (μm)	48.83	50.74	68.13	75.60	5-366 [90] (Human)
Mean vessel cross section area (μm^2)	1872.55	2021.69	3645.85	4488.59	400-2300 [90] (Human)
Length density (mm^{-2})	68.73	76.05	35.69	19.92	10-140 [274, 275](Human)
Maximum extravascular diffusion distance (μm)	68.06	64.70	94.44	126.41	10-630 [90] (Human)
Vessel surface area per unit tissue volume (mm^{-1})	12.046	15.018	9.814	4.815	15-95 [87](Mouse)
Vessel surface to volume ratio (mm^{-1})	93.598	106.529	75.424	82.431	122-376 [93] (Mouse)
Tortuosity	1.26±0.33	1.28±0.35	1.27±0.33	1.28±0.42	1.12-1.27 [276] (Human)

5.4   Summary

This chapter focuses on assessing the feasibility of imaging the vasculature in whole tumours on the order of cm scale at microscopic resolutions. Most imaging methods are only applicable to animal models, but mice exhibit different response to tumour transplantation which can influence their sensitivity to angiogenesis. Hence, human tumour samples extracted from patients should be studied to gain more insights into the vasculature and angiogenesis in different types of tumours.

Histocutter - an automated histology-based imaging method - was tested for the first time on tumour tissues in a hope to understand whether this imaging system could be used to extract tumour vasculature. Histocutter has been previously used to image bone, cartilage, and whole mouse eyes. The results show that although some vascular structures could be extracted, the single quality and strength were highly variable with the derived CD34 density being significantly lower than expected across different samples. Slight misalignments in the stacks were observed using a y-axis projection as shown in figure 5.12 which adds to the difficulty in segmentation of the vasculature. In order to limit image distortion, fluorescence from deeper parts of the tissue must be blocked out. The tissue infiltration and embedding protocol used to achieve this requires the tissue to be exposed to high temperature for long periods of time which can distort the morphology of the vasculature and visibly shrink the size of the tumour. Even when the embedding protocol is applied, vessels with high fluorescence signals can emit light from deeper parts of the block and distort the Z-stack image and alignment. The imaging system was found to have limited use in acquiring consistent, good quality data on microvasculature in a whole tumour.

OPT, a relatively new imaging method was pursued. The system is able to image tumours as large as 15 mm which is much larger compared to the Histocutter employed in this study. The clearing method required for OPT is not as harsh as the embedding method used in Histocutter, thereby limiting any potential distortion of the tissue. This is crucial given that the architecture of the vasculature is of interest. Additionally, the technique is non-intrusive, and samples can be fully preserved after image acquisition. It has recently been demonstrated that tissue samples can be cleared and re-embedded in paraffin for histology [276]. The resolutions that can be achieved using this imaging modality are dependent on the size of the sample and can be on the order of several microns.

Using the OPT system developed by a team in Physics (Imperial College London) for different applications, high resolution images of human tumour samples up to 12 mm in size were obtained. These acquired images were processed for segmentation of the vasculature and extraction of key parameters. These

parameters included CD34 density, MVD density, vascular volume density, average diameters, cross-sectional area, vascular to volume ratio and tortuosity. The derived parameters were within the range of available data found in the literature. CD34 density and MVD were found to vary both intratumourally and intertumourally. Assessment of the distribution of vessel diameters showed no significant difference intratumourally, however, differences were found across the tumour samples. The results obtained with the OPT system show great promise and warranty further application of the imaging technique along with the developed protocol to a large tumour sample size with the view of correlating vascular features and CD34 density to prognosis and treatment outcomes. More efforts are needed on developing robust segmentation methods for tumour vasculature from fluorescently labelled images, as demonstrated in recent studies [277, 278]. This would allow extraction of 3D vascular structure and its network in whole human tumour samples, which can be used as an input for model geometry in the fluid flow and drug transport model discussed in Chapters 3 & 4.

6 Conclusions and future work

In this chapter the main conclusions from the work described in this thesis are presented. A critical analysis of the methodology is performed, and their limitations are discussed. Finally, recommendations for future work are given.

6.1 General conclusions

The vasculature in tumours has been shown to be aberrant, tortuous and erratic which can have significant implications for fluid flow, drug transport and tumour aggressiveness. Within this work a mathematical modelling framework has been developed to investigate the role of tumour microvasculature on fluid flow and drug transport. Furthermore, two novel imaging techniques, Histocutter and OPT, have been tested for their capability of imaging the 3D vasculature at high resolutions in human tumour samples with sizes on the order of centimetres. In what follows the main findings of each chapter are summarised, and their implications are discussed.

6.1.1 Fluid flow in solid tumours

Fluid dynamics in tumour tissue needs to be understood as it plays a key role in tumour growth, metastasis and the delivery of therapeutics. Previous studies investigating fluid flow assumed the vasculature to be uniformly distributed without incorporating its explicit architecture. Other models that incorporated the distribution of the vasculature applied homogenization methods without accounting for real geometric features of the network. Furthermore, previous fluid flow models treated intravascular flow and interstitial flow in a decoupled manner, so that the effect of transvascular leakage on blood flow was not captured. The work described in chapter 3 addresses these issues by employing the fluid flow model developed by Pozikridis for a single capillary and extending this model to a large scale vascular network. The 2D angiogenesis model developed by Anderson and Chaplain has been implemented in 3D to generate complex vascular networks that capture several abnormalities of the tumour vasculature including blind ends, excessive branching, loops and arteriovenous shunts. By applying fluid flow based boundary conditions on the vessel wall and integrating the pressure over the vessel surface, explicit morphological features of the vasculature including each vessel's orientation, radius and length can be incorporated. The model enables a strong coupling between intravascular and interstitial flow with intravascular and interstitial pressures being resolved at the surface of the vessel, thereby providing a more accurate

description of transvascular flux. Furthermore, a new model has been developed which allows vessel permeability to vary depending on their maturity and local shear stress. The results demonstrate that the coupled angiogenesis and fluid flow model is able to capture the morphological and hemodynamic properties measured in real tumours. Important results and findings obtained with the model are summarized below.

1. Distributions of IFP on vessel surface and transvascular flux are heterogeneous with higher pressures and lower transvascular flux at the tumour center compared to the periphery. The Green's function-based method applied in this study is able to predict IFP at the outer surface of individual vessels, allowing for more accurate estimations of IFP and transvascular flux whilst reducing the computational demand.

2. Simulations of flow in different vascular geometries reveal the strong coupling and interplay between intravascular and interstitial flow. Whilst previous studies treating the vasculature as a uniformly distributed source term found IFP to be uniformly elevated across the tumour, simulations using the coupled model developed in this work show that heterogeneous vascular distribution can result in non-uniformly elevated IFP, leading to non-uniform transvascular pressure gradients. As an important step in drug delivery, penetration of the drug through the vessel walls into the interstitial space is governed by the transmural pressure, hence heterogeneous transvascular pressure gradients can exacerbate the non-uniformity of drug accumulation in tumour tissue, resulting in low or no drug exposure in some regions.

3. Analysis of flow in vascular networks with varying degrees of central necrosis reveal a dip in IFP within the tumour core where the extent of heterogeneity in IFP distribution increases with the degree of central necrosis. The presence of a necrotic core in tumours is common and has been associated with poor prognosis [279, 280]. Results obtained in this work suggest that the inward convective flux caused by pressure gradients in necrotic tumours can promote transport of therapeutic molecules towards the central region which is hypoxic and contains dead cells. This will reduce the availability of the drug to target actively proliferating cancer cells.

4. Subtle changes in the vascular network by removing blind ends and incorporating arterio-venous shunts to open flow pathways result in pronounced increase in blood flow rate and a reduction in

IFP. This highlights that although vascular networks may appear almost identical from a macroscopic point of view as determined by their vascular density and microvascular distribution, small differences on a microscopic scale can result in dramatically altered flow properties.

5. The incorporation of varying vascular permeability based on vessel maturity and local flow conditions using experimentally determined vessel pore sizes can result in significantly higher IFP values and more heterogeneous IFP distribution with larger gradients than originally predicted.

6.1.2 Drug transport in solid tumours

The spatial and temporal distributions of doxorubicin in tumour tissues are examined in Chapter 4. Fluid flow in tumours and the vascular architecture are important factors in determining the transport of intravenously injected therapeutics. Previous studies investigating the effectiveness of anticancer drugs mostly adopted PK compartmental models where the vasculature and tissue space were assumed to form compartments and drug concentration was averaged within each compartment. Other models that addressed the spatial distribution of chemotherapy drugs often neglect the heterogeneity of tumour vasculature and intravascular flow. Given the complexity of tumour tissues and vascular heterogeneity on a microscopic scale, steep gradients in drug concentration can occur on a spatial step of several microns. To address this challenge, the angiogenesis and fluid flow models developed in Chapter 3 have been coupled with a solute transport model to describe the spatial distribution of Doxorubicin within the microvessels, the interstitial space and its uptake by cells on a microscopic scale. The main findings and implications from this work are discussed as follows:

1. Drug distribution within the vascular network varies as a function of intravascular blood flowrate which in turn is a function of the microscopic features of the tumour vascular network. Regions near well perfused vessels experience high extracellular drug concentration which rapidly decays with the distance from the vessel due to diffusion limitation and high intracellular uptake.

2. Analysis of drug distributions in different vascular networks show that regions with equivalent microvascular densities exhibit significant differences in extracellular and intracellular concentrations due to differences in perfusion and intravascular flowrate, highlighting the importance of incorporating microscopic vascular properties and fluid dynamics when evaluating the effectiveness of chemotherapy drugs. The presence of blind ends, highly tortuous vessels and variations in blood vessel radius in tumours act together to reduce blood flow along some

pathways within the network, thereby limiting the delivery of the drug to these regions of the tumour tissue.

3. Increasing drug dose reduces the heterogeneity in drug distribution in high MVD tumours. However, the same effect is not observed in tumours with a low MVD and large extravascular diffusion distance, where the effect of high dose is only to increase the level of plasma concentration which would lead to an increased risk of cardiotoxicity.

4. Comparison of bolus injection and continuous infusion suggests that the latter helps to increase the peak intracellular concentration for infusion duration up to a certain point, with a 60-minute infusion time producing the highest peak intracellular concentration. Further increase in infusion duration causes the peak intracellular concentration to decrease, and a continuous infusion over 200-minute results in concentrations lower than that with a bolus injection. The intracellular AUC over the domain shows higher values in regions near well perfused vessels with longer infusion duration. However, the heterogeneity in AUC also increases as the infusion increased.

6.1.3   Imaging the 3D vasculature in whole human tumour tissues

In Chapter 5, two different imaging techniques are applied to human ovarian tumour samples in order to assess their ability to acquire images that can be used to visualise and extract the 3D vasculature from whole tumours on the order of cm. Whilst most imaging methods focus on animal models, the aim of chapter 5 is to explore methods that are able to image the vasculature in human tumours with high fidelity which can provide great insight into the morphology of the tumour vasculature and angiogenesis as the structure of the tissue is completely preserved. The tissue preparation protocol has been optimized for staining of wholes tissues on the order of mm to produce uniform signals across the tumour tissue. The Histocutter, an automated histology-based imaging set up, has been used to obtain a series of 2D images from which a 3D image of the tumour can be reconstructed. Although the Histocutter has shown considerable success in imaging hard tissues, it appears to have limited success when imaging soft tissues. The Histocutter uses a view and cut approach where the surface of the block is imaged after each cut to produce a series of 2D images. To exclusively image the surface of the block and block out light from deeper parts that could distort the 3D image, light absorbing Sudan dyes are mixed with the embedding medium. To ensure that the embedding medium is well mixed, high temperatures are required which can be harsh on soft tissues causing major shrinkage and distortion of the sample. Small distortions have also been observed in the alignment of the stacks and although this does not significantly affect the image of large structures, small vessels can become difficult to segment and extract. Another imaging method,

Optical projection tomography (OPT), has been investigated which offers the advantage of being applicable to larger samples on the order of cm whilst still maintaining high resolutions on the order of µm. The results show that OPT is able to produce high resolution images of the tumour vasculature which can be enhanced using image processing methods. Parameters that are often used to quantify angiogenesis, such as CD34 density and MVD, have been extracted on the whole tumour scale. The derived parameters are consistent with data extracted from relevant tumour studies. Images acquired with OPT can be used to quantify geometric properties of the tumour vasculature including vessel diameters, vessel surface area to tissue volume, length density and extravascular diffusion distance.

The ability to image whole tumours on the order of centimetre with a high resolution on the micron scale in human tumour samples has not been previously demonstrated. The potential impact of this work is significant as quantifying angiogenic parameters on the whole tumour scale will reduce errors introduced using standard 2D image-based angiogenesis assessment techniques which only consider a small patch of tissue or a representative volume. As tumour tissues are extremely complex and heterogeneous, traditional 2D microscopy may not be able to capture the true heterogeneity. High resolution 3D methods overcome this limitation by providing a whole picture of the tumour which can be applied to optimize treatment methods and improve diagnostics.

6.2   Limitations of current work

6.2.1   Tumour geometry model

The angiogenesis model used to describe the tumour vasculature in chapters 3 and 4 does well to capture the heterogeneous properties of the vasculature and incorporates various aspects of the angiogenesis process. In the model, the tumour is assumed to be of a fixed size and the effect of tumour growth during angiogenesis is neglected. This can be justified as the time scale on which tumour growth occurs is much larger than that of vascular growth. However, changes in oxygen concentration and gradients caused by vascular remodelling were not incorporated which can influence the distribution of chemical species secreted which would in turn influence the angiogenic process and vascular network generated. Mechanical forces such as solid stress induced by the growing tumour can affect the movement of endothelial cells which has not been incorporated in the angiogenesis model [73]. The stress caused by proliferating cancer cells can compress and shut down the function of some vessels. These factors could

influence the spatial arrangement and orientation of the vascular networks produced [41]. These limitations were not addressed in the current study so as to keep the model computationally tractable.

6.2.2   Fluid Flow model

In chapter 3 where fluid flow in the vascular geometry and tumour tissue was analysed, blood was modelled as a continuum Newtonian fluid with a constant viscosity. Blood is in fact a non-Newtonian fluid composed of multiple cellular components such as red blood cells, white bloods cells and platelets. In small capillaries the influence of these components can be significant. Spatial and time variations in these components can results in variable viscosity within the vessel network. Phase separation in bifurcations can occur in tumour vasculature where the haematocrit level can be higher in one branch than the others, results in different blood viscosities in different vessel segments. Additionally, the response of vessel diameter to changes in transmural pressure and metabolic stimuli has been neglected. Current models that incorporate these changes are developed using data obtained from vessel networks in normal tissues [169, 281]. Tumours exhibit a different functional behaviour and would be expected to respond differently. When considering interstitial flow, the tissue was assumed to be composed of a homogenous porous medium made up of cancer cells and extracellular matrix. In reality, tumour tissue can be heterogeneous with varying porosity and interstitial hydraulic conductivity which consequently affect fluid flow. Studies have been performed assessing the role of heterogeneous tissue characteristics on fluid flow and solute transport within the tissue. Incorporating this in tumours on a large scale will raise the computational demand of the simulation significantly. The present study was focused on investigating the role of heterogeneous tumour vasculature alone, so that heterogeneity in tissue properties has been ignored. Nevertheless, further research can be built on this model and to incorporate tissue heterogeneity as computation power increases. In tumours, lymphatic function is poor which combined with the lack of models addressing the formation and development of lymph vessels has not been included in the present study.

6.2.3   Drug transport model

In chapter 4 when modelling drug transport, the effect of binding was not incorporated however for doxorubicin this can be easily achieved given that binding is non saturable. The uptake of the drug by the cells affects its distribution and ability to penetrate the tissue. Whilst cancer cells were assumed to be uniformly distributed, the reality of heterogeneous cell distribution can lead to variable results from case

to case. Additionally, the uptake and efflux were modelled as a function of passive diffusion using data obtained for non-small cell lung carcinomas that were selected not to be resistant. For cancer cells with developed resistance the efflux through active transport by P-glycoprotein (P-gp) and/or by multidrug resistance protein (MRP1) needs to be considered. Whilst in chapter 3, it was possible to model large volume tumours, the time-dependent nature of drug transport substantially increases the computational demand, thereby restricting the size of tissue and vessels to be examined. However, provided enough time and computational power this can be achieved.

6.2.4 Tumour imaging

In chapter 5, the feasibility of analysing and assessing angiogenesis parameters on the whole tumour scale was explored. The tumour sample size was limited, and normal tissue samples should have been tested for reference when analysing the role of CD34 density and MVD in tumour tissue. The segmentation of the vasculature presents another problem. Manual segmentation is not feasible for large data sets as in our case. Whilst a large number of automated vascular segmentation algorithms have been developed, they are most applicable to angiography imaging techniques using modalities such as MRI and CT/µCT [260]. In these methods blood pool contrast agents are used to label the vessel lumen, the vessels then appear as a set of solid tubes which can be segmented and its centreline easily extracted using established methods [282]. In our case the vessels' laminae are labelled using molecular techniques which can result in uneven staining, low contrast, gaps on the vessel surface and autofluorescence. In addition, the vessels can appear as hollow tubes for which there are a limited number to segment and extract the vessel centreline. In this work large hollow vessels can be seen as multiple vessels when employing the skeletonization algorithm, resulting in some errors in the extraction of vessels centreline.

6.3 Perspectives for future work

It is evident that tumour microvascular properties have a significant influence on fluid flow and drug transport in solid tumours. The aim of computational based biological studies is to aid and complement experiment-based methods in tackling cancer. The advantage of these methods is that various aspects of the biology of tumours can be incorporated. Several promising directions can be followed based on the work of this thesis.

6.3.1 Oxygen transport

Hypoxia plays an important role in tumour development and resistance of cells to radiotherapy and chemotherapy [283, 284]. The transport and distribution of oxygen in tumours can be studied using the models applied in chapters 3 and 4. As described from the findings in this work, the assumption of drug distribution within the tissue being simply limited to the distance from the vessels is an oversimplification. Subtle features and changes in the vasculature can result in drastic differences in blood flow which consequently affects oxygen transport. Chemotherapeutics act by inhibiting DNA replication; therefore, as cells in poorly oxygenated regions are proliferating at slower rates, the effectiveness of chemotherapeutics is likely to be limited in these regions. Coupling oxygen transport with the transport of chemotherapeutics can provide better insight into their effectiveness.

6.3.2 Incorporate simulation of liposomes and nanoparticles in tumour tissues

Liposomes and nanoparticles provide an effective means to transport chemotherapeutics by reducing clearance and cardiotoxicity by targeting the pores sizes of the tumour vasculature through the enhanced permeability and retention effect (EPR) [285] [286]. The models used in chapters 3 and 4 can be readily applied to simulate the transport of these nanoparticles. Drug release from the liposomes can be incorporated as a source term provided that the data on drug release rate is available. The effect of heating on liposomal delivery release can also be investigated and can be used to complement experimental studies on liposome and thermosensitive liposome uptake in tumours, providing a microscopic view of their performance.

6.3.3 Incorporate real imaged vasculature into fluid flow and drug transport studies

The imaged vasculature from ovarian tumours presented in Chapter 5 can be segmented and a spatial graph can be generated from it as shown in figure 5.21. This network can be used as an input for the vascular geometry in the fluid flow and drug transport models applied in chapters 3 and 4 to understand the consequence of the vasculature on fluid flow and drug transport in real cases. The future works suggested above can also be applied using this vascular geometry to assess hypoxia and the performance of various treatment strategies in realistic tumour vasculature.

6.3.4 Assessing the prognostic value of angiogenesis in ovarian tumours

As discussed in chapter 2, angiogenesis plays a role in tumour growth, invasion and promoting its ability to limit the transport and distribution of anticancer therapeutics. Angiogenesis has been shown to be a strong prognostic factor in different types of tumours [287, 288]. However, in ovarian tumours the prognostic significance of angiogenesis remains unresolved as a number of different studies have produced conflicting results. One of the limitations of these studies was the limited area over which angiogenesis was assessed and the use of methods that can introduce bias. The methodology developed in chapter 5 allows for angiogenesis to be assessed over large areas and the automated method used to segment and measure the distribution of CD34 and the vasculature can reduce potential bias associated with manual microvessel counting techniques.

6.3.5 Mapping of tumour microenvironment on the whole tumour scale and assessing influence of microvasculature on distribution various tumour cells

Tumours can be extremely complex with heterogeneous cell populations that exhibit distinct morphological and phenotypic profiles. This intratumoural heterogeneity has been well documented which can lead to an increase in the chances of therapeutic resistance [289]. Developing a 3D understanding of this heterogeneity can provide better understanding of both intratumoural and intertumoural heterogeneity. The OPT method applied in chapter 5 can be modified and built on to stain different types of cells which can be imaged using multichannel OPT, hence different cells can be imaged and the vasculature and its relationship to the heterogeneity of the different cell populations can be examined.

References

1. McGuire, S., *World cancer report 2014. Geneva, Switzerland: World Health Organization, international agency for research on cancer, WHO Press, 2015*. 2016, Oxford University Press.
2. Varmus, H., *The new era in cancer research.* Science, 2006. **312**(5777): p. 1162-1165.
3. Jain, R.K. and T. Stylianopoulos, *Delivering nanomedicine to solid tumors.* Nature reviews Clinical oncology, 2010. **7**(11): p. 653.
4. Goh, Y.-M.F., H.L. Kong, and C.-H. Wang, *Simulation of the delivery of doxorubicin to hepatoma.* Pharmaceutical Research, 2001. **18**(6): p. 761-770.
5. Jain, R.K., *Barriers to drug delivery in solid tumors.* Scientific American, 1994. **271**(1): p. 58-65.
6. Rockwell, S., et al., *Hypoxia and radiation therapy: past history, ongoing research, and future promise.* Current molecular medicine, 2009. **9**(4): p. 442-458.
7. Huang, C.-Y., et al., *A review on the effects of current chemotherapy drugs and natural agents in treating non–small cell lung cancer.* Biomedicine, 2017. **7**(4).
8. Hanahan, D. and R.A. Weinberg, *The hallmarks of cancer.* cell, 2000. **100**(1): p. 57-70.
9. Kalluri, R., *The biology and function of fibroblasts in cancer.* Nature Reviews Cancer, 2016. **16**(9): p. 582.
10. Egeblad, M., E.S. Nakasone, and Z. Werb, *Tumors as organs: complex tissues that interface with the entire organism.* Developmental cell, 2010. **18**(6): p. 884-901.
11. Tannock, I.F., *Tumor physiology and drug resistance.* Cancer and Metastasis Reviews, 2001. **20**(1-2): p. 123-132.
12. Trédan, O., et al., *Drug resistance and the solid tumor microenvironment.* Journal of the National Cancer Institute, 2007. **99**(19): p. 1441-1454.
13. Jang, S.H., et al., *Drug delivery and transport to solid tumors.* Pharmaceutical research, 2003. **20**(9): p. 1337-1350.
14. Kerbel, R.S., *Tumor angiogenesis: past, present and the near future.* Carcinogenesis, 2000. **21**(3): p. 505-515.
15. Carmeliet, P., *Angiogenesis in life, disease and medicine.* Nature, 2005. **438**(7070): p. 932.
16. Bergers, G. and L.E. Benjamin, *Angiogenesis: tumorigenesis and the angiogenic switch.* Nature reviews cancer, 2003. **3**(6): p. 401.
17. Carmeliet, P. and R.K. Jain, *Angiogenesis in cancer and other diseases.* nature, 2000. **407**(6801): p. 249.
18. Liao, D. and R.S. Johnson, *Hypoxia: a key regulator of angiogenesis in cancer.* Cancer and Metastasis Reviews, 2007. **26**(2): p. 281-290.
19. Gavalas, N.G., et al., *Angiogenesis-related pathways in the pathogenesis of ovarian cancer.* International journal of molecular sciences, 2013. **14**(8): p. 15885-15909.
20. Folkman, J., *Opinion: Angiogenesis: an organizing principle for drug discovery?* Nature reviews Drug discovery, 2007. **6**(4): p. 273.
21. Ribatti, D. and E. Crivellato, *"Sprouting angiogenesis", a reappraisal.* Developmental biology, 2012. **372**(2): p. 157-165.
22. Nagy, J.A., et al. *Heterogeneity of the tumor vasculature*. in *Seminars in thrombosis and hemostasis*. 2010. © Thieme Medical Publishers.
23. Baluk, P., H. Hashizume, and D.M. McDonald, *Cellular abnormalities of blood vessels as targets in cancer.* Current opinion in genetics & development, 2005. **15**(1): p. 102-111.
24. McDonald, D.M. and A.J. Foss, *Endothelial cells of tumor vessels: abnormal but not absent.* Cancer and Metastasis Reviews, 2000. **19**(1-2): p. 109-120.
25. Carmeliet, P. and R.K. Jain, *Principles and mechanisms of vessel normalization for cancer and other angiogenic diseases.* Nature reviews Drug discovery, 2011. **10**(6): p. 417.

26. Morikawa, S., et al., *Abnormalities in pericytes on blood vessels and endothelial sprouts in tumors.* The American journal of pathology, 2002. **160**(3): p. 985-1000.

27. Baluk, P., et al., *Abnormalities of basement membrane on blood vessels and endothelial sprouts in tumors.* The American journal of pathology, 2003. **163**(5): p. 1801-1815.

28. Hashizume, H., et al., *Openings between defective endothelial cells explain tumor vessel leakiness.* The American journal of pathology, 2000. **156**(4): p. 1363-1380.

29. McDonald, D.M. and P. Baluk, *Significance of blood vessel leakiness in cancer*. 2002, AACR.

30. Gerlowski, L.E. and R.K. Jain, *Microvascular permeability of normal and neoplastic tissues.* Microvascular research, 1986. **31**(3): p. 288-305.

31. Yuan, F., et al., *Vascular permeability and microcirculation of gliomas and mammary carcinomas transplanted in rat and mouse cranial windows.* Cancer research, 1994. **54**(17): p. 4564-4568.

32. Yuan, F., et al., *Vascular permeability in a human tumor xenograft: molecular size dependence and cutoff size.* Cancer research, 1995. **55**(17): p. 3752-3756.

33. Bjørnæs, I. and E.K. Rofstad, *Microvascular permeability to macromolecules in human melanoma xenografts assessed by contrast-enhanced MRI—intertumor and intratumor heterogeneity.* Magnetic resonance imaging, 2001. **19**(5): p. 723-730.

34. Skinner, S.A., P.J. Tutton, and P.E. O'Brien, *Microvascular architecture of experimental colon tumors in the rat.* Cancer research, 1990. **50**(8): p. 2411-2417.

35. Jain, R.K., *Molecular regulation of vessel maturation.* Nature medicine, 2003. **9**(6): p. 685.

36. Less, J.R., et al., *Microvascular architecture in a mammary carcinoma: branching patterns and vessel dimensions.* Cancer research, 1991. **51**(1): p. 265-273.

37. Groebe, K. and P. Vaupel, *Evaluation of oxygen diffusion distances in human breast cancer xenografts using tumor-specific in vivo data: role of various mechanisms in the development of tumor hypoxia.* International Journal of Radiation Oncology* Biology* Physics, 1988. **15**(3): p. 691-697.

38. Konerding, M., et al., *Evidence for characteristic vascular patterns in solid tumours: quantitative studies using corrosion casts.* British journal of cancer, 1999. **80**(5-6): p. 724.

39. Weiss, L., E. Tveit, and R. Hultborn, *Vascular resistance characteristics of 7, 12-dimethylbenz (a) anthracene-induced rat mammary tumors and normal tissues as studied in vitro.* Cancer research, 1985. **45**(6): p. 2478-2480.

40. Less, J.R., et al., *Geometric resistance and microvascular network architecture of human colorectal carcinoma.* Microcirculation, 1997. **4**(1): p. 25-33.

41. Jain, R.K., J.D. Martin, and T. Stylianopoulos, *The role of mechanical forces in tumor growth and therapy.* Annual review of biomedical engineering, 2014. **16**: p. 321-346.

42. Sensky, P., et al., *Resistance to flow through tissue-isolated transplanted rat tumours located in two different sites.* British journal of cancer, 1993. **67**(6): p. 1337.

43. Sevick, E.M. and R.K. Jain, *Viscous resistance to blood flow in solid tumors: effect of hematocrit on intratumor blood viscosity.* Cancer research, 1989. **49**(13): p. 3513-3519.

44. Jain, R.K., *Determinants of tumor blood flow: a review.* Cancer research, 1988. **48**(10): p. 2641-2658.

45. Kimura, H., et al., *Fluctuations in red cell flux in tumor microvessels can lead to transient hypoxia and reoxygenation in tumor parenchyma.* Cancer research, 1996. **56**(23): p. 5522-5528.

46. Pries, A.R., et al., *The shunt problem: control of functional shunting in normal and tumour vasculature.* Nature Reviews Cancer, 2010. **10**(8): p. 587.

47. Kesler, C.T., et al., *Lymphatic vessels in health and disease.* Wiley Interdisciplinary Reviews: Systems Biology and Medicine, 2013. **5**(1): p. 111-124.

48. Padera, T.P., et al., *Pathology: cancer cells compress intratumour vessels.* Nature, 2004. **427**(6976): p. 695.

49. Isaka, N., et al., *Peritumor lymphatics induced by vascular endothelial growth factor-C exhibit abnormal function.* Cancer research, 2004. **64**(13): p. 4400-4404.

50. Ji, R.-C., *Lymphatic endothelial cells, tumor lymphangiogenesis and metastasis: New insights into intratumoral and peritumoral lymphatics.* Cancer and Metastasis Reviews, 2006. **25**(4): p. 677-694.

51. Sevick, E.M. and R.K. Jain, *Measurement of capillary filtration coefficient in a solid tumor.* Cancer research, 1991. **51**(4): p. 1352-1355.

52. Less, J.R., et al., *Interstitial hypertension in human breast and colorectal tumors.* Cancer research, 1992. **52**(22): p. 6371-6374.

53. Gutmann, R., et al., *Interstitial hypertension in head and neck tumors in patients: correlation with tumor size.* Cancer research, 1992. **52**(7): p. 1993-1995.

54. Boucher, Y., L.T. Baxter, and R.K. Jain, *Interstitial pressure gradients in tissue-isolated and subcutaneous tumors: implications for therapy.* Cancer research, 1990. **50**(15): p. 4478-4484.

55. Heldin, C.-H., et al., *High interstitial fluid pressure—an obstacle in cancer therapy.* Nature Reviews Cancer, 2004. **4**(10): p. 806-813.

56. Stohrer, M., et al., *Oncotic pressure in solid tumors is elevated.* Cancer research, 2000. **60**(15): p. 4251-4255.

57. Boucher, Y. and R.K. Jain, *Microvascular pressure is the principal driving force for interstitial hypertension in solid tumors: implications for vascular collapse.* Cancer research, 1992. **52**(18): p. 5110-5114.

58. Hacker, M.P. and G. Powis, *The toxicity of anticancer drugs*. 1991: Pergamon Press.

59. Jain, R.K., *Transport of molecules across tumor vasculature.* Cancer and Metastasis Reviews, 1987. **6**(4): p. 559-593.

60. Szachowicz-Petelska, B., Z. Figaszewski, and W. Lewandowski, *Mechanisms of transport across cell membranes of complexes contained in antitumour drugs.* International journal of pharmaceutics, 2001. **222**(2): p. 169-182.

61. Jain, R.K., *Vascular and interstitial barriers to delivery of therapeutic agents in tumors.* Cancer and Metastasis Reviews, 1990. **9**(3): p. 253-266.

62. Jain, R.K., *Transport of molecules, particles, and cells in solid tumors.* Annual review of biomedical engineering, 1999. **1**(1): p. 241-263.

63. Baxter, L.T. and R.K. Jain, *Transport of fluid and macromolecules in tumors. I. Role of interstitial pressure and convection.* Microvascular research, 1989. **37**(1): p. 77-104.

64. Netti, P.A., et al., *Role of extracellular matrix assembly in interstitial transport in solid tumors.* Cancer research, 2000. **60**(9): p. 2497-2503.

65. Grantab, R.H. and I.F. Tannock, *Penetration of anticancer drugs through tumour tissue as a function of cellular packing density and interstitial fluid pressure and its modification by bortezomib.* BMC cancer, 2012. **12**(1): p. 214.

66. Folkman, J., *The influence of angiogenesis research on management of patients with breast cancer.* Breast cancer research and treatment, 1995. **36**(2): p. 109-118.

67. Holmgren, L., M.S. O'Reilly, and J. Folkman, *Dormancy of micrometastases: balanced proliferation and apoptosis in the presence of angiogenesis suppression.* Nature medicine, 1995. **1**(2): p. 149.

68. Zhao, Y. and A.A. Adjei, *Targeting angiogenesis in cancer therapy: moving beyond vascular endothelial growth factor.* The oncologist, 2015. **20**(6): p. 660-673.

69. Scianna, M., C. Bell, and L. Preziosi, *A review of mathematical models for the formation of vascular networks.* Journal of theoretical biology, 2013. **333**: p. 174-209.

70. Balding, D. and D. McElwain, *A mathematical model of tumour-induced capillary growth.* Journal of theoretical biology, 1985. **114**(1): p. 53-73.

71.   Chaplain, M.A., et al., *A mathematical analysis of a model for tumour angiogenesis.* Journal of mathematical biology, 1995. **33**(7): p. 744-770.

72.   Anderson, A.R. and M. Chaplain, *Continuous and discrete mathematical models of tumor-induced angiogenesis.* Bulletin of mathematical biology, 1998. **60**(5): p. 857-899.

73.   Welter, M. and H. Rieger, *Physical determinants of vascular network remodeling during tumor growth.* The European Physical Journal E, 2010. **33**(2): p. 149-163.

74.   Vavourakis, V., et al., *A validated multiscale in-silico model for mechano-sensitive tumour angiogenesis and growth.* PLoS computational biology, 2017. **13**(1): p. e1005259.

75.   Haenssgen, K., A.N. Makanya, and V. Djonov, *Casting materials and their application in research and teaching.* Microscopy and microanalysis, 2014. **20**(2): p. 493-513.

76.   Konerding, M., A. Miodonski, and A. Lametschwandtner, *Microvascular corrosion casting in the study of tumor vascularity: a review.* Scanning microscopy, 1995. **9**(4): p. 1233-43; discussion 1243-4.

77.   Verli, F.D., et al., *Vascular corrosion casting technique steps.* Scanning: The Journal of Scanning Microscopies, 2007. **29**(3): p. 128-132.

78.   Miettinen, M., A.E. Lindenmayer, and A. Chaubal, *Endothelial cell markers CD31, CD34, and BNH9 antibody to H-and Y-antigens--evaluation of their specificity and sensitivity in the diagnosis of vascular tumors and comparison with von Willebrand factor.* Modern pathology: an official journal of the United States and Canadian Academy of Pathology, Inc, 1994. **7**(1): p. 82-90.

79.   Pusztaszeri, M.P., W. Seelentag, and F.T. Bosman, *Immunohistochemical expression of endothelial markers CD31, CD34, von Willebrand factor, and Fli-1 in normal human tissues.* Journal of Histochemistry & Cytochemistry, 2006. **54**(4): p. 385-395.

80.   Siemerink, M.J., et al., *CD34 marks angiogenic tip cells in human vascular endothelial cell cultures.* Angiogenesis, 2012. **15**(1): p. 151-163.

81.   McDonald, D.M. and P.L. Choyke, *Imaging of angiogenesis: from microscope to clinic.* Nature medicine, 2003. **9**(6): p. 713.

82.   Maniotis, A.J., et al., *Vascular channel formation by human melanoma cells in vivo and in vitro: vasculogenic mimicry.* The American journal of pathology, 1999. **155**(3): p. 739-752.

83.   Degani, H., et al., *Magnetic resonance imaging of tumor vasculature.* Thrombosis and Haemostasis, 2003. **89**(01): p. 25-33.

84.   Zhu, W., Y. Kato, and D. Artemov, *Heterogeneity of tumor vasculature and antiangiogenic intervention: insights from MR angiography and DCE-MRI.* PloS one, 2014. **9**(1): p. e86583.

85.   Jackson, A., et al., *Imaging tumor vascular heterogeneity and angiogenesis using dynamic contrast-enhanced magnetic resonance imaging.* Clinical Cancer Research, 2007. **13**(12): p. 3449-3459.

86.   Secomb, T.W., et al., *Analysis of oxygen transport to tumor tissue by microvascular networks.* International Journal of Radiation Oncology* Biology* Physics, 1993. **25**(3): p. 481-489.

87.   Reitan, N.K., et al., *Characterization of tumor microvascular structure and permeability: comparison between magnetic resonance imaging and intravital confocal imaging.* Journal of biomedical optics, 2010. **15**(3): p. 036004.

88.   Ameer-Beg, S., et al. *Application of multiphoton steady state and lifetime imaging to mapping of tumor vascular architecture in vivo*. in *Multiphoton Microscopy in the Biomedical Sciences II*. 2002. International Society for Optics and Photonics.

89.   Kim, E., et al., *Multiscale imaging and computational modeling of blood flow in the tumor vasculature.* Annals of biomedical engineering, 2012. **40**(11): p. 2425-2441.

90.   Folarin, A., et al., *Three-dimensional analysis of tumour vascular corrosion casts using stereoimaging and micro-computed tomography.* Microvascular research, 2010. **80**(1): p. 89-98.

91. Savai, R., et al., *Evaluation of angiogenesis using micro-computed tomography in a xenograft mouse model of lung cancer.* Neoplasia (New York, NY), 2009. **11**(1): p. 48.

92. Kim, E., et al., *Assessing breast cancer angiogenesis in vivo: which susceptibility contrast MRI biomarkers are relevant?* Magnetic resonance in medicine, 2013. **70**(4): p. 1106-1116.

93. Stamatelos, S.K., et al., *A bioimage informatics based reconstruction of breast tumor microvasculature with computational blood flow predictions.* Microvascular research, 2014. **91**: p. 8-21.

94. Downey, C.M., et al., *Quantitative ex-vivo micro-computed tomographic imaging of blood vessels and necrotic regions within tumors.* PloS one, 2012. **7**(7): p. e41685.

95. Kay, P.A., R.A. Robb, and D.G. Bostwick, *Prostate cancer microvessels: a novel method for three-dimensional reconstruction and analysis.* The Prostate, 1998. **37**(4): p. 270-277.

96. Brey, E.M., et al., *A technique for quantitative three-dimensional analysis of microvascular structure.* Microvascular research, 2002. **63**(3): p. 279-294.

97. Gijtenbeek, J.M., et al., *Three-dimensional reconstruction of tumor microvasculature: simultaneous visualization of multiple components in paraffin-embedded tissue.* Angiogenesis, 2006. **8**(4): p. 297.

98. Burgoyne, C.F., et al., *Three-dimensional reconstruction of normal and early glaucoma monkey optic nerve head connective tissues.* Investigative ophthalmology & visual science, 2004. **45**(12): p. 4388-4399.

99. Tang, J., et al., *Visual receptive field properties of neurons in the mouse lateral geniculate nucleus.* PloS one, 2016. **11**(1): p. e0146017.

100. Andrikakou, P., K. Vickraman, and H. Arora, *On the behaviour of lung tissue under tension and compression.* Scientific reports, 2016. **6**: p. 36642.

101. Sharpe, J., et al., *Optical projection tomography as a tool for 3D microscopy and gene expression studies.* Science, 2002. **296**(5567): p. 541-545.

102. Sharpe, J., *Optical projection tomography as a new tool for studying embryo anatomy.* Journal of anatomy, 2003. **202**(2): p. 175-181.

103. Bassi, A., et al., *In vivo label-free three-dimensional imaging of zebrafish vasculature with optical projection tomography.* Journal of biomedical optics, 2011. **16**(10): p. 100502.

104. Kumar, S., et al., *Quantitative in vivo optical tomography of cancer progression & vasculature development in adult zebrafish.* Oncotarget, 2016. **7**(28): p. 43939.

105. d'Esposito, A., et al., *Computational fluid dynamics with imaging of cleared tissue and of in vivo perfusion predicts drug uptake and treatment responses in tumours.* Nature biomedical engineering, 2018. **2**(10): p. 773.

106. Weidner, N., et al., *Tumor angiogenesis and metastasis—correlation in invasive breast carcinoma.* New England Journal of Medicine, 1991. **324**(1): p. 1-8.

107. Weidner, N., *Measuring intratumoral microvessel density.* Methods in enzymology, 2008. **444**: p. 305-323.

108. Inda, A., et al., *Evaluation of angiogenesis with the expression of VEGF and CD34 in human non-small cell lung cancer.* J Exp Clin Cancer Res, 2007. **26**(3): p. 375-8.

109. Hollingsworth, H.C., et al., *Tumor angiogenesis in advanced stage ovarian carcinoma.* The American journal of pathology, 1995. **147**(1): p. 33.

110. Gasparini, G., et al., *Prognostic and predictive value of tumour angiogenesis in ovarian carcinomas.* International Journal of Cancer, 1996. **69**(3): p. 205-211.

111. Volm, M., et al., *Microvessel density, expression of proto-oncogenes, resistance-related proteins and incidence of metastases in primary ovarian carcinomas.* Clinical & experimental metastasis, 1996. **14**(3): p. 209-214.

112. Abulafia, O., W.E. Triest, and D.M. Sherer, *Angiogenesis in primary and metastatic epithelial ovarian carcinoma.* American journal of obstetrics and gynecology, 1997. **177**(3): p. 541-547.

113. Schoell, W.M., et al., *Tumor angiogenesis as a prognostic factor in ovarian carcinoma: quantification of endothelial immunoreactivity by image analysis.* Cancer: Interdisciplinary International Journal of the American Cancer Society, 1997. **80**(12): p. 2257-2262.

114. Brustmann, H., P. Riss, and S. Naudé, *The relevance of angiogenesis in benign and malignant epithelial tumors of the ovary: a quantitative histologic study.* Gynecologic oncology, 1997. **67**(1): p. 20-26.

115. Darai, E., et al., *CD31 expression in benign, borderline, and malignant epithelial ovarian tumors: an immunohistochemical and serological analysis.* Gynecologic oncology, 1998. **71**(1): p. 122-127.

116. Obermair, A., et al., *Prognostic significance of tumor angiogenesis in epithelial ovarian cancer.* Cancer letters, 1999. **138**(1-2): p. 175-182.

117. Alvarez, A.A., et al., *The prognostic significance of angiogenesis in epithelial ovarian carcinoma.* Clinical Cancer Research, 1999. **5**(3): p. 587-591.

118. Abulafia, O., et al., *Angiogenesis in early-invasive and low-malignant-potential epithelial ovarian carcinoma.* Obstetrics & Gynecology, 2000. **95**(4): p. 548-552.

119. Nakayama, K., et al., *Different features of angiogenesis between ovarian and breast carcinoma.* Cancer letters, 2001. **170**(2): p. 161-167.

120. Ogawa, S., et al., *Prognostic significance of microvessel density, vascular cuffing and vascular endothelial growth factor expression in ovarian carcinoma: a special review for clear cell adenocarcinoma.* Cancer letters, 2002. **176**(1): p. 111-118.

121. Stone, P.J., et al., *The influence of microvessel density on ovarian carcinogenesis.* Gynecologic oncology, 2003. **90**(3): p. 566-571.

122. Emoto, M., et al., *Differences in the angiogenesis of benign and malignant ovarian tumors, demonstrated by analyses of color Doppler ultrasound, immunohistochemistry, and microvessel density.* Cancer: Interdisciplinary International Journal of the American Cancer Society, 1997. **80**(5): p. 899-907.

123. Gadducci, A., et al., *Intratumoral microvessel density, response to chemotherapy and clinical outcome of patients with advanced ovarian carcinoma.* Anticancer research, 2003. **23**(1B): p. 549-556.

124. Suhonen, K.A., et al., *Quantification of angiogenesis by the Chalkley method and its prognostic significance in epithelial ovarian cancer.* European Journal of Cancer, 2007. **43**(8): p. 1300-1307.

125. Rubatt, J.M., et al., *Independent prognostic relevance of microvessel density in advanced epithelial ovarian cancer and associations between CD31, CD105, p53 status, and angiogenic marker expression: a Gynecologic Oncology Group study.* Gynecologic oncology, 2009. **112**(3): p. 469-474.

126. Pirtea, L., M. Raica, and A.M. Cimpean, *Endothelial cell activation and proliferation in ovarian tumors: two distinct steps as potential markers for antiangiogenic therapy response.* Molecular medicine reports, 2012. **5**(5): p. 1181-1184.

127. Ruscito, I., et al., *Characterisation of tumour microvessel density during progression of high-grade serous ovarian cancer: clinico-pathological impact (an OCTIPS Consortium study).* British journal of cancer, 2018. **119**(3): p. 330.

128. Kuzu, I., et al., *Heterogeneity of vascular endothelial cells with relevance to diagnosis of vascular tumours.* Journal of clinical pathology, 1992. **45**(2): p. 143-148.

129. Traweek, S.T., et al., *The Human Hematopoietic Progenitor Cell Antigen (CD 3 4) in Vascular Neoplasia.* American journal of clinical pathology, 1991. **96**(1): p. 25-31.

130. Vieira, S.C., et al., *CD34 as a marker for evaluating angiogenesis in cervical cancer.* Pathology-Research and practice, 2005. **201**(4): p. 313-318.

131. Leek, R.D., *The prognostic role of angiogenesis in breast cancer.* Anticancer research, 2001. **21**(6B): p. 4325-4331.

132. Krause, D.S., et al., *CD34: structure, biology, and clinical utility [see comments].* Blood, 1996. **87**(1): p. 1-13.

133. Fox, S.B., et al., *Quantitation and prognostic value of breast cancer angiogenesis: comparison of microvessel density, Chalkley count, and computer image analysis.* The Journal of pathology, 1995. **177**(3): p. 275-283.

134. Schoenfeld, A., et al., *Three-dimensional modelling of tumor-induced ovarian angiogenesis.* Cancer letters, 1994. **87**(1): p. 79-84.

135. Zhang, L., et al., *A feasible method of angiogenesis assessment in gastric cancer using 3D microvessel density.* Stem cells international, 2018. **2018**.

136. Netti, P.A., et al., *Time-dependent behavior of interstitial fluid pressure in solid tumors: implications for drug delivery.* Cancer Research, 1995. **55**(22): p. 5451-5458.

137. Jain, R.K. and L.T. Baxter, *Mechanisms of heterogeneous distribution of monoclonal antibodies and other macromolecules in tumors: significance of elevated interstitial pressure.* Cancer research, 1988. **48**(24 Part 1): p. 7022-7032.

138. DiResta, G.R., et al., *Characterization of neuroblastoma xenograft in rat flank. I. Growth, interstitial fluid pressure, and interstitial fluid velocity distribution profiles.* Microvascular research, 1993. **46**(2): p. 158-177.

139. Hofmann, M., et al., *Lowering of tumor interstitial fluid pressure reduces tumor cell proliferation in a xenograft tumor model.* Neoplasia, 2006. **8**(2): p. 89-95.

140. Jain, R.K., *Normalizing tumor microenvironment to treat cancer: bench to bedside to biomarkers.* Journal of Clinical Oncology, 2013. **31**(17): p. 2205.

141. Hompland, T., et al., *Peritumoral interstitial fluid flow velocity predicts survival in cervical carcinoma.* Radiotherapy and Oncology, 2014. **113**(1): p. 132-138.

142. Boucher, Y., et al., *Interstitial hypertension in superficial metastatic melanomas in humans.* Cancer research, 1991. **51**(24): p. 6691-6694.

143. Hompland, T., et al., *Assessment of the interstitial fluid pressure of tumors by dynamic contrast-enhanced magnetic resonance imaging with contrast agents of different molecular weights.* Acta Oncologica, 2013. **52**(3): p. 627-635.

144. Gulliksrud, K., K.G. Brurberg, and E.K. Rofstad, *Dynamic contrast-enhanced magnetic resonance imaging of tumor interstitial fluid pressure.* Radiotherapy and Oncology, 2009. **91**(1): p. 107-113.

145. Baxter, L.T. and R.K. Jain, *Transport of fluid and macromolecules in tumors. II. Role of heterogeneous perfusion and lymphatics.* Microvascular research, 1990. **40**(2): p. 246-263.

146. El-Kareh, A.W. and T.W. Secomb, *Effect of increasing vascular hydraulic conductivity on delivery of macromolecular drugs to tumor cells.* International Journal of Radiation Oncology• Biology• Physics, 1995. **32**(5): p. 1419-1423.

147. Soltani, M. and P. Chen, *Numerical modeling of fluid flow in solid tumors.* PloS one, 2011. **6**(6): p. e20344.

148. Soltani, M. and P. Chen, *Effect of tumor shape and size on drug delivery to solid tumors.* Journal of biological engineering, 2012. **6**(1): p. 4.

149. Zhan, W., W. Gedroyc, and X.Y. Xu, *The effect of tumour size on drug transport and uptake in 3-D tumour models reconstructed from magnetic resonance images.* PloS one, 2017. **12**(2): p. e0172276.

150.   Zhan, W., M. Alamer, and X.Y. Xu, *Computational modelling of drug delivery to solid tumour: understanding the interplay between chemotherapeutics and biological system for optimised delivery system.* Advanced drug delivery reviews, 2018.

151.   Zhan, W., W. Gedroyc, and X.Y. Xu, *Effect of heterogeneous microvasculature distribution on drug delivery to solid tumour.* Journal of Physics D: Applied Physics, 2014. **47**(47): p. 475401.

152.   Mohammadi, M. and P. Chen, *Effect of microvascular distribution and its density on interstitial fluid pressure in solid tumors: a computational model.* Microvascular research, 2015. **101**: p. 26-32.

153.   Zhao, J., H. Salmon, and M. Sarntinoranont, *Effect of heterogeneous vasculature on interstitial transport within a solid tumor.* Microvascular research, 2007. **73**(3): p. 224-236.

154.   Pishko, G.L., et al., *Sensitivity analysis of an image-based solid tumor computational model with heterogeneous vasculature and porosity.* Annals of biomedical engineering, 2011. **39**(9): p. 2360.

155.   Pishko, G.L., et al., *Role of convection and diffusion on DCE-MRI parameters in low leakiness KHT sarcomas.* Microvascular research, 2012. **84**(3): p. 306-313.

156.   Netti, P.A., et al., *Effect of transvascular fluid exchange on pressure–flow relationship in tumors: a proposed mechanism for tumor blood flow heterogeneity.* Microvascular research, 1996. **52**(1): p. 27-46.

157.   Baish, J.W., P.A. Netti, and R.K. Jain, *Transmural coupling of fluid flow in microcirculatory network and interstitium in tumors.* Microvascular research, 1997. **53**(2): p. 128-141.

158.   Milosevic, M.F., A.W. Fyles, and R.P. Hill, *The relationship between elevated interstitial fluid pressure and blood flow in tumors: a bioengineering analysis.* International Journal of Radiation Oncology* Biology* Physics, 1999. **43**(5): p. 1111-1123.

159.   Pozrikidis, C. and D. Farrow, *A model of fluid flow in solid tumors.* Annals of biomedical engineering, 2003. **31**(2): p. 181-194.

160.   Fleischman, G.J., T.W. Secomb, and J.F. Gross, *Effect of extravascular pressure gradients on capillary fluid exchange.* Mathematical biosciences, 1986. **81**(2): p. 145-164.

161.   McDougall, S.R., et al., *Mathematical modelling of flow through vascular networks: implications for tumour-induced angiogenesis and chemotherapy strategies.* Bulletin of mathematical biology, 2002. **64**(4): p. 673-702.

162.   Stephanou, A., et al., *Mathematical modelling of flow in 2D and 3D vascular networks: applications to anti-angiogenic and chemotherapeutic drug strategies.* Mathematical and Computer Modelling, 2005. **41**(10): p. 1137-1156.

163.   McDougall, S.R., A.R. Anderson, and M.A. Chaplain, *Mathematical modelling of dynamic adaptive tumour-induced angiogenesis: clinical implications and therapeutic targeting strategies.* Journal of theoretical biology, 2006. **241**(3): p. 564-589.

164.   Wu, J., et al., *Coupled modeling of blood perfusion in intravascular, interstitial spaces in tumor microvasculature.* Journal of Biomechanics, 2008. **41**(5): p. 996-1004.

165.   Zhao, G., et al., *Numerical simulation of blood flow and interstitial fluid pressure in solid tumor microcirculation based on tumor-induced angiogenesis.* Acta Mechanica Sinica, 2007. **23**(5): p. 477-483.

166.   Soltani, M. and P. Chen, *Numerical modeling of interstitial fluid flow coupled with blood flow through a remodeled solid tumor microvascular network.* PloS one, 2013. **8**(6): p. e67025.

167.   Chapman, S.J., R.J. Shipley, and R. Jawad, *Multiscale modeling of fluid transport in tumors.* Bulletin of mathematical biology, 2008. **70**(8): p. 2334.

168.   Wu, J., et al., *Study of tumor blood perfusion and its variation due to vascular normalization by anti-angiogenic therapy based on 3D angiogenic microvasculature.* Journal of biomechanics, 2009. **42**(6): p. 712-721.

169.   Pries, A., B. Reglin, and T.W. Secomb, *Structural adaptation of microvascular networks: functional roles of adaptive responses.* American Journal of Physiology-Heart and Circulatory Physiology, 2001. **281**(3): p. H1015-H1025.

170.   Stylianopoulos, T., et al., *Cationic nanoparticles have superior transvascular flux into solid tumors: insights from a mathematical model.* Annals of biomedical engineering, 2013. **41**(1): p. 68-77.

171.   Chauhan, V.P., et al., *Normalization of tumour blood vessels improves the delivery of nanomedicines in a size-dependent manner.* Nat Nanotechnol, 2012. **7**(6): p. 383-8.

172.   Cai, Y., et al., *Coupled modelling of tumour angiogenesis, tumour growth and blood perfusion.* Journal of Theoretical Biology, 2011. **279**(1): p. 90-101.

173.   Hsu, R. and T.W. Secomb, *A Green's function method for analysis of oxygen delivery to tissue by microvascular networks.* Mathematical biosciences, 1989. **96**(1): p. 61-78.

174.   Welter, M. and H. Rieger, *Interstitial fluid flow and drug delivery in vascularized tumors: a computational model.* PloS one, 2013. **8**(8): p. e70395.

175.   Cattaneo, L. and P. Zunino, *A computational model of drug delivery through microcirculation to compare different tumor treatments.* International journal for numerical methods in biomedical engineering, 2014. **30**(11): p. 1347-1371.

176.   Pozrikidis, C., *Numerical simulation of blood and interstitial flow through a solid tumor.* Journal of mathematical biology, 2010. **60**(1): p. 75-94.

177.   Sweeney, P.W., et al., *Modelling the transport of fluid through heterogeneous, whole tumours in silico.* PLoS computational biology, 2019. **15**(6): p. e1006751.

178.   Pang, K.S. and M.R. Durk, *Physiologically-based pharmacokinetic modeling for absorption, transport, metabolism and excretion.* Journal of pharmacokinetics and pharmacodynamics, 2010. **37**(6): p. 591-615.

179.   El-Kareh, A.W. and T.W. Secomb, *A mathematical model for comparison of bolus injection, continuous infusion, and liposomal delivery of doxorubicin to tumor cells.* Neoplasia, 2000. **2**(4): p. 325-338.

180.   Liu, C., et al., *Use of mathematical models to understand anticancer drug delivery and its effect on solid tumors.* Pharmacogenomics, 2011. **12**(9): p. 1337-1348.

181.   Sefidgar, M., et al., *Numerical modeling of drug delivery in a dynamic solid tumor microvasculature.* Microvascular research, 2015. **99**: p. 43-56.

182.   Rejniak, K.A., et al., *The role of tumor tissue architecture in treatment penetration and efficacy: an integrative study.* Frontiers in oncology, 2013. **3**.

183.   Thalhauser, C.J., et al., *Explicit separation of growth and motility in a new tumor cord model.* Bulletin of mathematical biology, 2009. **71**(3): p. 585.

184.   Eikenberry, S., *A tumor cord model for doxorubicin delivery and dose optimization in solid tumors.* Theoretical Biology and Medical Modelling, 2009. **6**(1): p. 16.

185.   Groh, C.M., et al., *Mathematical and computational models of drug transport in tumours.* J R Soc Interface, 2014. **11**(94): p. 20131173.

186.   Hubbard, M.E., et al., *Drug delivery in a tumour cord model: a computational simulation.* R Soc Open Sci, 2017. **4**(5): p. 170014.

187.   Kojic, M., et al., *A multi-scale FE model for convective–diffusive drug transport within tumor and large vascular networks.* Computer Methods in Applied Mechanics and Engineering, 2015. **294**: p. 100-122.

188.   Secomb, T.W., *A Green's function method for simulation of time-dependent solute transport and reaction in realistic microvascular geometries.* Mathematical medicine and biology: a journal of the IMA, 2015. **33**(4): p. 475-494.

189. Troendle, E.P., et al., *Predicting drug delivery efficiency into tumor tissues through molecular simulation of transport in complex vascular networks.* Journal of controlled release, 2018. **292**: p. 221-234.

190. Secomb, T.W., et al., *Green's function methods for analysis of oxygen delivery to tissue by microvascular networks.* Annals of biomedical engineering, 2004. **32**(11): p. 1519-1529.

191. Sefidgar, M., et al., *Effect of fluid friction on interstitial fluid flow coupled with blood flow through solid tumor microvascular network.* Computational and mathematical methods in medicine, 2015. **2015**.

192. Hobbs, S.K., et al., *Regulation of transport pathways in tumor vessels: role of tumor type and microenvironment.* Proceedings of the National Academy of Sciences, 1998. **95**(8): p. 4607-4612.

193. Zhan, W. and X.Y. Xu, *A mathematical model for thermosensitive liposomal delivery of Doxorubicin to solid tumour.* Journal of drug delivery, 2013. **2013**.

194. He, L., Q. Wang, and X. Zhao, *Microvessel density as a prognostic factor in ovarian cancer: a systematic review and meta-analysis.* Asian Pac J Cancer Prev, 2015. **16**(3): p. 869-74.

195. Munson, J.M. and A.C. Shieh, *Interstitial fluid flow in cancer: implications for disease progression and treatment.* Cancer management and research, 2014. **6**: p. 317.

196. Gimbrone Jr, M.A., et al., *Tumor growth and neovascularization: an experimental model using the rabbit cornea.* Journal of the National Cancer Institute, 1974. **52**(2): p. 413-427.

197. Muthukkaruppan, V., L. Kubai, and R. Auerbach, *Tumor-induced neovascularization in the mouse eye.* Journal of the National Cancer Institute, 1982. **69**(3): p. 699-708.

198. Rupnick, M., et al., *Quantitative analysis of random motility of human microvessel endothelial cells using a linear under-agarose assay.* Laboratory investigation; a journal of technical methods and pathology, 1988. **59**(3): p. 363-372.

199. Stokes, C., et al., *Chemotaxis of human microvessel endothelial cells in response to acidic fibroblast growth factor.* Laboratory investigation; a journal of technical methods and pathology, 1990. **63**(5): p. 657-668.

200. Sherratt, J.A. and J.D. Murray, *Models of epidermal wound healing.* Proceedings of the Royal Society of London. Series B: Biological Sciences, 1990. **241**(1300): p. 29-36.

201. Clark, R.A., et al., *Blood vessel fibronectin increases in conjunction with endothelial cell proliferation and capillary ingrowth during wound healing.* Journal of Investigative Dermatology, 1982. **79**(5): p. 269-276.

202. Sevick, E.M. and R.K. Jain, *Geometric resistance to blood flow in solid tumors perfused ex vivo: effects of tumor size and perfusion pressure.* Cancer research, 1989. **49**(13): p. 3506-3512.

203. Chary, S.R. and R.K. Jain, *Direct measurement of interstitial convection and diffusion of albumin in normal and neoplastic tissues by fluorescence photobleaching.* Proceedings of the National Academy of Sciences, 1989. **86**(14): p. 5385-5389.

204. Kamoun, W.S., et al., *Simultaneous measurement of RBC velocity, flux, hematocrit and shear rate in vascular networks.* Nature methods, 2010. **7**(8): p. 655.

205. Stokes, C.L. and D.A. Lauffenburger, *Analysis of the roles of microvessel endothelial cell random motility and chemotaxis in angiogenesis.* Journal of theoretical biology, 1991. **152**(3): p. 377-403.

206. Nugent, L.J. and R.K. Jain, *Extravascular diffusion in normal and neoplastic tissues.* Cancer research, 1984. **44**(1): p. 238-244.

207. Gas, P., *Temperature inside tumor as time function in RF hyperthermia.* arXiv preprint arXiv:1710.00656, 2017.

208. Jensen, M.M., et al., *Tumor volume in subcutaneous mouse xenografts measured by microCT is more accurate and reproducible than determined by 18 F-FDG-microPET or external caliper.* BMC medical imaging, 2008. **8**(1): p. 16.

209. Sarin, H., *Physiologic upper limits of pore size of different blood capillary types and another perspective on the dual pore theory of microvascular permeability.* Journal of angiogenesis research, 2010. **2**(1): p. 14.

210. Nagy, J.A., A.M. Dvorak, and H.F. Dvorak, *Vascular hyperpermeability, angiogenesis, and stroma generation.* Cold Spring Harbor perspectives in medicine, 2012. **2**(2): p. a006544.

211. Sitohy, B., J.A. Nagy, and H.F. Dvorak, *Anti-VEGF/VEGFR therapy for cancer: reassessing the target.* Cancer research, 2012. **72**(8): p. 1909-1914.

212. Kuszyk, B.S., et al., *Tumor transport physiology: implications for imaging and imaging-guided therapy.* American Journal of Roentgenology, 2001. **177**(4): p. 747-753.

213. Chugh, B.P., et al., *Measurement of cerebral blood volume in mouse brain regions using micro-computed tomography.* Neuroimage, 2009. **47**(4): p. 1312-1318.

214. Pathak, A.P., et al., *Three-dimensional imaging of the mouse neurovasculature with magnetic resonance microscopy.* PloS one, 2011. **6**(7): p. e22643.

215. Brizel, D.M., et al., *A comparison of tumor and normal tissue microvascular hematocrits and red cell fluxes in a rat window chamber model.* International Journal of Radiation Oncology* Biology* Physics, 1993. **25**(2): p. 269-276.

216. Kurbel, S., et al., *Model of interstitial pressure as a result of cyclical changes in the capillary wall fluid transport.* Medical hypotheses, 2001. **57**(2): p. 161-166.

217. Cantelmo, A.R., et al., *Vessel pruning or healing: endothelial metabolism as a novel target?* Expert opinion on therapeutic targets, 2017. **21**(3): p. 239-247.

218. Martin, J.D., G. Seano, and R.K. Jain, *Normalizing function of tumor vessels: progress, opportunities, and challenges.* Annual review of physiology, 2019. **81**: p. 505-534.

219. Au, J.-S., et al., *Determinants of drug delivery and transport to solid tumors.* Journal of controlled release, 2001. **74**(1-3): p. 31-46.

220. El-Kareh, A.W. and T.W. Secomb, *A mathematical model for cisplatin cellular pharmacodynamics.* Neoplasia, 2003. **5**(2): p. 161-169.

221. Dewhirst, M.W. and T.W. Secomb, *Transport of drugs from blood vessels to tumour tissue.* Nature Reviews Cancer, 2017. **17**(12): p. 738.

222. Kerr, D.J., et al., *Comparative intracellular uptake of adriamycin and 4'-deoxydoxorubicin by nonsmall cell lung tumor cells in culture and its relationship to cell survival.* Biochemical pharmacology, 1986. **35**(16): p. 2817-2823.

223. Friedman, M.H., *Principles and models of biological transport*. 2008: Springer Science & Business Media.

224. Greene, R.F., et al., *Plasma pharmacokinetics of adriamycin and adriamycinol: implications for the design of in vitro experiments and treatment protocols.* Cancer research, 1983. **43**(7): p. 3417-3421.

225. McGowan, J.V., et al., *Anthracycline chemotherapy and cardiotoxicity.* Cardiovascular drugs and therapy, 2017. **31**(1): p. 63-75.

226. Sacco, J.J., et al., *The average body surface area of adult cancer patients in the UK: a multicentre retrospective study.* PloS one, 2010. **5**(1): p. e8933.

227. Quintana, R.A., et al., *Early evidence of cardiotoxicity and tumor response in patients with sarcomas after high cumulative dose doxorubicin given as a continuous infusion.* Sarcoma, 2017. **2017**.

228. Ferguson, J., et al., *High dose, dose-intensive chemotherapy with doxorubicin and cyclophosphamide for the treatment of advanced breast cancer.* British journal of cancer, 1993. **67**(4): p. 825.

229. Esteban, L.L., et al., *CP-179 Patients exceeding doxorubicin recommended cumulative dose*. 2016, British Medical Journal Publishing Group.

230. Robert, J., et al., *Pharmacokinetics of adriamycin in patients with breast cancer: correlation between pharmacokinetic parameters and clinical short-term response.* European Journal of Cancer, 1982. **18**(8): p. 739-745.

231. Swabb, E.A., J. Wei, and P.M. Gullino, *Diffusion and convection in normal and neoplastic tissues.* Cancer research, 1974. **34**(10): p. 2814-2822.

232. Wu, N.Z., et al., *Measurement of material extravasation in microvascular networks using fluorescence video-microscopy.* Microvascular research, 1993. **46**(2): p. 231-253.

233. Kerns, E.H., et al., *Cellular uptake profile of paclitaxel using liquid chromatography tandem mass spectrometry.* Rapid communications in mass spectrometry, 1998. **12**(10): p. 620-624.

234. Kallinowski, F., et al., *Tumor blood flow: the principal modulator of oxidative and glycolytic metabolism, and of the metabolic micromilieu of human tumor xenografts in vivo.* International journal of cancer, 1989. **44**(2): p. 266-272.

235. Wehbe, K., et al., *Differentiation between normal and tumor vasculature of animal and human glioma by FTIR imaging.* Analyst, 2010. **135**(12): p. 3052-3059.

236. Forster, J.C., et al., *A review of the development of tumor vasculature and its effects on the tumor microenvironment.* Hypoxia, 2017. **5**: p. 21.

237. Legha, S.S., et al., *Reduction of doxorubicin cardiotoxicity by prolonged continuous intravenous infusion.* Annals of internal medicine, 1982. **96**(2): p. 133-139.

238. Hortobagyi, G., et al., *Decreased cardiac toxicity of doxorubicin administered by continuous intravenous infusion in combination chemotherapy for metastatic breast carcinoma.* Cancer, 1989. **63**(1): p. 37-45.

239. Lutz, A.M., et al., *Early diagnosis of ovarian carcinoma: is a solution in sight?* Radiology, 2011. **259**(2): p. 329-345.

240. Desai, A., et al., *Epithelial ovarian cancer: An overview.* World journal of translational medicine, 2014. **3**(1): p. 1.

241. Matulonis, U.A., et al., *Ovarian cancer.* Nature Reviews Disease Primers, 2016. **2**: p. 16061.

242. Mesiano, S., N. Ferrara, and R.B. Jaffe, *Role of vascular endothelial growth factor in ovarian cancer: inhibition of ascites formation by immunoneutralization.* The American journal of pathology, 1998. **153**(4): p. 1249-1256.

243. Ramos, I., et al., *Detection of neovascular signals in a 3 day Walker 256 rat carcinoma by CW Doppler ultrasound.* Ultrasound in medicine & biology, 1988. **14**(2): p. 123-126.

244. Konerding, M., E. Fait, and A. Gaumann, *3D microvascular architecture of pre-cancerous lesions and invasive carcinomas of the colon.* British journal of cancer, 2001. **84**(10): p. 1354.

245. Moreno, L. and A.D. Pearson, *How can attrition rates be reduced in cancer drug discovery?* 2013, Taylor & Francis.

246. Eklund, L., M. Bry, and K. Alitalo, *Mouse models for studying angiogenesis and lymphangiogenesis in cancer.* Molecular oncology, 2013. **7**(2): p. 259-282.

247. Dong, Z., et al., *Xenograft tumors vascularized with murine blood vessels may overestimate the effect of anti-tumor drugs: a pilot study.* PloS one, 2013. **8**(12): p. e84236.

248. Katt, M.E., et al., *In vitro tumor models: advantages, disadvantages, variables, and selecting the right platform.* Frontiers in bioengineering and biotechnology, 2016. **4**: p. 12.

249. Pautu, V., et al., *Melanoma tumour vasculature heterogeneity: from mice models to human.* Journal of cancer research and clinical oncology, 2019. **145**(3): p. 589-597.

250. Jackson, S.J. and G.J. Thomas, *Human tissue models in cancer research: looking beyond the mouse*. 2017, The Company of Biologists Ltd.

251. Eltoum, I., et al., *Introduction to the theory and practice of fixation of tissues.* Journal of Histotechnology, 2001. **24**(3): p. 173-190.

252. Williams, J., B. Mepham, and D. Wright, *Tissue preparation for immunocytochemistry.* Journal of clinical pathology, 1997. **50**(5): p. 422-428.

253. Weninger, W.J. and T. Mohun, *Phenotyping transgenic embryos: a rapid 3-D screening method based on episcopic fluorescence image capturing.* Nature genetics, 2001. **30**(1): p. 59.

254. Das Neves Borges, P., T.L. Vincent, and M. Marenzana, *Application of autofluorescence robotic histology for quantitative evaluation of the 3-dimensional morphology of murine articular cartilage.* Microscopy research and technique, 2017. **80**(12): p. 1351-1360.

255. Taniguchi, M. and J.S. Lindsey, *Database of Absorption and Fluorescence Spectra of> 300 Common Compounds for use in Photochem CAD.* Photochemistry and photobiology, 2018. **94**(2): p. 290-327.

256. Li, L., et al., *Binding of Sudan II and IV to lecithin liposomes and E. coli membranes: insights into the toxicity of hydrophobic azo dyes.* BMC structural biology, 2007. **7**(1): p. 16.

257. GRANDE, D.J. and F.W. PHILLIPS, *Histo-clear to replace xylene in the dermatopathology laboratory.* Dermatologic Surgery, 1985. **11**(2): p. 103-105.

258. Schindelin, J., et al., *Fiji: an open-source platform for biological-image analysis.* Nature methods, 2012. **9**(7): p. 676.

259. Pang, Z., N. Laplante, and R. Filkins, *Dark pixel intensity determination and its applications in normalizing different exposure time and autofluorescence removal.* Journal of microscopy, 2012. **246**(1): p. 1-10.

260. Kirbas, C. and F. Quek, *A review of vessel extraction techniques and algorithms.* ACM Computing Surveys (CSUR), 2004. **36**(2): p. 81-121.

261. Sternberg, S.R., *Biomedical image processing.* Computer, 1983(1): p. 22-34.

262. Zack, G.W., W.E. Rogers, and S. Latt, *Automatic measurement of sister chromatid exchange frequency.* Journal of Histochemistry & Cytochemistry, 1977. **25**(7): p. 741-753.

263. Lee, T.-C., R.L. Kashyap, and C.-N. Chu, *Building skeleton models via 3-D medial surface axis thinning algorithms.* CVGIP: Graphical Models and Image Processing, 1994. **56**(6): p. 462-478.

264. Tustison, N. and J. Gee, *Introducing Dice, Jaccard, and other label overlap measures to ITK.* Insight J, 2009. **2**.

265. Legland, D., I. Arganda-Carreras, and P. Andrey, *MorphoLibJ: integrated library and plugins for mathematical morphology with ImageJ.* Bioinformatics, 2016. **32**(22): p. 3532-3534.

266. Mineo, T., et al., *Prognostic impact of VEGF, CD31, CD34, and CD105 expression and tumour vessel invasion after radical surgery for IB–IIA non-small cell lung cancer.* Journal of clinical pathology, 2004. **57**(6): p. 591-597.

267. Arganda-Carreras, I., et al., *3D reconstruction of histological sections: Application to mammary gland tissue.* Microscopy research and technique, 2010. **73**(11): p. 1019-1029.

268. Bolte, S. and F.P. Cordelières, *A guided tour into subcellular colocalization analysis in light microscopy.* Journal of microscopy, 2006. **224**(3): p. 213-232.

269. Grahn, A., et al., *Volumetric imaging: a potential tool to stage upper tract urothelial carcinoma.* World journal of urology, 2019: p. 1-6.

270. Narmadha, C. and V. Malaichamy, *Expression of p53 and CD34 in Surface Epithelial Tumors of Ovary.*

271. Brissova, M., et al., *Human islets have fewer blood vessels than mouse islets and the density of islet vascular structures is increased in type 2 diabetes.* Journal of Histochemistry & Cytochemistry, 2015. **63**(8): p. 637-645.

272. Müller, B., et al. *High-resolution tomographic imaging of microvessels.* in *Developments in X-Ray Tomography VI*. 2008. International Society for Optics and Photonics.

273. Fallowfield, M.E., *Vascular volume in B16 allografts and human melanoma xenografts estimated by means of Hoechst 33342.* The Journal of pathology, 1989. **157**(3): p. 249-252.

274.   Tolaney, S.M., et al., *Role of vascular density and normalization in response to neoadjuvant bevacizumab and chemotherapy in breast cancer patients.* Proceedings of the National Academy of Sciences, 2015. **112**(46): p. 14325-14330.

275.   Okubo, Y., et al., *Risk factors associated with the progression and metastases of hindgut neuroendocrine tumors: a retrospective study.* BMC cancer, 2017. **17**(1): p. 769.

276.   Tanaka, N., et al., *Whole-tissue biopsy phenotyping of three-dimensional tumours reveals patterns of cancer heterogeneity.* Nature biomedical engineering, 2017. **1**(10): p. 796.

277.   Bates, R., et al., *Segmentation of Vasculature from Fluorescently Labeled Endothelial Cells in Multi-Photon Microscopy Images.* IEEE transactions on medical imaging, 2017. **38**(1): p. 1-10.

278.   Narayanaswamy, A., et al., *Robust adaptive 3-D segmentation of vessel laminae from fluorescence confocal microscope images and parallel GPU implementation.* IEEE transactions on medical imaging, 2009. **29**(3): p. 583-597.

279.   Lee, S.Y., et al., *Regulation of tumor progression by programmed necrosis.* Oxidative medicine and cellular longevity, 2018. **2018**.

280.   Li, X.-F., et al., *Visualization of hypoxia in microscopic tumors by immunofluorescent microscopy.* Cancer research, 2007. **67**(16): p. 7646-7653.

281.   Pries, A.R., et al., *Structural adaptation and heterogeneity of normal and tumor microvascular networks.* PLoS computational biology, 2009. **5**(5): p. e1000394.

282.   Lesage, D., et al., *A review of 3D vessel lumen segmentation techniques: Models, features and extraction schemes.* Medical image analysis, 2009. **13**(6): p. 819-845.

283.   Cosse, J.-P. and C. Michiels, *Tumour hypoxia affects the responsiveness of cancer cells to chemotherapy and promotes cancer progression.* Anti-Cancer Agents in Medicinal Chemistry (Formerly Current Medicinal Chemistry-Anti-Cancer Agents), 2008. **8**(7): p. 790-797.

284.   Graham, K. and E. Unger, *Overcoming tumor hypoxia as a barrier to radiotherapy, chemotherapy and immunotherapy in cancer treatment.* International journal of nanomedicine, 2018. **13**: p. 6049.

285.   Iyer, A.K., et al., *Exploiting the enhanced permeability and retention effect for tumor targeting.* Drug discovery today, 2006. **11**(17-18): p. 812-818.

286.   Olusanya, T.O., et al., *Liposomal drug delivery systems and anticancer drugs.* Molecules, 2018. **23**(4): p. 907.

287.   Salgia, R., *Prognostic significance of angiogenesis and angiogenic growth factors in nonsmall cell lung cancer.* Cancer, 2011. **117**(17): p. 3889-3899.

288.   Sauer, G. and H. Deissler, *Angiogenesis: prognostic and therapeutic implications in gynecologic and breast malignancies.* Current Opinion in Obstetrics and Gynecology, 2003. **15**(1): p. 45-49.

289.   Stanta, G. and S. Bonin, *Overview on clinical relevance of intra-tumor heterogeneity.* Frontiers in Medicine, 2018. **5**: p. 85.

Appendix A   Supplementary information

A.1 Tumour induced angiogenesis model

A set of probability coefficients were calculated which represent the potential movement of endothelial cells in a certain direction where P0 is the probability of no movement, and P1 ~ P6 represent the probability of movement in six directions along the x,y and z axis. The coefficients were calculated as follows:

$$P_0 = 1 - \frac{6kD}{h^2} + \frac{k\sigma\chi}{4h^2(1 + \sigma c_{l,m,n}^q)}\left[\left(c_{l+1,m,n}^q - c_{l-1,m,n}^q\right)^2 + \left(c_{l,m+1,n}^q - c_{l,m-1,n}^q\right)^2\right.$$

$$\left. + \left(c_{l,m,n+1}^q - c_{l,m,n-1}^q\right)^2\right]\ldots\ldots$$

$$- \frac{k\chi}{h^2(1 + \sigma c_{l,m,n}^q)}\left(c_{l+1,m,n}^q + c_{l-1,m,n}^q + c_{l,m+1,n}^q + c_{l,m-1,n}^q + c_{l,m,n+1}^q + c_{l,m,n-1}^q - 6c_{l,m,n}^q\right)\ldots\ldots$$

$$- \frac{k\rho}{h^2}\left(f_{l+1,m,n}^q + f_{l-1,m,n}^q + f_{l,m+1,n}^q + f_{l,m-1,n}^q + f_{l,m,n+1}^q + f_{l,m,n-1}^q - 6f_{l,m,n}^q\right)$$

$$P_1 = \frac{kD}{h^2} - \frac{k}{4h^2}\left[\frac{\chi}{(1 + \sigma c_{l,m,n}^q)}\left(c_{l+1,m,n}^q - c_{l-1,m,n}^q\right) + \rho\left(f_{l+1,m,n}^q - f_{l-1,m,n}^q\right)\right]$$

$$P_2 = \frac{kD}{h^2} + \frac{k}{4h^2}\left[\frac{\chi}{(1 + \sigma c_{l,m,n}^q)}\left(c_{l+1,m,n}^q - c_{l-1,m,n}^q\right) + \rho\left(f_{l+1,m,n}^q - f_{l-1,m,n}^q\right)\right]$$

$$P_3 = \frac{kD}{h^2} - \frac{k}{4h^2}\left[\frac{\chi}{(1 + \sigma c_{l,m,n}^q)}\left(c_{l,m+1,n}^q - c_{l,m-1,n}^q\right) + \rho\left(f_{l,m+1,n}^q - f_{l,m-1,n}^q\right)\right]$$

$$P_4 = \frac{kD}{h^2} + \frac{k}{4h^2}\left[\frac{\chi}{(1 + \sigma c_{l,m,n}^q)}\left(c_{l,m+1,n}^q - c_{l,m-1,n}^q\right) + \rho\left(f_{l,m+1,n}^q - f_{l,m-1,n}^q\right)\right]$$

$$P_5 = \frac{kD}{h^2} - \frac{k}{4h^2}\left[\frac{\chi}{(1 + \sigma c_{l,m,n}^q)}\left(c_{l,m,n+1}^q - c_{l,m,n-1}^q\right) + \rho\left(f_{l,m,n+1}^q - f_{l,m,n-1}^q\right)\right]$$

$$P_6 = \frac{kD}{h^2} + \frac{k}{4h^2}\left[\frac{\chi}{(1 + \sigma c_{l,m,n}^q)}\left(c_{l,m,n+1}^q - c_{l,m,n-1}^q\right) + \rho\left(f_{l,m,n+1}^q - f_{l,m,n-1}^q\right)\right]$$

The parameters used in the angiogenesis model are as follows.

Table A.1 Dimensionless parameters in model

Dimensionless parameter	Description	Value
D	Endothelial cell diffusion coefficient	0.00035
χ	Chemotactic coefficient	0.38
ρ	Hapotactic coefficient	0.34
β	Fibronectin production rate	0.05
γ	Fibronectin consumption rate	0.1
η	TAF consumption rate	0.1
φ	Threshold branching age	0.5

Appendix B   List of Publications

Journal Papers:

Wenbo Zhan*, Moath Alamer* and Xiao Yun Xu, "Computational modelling of drug delivery to solid tumour: Understanding the interplay between chemotherapeutics and biological system for optimised delivery systems", *Advanced Drug Delivery Reviews*, Vol: 132, Pages: 81-103, ISSN: 0169-409X

* Authors contributed equally

Conferences:

Moath Alamer and Xiao Yun Xu, "Computational Study of Microscopic Drug Transport and Distribution in Tumor Vasculature. *AIChE annual meeting,* Pittsburgh, US, 2018.

Moath Alamer and Xiao Yun Xu, "Investigating the Effect of Tumor Microvascular Architecture on Drug Transport and Distribution. *The 4th World Congress on Electrical Engineering and Computer Systems and Science,* Madrid, Spain, 2018.

Moath Alamer and Xiao Yun Xu, "Effect of Vascular heterogeneity on Fluid flow and transport in solid tumours. *Summer Biomechanics, Bioengineering, and Biotransport Conference,* Tucson, US, 2017.

Appendix C   Summary of permissions

Figure 1.1	
Figure 1.2	
Figure 1.3	

Figure 1.4

Figure 1.5

Figure 2.1

Figure 2.2